

A novel, internally structured stainless steel
implant with titanium characteristics

A thesis submitted for the degree of Doctor of Philosophy
By

Mohammadreza Yazdifar



College of Engineering, Design and Physical Sciences
Brunel University
February 2018

Table of Content

Table of Content	i
Table of Figures	vi
Table of Tables	xi
Abstract	xii
List of Publication	xiv
Acknowledgment	xv
Abbreviation	xvi
Notations	xviii
1 Introduction.....	1
1.1 Background and motivation for the study	1
1.2 Biomedical devices	3
1.3 Hollow porous spherical structure.....	4
1.4 The aim and objectives of the study.....	4
1.5 Structure of the thesis.....	5
2 Literature Review.....	7
2.1 Bone	7
2.1.1 Bone structure	7
2.1.2 Bone biomechanics and strength	8
2.1.3 Mechanical properties of bone.....	10
2.2 Hip replacement	11
2.2.1 Hip anatomy and symptoms for surgery	11
2.2.2 Total hip replacement devices	13
2.2.3 Stem material	15
2.2.4 Stem geometry	19
2.2.5 Stem surface finish.....	20
2.2.6 Failure after THR.....	21

2.2.7	Price of Implants	24
2.3	Factors in THR	25
2.3.1	Effect of bone geometry and quality	26
2.3.2	Effect of implant material, design and positioning	26
2.4	Stress Shielding	28
2.4.1	Bone loss	31
2.4.2	Implant materials	32
2.4.3	Implant stiffness	33
2.4.4	Optimising implants	34
2.5	Steel foams	35
2.5.1	Advantages	35
2.5.2	Steel foam manufacturing	36
2.5.2.1	Powder metallurgy	36
2.5.2.2	Hollow spheres	37
2.5.2.3	Lotus-type	38
2.5.3	Foams vs structures in this study	38
2.5.4	Auxetic materials	38
2.5.5	Tantalum	39
2.6	3D printing	39
2.6.1	Stereolithography (SLA)	39
2.6.2	Digital light processing (DLP)	40
2.6.3	Fused deposition modelling (FDM)	40
2.6.4	Selective laser sintering (SLS)	40
2.6.5	Selective laser melting (SLM)	41
2.6.6	Electronic beam melting (EBM)	41
2.6.7	Laminated object manufacturing (LOM)	42
2.6.8	Direct metal laser sintering (DMLS)	42

2.7	Finite element analysis in a biomedical study.....	43
2.7.1	ABAQUS Software.....	44
2.7.2	Material properties.....	44
2.7.3	Mesh element type and size.....	45
2.7.4	Modelling the interface between bone and implant.....	47
2.7.5	Applying boundary conditions such as muscle loads and constraints.....	48
2.7.6	Solution.....	54
2.7.7	Validation of results.....	54
2.7.8	Interpretation of the results.....	55
2.8	Conclusion.....	55
3	Research Method.....	58
3.1	Rule of mixtures.....	63
3.2	Finite element method.....	63
3.3	Compression test.....	63
4	Investigation of cylinder with hollow spheres close to the surface behaviour.....	64
4.1	Introduction.....	64
4.2	Study of 3-dimensional designs.....	65
4.3	Method.....	67
4.3.1	Rule of mixtures.....	67
4.3.1.1	Upper bound.....	68
4.3.1.2	Lower Bound.....	69
4.3.2	FEA Simulation.....	70
4.3.2.1	Cylinder Modelling.....	71
4.3.2.2	Cylinder material.....	71
4.3.2.3	Cylinders boundary conditions.....	72
4.3.2.4	Force and pin area.....	72
4.3.2.5	Cylinder mesh accuracy.....	73

4.3.3	Experiment to validate the FEA results	73
4.4	Results	75
4.4.1	Results of the rule of mixtures	75
4.4.2	Finite element analysis.....	77
4.4.3	Compression Results.....	84
4.5	Minimising stress shielding by changing the volumetric ratio	85
4.6	Conclusion.....	91
5	Investigation of cylinders with evenly distributed hollow spheres within a constant mass behaviour.....	93
5.1	Introduction	93
5.2	Study of 3-dimensional designs	94
5.3	Method	96
5.3.1	Rule of mixtures.....	96
5.3.2	FEA simulation	96
5.3.2.1	Cylinder modelling	97
5.3.2.2	Cylinder material	97
5.3.2.3	Cylinder boundary condition	98
5.3.2.4	Force and pin area.....	98
5.3.2.5	Cylinder mesh accuracy.....	98
5.3.3	Experiment to validate the FEA results	99
5.3.3.1	3-D model	99
5.3.3.2	Samples measurements.....	99
5.3.3.3	Compression test.....	100
5.4	Results	100
5.4.1	Results of the rule of mixtures	100
5.4.2	Finite element analysis.....	102
5.4.3	Compression results	113

5.5	Minimising stress shielding by changing the volumetric ratio	114
5.6	Conclusion.....	121
6	Investigation of hollow sphered implant behaviour.....	122
6.1	Introduction	122
6.2	Methodology	123
6.2.1	FEA analysis	123
6.2.1.1	Part module.....	123
6.2.1.2	Property module	127
6.2.1.3	Implant boundary condition.....	129
6.2.1.4	Force and pin area.....	129
6.2.1.5	Implant mesh accuracy	130
6.2.2	Rule of mixtures.....	131
6.3	Implant finite element results	132
6.4	Conclusion.....	140
7	Discussion and Conclusion	141
7.1	Discussion	141
7.2	Final Conclusion	147
7.3	Recommendations for future works	148
	Bibliography	149
	Appendix.....	165

Table of Figures

Figure 1-1 Reported hip procedures in Australia per year based on Australian Orthopaedic Association (NJRR, 2017)	3
Figure 2-1 Bone shapes: Long bones, such as the femur (left); short bones, such as the vertebra (centre); and plate-like bones, such as the skull (right) (Fratzl & Weinkamer, 2007) 8	8
Figure 2-2 The spongy structure of trabecular bones found in the vertebra or the femoral head (Fratzl & Weinkamer, 2007).....	8
Figure 2-3 Illustration of bone architecture (Pierce, et al., 2004).....	9
Figure 2-4 Typical values of stiffness (Young’s modulus) and toughness (fracture energy) for tissues mineralised with hydroxyapatite (Ashby, et al., 1995)	9
Figure 2-5 Difference between the ultimate stress of cortical and cancellous bone (Nigg & Herzog, 1999)	10
Figure 2-6 Schematic of total hip replacement (English, et al., 2015)	11
Figure 2-7 Components of the natural hip (Anon., 2014).....	12
Figure 2-8 Phases of the human gait (Kernozek & Willson, 2015).....	13
Figure 2-9 (a) Femoral bone structure and (b) typical hip implant (Yongtae & Kuiwoon, 2010)	14
Figure 2-10 A cemented and un-cemented implant (Schmidler, 2016).....	15
Figure 2-11 Load transfer patterns (a) within the natural femur (b) around the C stem (Zhang, 2009)	19
Figure 2-12 Various causes of implant failure (Geetha, et al., 2009).....	24
Figure 2-13 Simple schema of stress shielding zone (Surin, 2005).....	29
Figure 2-14 Stress distribution along medial and lateral sides when a 4,000 N applied load was given onto proximal head (Ridzwan, et al., 2007).....	30
Figure 2-15 Preoperative femoral bone loss among the 35 hips is graded based on the American Academy of Orthopaedic Surgeons (AAOS) classification system (Engh, et al., 2002)	32
Figure 2-16 Implant designed proposed by (Chang , et al., 2001).....	35
Figure 2-17 Typical stress–strain curve for metal foams in compression (Smith, et al., 2012)	36
Figure 2-18 Electronic beam melting (EBM)	42
Figure 2-19 Direct metal laser sintering (DMLS) (whiteclouds, 2015).....	43
Figure 2-20 Illustration of simplex, complex and multiplex elements (Fagan, 1992).....	46

Figure 2-21 Two rectangular elements with the same aspect ratio with different behaviours (Fagan, 1992)	47
Figure 2-22 The force components in x,y,z directions. The axis x is parallel to the dorsal contour of the femoral condyles in the transverse plane and z is parallel to the idealised midline of the femur (Bergmann, et al., 2001)	49
Figure 2-23 Muscles of the hip (González, 2009)	50
Figure 2-24 Average, minimum and maximum values for hip contact force (Bergmann, et al., 2001)	51
Figure 2-25 Top: muscle sets included in the analysis. Bottom: oblique view of the femur solid model showing the location of node constraints for each configuration (Speirs, et al., 2007)	52
Figure 2-26 Deflected femur (solid) under walking loads in the anterior (top) and medial (bottom) views compared to the undeflected shape (outline) (Speirs, et al., 2007)	53
Figure 2-27 Unacceptable element combinations (Fagan, 1992)	54
Figure 3-1 Schematic view of the logics behind each chapter of this thesis	59
Figure 3-2 Contents of the chapters for this thesis	60
Figure 3-3 Summary of chapters 4 and 5	61
Figure 3-4 Summary of chapter 6	62
Figure 4-1 Schematic view of a hollow shell cylinder	65
Figure 4-2 Hollow shell cylinder views a) defined parameters; b) examples of hollow shell cylinder dimensions	66
Figure 4-3 The matrix and fibres in the composite materials	68
Figure 4-4 Force and pin area	72
Figure 4-5 Compression machine used to carry out stress-strain tests	74
Figure 4-6 ABS models of solid and hollow shell cylinders	75
Figure 4-7 Von Mises stress and displacement for different distance from each other vertically: a) 4mm; b) 5mm	78
Figure 4-8 Von Mises stress and displacement for different distance from the side-surface: a) 2mm; b) 5mm.....	79
Figure 4-9 Von Mises stress and displacement for different numbers of spheres in each row (different distance horizontally): a) 24 spheres; b) 12 spheres	80
Figure 4-10 Von Mises stress and displacement for different sphere radius sizes: a) 1mm; b) 2mm	81
Figure 4-11 Von Mises stress and displacement of solids: a) titanium; and b) stainless steel	82

Figure 4-12 Von Mises stress and displacement for the experiment case	83
Figure 4-13 Stress-strain graph of solid and hollow spheres close to the surface of the structure.....	85
Figure 4-14 The relationship between the radius of the spheres in (mm) and their number ...	87
Figure 4-15 The relationship between hollow shell thickness (mm) and the height of the cylinder (mm).....	89
Figure 4-16 Relationship between the number of spheres and radius of the cylinder (mm) ...	90
Figure 4-17 Relationship between hollow shell thickness (mm) and radius of the cylinder (mm).....	91
Figure 5-1 Uniformly hollow sphere in the cylinder samples	94
Figure 5-2 The other two specimens with different porous structures	97
Figure 5-3 Pin and force area of the hollow cylinder	98
Figure 5-4 One of the samples between compression anvils.....	100
Figure 5-5 Solid stainless steel FEA results: a) von Mises stress distribution (MPa); b) displacement (mm) Solid Titanium FEA results; c) von Mises stress distribution (MPa); d) displacement (mm).....	102
Figure 5-6 R1 FEA results: a) von Mises stress distribution (MPa); b) displacement (mm)	103
Figure 5-7 R1/2 FEA results: a) von Mises stress distribution (MPa); b) displacement (mm)	104
Figure 5-8 R1.5 FEA results: a) von Mises stress distribution (MPa); b) displacement (mm)	105
Figure 5-9 R1.5/2 FEA results: a) von Mises stress distribution (MPa); b) displacement (mm)	106
Figure 5-10 R2 FEA results: a) von Mises stress distribution (MPa); b) displacement (mm)	107
Figure 5-11 R2/2 FEA results: a) von Mises stress distribution (MPa); b) displacement (mm)	108
Figure 5-12 R3 FEA results: a) von Mises stress distribution (MPa); b) displacement (mm)	109
Figure 5-13 R3.5 FEA results: a) von Mises stress distribution (MPa); b) displacement (mm)	110
Figure 5-14 R4 FEA results: a) von Mises stress distribution (MPa); b) displacement (mm)	111

Figure 5-15 FEA results for four cylindrical holes (new design/2): a) von Mises stress distribution (MPa); b) displacement (mm)	111
Figure 5-16 FEA results for four hollow ellipsoids (new design/1): a) von Mises stress distribution (MPa); b) displacement (mm)	112
Figure 5-17 The relationship between the radius of spheres (mm) and their number	116
Figure 5-18 Relationship between the number of spheres and the radius of the cylinder (mm)	117
Figure 5-19 Parameter of a cylinder with 38mm height and 6mm radius	118
Figure 5-20 Relationship between r_{air} and d when $2r_{air} + 2d > r_{all}$	119
Figure 5-21 Relationship between r_{air} and d when $2r_{air} + 2d < r_{all}$	120
Figure 6-1 Hip stem dimensions	123
Figure 6-2 Wireframe vs shaded view of the stem	124
Figure 6-3 Wireframe vs shaded view of the bone shaped design	127
Figure 6-4 Schematic diagram of bone material	128
Figure 6-5 Force and pin area	130
Figure 6-6 Mesh of the implant	131
Figure 6-7 Relationship between the number of spheres in an implant and their radius (mm)	132
Figure 6-8 Von Mises stress for solid stainless steel: a) bone; b) bone and implant; c) implant	133
Figure 6-9 Von Mises stress for solid titanium: a) bone; b) bone and implant; c) implant ..	134
Figure 6-10 Von Mises stress in implant containing spheres with 1mm radius: a) bone; b) bone and implant; c) implant	135
Figure 6-11 Von Mises stress in an implant containing unlimited hollow spheres with 1.5mm radius: a) bone; b) bone and implant; c) implant	136
Figure 6-12 Von Mises stress in an implant containing limited spheres with 1.5mm radius: a) bone; b) bone and implant; c) implant	137
Figure 6-13 Von Mises stress in an implant containing limited spheres with 2mm radius: a) bone; b) bone and implant; c) implant	138
Figure 6-14 Von Mises stress in an implant containing unlimited spheres with 2mm radius: a) bone; b) bone and implant; c) implant	139
Figure 7-1 Transferred stress to bone from two specimens	142
Figure 7-2 Stress distribution in implants for titanium, stainless steel and hollow structure sample	145

Figure 7-3 Stress distribution in bone for titanium, stainless steel and hollow structure sample146

Figure 7-4 Stress distribution in bone for titanium and stainless steel implants containing different hollow sphere sizes147

Table of Tables

Table 1-1 Summary of annual statistics of hip replacement in the UK based on National Joint Registry (Registry, 2017).....	3
Table 2-1 Comparison of mechanical properties of metallic biomaterials with bone (Ratner, et al., 1996)	10
Table 2-2 Comparison of metallic biomaterials used in the human body (Hussein, et al., 2015)	18
Table 4-1 Various designs used for this chapter based on distribution and sphere size	67
Table 4-2 Mechanical properties of common biomaterials (Sabatini & Goswami, 2008)	72
Table 4-3 Calculation results according to the rule of mixtures	77
Table 4-4 Von Mises stress results for the different study cases	84
Table 5-1 Twelve samples of hollow cylinders	95
Table 5-2 Weight and dimension of the samples measured by scale and a digital Vernier caliper.....	99
Table 5-3 Calculation results for different hollow cylinder designs.....	101
Table 5-4 Finite element results for sphered cylinders	113
Table 5-5 Experimental results for hollow cylinders.....	114
Table 6-1 Implant samples information	125
Table 6-2 Schematic view of the designed implants with 2 mm and 1.5 mm sphere radius .	125
Table 6-3 Results of calculations for the implants.....	140
Table 7-1 Comparison of the modulus in different samples for computational, the rule of mixtures and experimental results	143
Table 7-2 Percentage reduction in Young's modulus compared to the solid model	144

Abstract

There are many aspects that have direct effects on total hip replacement performance (THR), such as material properties, applied loads, surgical approach, femur size and quality, prosthesis design, bone-implant interface etc. Bone mechanics and traditional implant materials cause a frequent problem for patients of total hip arthroplasty (THA): the bone becomes shielded from the loading. Bone structure follows what is called “Wolff’s Law”, meaning it has an adaptive structure, which alters its geometry when experiencing forces over its life (Goldstein, 1987); (Pearson & Lieberman, 2004). The improved femoral stems act weakly in transferring stress onto the remnant bone and bone tissue atrophies at the interface, which will result in loosening of the implant, pain and thus, revision surgery will need to take place to correct the issue (Feldt, 2011).

For the current study, an innovative hollow spherical structure is developed for femoral hip stems. The aim is to extract volume in the spherical shape from the stainless steel hip implant stems, in order to focus solely on correlating with titanium behaviour. Internal geometry for the femoral stem is optimised in order to transfer more stress onto the bone. Moreover, the approach involves extracting volume in the spherical shape from internal structure to reduce stress shielding. New novel implant is proposed that demonstrated reduction in stress shielding.

A new structure has been developed in this study for biomedical applications, such as implants, with the aid of the rule of mixtures and finite element analysis was applied to various models with different complex internal structures. Firstly, the rule of mixtures was used as finite element could not handle the simulation due to the large number of elements created, and also helped developing the designs analysed in this study. Secondly, computational analysis was applied to simplified finite elements containing hollow spheres in their outer shell. Moreover, a compression test was applied to a solid sample and the experimental case. This approach was adopted to investigate the effects of a hollow structure near the side surface and the bone-implant interface. The same method was applied to samples containing uniformly distributed hollow spheres. In the both scenarios, the specimens were designed differently based on the sphere size, their distance from wall and that from each other. Finally, finite element was applied to actual implant samples containing hollow spheres.

The sphered models have a smaller Young's modulus and strength than the solid stainless steel sample. The spheres in hollowed structures reduce the stress shielding and they transfer more stress onto the bone when compared to the solid stainless steel models. This approach also involves restructuring a hard material, such as stainless steel, to enhance osseointegration. The reduction of the Young's modulus and stress directly depends on the volume of the hollow spheres in the models; however, there is certain volume that can be extracted from solid.

List of Publication

- Yazdifar, M, Esat, I. & Yazdifar, M., 2018. The effect of hollow sphered structure on stress shielding reduction. *European Scientific Journal*, 14(6).
- Yazdifar , M., Yazdifar, M. & Esat, I., 2017. The Effect of Soft Tissue on Detecting Hip. *European Scientific Journal*, 13(18), pp. 57-72.
- Yazdifar , M. & Yazdifar , M., 2015. Evaluating the hip range of motion using the goniometer, the nintendo wiimote and video tracking methods. *European Scientific Journal*, 11(21).
- Yazdifar, M. & Yazdifar, M., 2015. Review of research and methods regarding the diagnosis of hip impingement. *European Scientific Journal*, 11(15).
- 3-D modelling of hip in mimics software paper presented in materialise world summit 2015, Brussels, Belgium.
- “Peridynamics via FEA” paper presented in 6th annual research student conference (Rescon14), 2014, Brunel University, London, UK.

Acknowledgment

I wish to extend my sincerest gratefulness to my supervisor, Professor Ibrahim Esat who has been a continuous supporter throughout all stages of the study.

I would like to also convey my deepest appreciation to my sister, Dr Mahshid Yazdi Far, who made this work possible. I would not have been able to finish this work without her every day support. Indeed without her constant emotional and supports, the completion of this thesis would have had no meaning.

I am forever indebted to my parents, for supporting me throughout this journey, providing the opportunity to study PhD, without them the completion of this work would have been impossible.

I would also like to thank Brunel University, Brunel Civil Engineering department's laboratory, Tony Morris for their support.

Abbreviation

1D	One dimensional
2D	Two dimensional
3D	Three dimensional
ABS	Acrylonitrile butadiene styrene
AM	Additive manufacturing
BMC	Bone mineral content
BMD	Bone mineral density
BMI	Body mass index
CAD	Computer-Aided Design
CAE	Complete Abaqus environment
CFD	Computational Fluid Dynamics
DEXA	Dual energy x-ray of absorptiometry
DLP	Digital light processing
DMLS	Direct metal laser sintering
DNA	DeoxyriboNucleic Acid
EBM	Electronic beam melting
FDM	Fused deposition modelling
FE	Finite element
FEA	Finite element analysis
FEM	Finite element modelling
Inp	Abaqus Input extension
LOM	Laminated object manufacturing
N/A	Not applicable
NHS	National health service
PTC	Parametric technology corporation
PTFE	polytetrafluoroethylene
SLA	Stereolithography
SLM	Selective laser melting
SLS	Selective laser sintering
SP	Service pack
STL	Standard Tessellation Language

THR	Total hip replacement
UHMWPE	Ultra-high molecular weight polyethylene
UK	United Kingdom
UTS	Ultimate tensile strength
UTS _c	Composite ultimate tensile strength

Notations

$Area_{shell}$	Area of the sphered shell
E_{air}	Young modulus of air
E_c	Compression modulus
E_f	Material property of the fibres
E_m	Material property of the matrix
E_{steel}	Young modulus of steel
V_f	Volume of fibre (volume of air)
V_m	Volume of matrix (volume of solid)
V_{total}	Total volume
m'	number of spheres each column
r^3	Sphere radius
r_{air}	Radius of vacuum
r_{total}	Radius of the objects
$volume_{implant}$	Total volume of implant
σ_c	Composite strength
σ_{steel}	Stress of steel
Al	Aluminium
cm^3	cubic centimetre
Co	Cobalt
Co-Cr-Mo	Cobalt-chromium-molybdenum
Cr	Chromium
Fe	Iron
g	Gram
GPa	Gigapascal
h	Height
KN	Kilo-newtons
mm	Millimetre
mm^3	Cubic millimetre
Mo	Molybdenum
MPa	Megapascal
Nb	Niobium

Ni	Nickle
Ti	Titanium
V	Vanadium
Zr	Zirconium
ν	Poisson's ratio
E	Young modulus
d	Distance of spheres from the wall of cylinder
f	Volume fraction of the fibres
m	number of spheres each row
n	Number of spheres

1 Introduction

1.1 Background and motivation for the study

Introducing new materials or optimising current materials or their structures is an important aspect in biomedical engineering to improve functionality of biomedical devices. Furthermore, new biomaterials with enhanced materials properties or structure could be developed. These improvements in biomedical devices will result in disappearing issues and existing problems that current devices have. This research focuses on new controlled porous structure in closed volumes for biomedical device applications. Total hip replacement (THR) is one of the most successful and usual operations implemented hundreds of thousands of times each annum worldwide to improve daily activities. In THR, the hip joint is replaced with artificial femoral stem and acetabular shell. The importance of designing a new structure for a better performance of the implants for THR lies in the fact that, as above mentioned, many of these surgeries are accomplished every year all over the world.

Figure 1-1 shows the number of hip procedures performed in Australia for each year. It can be observed that, between 2006 and 2016, the number of hip procedures increased by over 15,000. As can also be seen, the number of hip procedures increased year on year and hence, the need for an adequate hip implant would appear to be growing. Table 1-1 illustrates the number of operations implemented by NHS and independent hospitals in the UK. As is shown, the number of hip replacements performed by the NHS is approximately twice that of independent hospitals. Furthermore, these operations are very costly for the NHS, not only in terms of the operation, but also regarding the cost of implant production. In sum, the rates for hip procedures for Australia and the UK have been exhibiting an upward trend. Moreover, according to the National Joint Registry, most patients have a revision risk of 5% or less at 12 years after their first surgery. However, these results are slightly higher for younger patients,

especially those under 55 years of age. Therefore, implants may be replaced within the first year due to fracture, dislocation or infection or it could be after five years due to implant loosening or pain (National joint registry, 2016).

Whilst the biological joint may require replacement, the replacement joint could also need revision surgery when facing complications. Finite element analysis (FEA) is a common tool used to solve complicated problems at the lowest cost possible. That is, this method can be used without prototyping to reduce the costs significantly. In addition, FEA can be performed for the analysis of hip implants to avoid in vivo testing, if the implant is going to have negative impact.

It has to be mentioned that there are uncertainties in THR constructs, which will influence the performance of the implanted hip. These uncertainties could relate to external factors such as temperature, surgeon's skill, patient collaboration in the recovery, etc. On the other hand, it could be due to the surgical interposition process such as patient geometry, implant selection, insertion method, etc (González, 2009). However, most FEA research to date has looked into specific matters, instead of including random factors. Moreover, it could also be deployed to recognise the factors that are the most salient causes of failure, thereby guide researchers in providing new solutions.

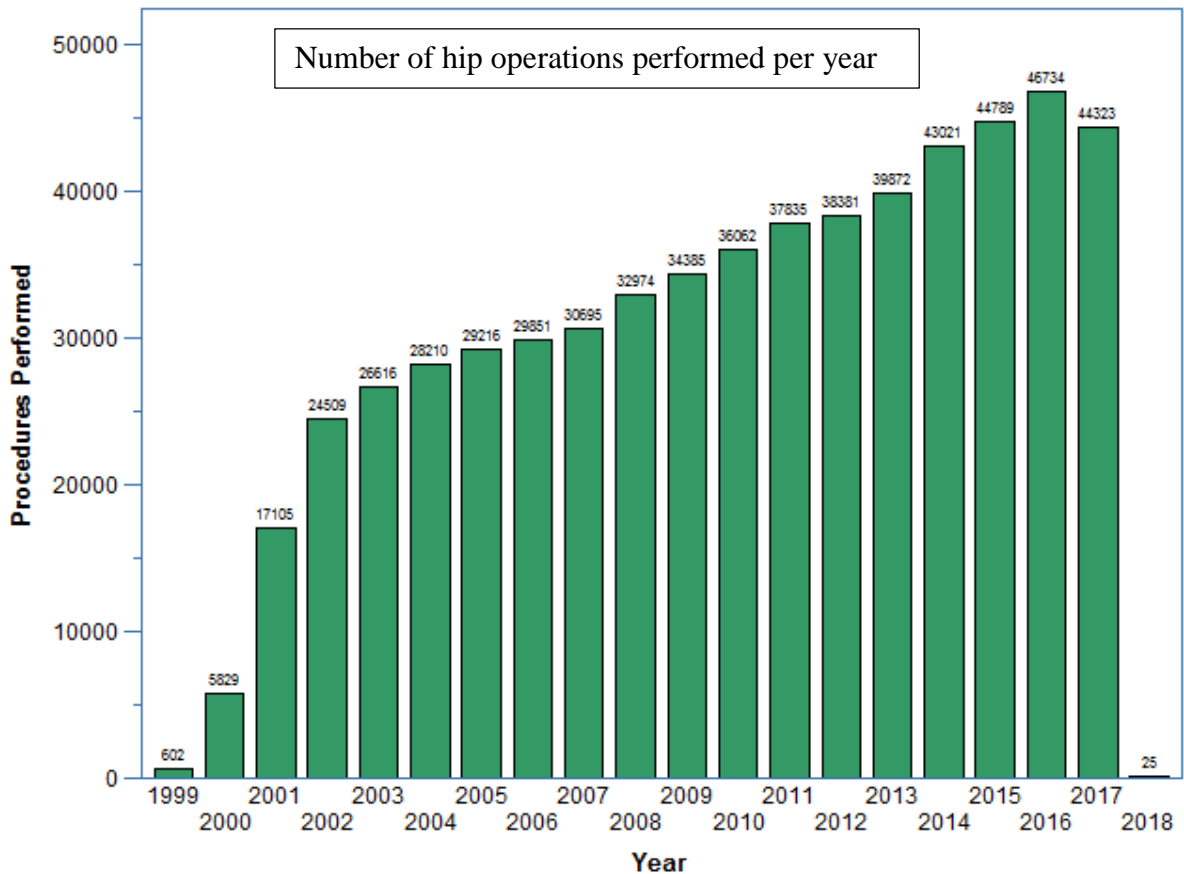


Figure 1-1 Reported hip procedures in Australia per year based on Australian Orthopaedic Association (NJRR, 2017)

Table 1-1 Summary of annual statistics of hip replacement in the UK based on National Joint Registry (Registry, 2017)

Provider	Number of operations (Hip procedures)	
	2016	Year to date:2017
NHS	67,374	32,356
Independent Hospitals	36,853	20,496
Total	104,227	52,852

1.2 Biomedical devices

A biomedical device can take many forms, such as an instrument, apparatus, implement, machine, appliance or implant, used on its own or in combination, to diagnose, prevent, monitor, treat or alleviate disease as well as to replace or modify the human anatomy (Goad

& Goad, 2002). However, in this study, the focus is on hip implants in terms of improving their material properties.

Designing a biomedical device requires knowledge in various fields such as human anatomy and physiology, material science, device engineering and different engineering disciplines. Additional knowledge in other areas may be needed depending on the specific application. Such other fields could include immunology and neurology, or biomedical materials properties which could be used in certain biological applications.

1.3 Hollow porous spherical structure

Having structure like spheres within a mass will force the stress to distribute. Specially, having the right number of spheres based on the material's property and its volume, will decrease the Young's modulus, whilst having the same strength as the solid form. This type of porous structure could be used widely in biomedical applications to improve the implant models by reducing stress shielding. Stress shielding is a phenomenon that occurs in the femur after implanting, which results in bone density reduction.

There are many types of porous stainless steel, such as steel foams, that are widely used in different applications, such as aerospace, civil engineering, automobiles and etc. Having porous structure will improve the material properties of metals without weakening them. In sum, the idea of having hollow spheres within a closed and controlled mass will enhance current hip implant designs, in terms of improved stress distribution.

1.4 The aim and objectives of the study

The main aim of this project is to develop cost-effective implants by creating a novel hollow spherical structure within a stainless steel femoral stem to mimic the behaviour of titanium implants. In addition, the structure would be ideal for stress shielding reduction in comparison to titanium.

The price of raw titanium is 14 times more expensive than the price of raw stainless steel. Considering the manufacturing technique for the proposed structure (additive manufacturing) being better in comparison to the conventional method (subtractive manufacturing); not only it is more cost-effective, it is also efficient in terms of detailed and complex geometries. Therefore, mass production could be less wasteful, cost-effective and more detailed while using the additive manufacturing.

It is proposed that having hollow spheres, not only reduces the Young's modulus and stiffness of the material, for it also decreases stress shielding and prevents bone resorption, thereby improving the life of the implant.

In order to achieve this aim:

- Simplified cylindrical specimens containing hollow spheres near the surface are modelled;
- Finite element analysis is used for every model in Abaqus environment;
- Solid cylinders and others with hollow spheres are printed in ABS plastics to test under compression;
- Rule of mixtures is used at every step to design the samples as simulation was impossible due to the high number of elements;
- The study involves developing uniformly distributed spheres within a constant cylindrical volume based on compression testing standard to illustrate the wider principles of a hollow structure;
- Stainless steel 3D printing is used to create simplified uniformly distributed sphered samples to conduct compression tests;
- The hollow sphered structure is applied to a model of hip prosthesis based on rule of mixtures to carry out finite element analysis.

1.5 Structure of the thesis

This research is set out as follows:

Chapter 2 provides a review of the background literature on hip anatomy, hip implants, porous structures and foams, the price of hip implants, different types of three dimensional printing, total hip replacement and stress shielding.

Chapter 3 presents the methods used for this study and the process to achieve the aim of the study.

Chapter 4 presents finite element analysis (FEA) of having hollow spheres in the outer shell of a cylinder and using plastic printing for experimentation. The difference that hollow shell spheres makes to the stress distribution is demonstrated using stress-strain graphs.

Chapter 5 describes FEA on cylinders with even hollow spheres distribution based on a British Standards compression test. It also looks at the results for compression tests

accomplished on printed samples. It also provides the stress-strain relationship graphs for further analysis.

Chapter 6 contains FEA of actual implant designs and how the spheres effect the stress distribution. It also subjects the stress-strain graphs to further detailed analysis.

Chapter 7 includes discussion and conclusion of this thesis along with how the present work could be improved and developed in the future works towards actual applications.

2 Literature Review

2.1 Bone

An introduction to bone is provided here to understand the structure and mechanical properties of the femur. Structural support and protection for internal organs are contributed by the bones in our body, which comprise dense and hard tissue.

2.1.1 Bone structure

Bones are split into two main categories, Long bones, such as the femur or tibia and short bones, such as vertebra or the head of the femur, which are filled with spongy material and are known as trabecular or cancellous bone. Stability is provided by bones against bending and bulking. Another bone category is plate-like bones, such as the skull. There are also bones that do not undergo fit into any category, such as the flat bones of the cranium and irregular bones. In addition, the morphology of bones at the organ, tissue and cellular levels is fairly stable. The classification of the bone is related to the size and shape of it (Fratzl & Weinkamer, 2007). Figure 2-1 displays different types of bone and Figure 2-2 shows their molecular structure.

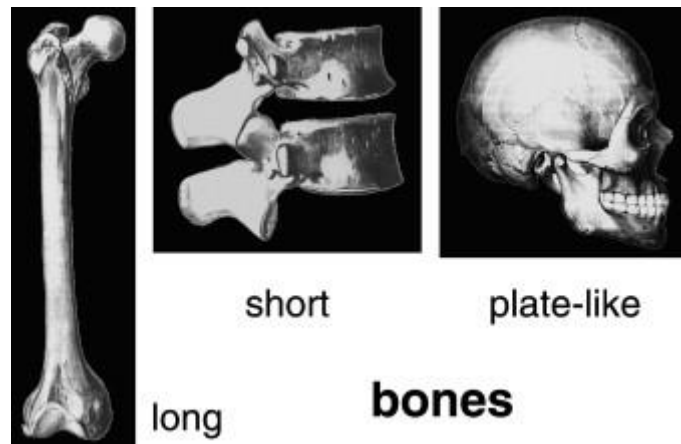


Figure 2-1 Bone shapes: Long bones, such as the femur (left); short bones, such as the vertebra (centre); and plate-like bones, such as the skull (right) (Fratzl & Weinkamer, 2007)

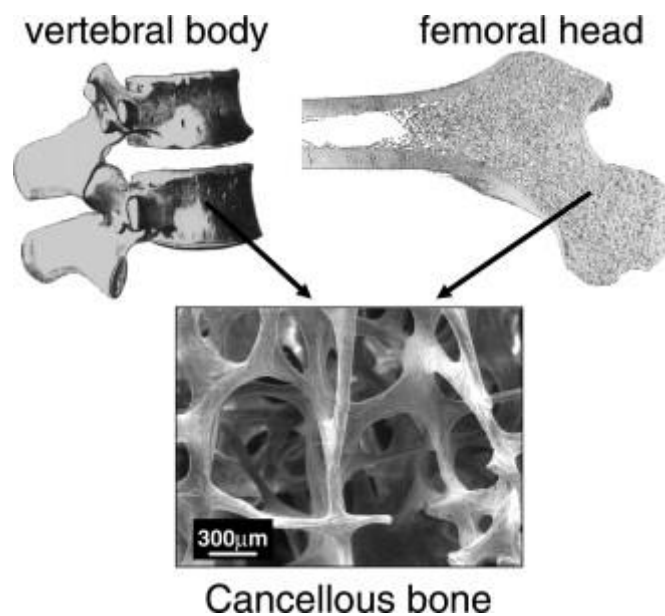


Figure 2-2 The spongy structure of trabecular bones found in the vertebra or the femoral head (Fratzl & Weinkamer, 2007)

2.1.2 Bone biomechanics and strength

The biomechanics of bone should be firm enough to avoid bulking and bending when force is applied. It should also be flexible enough not to break when the load is more than normal activity. These two combinations of mechanical properties are designed in bone material such that it consists of two types: cortical and trabecular. Figure 2-3 demonstrates a long bone structure in detail, with the two ends called the metaphyseal regions, being in contact with cartilage. Whilst the area between these ends is known as the diaphyseal region, which has a hollow tube structure surrounding the medullary cavity (Pierce, et al., 2004).

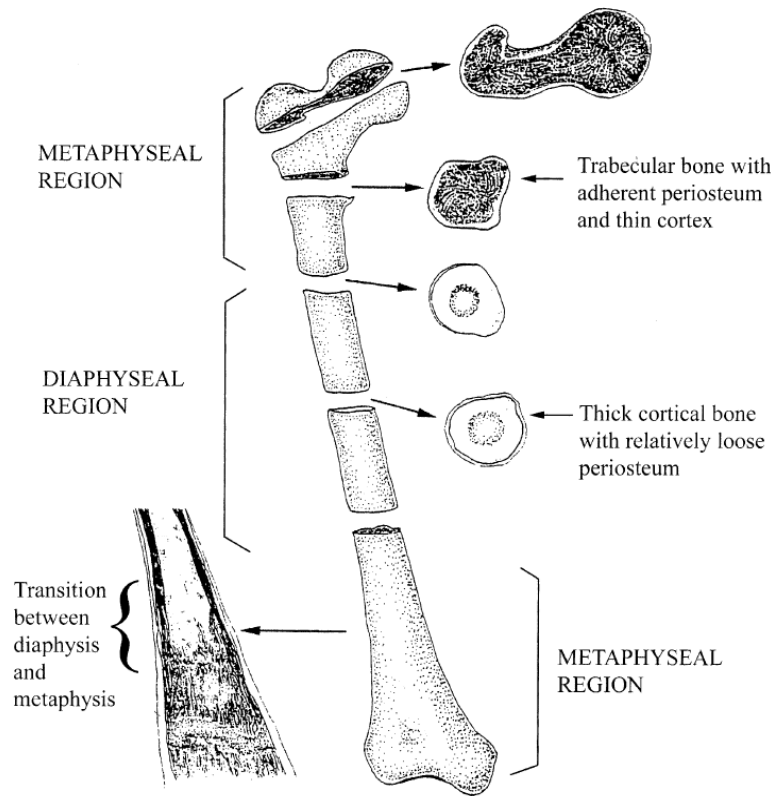


Figure 2-3 Illustration of bone architecture (Pierce, et al., 2004)

Bones consist of two important characteristics: stiffness and toughness. They are stiff to avoid bending and buckling, whilst they also need to be tough to avoid breaking when under higher load than the normal range. Proteins (collagen in the case of bone and dentin) are tough and the mineral is stiff. Based on a map, as provided in Figure 2-4, bone and dentin can be seen as having good properties in relation to both (Ashby, et al., 1995).

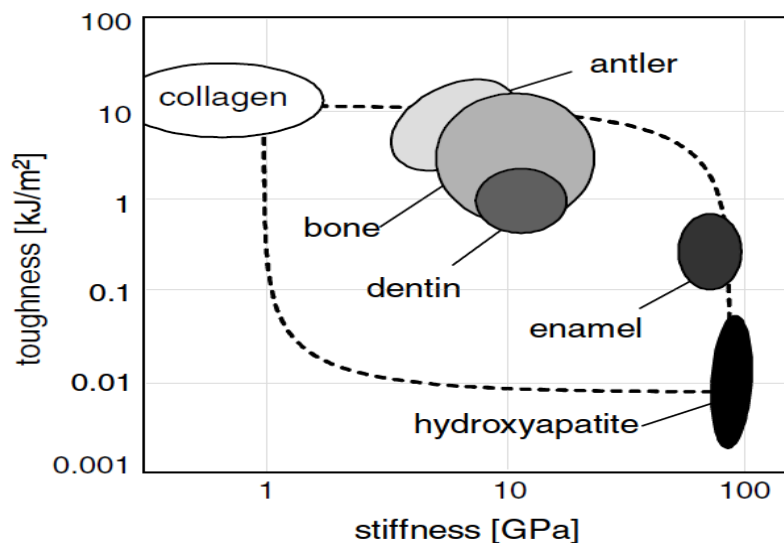


Figure 2-4 Typical values of stiffness (Young's modulus) and toughness (fracture energy) for tissues mineralised with hydroxyapatite (Ashby, et al., 1995)

Trabeculae position themselves in the direction of the forces applied to the bone (Mittra, et al., 2005). The volume of cortical and cancellous bone in each individual is different, but about 80% of the total skeletal volume in an adult human skeleton comprises the former (Jee, 2001).

2.1.3 Mechanical properties of bone

Bone strength can vary under different circumstances, such as age, sex, location, orientation of the load and test condition. Furthermore, bone is a living organ and has a basic stress-strain relationship. Figure 2-5 shows the difference in cortical and cancellous bone, where it can be seen that the former has higher strength than the latter (Nigg & Herzog, 1999). It is now clear that bone is stiff and also soft. In addition, this combination makes bones a non-homogeneous and anisotropic material.

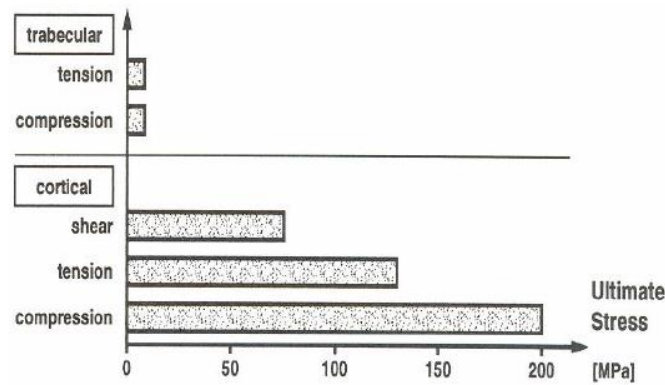


Figure 2-5 Difference between the ultimate stress of cortical and cancellous bone (Nigg & Herzog, 1999)

There are many ways of determining bone properties. In past studies, various mechanical testing was in use, such as uniaxial tensile, compressive and three-point bending. In contrast, nowadays, techniques like ultrasound and nano-indentation are being applied, as less material is used and the directional effects can be measured. Table 2-1 compares the mechanical properties for metallic biomaterials with bone.

Table 2-1 Comparison of mechanical properties of metallic biomaterials with bone (Ratner, et al., 1996)

Material	Young's Modulus, E (GPa)	Yield strength, (MPa)	Tensile Strength, (MPa)	Fatigue Limit, (MPa)
Stainless steel	190	221-1213	586-1351	241-820
Co-Cr alloys	210-253	448-1606	655-1896	207-950
Titanium (Ti)	110	485	760	300
Ti-6Al-4V	116	896-1034	956-1103	620
Cortical bone	15-30	30-70	70-150	

2.2 Hip replacement

Total hip replacement (THR) is one of the most common and effective orthopaedic procedures accomplished worldwide. In this part, the hip anatomy and disorders that result in THR are discussed. In addition, surgical procedure and failure after the replacement is discussed. Figure 2-6 shows the schematic of total hip replacement.

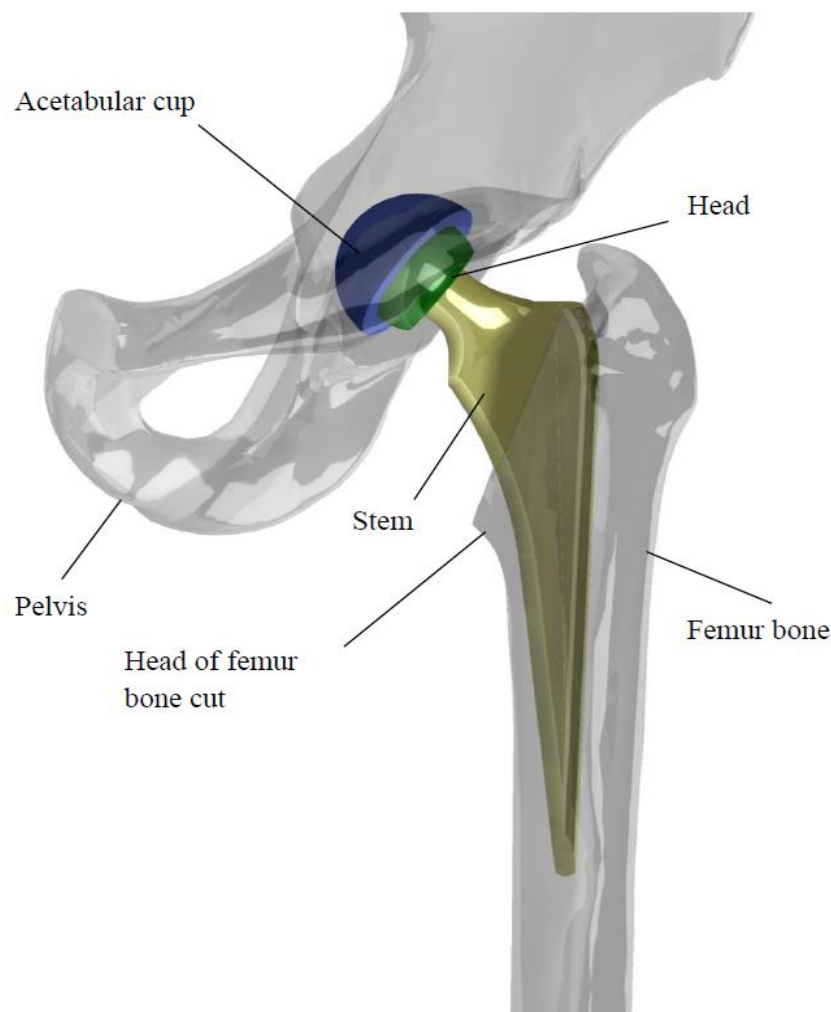


Figure 2-6 Schematic of total hip replacement (English, et al., 2015)

2.2.1 Hip anatomy and symptoms for surgery

The hip anatomy consists of many parts, including bones, ligaments, muscles, cartilage and tendons, which are in contact with one another so as to make daily activities, such as walking, sitting, bending and turning, possible. In addition, the hip carries most of the body's weight during daily activities.

In hip structure, there are three main bone parts: A ball positioned at the top of the femur (thighbone), which fits into a rounded socket or cup-like cavity (acetabulum) in the pelvis; ligaments, which are tough bundles of fibre forming a capsule connecting the ball to the socket together and keeping bones in place; and cartilage, which is positioned at the surface of the bones to ease the rotation of the ball in the socket and decrease friction between the bones. The area that is covered by muscles or tendons across the bone is filled with fluid sacs known as bursae and there is an oily liquid called synovial fluid that lies in a lining (synovium) that exists in the capsule surrounding the joint. This fluid helps to make daily activities easier and frictionless, acting as a lubricant (González, 2009). Figure 2-7 shows the components of the natural hip.

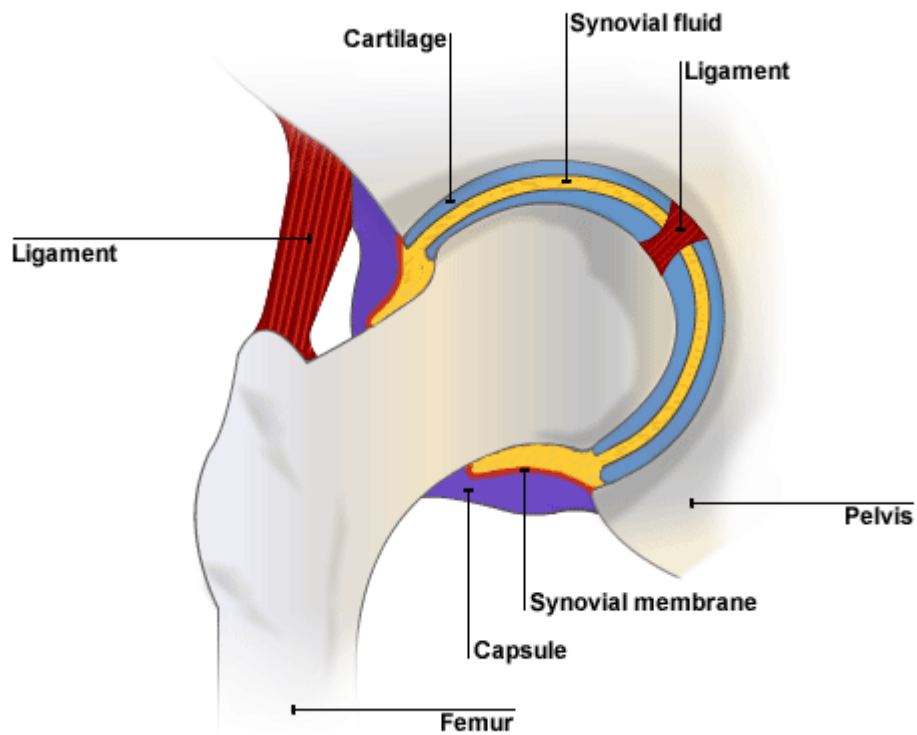


Figure 2-7 Components of the natural hip (Anon., 2014)

In experimental or computer simulations for lower limb models, the gait cycle becomes very important, because this is one of the most common human activities. Figure 2-8 shows the various phases of the human gait cycle, which pertain to the time between consecutive foot contact of the same limbs (González, 2009).

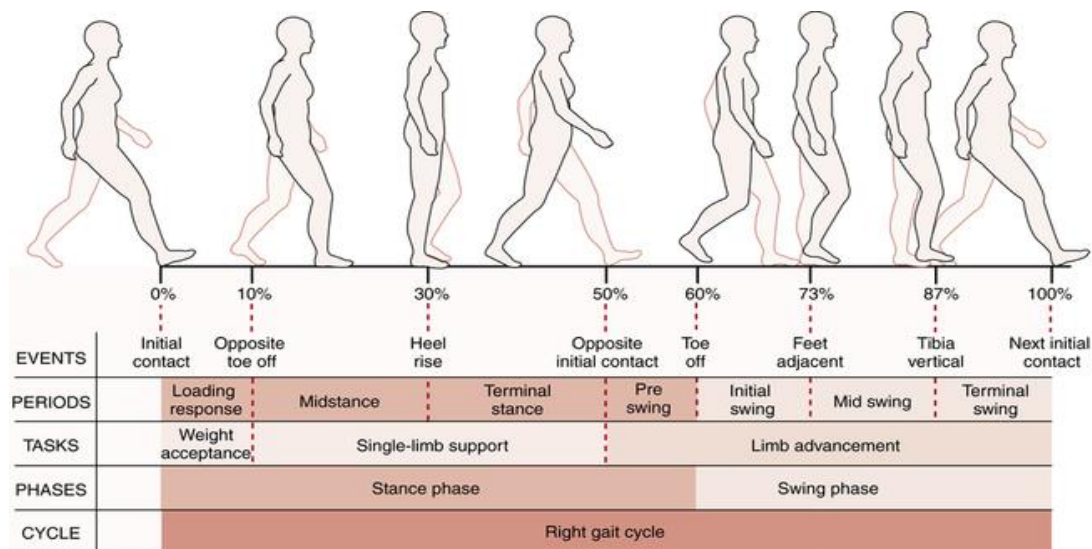


Figure 2-8 Phases of the human gait (Kernozek & Willson, 2015)

“Hip replacement is one of the most successful and cost effective interventions in medicine” (González, 2009). The purpose of these operations is to improve the quality of life for the patients suffering from a hip disorder, such as osteoarthritis, rheumatoid arthritis or avascular necrosis. At the present, there are 50,000 hip replacements implemented across the United Kingdom yearly and this number reaches 300,000 worldwide. The main symptoms for hip replacements are pain and functional limitations, which are caused by deformation of joints and capsular contractions. Furthermore, these will result in a reduction in the range of motion (González, 2009). The replacement procedure can lead to instant relief from the constant pain from daily activities, especially for older patients with arthritic hips. Performing such surgery is not age dependent. However, most of the patients for THR are aged 60 years or more, who have osteoarthritis and rheumatoid arthritis. Rheumatoid arthritis usually occurs in young adults; however, osteoarthritis happens as age advances. There are other hip disorders, such as avascular necrosis, congenital dislocation, Paget’s disease, ankylosing spondylitis and traumatic arthritis (González, 2009).

2.2.2 Total hip replacement devices

Total hip replacement (THR) is one of the common operations that is used when the cartilage has degenerated. In this surgery, the hip is replaced with an implant and mostly, it is successful (Savilanti, et al., 1997). Hip implants contain three parts: the stem, the ball and the cup. The hip stem is the part that goes into the femur, whilst the ball is placed on the stem and the cup is placed in the acetabulum cartilage position. The cup is an empty semi-sphere. Furthermore, the cup and the ball move against each other to control the movement of the joint (Jinno, et al., 2004). Figure 2-9 displays femoral structure and when it is implanted.

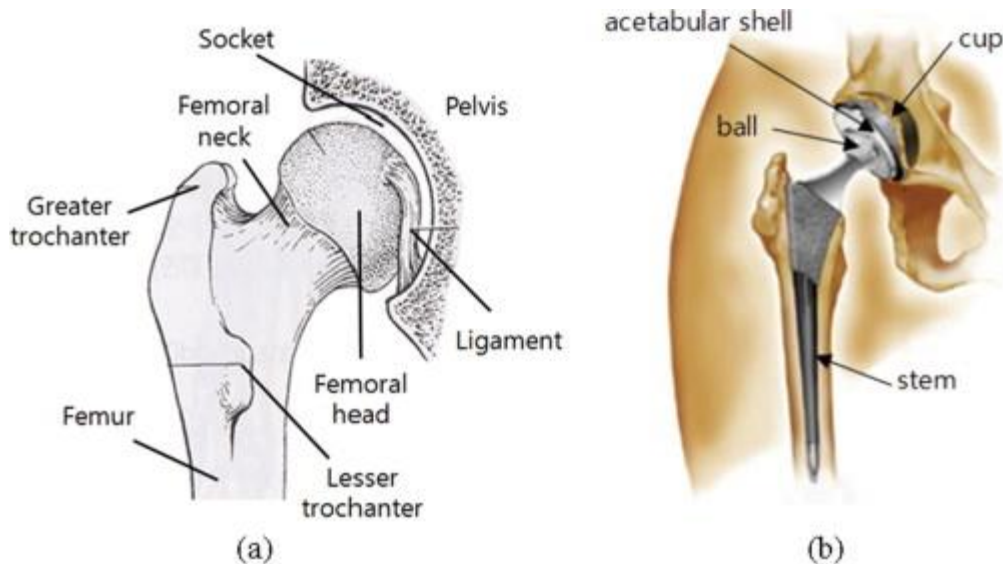


Figure 2-9 (a) Femoral bone structure and (b) typical hip implant (Yongtae & Kuiwoon, 2010)

Hip stems are made of three different materials: steel, Co-Cr-Mo and Ti-6Al-4V. The structures of these metals should be the same as the bone structure. However, the current metals do not have the exact same mechanical properties of the bone. Ceramics and polymers are not suitable materials for the stem; the former are very hard materials, strong in compression, but with low fracture resistance, whilst the latter have low stiffness and reasonable fracture toughness, but poor strength (Thielen, et al., 2009). All the materials used in THR should have resistance to corrosion, biocompatibility, degradation and wear, with the highest standards of fabrication and quality control at a reasonable cost.

Cementless implants have a porous surface for new bone growth instead of bond creation using cement, with these designs being larger and longer than cemented ones, generally (Sotereanos & Engh, 1995). In cemented implants, cement is used to fix the femoral and acetabular components; however they can crack over time, which results in loosening of the prosthetic stem (Jeffers, et al., 2007). When the microscopic debris particles are absorbed, inflammation occurs around the implant, which results in the removal of fragments of bone (Nikolaus, et al., 2007). Figure 2-10 shows the difference between a cemented and uncemented implant.

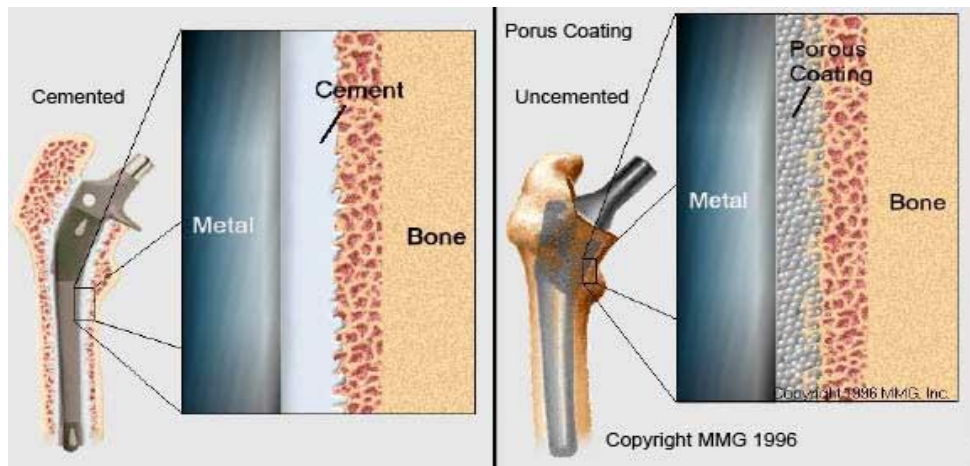


Figure 2-10 A cemented and un-cemented implant (Schmidler, 2016)

There are several possibilities for the choice of bearing surface between ball and socket, including: polyethylene, ceramic and metal-on-metal bearings. The upper part of the thighbone becomes weaker when an implant is placed in the femur, which is due to the load being carried by the implant. Most of the body weight is carried by the implant due to being stiffer than bone. On the other hand, the skeleton around the end of the femoral component is overloaded, which results in stronger and thicker bone, often ending up with significant pain (Boyle & Yong, 2011).

2.2.3 Stem material

Metals have been used have been used for many in the biomedical field for a variety of applications. They have been used extensively for internal support and biological tissue replacements, such as dental roots, orthopaedic fixation, joint replacement and stents (Park & Lakes, 2007). The main metals and alloys that are used in this field are stainless steel, Co alloys and Ti alloys (Ninomi, 2008) (Karanjai, et al., 2007). All biomaterials have to meet specific criteria, such as high resistance to corrosion, adequate strength, bio adhesion, bio functionality, high wear resistance, low friction and biocompatibility in order to achieve the best outcome (Patel & Gohil, 2012). However, placing all the mentioned requirements in a single implant has been impossible so far. Moreover, all implants used inside human bodies must be biocompatible to avoid rejection and possible toxicity. The environment of the human body is extremely corrosive, which makes it important to choose the right material for the longevity of implants.

There are many important factors involved when designing a femoral stem, including the material, surface finish, geometry, etc. The material that is used for an implant must, as abovementioned, be biocompatible and have similar mechanical properties to bone. Stem

material should also have optimum tribological properties and be strong enough in the complicated loading and human body environment (Semlitsch & Willert, 1980). Most materials used in biomedical engineering are stronger than expected for fatigue and yielding, thus the strength of the material is not a critical subject. However, stress shielding is extremely important when designing a hip stem. As it has been explained before, stress shielding refers to the reduction in bone density around the hip stem, which is due to body weight being carried by the implant. This could result in discomfort and pain for the patients. To conclude, it is essential to use materials with similar mechanical properties, such as strength, stiffness and density, as bone. This will decrease the stress shielding between the cancellous bone and the lower part of the femur. There are three main alloys used in biomedical engineering nowadays, namely: stainless steel, cobalt chrome alloys and titanium. These are the most used materials due to their biocompatibility and strong mechanical and tribological properties. Femoral stems made with titanium alloys were notorious for failure prior to the cobalt chrome and stainless steel alternatives, which is due to its susceptibility to crevice corrosion. This is caused by the generation of a gap between the stem and the cement as well as between the head and the taper. In sum, titanium alloys used in femoral stems have raised certain concerns, while manufacturing and titanium articulating surfaces are not recommended for biomedical use anymore (Zhang, 2009). Table 2-2 shows the advantages and disadvantages of metallic biomaterials.

There are several key desired properties for biomaterials that can be summarised as follows.

- **Mechanical properties:** if the modulus of elasticity of a biomaterial matches the bone which is between 4 to 30 GPa, stress shielding could be prevented (Lawrence, 1980) (Black & Hastings, 1998). Furthermore, despite having low modulus, the material should also have adequate strength to increase the life period of the implant and prevent loosening. As a result, revision surgery could be avoided.
- **Biocompatibility:** the material used for the human body must be compatible with human organs and reduce the harm to the smallest possible. A non-biocompatible material could result in infection and hence, have a negative effect on body organs and tissues (Walowitz, et al., 1997).
- **High wear resistance:** another positive property a material could have is high wear resistance and a low friction coefficient when sliding against body tissues. Moreover, reduction in wear resistance or a high friction coefficient could cause loosening

(Alvarado, et al., 2003); (Ramsden, et al., 2007). The friction could generate debris particles causing inflammation that is harmful for the supporting bone.

- **High corrosion resistance:** a low corrosion resistance material could cause toxicity when the metal ions are released (Hallab, et al., 2005).
- **Osseointegration:** Osseointegration is described as “a direct structural and functional connection between ordered, living bone and the surface of a load-carrying implant” (Branemark, 1983). The surface properties of the implant, such as the roughness, topography and chemistry, play an important role in good osseointegration (Geetha, et al., 2009). A non-integrated implant surface could result in implant loosening and revision surgery (Viceconti, et al., 2000). There are some studies that say osseointegration is not necessary due to the risk of not being able to take out the implant after use. On the other hand, other studies that the implant can be removed safely (Wennerberg, et al., 2015). Therefore, osseointegration is an essential biomedical property for implants. In addition, the implant has to integrate properly with the bone and surrounding tissues to avoid loosening (Barfeie, et al., 2015).
- **Non-toxic:** the material used for implant should not be either genotoxic (change the DNA of the genome) or cytotoxic (can damage individual cells) (Hussein, et al., 2015).
- **Long fatigue life:** failure due to fatigue occurs with hip prostheses. Hence, the material should have high resistance to fatigue failure to avoid implant failure and stress shielding from fatigue fracture (Teoh, 2000).

Table 2-2 Comparison of metallic biomaterials used in the human body (Hussein, et al., 2015)

<i>Metals and alloys</i>	<i>Selected examples</i>	<i>Advantages</i>	<i>Disadvantages</i>	<i>Principal applications (Williams, 1990)</i>
<i>Titanium-based alloys</i>	CP-Ti, Ti-Al-V, Ti-Al-Nb, Ti-13Nb-13Zr, Ti-Mo-Zr-Fe	High biocompatibility (Henriques, et al., 2010) (Niespodziana, et al., 2008) (Ribeiro, et al., 2009). Low Young's modulus, excellent corrosion resistance, low density	Poor tribological properties (Ohidul Alam & Haseeb, 2002), toxic effect of Al and V over the long term	Bone and joint replacement, fracture fixation, dental implants, pacemaker encapsulation
<i>Cobalt and Cr alloys</i>	Co-Cr-Mo, Cr-Ni-Cr-Mo	High wear resistance (Wennerberg, et al., 2015)	Allergy consideration with Ni, Cr and Co (Niinomi, 2008) much higher modulus than bone	Bone and joint replacement, dental implants, dental restorations, heart valves
<i>Stainless steel</i>	316L stainless steel	High wear resistance (NIINOMI, 2002)	Allergy consideration with Ni, Cr and Co (Niinomi, 2008) much higher modulus than bone	Fracture fixation, stents, surgical instruments

2.2.4 Stem geometry

Another important factor regarding the femoral stem is the geometry of the implant, which is because this may have an impact on in vivo behaviour. Many femoral stem designs have been removed from the market, such as the 3M Capital hip, due to its short term survival rate. The most successful femoral stem is the one that transfers the body weight, axial and torsional to the bone cement. In addition, this load should be transferred without causing destructive peak stresses and with no extreme micro-motion. There are also many important factors when designing the stem. These factors are the general shape (symmetrical or anatomical), the presence or absence of a collar and a flange, the cross section (oval or square), the length of the stem and the shape of the stem tip. There are three different symmetrical stem designs with a good clinical track record: Charnley, Exeter, and Müller stems. In contrast, anatomical stem designs, such as Lubinus SP2, can create various strains in the cement mantle due to their specific shape. The cross-section is also important as it effects the stress distribution surrounded by the cement mantle, the rotational strength of the implant and the distribution of the cement within the mantle. The difference between the stems with oval and square cross-sections is their rotational stability. A square cross-section offers more rotational stability. On the other hand, sharp edges generate peak stresses, which could result in micro cracks (Scheerlinck & Casteleyn, 2006). Finally, the number of hip implants ready to be used by the surgeons is going up. Figure 2-11 shows the load transfer pattern in a natural hip and when it is implanted.

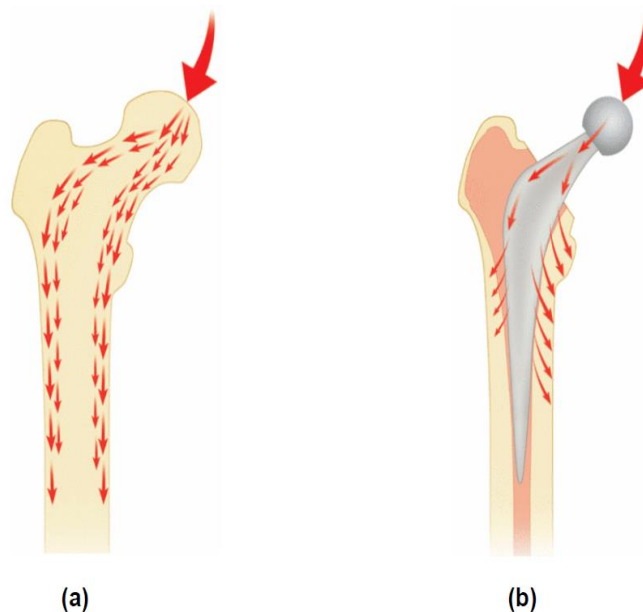


Figure 2-11 Load transfer patterns (a) within the natural femur (b) around the C stem (Zhang, 2009)

2.2.5 Stem surface finish

Another important factor in designing femoral stem is the surface finish. There are many different ways of finishing the surface of the femoral stem as it can be seen by considering various designs. There is much debate regarding the matt surface finish, regarding whether it could solve permanent fixation of the femoral stem during long term in vivo service. The surface of the stem is very important due to its direct effect interaction with bone. The bond created at the interface is determined by the surface texture and the strength of it. It should also be mentioned that a matt surface creates better bone-stem interface bonding than a polished one in regards to mechanical prospective (Zhang, 2009). “Shape closed design” is the name given to a matt femoral stem with a collar and a flange. In addition, this type of surface finish keeps its stability through its created bone between the stem and the cement. “force closed design” is the name given to a polished femoral stem with a collarless design (Huiskes, et al., 1998). The Exeter femoral stem design is one of the most used femoral stems and was extremely polished before 1976. After 1976, the Exeter femoral stem surface was matt until 1985 due to the cost of polishing. A matt surface in the stem causes more loosening than a polished one and that is the reason that the polished surface was reused again at the beginning of 1986 (Anthony, et al., 1990). In addition, a matt femoral stem tends to create more debris and causes intense damage to the cement mantle. Nowadays, there have been so many articles published proving the advantages of a polished femoral stem over a matt one. In addition, it has been ascertained that in some cases a matt surface fails earlier than polished surface, such as with the Exeter stem and the Iowa stem (Howie, et al., 1998).

Hip implants are placed in the hip by two methods: cemented and uncemented, with which being used depending on the surgeon’s experience.

Cemented implants rehabilitate faster compare to uncemented ones. However, fatigue fracture in cemented implants, over time, may result in loosening of the prosthetic stem. Another problem with them is that the cement could be absorbed by cells and result in initiating an inflammatory response from the body. In addition, this may also result in osteolysis, which refers to resorption of bone around the cement. People over 60 years old mostly have cemented THRs, which are more stable as they are less likely to have high stress on the cement, which can result in fatigue fractures (Nelson, 2002). A study stated 90% success rate for the patients at 25 years of Charnley total hip replacement implemented with cement (Callaghan, et al., 2000). There is a relationship between the thickness of cement and stress levels and micro movements. That is, the greater the cement thickness, the more shear

stress and micro movements over the bone-cement interface. “Slipping of the implant causes osteolysis, which is due to the releasing of cemented particles” (Willert, et al., 1990).

Uncemented fixation has also been studied to stop implant loosening problems (El-warrak, et al., 2004) and they have coating or texture with different porous material structure for bone-growth. They take longer to heal (6-12 weeks) and to become stable due to new bone in-growth. The gap between the new bone growth and implants must be within 0-2 mm, for, bone cannot grow into the implant if the distance is more than this.

If a bond between the bone and implant is not achieved, it may result in loosening. Nowadays, uncemented implants are recommended by most surgeons and patients under the age of 50 have uncemented THR depending on their bone quality. Uncemented stems are also better for patients with an active life style. The new bone in-growth cannot fill gaps wider than 1 to 2 mm. Therefore, the initial bond is important in uncemented stems to allow bone in-growth (Sanami, 2015).

307 patients over two years and 89 patients over five years were studied for their THRs implemented with porous coated. It was elicited that a good press fit at the isthmus of the femur and the medullary canal can reduce the pain and results in better bone-ingrowth. It was also elicited that the stress shielding for 88% of the cases was small as the diameter for the stem was smaller. In addition, more bone loss is more likely to happen in larger diameter stems (Engh & Bobyn, 1988); (Engh, et al., 1987).

Cemented fixation in younger patients proved to be less adequate (Sancez-Sotelo, et al., 2002), involving some intense problems such as “the release of toxic monomers and heat necrosis” (Gough & Downes, 2001); (Moreau, et al., 1998). On the other hand, uncemented implants are better in terms of osseointegration into the porous stem surface with strong connection for long term survival. It has also been reported as providing successful result with resistance to osteolysis when compared to a cemented fixation (LaPorte, et al., 1999); (Sancez-Sotelo, et al., 2002).

2.2.6 Failure after THR

Failure of THR occurs even with the most advanced designs and the original prosthesis device has to be replaced with a new one, which is known as revision surgery and is less likely to be as successful as the primary surgery (González, 2009).

There are several factors that lead to such failure related to the femoral stem, such as loosening of the joint components, migration of the implant, infection of the joint, fatigue failure and accumulated damage, dislocation and deep vein thrombosis (González, 2009).

Dislocation occurs when the femoral head, the ball, comes out of the joint, the socket in the pelvis. This is a very painful state, which may be caused by loosening of the surrounding tissues, like the muscles, hip joint capsule and ligaments, after THR. Furthermore, as head-neck ratios reduce, the angle of motion allowed before the neck-acetabulum decreases, and dislocation occurs (González, 2009). There were 62,175 THRs recorded by the Scottish National Arthroplasty from April 1989 to March 2004 and the rate of dislocation incidence was 0.9% per annum (Meek, et al., 2008).

Aseptic loosening is another failure condition in which any form of loosening is accountable except for that due to infection. This condition will lead to losing component fixation and removal. The reason for such incidents is the lack of bone in-growth or when wear particles around the prosthesis access the interface and create weak pockets of bone around the implant (osteolysis). Stress shielding of the cortical bone could be another cause of aseptic loosening. A stiffer component will carry most of the load, which results in the reduction of the load transferred and thinning of the femoral cortex around the prosthesis. Stress bypass is another condition for failure in which the fixation of stem in the proximal region is poor and there is good fixation at the distal end. This will result in load transferred down to the distal end causing the proximal femur to go under lesser stress and become subject to bone resorption (González, 2009). Prevalence of aseptic loosening has been reported to be between 32 and 62% over 10 years, depending on the type of implant used (Dattani, 2007).

Infection may occur in the first twelve weeks after THR, which is caused by intra-operative contamination. However, it could occur after twelve weeks, which could be from distant sources, such as skin, ulcers, dental caries or the urinary tract. Furthermore, in cases like these, antibiotics have difficulties intervening due to the environment formed around the infected area (Puolakka, et al., 2001).

Migration is a displacement that occurs mostly in uncemented implants between the host bone and implant, permanently, one year after THR. The gait cycle load could eventually result in crack growth within the femur (González, 2009). Furthermore, micro-cracking of the trabeculae extracts a portion of the implant support, letting it to sink down within the bone,

and this is noticeable where there is high stress such as the end part of the femoral stem (Glyn-Jones, et al., 2004).

Another failure condition is fatigue and accumulated damage caused by cyclic loading. In addition, this damage could gradually build up and harm materials and interfaces. This condition in uncemented implants is unlikely to occur due to their strong bond with the host bone and the lack of a weak cement link (González, 2009).

The last condition of failure is deep vein thrombosis, where blood clots may form in larger veins in the thigh after THR. The way to treat this condition is through blood thinning medication, compression stockings to assist circulation and early mobilisation (González, 2009).

When failure occurs, revision surgery must take place, which is complex and as aforementioned, the success rate is lower than with primary replacement. In addition, it also costs more than primary replacement, with more discomfort and pain for patients. Failure, after the expected lifetime of implants, which is 10 to 15 years, is termed fairly successful and under this duration is called premature failure. Figure 2-12 displays the reported causes of implant failure.

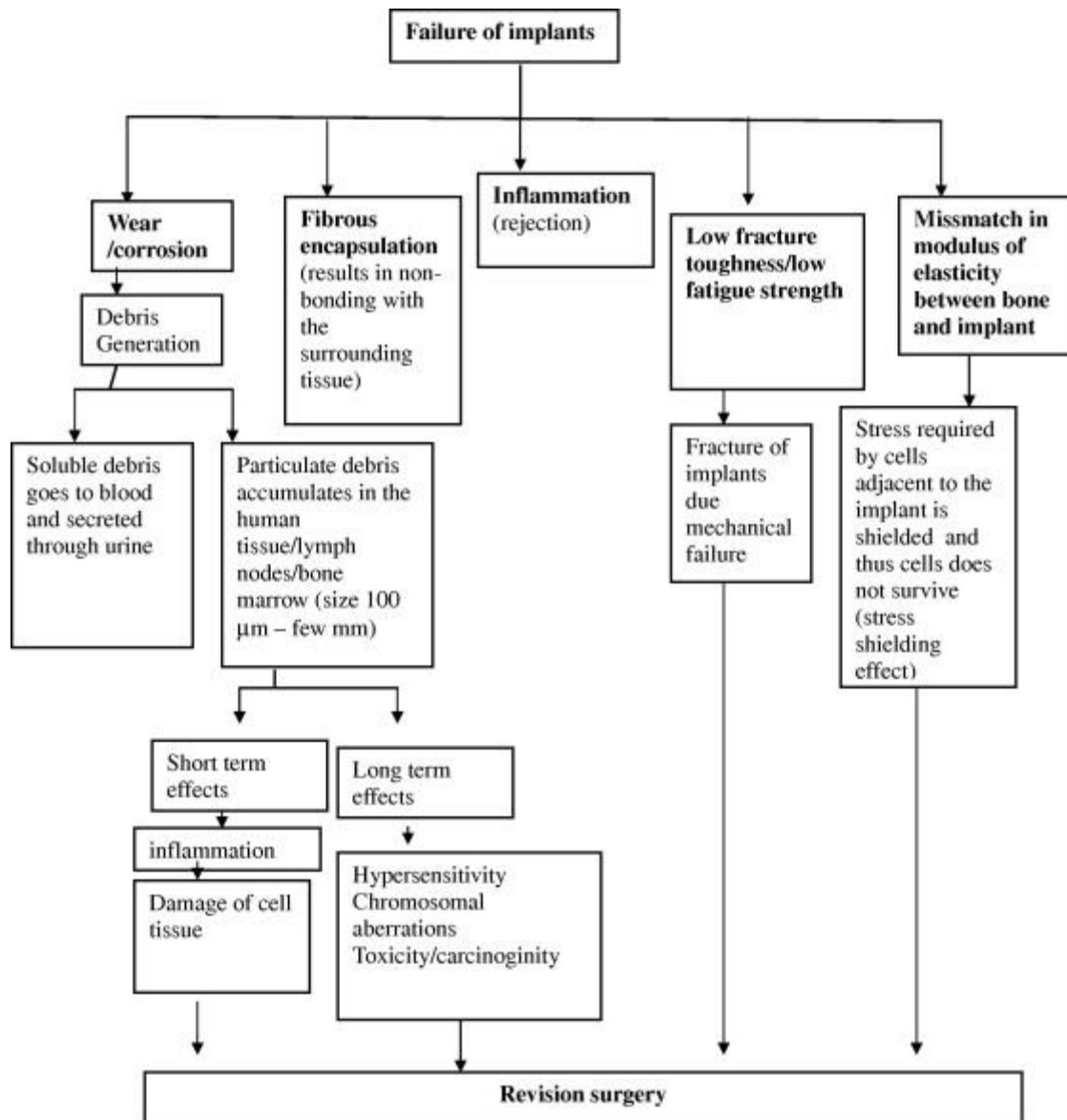


Figure 2-12 Various causes of implant failure (Geetha, et al., 2009)

2.2.7 Price of Implants

The price of implants differs across countries depending on their manufacturing costs. For instance, in Asia, they cost \$150 to manufacture, whereas in the United States, this rises to \$350. These differences in price could be due to low labour costs; however, some orthopaedists believe that there may also be some “corner cutting” to improve the quality of the components. These prices will be inflated regardless of the place of manufacture once they are ready to be used. For instance, in the US, \$7,000 needs to be paid for just the implant regardless of surgery cost. The basic design for an implant has not changed significantly, yet every year the price continues to increase substantially. Many people consider having their

hip replacement in other countries for a cheaper price (for instance \$4,000 in Belgium) (trip4care.com, 2014).

2.3 Factors in THR

Studies about the reasons for THR can be classified in two ways: experimental and finite element analysis. There are many factors playing a failure role after operations that need to be taken into consideration. Many of these failures are due to abnormal stresses and strains caused by inadequate component design and imprecise implantation. Validation of results using an experimental approach to THR is limited, which is due to difficulties presented when simulating components in a laboratory. Furthermore, the experimental approach in a laboratory requires many scenarios that cover combinations of alignment, geometries, bone density and quality and etc. In addition, experimental examinations will be unpractical soon due to the complex biological environment. On the other hand, computational modelling of THRs takes much less time to process and many scenarios can be speedily investigated. Validation of results using FEA can be as straight forward as two components being investigated in the same environment. There are some factors below that have an effect on THR performance.

The first is the surgical approach, which affects soft tissues directly during the operation and there are two types: posterolateral and anterolateral (Kennon, et al., 2003). With the posterolateral approach, the rate of dislocation is at its highest due to straightening of the spine and flexing of the pelvis in the side-lying position used on the operating table, which may result in an improper socket position. The chance of dislocation with this approach decreases the more experienced the surgeon (González, 2009). The anterolateral approach involves using the intermuscular plane between the tensor fascia latae and the gluteus medius. The patient is positioned supine on the operating table, with a moveable (kidney rest) segment to let the buttock skin hang smoothly (Kelmanovich, et al., 2003).

Other examples of variables are prosthetic component design and orientation. The most important variable to stop future dislocation failure is having proper component orientation. The position of the femoral stem depends on the surgical approach. A misplaced prosthesis can be saved from dislocation after the early stages of the operation, because of soft tissue and capsular healing (González, 2009).

It is also important to mention patient features, whereby if enough precaution is not taken, this may result in dislocation. Other variables that can be contributory are femur geometry

and quality as well as bone properties. These factors are different in patients and bone properties may differ even within the same bone (González, 2009).

2.3.1 Effect of bone geometry and quality

It is important to be extra cautious after THR, in particular, for those with greater height and weight, as these can have a negative impact through loading. For instance, for two patients with the same femur size, but different body weights, having THR done, the heavier one will experience higher stresses on the femur, which may result in deformation. Internal forces could be predictable, if muscle forces were the same; however, these vary in each individual significantly. Bones are living organs in our body and their properties differ for each individual. When the variability of bone geometry is considered, the force is transferred in different directions and hence, differing stresses and deformations are created. Furthermore, regarding bone quality, every individual internal point of the bone has certain material properties, which differ from person to person. Moreover, bone has specific properties in each individual at different periods of her/his life and it is unwise to associate an obtained femur simulation result the whole population. In addition, the outcome from a simulation must quantify the effect of the variability (González, 2009).

2.3.2 Effect of implant material, design and positioning

THR is one of the most successful operations in medical science history; however, the variability of different implants remains a major issue. There is strong evidence showing different survival rates of various prostheses and the effect of the implant material on THR performance (González, 2009). A study by Sarmiento and Gruen, showed differences between a low-modulus titanium alloy femoral stem and a Charnley prostheses. That is, in this research, the former showed fewer tendencies to incidences, such as loosening, calcar resorption and cortical hypertrophy than the latter (Sarmiento & Gruen, 1985).

In another study conducted by Weinans et al. (1992), cobalt-chrome and titanium alloy materials for cemented and uncemented THR were compared as well as an additional hypothetical uncemented implant, termed isoelastic. Implant material was found to have a direct influence on the bone in the femur around the femoral stem. Specifically, in their study, cemented stems showed lower bone resorption and interface stresses than uncemented implants created from the same material (Weinans, et al., 1992). Interface stresses and bone growth were investigated for fully bonded situations and a little bone resorption was observed

around the isoelastic femoral stem. However, proximal interface stresses went up dramatically compared to other uncemented prostheses (González, 2009).

It has been demonstrated how the position between the cup and head of a femoral stem is important so as to avoid the risk of dislocation (Barrack, 2003). Interface contact stress levels have shown a decrease under the proximal neck with full length femoral stems when compared to shorter ones (González, 2009).

Femoral stems have many types of surface finishes, but these variations do not have a significant impact on the cortical strain distribution of the bone or the steadfastness of the implant. Regarding which, six cadaveric uncemented titanium femoral stems were studied to investigate whether there was any impact of the design features on the cortical strain distribution, with this involving one intact femur and five implanted ones (Gillies, et al., 2002). The design characteristics identified were as follows: distal flutes, a distal coronal slot, proximal steps and a proximal porous bead layer and a blank implant with no features on. The results showed greater strain distribution in the proximal anterior than the intact one. In addition, there were no significant differences in the cortical bone strain distributions (Gillies, et al., 2002). In another study conducted by Biegler et al, two designs with different surface finishes were investigated: smooth and porous coated surfaces. These two designs were investigated in two situations, namely, a one-legged stance and stair climbing. Micro-motion and the amount of contact at the implant-bone interface were calculated and the results show load type plays a more important role than the implant geometry or surface coating type. In these studies, it was concluded that surface finishes may not have a substantial impact on THR performance when compared with other characteristics (Biegler, et al., 1995).

There have been many studies that have analysed the impact of implant geometry on THR. In 2006, Decking et al. worked on the impact that three varying femoral stems had on in-vitro strains in the proximal femur: alloclassic (a straight stem), optan (anatomically adapted implant) and a stemless femoral neck prosthesis. The results showed a reduction in the longitudinal strains in the proximal femur. On the other hand, the femoral neck implant showed a growth of calculated strains on the lateral side of the greater trochanter. The medial strain of the stemless prosthesis showed closer values to physiological than the other full-stem implants. Furthermore, this may result in better bone growth in the inferior base of the neck. In sum, the implant geometries used in this study had a noticeable impact on the strain distribution (Decking, et al., 2006).

To summarise all the above studies, the surface finish of a femoral stem does not have a significant impact on THR performance. However, it has been evidenced that the material and geometric factors, such as the dimensions, shape and relative position with the bone, should be taken into consideration as this can lead to better performance of THR.

2.4 Stress Shielding

Stress shielding refers to the reduction of bone density, which usually occurs when the implant is placed inside a bone, such as the femur, with the entire load being carried by the implant. This will result in weaker and less dense bone. The upper part of the femur receives less load when implanted and thus, is shielded from the stress, whereas the distal end of the femur is overloaded when this is done (Huiskes, 1990). When body is in its natural form, the entire load is on the femurs, whilst when THR takes place and a stem is implanted, the implant and bone will share the load. The bone is subjected to reduced stresses, that is, the stress is shielded. Based on Wolff's Law, the bone remodels itself by reducing its mass internally (becoming porous) or externally (getting thinner) in its natural situation. In other words, the bone improves its structure based on the force upon it (Roesler, 1987).

Stress shielding is the stress difference in the femur before and after the implant is placed. In one study, the stress of an element was measured before and after implantation, with the difference being divided by the stress at that element in the before state (Joshi, et al., 2000). There are other studies that focused on the specific volume of the femur before and after implantation. These studies considered the average stress in that volume, with the difference before and after implantation being taken as the stress shielding of that volume (Weinans, et al., 2000). Figure 2-13 displays stress shielding zone in a femur.

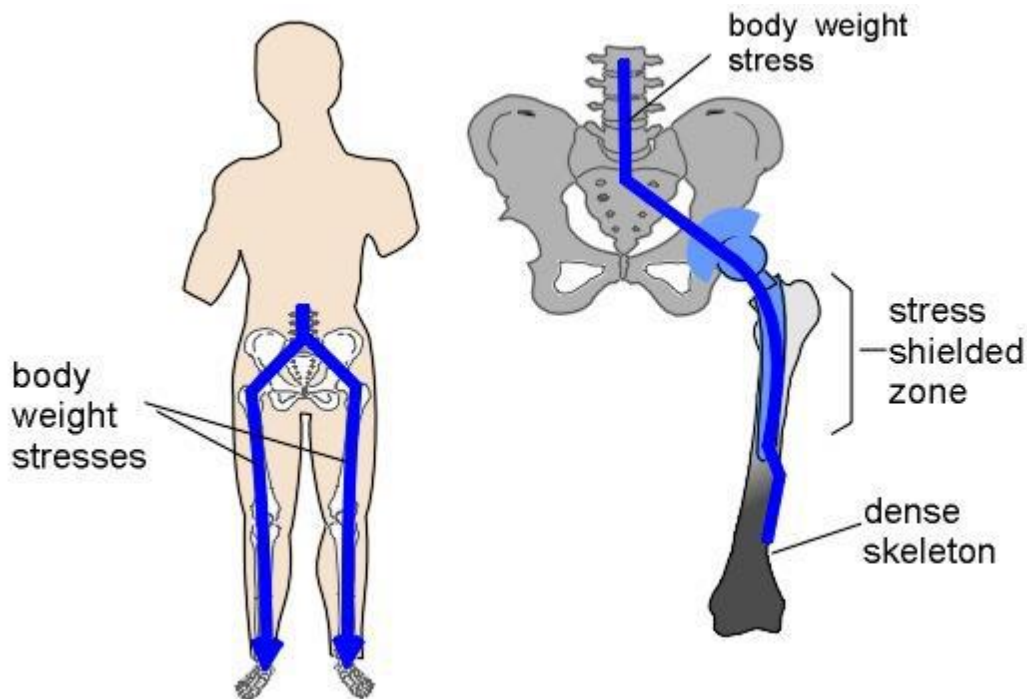


Figure 2-13 Simple schema of stress shielding zone (Surin, 2005)

As aforementioned, choosing the implant material is one of the most important factors in THR as this can impact on the bone resorption of the surrounding bone. The higher the rigidity of the implant, the more chance of getting bone resorption, because the implant will transfer a smaller amount of load to the bone (Bitsakos, et al., 2005). That is, rigid stems deliver greater stress shielding. In contrast, femurs fitted with flexible stems have demonstrated less bone resorption than stiff ones (Sumner & Galante, 1992). Titanium, amongst all the alloys used in THR, is the most suitable due to its low modulus and high fatigue strength.

Huiskes et al. (1992) discovered that, there is a non-linear relationship between the proximal interface stresses and stress shielding. That is, this study showed that when the stem becomes less stiff, it gradually raises interface stresses and gradually decreases stress shielding. FE modelling was used in this study with different elastic moduli for the stem. In addition, it emerged that stiff stems result in bone resorption, whereas flexible stems decrease resorption, if the interface bond is strong. It was concluded that flexible stems are the solution to bone resorption, but this may also result in increased loosening rates (Huiskes, et al., 1992).

Where stress shielding occurs can also be observed in finite element analysis. Figure 2-14 shows the position where stress distribution happened in intact and post implantation situations along the medial and lateral sides at 16 different points. As is shown, the stress at

each point was decreased after the implant had been placed, which can be observed in both the lateral and medial sides (Ridzwan, et al., 2007).

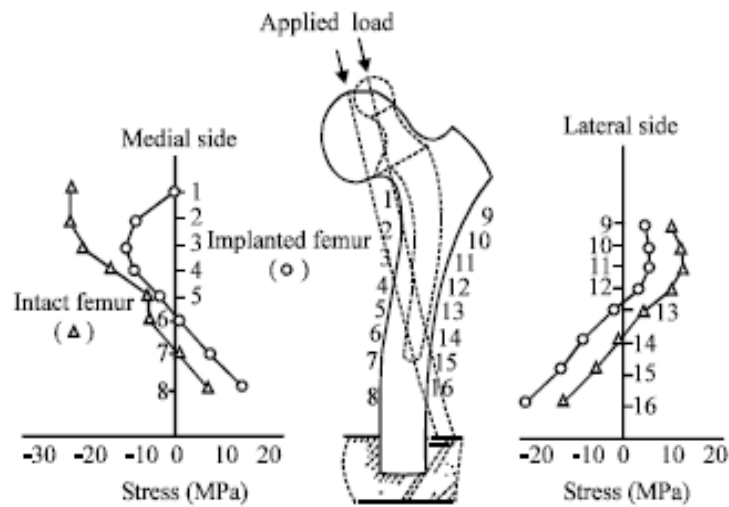


Figure 2-14 Stress distribution along medial and lateral sides when a 4,000 N applied load was given onto proximal head (Ridzwan, et al., 2007)

Comparing the strain distribution on a human cadaver for a hip with and without an implant, showed the strain in the calcar in the former case increases by 30-40% than with the normal hip. A hollow stem implant decreases the stress peak beneath the tip of the prosthesis and raises the stress in the proximal cortical bone by about 20 percent (Mattheck, et al., 1990). Having a mesh structure in the stem has been proposed lately to reduce stress shielding after implantation (Cansizoglu, 2008).

As abovementioned, revision surgery refers to the procedure where the existing THR or a component (head or stem) has to be replaced. It is needed when the patient is in pain, where the implant has been infected or it is not functioning. In the year 2012, 80,000 THR were implemented in the UK, whilst revision surgery was performed on approximately 8600 of them and there is evidence that says the number regarding this is increasing (Sood, 2013).

A study in 2004 worked on three femoral stems with various cement fixation configurations. These stems were configured as follows: cementless, proximally-cemented and fully-cemented. Stress shielding occurs regardless of cement fixation configurations, which is mostly to occur at the proximal femur. The case with fully cemented fixation showed less stress shielding. However, the cementless fixation had the most stress shielding. The purpose of bone cement was to generate more external force transmission uniformly, which results in the decrease of stress shielding (Chen, et al., 2004).

The aforementioned study demonstrated higher compressive strains on the proximal femur with cemented fixation in comparison to those with cementless fixation. Regardless of which cement fixation configuration is used in the process of the stem replacement, implanted femurs encountered a noteworthy reduction in axial normal strains at both medial and lateral sides of the proximal region. The most substantial reduction in strain was observed in the femur with cementless fixation, which resulted in bone loss in the proximal femur for long period application. On the other hand, the cemented fixation configurations demonstrated a less strain reduction. The outcome proved that bone cement might conduct more uniform stress distribution on the proximal femur over a long period. One important factor to mention is that the axial normal strains increase at the distal end of the femur once implanted. Furthermore, this is due to the compacting of bone at the distal end of the femur which might increase bone density at the distal end over long-time application (Chen, et al., 2004).

2.4.1 Bone loss

As it has been described earlier, stress reduction in implanted bones causes bone loss. There is a way of measuring bone mass and bone mineral density (BMD) at the lumbar spine, proximal femur, distal radius and other skeletal sites, called dual energy x-ray of absorptiometry (DEXA). A study in 2001, determined bone loss as the variance between the operated and non-operated sides. If this is observed through x-ray film, there will be small gaps along the bone/implant interface (Niinimäki, et al., 2001). In 1996, a study was conducted to work out the bone mineral content (BMC) and bone mineral density (BMD) of the proximal femur in necropsy recovered from cemented femoral stems. Specifically, DEXA was used to measure bone content and bone density in 13 femurs having cemented implants for 12-191 months. The results showed significant bone loss in the proximal region, of 40% on average (Lozynsky, et al., 1996). Furthermore, another study looked at 426 patients with uncemented stems and 24% of them demonstrated a loss of BMC on average (Ridzwan, et al., 2007). In another study conducted in 2002, 34 patients (35 hips) out of 275 femoral revisions were recognised as the most difficult cases due to significant femoral bone loss at least 10 cm below the lesser trochanter. Figure 2-15 demonstrates how in the metaphysis (level 1) and the proximal diaphysis (level 2), all the patients involved in the study had cancellous deficits. In level 1 and level 2, the cortical deficits were 91% and 100%, respectively. At the mid-diaphysis (level 3), 80% had cancellous deficits and 54% had cortical ones (Engh, et al., 2002).

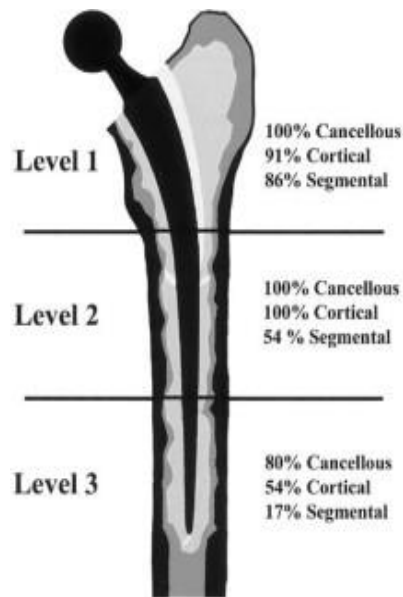


Figure 2-15 Preoperative femoral bone loss among the 35 hips is graded based on the American Academy of Orthopaedic Surgeons (AAOS) classification system (Engh, et al., 2002)

All of the above studies prove that there will be a fall in femur volume and mass in the post operation period, but stress shielding will take a few years to occur due to its slow reaction to the surrounding environment (Bagge, 2000). That is, the stability of implant will reduce after a certain period of time due to the lack of support caused by stress shielding. In addition, this may result in implant loosening. The impacts from implant loosening and micromotion can result in pain while performing routine activities. At this stage, revision surgery could become a significant help in pain relief (Ridzwan, et al., 2007).

When the femoral stem is removed, a significant reduction will be observed in the bone stock. Hence, a thicker and longer implant is required for replacement due to the bone loss. However, stress shielding may occur again. In other words, the new replaced implant will possibly function for couple of years before loosening starts to happen due to stress shielding. These revision surgeries could continue depending on the patient's bone density and after reaching the limit, bone grafting could be considered to improve a patient's bone stock (Ridzwan, et al., 2007).

2.4.2 Implant materials

There are two main problems when considering devices replacing bone and body tissues: biocompatibility and mechanical properties (Katti, 2004). Biocompatibility can be defined as the reaction of body tissues to the biomaterial, which refers to man-made material for replacing the function of living tissues or an organ (Katti, 2004). To decrease the chance of

hip implant rejection due to a body auto-immune response, the right material must be chosen, thus improving the success rate.

As previously explained, different materials have been used to make hip implants, including metals, ceramics, polymers and composites. In the early sixties, the stainless steel femoral stem was assembled with a polytetrafluoroethylene (PTFE) acetabular cup. Subsequently, the stainless steel was replaced by Cobalt-chromium-molybdenum (Co-Cr-Mo) alloy, because of inadequate wearability (Ridzwan, et al., 2007). In addition, the PTFE was also replaced by ultra-high molecular weight polyethylene (UHMWPE). Both materials have demonstrated good wear resistance and ceramics, such as alumina and zirconia are extensively used for the femoral head. The wear rates for alumina on UHMWPE are 20 times less than with metal on UHMWPE (Katti, 2004). Co-Cr-Mo and alumina are, respectively, about 10 and 19 times stiffer than a femur. These differences are a sign of stress shielding which is a result of high stiffness in comparison to femur (Ridzwan, et al., 2007). Titanium alloy, in comparison to Co-Cr-Mo alloy and alumina, has a lower elastic modulus. Moreover, improvements have been observed in the wear properties of Titanium alloy and it has the highest fatigue strength among all the extant alloys (Ridzwan, et al., 2007).

2.4.3 Implant stiffness

If the stiffness of an implant decreases, an increase in load transfer from the femoral stem to the proximal femur will occur, which results in decreasing of the stress shielding (Diegel, et al., 1989). Implant stiffness depends on the implant material and its cross sections. The elastic modulus of implant material has a significant impact on load transferring from the implant to the surrounding bone. The elastic modulus of femoral stems is usually higher (e.g. Cobalt Chromium is 100 GPa) than the cortical bone (20.3 GPa) (Bitsakos, et al., 2005). Stress shielding will increase if the rigidity of femoral stem increases. Which will result in bone density reduction in the proximal femur. Reducing the implant elastic modulus could help in load transferring at the bone-implant interface and decreasing stress shielding. Improving femoral stem cross sections is important to help decreasing their flexural stiffness and the thicker the stem, the more bone resorption will occur in the femur. Jergesen and Karlen (2002) looked at patient data covering large, medium and small stems. They found greater stress shielding in patients with large stems those with smaller ones. Nowadays, most of the stem designs are aimed at improving the load-transfer mechanism through the femur (Jergesen & Karlen, 2002).

2.4.4 Optimising implants

A study in 1990, focused on a hollowed stem prosthesis using FEM and it was discovered that a hollowed structure reduces the stress peak below the end of the prosthesis. In addition, in the proximal cortical bone, stress is increased by about 20% (Mattheck, et al., 1990). In another study, 40 patient data, of those who had their hip replaced with hollow structure implants were analysed. The results obtained from their clinical records after one year, showed adequate improvements and no thigh pain being reported. This could all be the result of the increased elasticity and better stem fitting (Schmidt & Hackenbroch, 1994).

A study in 2001, focused on optimising a hollow structure stem to decrease stress shielding as well as reducing the maximum stress in cement. In this research, the inner diameter was the variable and cement stress was defined as the design constraint. The obtained results were compared with a solid structure stem, but the implant was only cylindrical with simple boundary conditions. The stem with hollow structure showed an increase in proximal bone stress of about 15% and it was 32% for the case with high strength cement (Gross & Abel, 2001). In another approach in 2001, a new thin mid-stem design was introduced. Figure 2-16 shows the introduced design with a thin mid-stem diameter to improve stability of the implant within the femur. Another variable in this design is the distance from distal end, which is provided in Figure 2-16. These variables help to increase load transfer by decreasing the cross-sectional area of the stem (Chang , et al., 2001). Topology optimisation refers to achieving the best design to distribute stress within a fixed body, while the boundary conditions are applied. Optimised implants have been more successful in passing the load on to the femur, thereby decreasing stress shielding, than traditional femoral stems (Ridzwan, et al., 2007).

Hips play a very important role in our body as we need them in our daily activities, such as walking, going up and down stairs, getting up from a seat, cycling etc. Hips can get damaged either by accident, through osteoporosis or other hip diseases, such as rheumatoid arthritis (Ridzwan, et al., 2007).

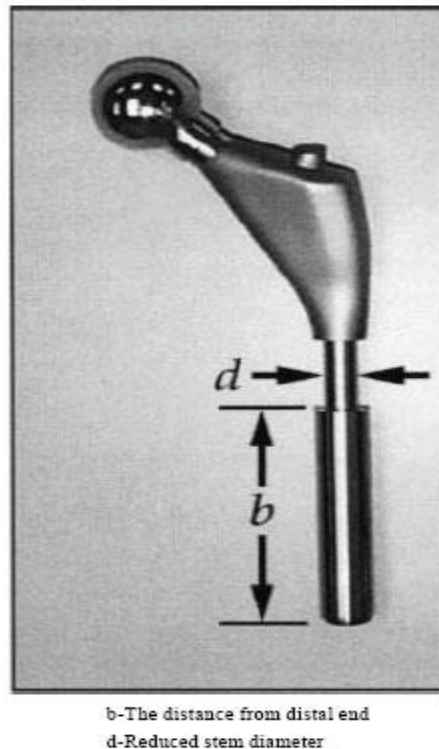


Figure 2-16 Implant designed proposed by (Chang , et al., 2001)

2.5 Steel foams

The properties of steel have been unchanged for many years. Changing the modulus of elasticity and yield stress have been proven to be impossible, however, yield stress has increased slightly lately (Smith, et al., 2012). Foaming the metal is a way of changing the properties of the material. Foaming can be accomplished by creating voids in the microstructure, which results in a reduction in density and increase in the apparent thickness. Once the method was introduced, the applications were limited. As the costs decrease and mass production increases, a variety of applications will be possible using metal foams. That is, steel applications could grow substantially in future with density as a variable. In addition, if the process is carried out with precision, the outcome foamed object could have higher plate bending stiffness ($\propto Et^3$) and will be lighter than solid steel (Smith, et al., 2012).

2.5.1 Advantages

Utilising steel foams is rapidly growing in various applications and once their advantages become widely known, the demand to use them will increase significantly. Among the most important advantages are the reduction in weight, increase in stiffness, energy dissipation and mechanical damping. Other advantages that should be mentioned are deduction in thermal

conductivity, electromagnetic and radiation shielding, tune vibration frequency, improvement in acoustical performance and providing air/fluid transport within materials (Smith, et al., 2012).

2.5.2 Steel foam manufacturing

Figure 2-17 demonstrates the stress-strain curve for steel foam, which consists of three regions: an elastic region; a plateau region, where the voids start plastic deformation; and a densification region, where cell walls come into contact with one another and compressive resistance immensely escalates (Smith, et al., 2012).

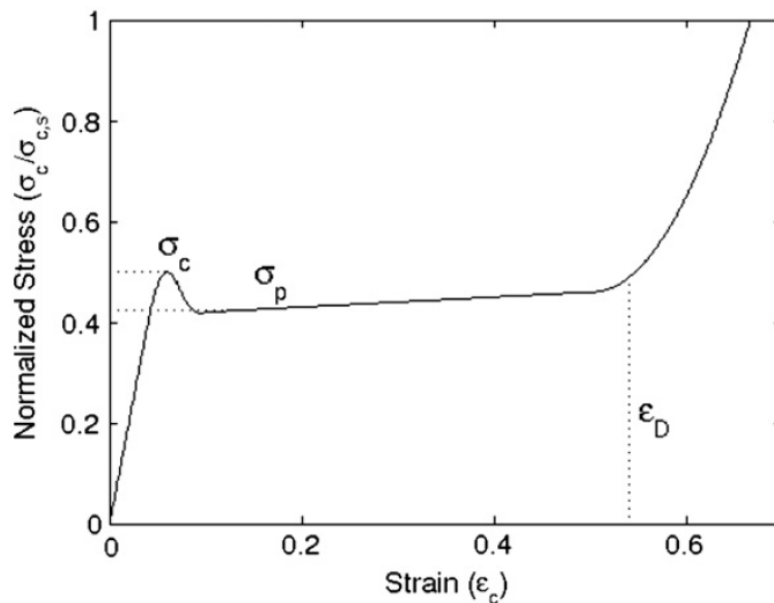


Figure 2-17 Typical stress–strain curve for metal foams in compression (Smith, et al., 2012)

There have many studies conducted regarding optimal manufacturing methods for metal foams, such as aluminium, titanium, and copper; however, steel raises unusual challenges due to its high melting point. Steel foams with varying regularity, isotropy and density can be created in two forms using current manufacturing methods: open-celled (permeable voids) or closed-cell (sealed voids) and there are three main methods to make them (Smith, et al., 2012).

2.5.2.1 Powder metallurgy

This was one of the first methods used for producing metal foams and primarily, it was for aluminium. It creates closed-cell foams and can develop highly anisotropic cell morphologies (Smith, et al., 2012). Powder metallurgy pertains to the combination of metal powders with a foaming agent, then the outcome mixture is compressed, and subsequently, the compressed

blank is sintered at pressures of 900-1000 MPa (Muriel, et al., 2009). The metal reaches its melting point and is held there for about 15 minutes. The final product may receive heat treatment to make the most effective crystal structure of the base metal. In addition, the range of densities is from 4% to 65% (Smith, et al., 2012).

2.5.2.2 Hollow spheres

In this method, which is the second most popular, closed-cell or mixed open and closed cell morphologies are possible with the densities from 4% to 20%, but high relative densities are not. In this method, the void sizes are controllable, which makes the material properties predictable and highly stable (Friedl, et al., 2008). The processes for this method use pre-manufactured hollow spheres to combine them using an adhesive matrix, compressing through powder metallurgy techniques, or sintering the spheres (Brown, et al., 2010). A difference that should be mentioned, is manufacturing spheres using blowing agent within and then letting the spheres expand and sinter into the final shape (Smith, et al., 2012).

A main assortment of porous metals is between open-cell and closed-cell. In open cell foams, each cell is interconnected, letting tissue to enter and integrate the foam and anchor it into position. Whereas, in closed cell foams, each cell is surrounded by a thin wall or a membrane of metal (Ryan, Pandit, & Apatsidis, 2006).

Mainly, there are three different types of porous implants:

- partly or fully porous-coated solid substrates
- fully porous materials
- Porous metal segment joined to a solid metallic part (Ryan, Pandit, & Apatsidis, 2006).

These porous structures are mostly suitable for use as coatings due to not having the adequate mechanical properties for use as bulk structural materials for implantations, bone augmentation, or replacement for bone graft (Balla, Bodhak, Bose, & Bandyopadhyay, 2010). In addition, the porous coated titanium implants demonstrate 50 to 75% smaller fatigue strength in comparison to their conventional fully dense implants. Other limitations of these porous structures to mention is the tendency for controlled porosity features, moderately high modulus of coatings, also hard to create independent structures and limited part geometries and sizes (Balla, Bodhak, Bose, & Bandyopadhyay, 2010). Some of these issues could be resolved by development of manufacturing procedure that consist of forming a reticulated

skeleton with deposition of a metal onto the surface (Matassi, Botti, Sirleo, Carulli, & Innocenti, 2013).

The hollow shell structure or the one that was introduced in this study, could be used either in matt surfaced implants or the polished ones. The voids in comparison to foams are controllable and significantly larger than the voids in metal foams.

2.5.2.3 Lotus-type

The lotus-type or gasar method can produce high density foams from 35% to 100%, with highly anisotropic, closed morphology. The great advantage of this method is manufacturing by continuous production techniques (Smith, et al., 2012). In this method, hydrogen or a hydrogen-helium mixture are the two gases used to spread into molten steel and as the steel solidifies, pores will be created within the body. There are two other similar methods for achieving the same results: continuous zone melting and continuous casting (Smith, et al., 2012).

2.5.3 Foams vs structures in this study

Metal foams (metal-air composites) could be a solution to stress shielding as well as bone resorption and reduction in the elastic modulus of an implant. A study was conducted in 2002 on the functionality of a cellular metallic alloy implant. When porosity goes up, Young's modulus will decrease. In that study, the cellular implant has a structure like a spongy bone and it acts almost like a solid femoral stem. The cellular implant demonstrated a rise in the load-transfer mechanism in comparison to a solid one. Hence, metal foams may result in it taking a longer time for stress shielding to happen (Rahman & Mahamid, 2002). In contrast, having a porous structure could result in considerable strength reduction of the implant.

2.5.4 Auxetic materials

Auxetic materials were introduced in 2014 for impact protector devices, such as pads, gloves, helmets and mats. These have a negative Poisson ratio or when they are under one directional force, they are thicker in one or more perpendicular directions (Sanami, et al., 2014). Furthermore, honeycomb geometries were added to the stem design in new total hip replacement implants. These geometries were analysed using the finite element method and the auxetic stems showed a reduction in the stress shielding effect (Sanami, 2015).

2.5.5 Tantalum

Tantalum is an element with the symbol Ta, which has been used in the form of a porous structure in the biomedical industry. It has outstanding strength with anticorrosion properties. A tantalum open cell structure is created by chemical vapour accumulation on an interlaced carbon foam layer and porous tantalum implants could be a solution to the bone resorption issue. This type of metal could slow down the stress shielding process significantly. This lightweight metal has a long history of being used as an implant material in bone and soft tissue (Eldridge, et al., 2014); (Steven, et al., 2007). The porous structure mimics the microstructure of natural cancellous bone, providing optimum penetrance with a large surface area to expedite the ingrowth of living tissue inside the pores. Moreover, the ingrowth interface enhances the mechanical anchorage of the implant (Kaplan, 1994). The Young's modulus of tantalum in the compression of the foams was studied in 2007 and it was found to be very similar to that of cancellous bone. This similarity could help minimising the effects of stress shielding in the load transfer at the bone-implant interface (Sevilla, et al., 2007).

2.6 3D printing

In 3D printing, objects are printed by adding layer-upon-layer of material. Additive manufacturing (AM) is the term used to define technologies that create 3D objects. Materials for AM vary; however, every 3D printing technology requires a CAD (computer aid design) file to print. The obtained data from the CAD file will be structured layer by layer from printing material, such as plastic, liquid, powder filaments or even sheets of paper. Different types of 3D printing are as follows,

2.6.1 Stereolithography (SLA)

The first type of 3D printing in the history of AM was stereolithography, which is still in use today. With this method, liquid plastic is converted into 3D solid objects using a 3D printing machine known as stereolithograph apparatus (SLA), with the objects being printed using the layer-by-layer technique. In additive manufacturing, the Standard Tessellation Language (STL) format is usually used and for stereolithography, STL file format is deployed. The CAD file must contain enough information for each layer and there could be 10 layers in each millimetre. When all the layers are completed, the object needs to be rinsed with a solvent and then, placed in an ultraviolet oven to achieve the best result. The time required to print an object depends on its size, which can vary from 6 hours for small pieces up to a few days for

large ones. This type of 3D printing method is good for prototyping, because it is cheap and the production time is quicker when compared to other methods (3D printing from scratch, 2017).

2.6.2 Digital light processing (DLP)

This type of method was created in 1987 and it is very common in projectors, cell phones and 3D printing production. DLP and SLA are almost identical methods; they both work with photopolymers. However, what makes them different is their source of light, for DLP uses more conventional sources of light, such as arc lamps. The material used in this method for printing is liquid plastic resin, which hardens quickly owing to the large amount of light. DLP uses less material in comparison to SLA, which makes it cheaper and it produces more detailed products (3D printing from scratch, 2017).

2.6.3 Fused deposition modelling (FDM)

Fused deposition modelling (FDM) can print functional prototypes as well as concept models, high performance, adequate and engineering-grade thermoplastic products for engineers. Parts printed with FDM contain high quality thermoplastic material, has proved beneficial to industry and manufacturing. FDM uses almost the same technique as stereolithography by creating the object layer by layer using a thermoplastic filament. Thermoplastic is extruded onto the base when it is melted with support material, which can be removed after the job is complete. This technique is slower than stereolithography in terms of processing. Furthermore, FDM is easy to use and environment-friendly, being utilised for complex geometries due to its accuracy in detailed printing. There are different types of thermoplastic, but the most common ones are ABS (acrylonitrile butadiene styrene) and PC (polycarbonate) filaments, whilst the support materials are water-soluble wax or PPSF (polyphenylsulfone) (3D printing from scratch, 2017).

2.6.4 Selective laser sintering (SLS)

Selective laser sintering (SLS) is another 3D printing technology, where a laser is used as the power source to create objects. This technique is very similar to SLA, with the only differences being the base material and SLS uses powder material in the vat, whereas SLA uses liquid resin. There is no support material in this technique, as the object is supported constantly by unsintered powders surrounding it. The method can be used to print many materials such as nylon, ceramics and glass, including some metals, like aluminium, steel or

silver. It is also more widely employed than other methods due to this variety materials that can be used and its precision is high (3D printing from scratch, 2017).

2.6.5 Selective laser melting (SLM)

The selective laser melting (SLM) method uses a high - power laser beam to fuse and melt metallic powders to form a 3D object, with it melting the metal material into a solid part. Like the other methods a CAD file is needed for the process and the file is converted into 2D layers, with the 2D layer images then being fused by high laser energy. The energy of the beam is so high that it melts the metal powders intensely to create a solid object. This is a layer-by-layer process and stainless steel, titanium, cobalt chrome and aluminium can be used as the powder for printing. This technology is good for complex geometries with thin walls and hidden voids or channels. Furthermore, it is extensively used in many different industries, such as medical orthopaedics, aerospace and the automotive industry (3D printing from scratch, 2017).

2.6.6 Electronic beam melting (EBM)

Electronic beam melting (EBM) is another method similar to SLM, but with a different power source. It is a technology where metal powders are fused by an electron beam layer by layer. EBM is slow and expensive, with the materials used being pure titanium, inconel 718 and inconel 625. The difference between EBM and SLS is the high temperature that is accomplished by the former of up to 1000°C to achieve full melting of the metal powder. It is mostly used for medical implants and the aerospace field (3D printing from scratch, 2017). Figure 2-18 shows the different parts of an EBM machine and how it works.

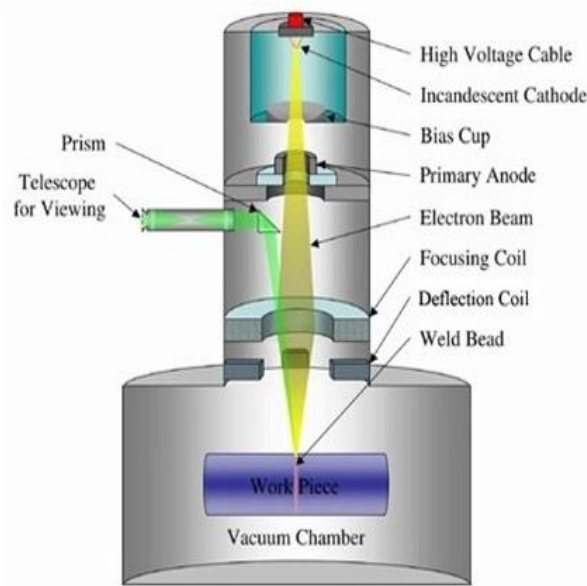


Figure 2-18 Electronic beam melting (EBM)

2.6.7 Laminated object manufacturing (LOM)

The process of this technology is different to the above methods, for which sheets coated with an adhesive are moved across a substrate with a heated roller. The heated roller melts the adhesive material and then, a laser beam is used to cut the part dimensions. When the layer cutting is accomplished, the platform is lowered by about one-sixteenth of an inch and the process is repeated until the part is fully printed. LOM is not as commonly used as the other methods; however, it is capable of working with cheap raw materials and fast (3D printing from scratch, 2017).

2.6.8 Direct metal laser sintering (DMLS)

Metal additive manufacturing (AM) is quick, precise and cost effective for creating prototypes, test parts or even final components. In this technique, metal powders are fused by a focused laser beam to create complex structures, which may not be possible by traditional manufacturing techniques. There is a platform where objects are attached to carry out the process and a support material (a liquid phase) is needed when powders are being scanned by a laser (3trpd, 2015). This technique was used to print samples for this study in order to run tests on them. Figure 2-19 shows the steps of direct metal laser sintering (DMLS).

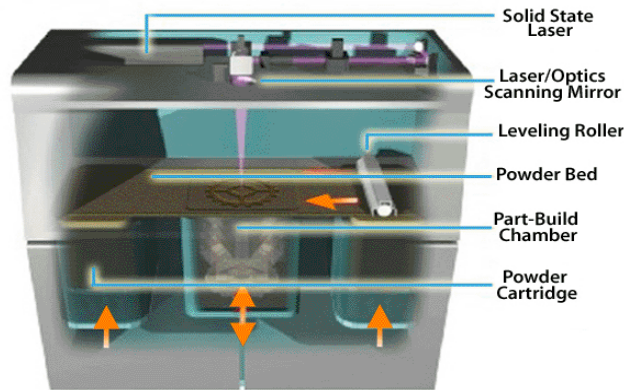


Figure 2-19 Direct metal laser sintering (DMLS) (whiteclouds, 2015)

2.7 Finite element analysis in a biomedical study

Finite element analysis (FEA) is a numerical technique for obtaining approximate results to boundary value problems for partial differential equations. With this method, the structure is divided into limited elements. FEA has eased the study of the human body and it has helped much research about loading, such as gait and muscle forces. Specifically, it involves using partial differential equations to solve any loading situation, where the stress is distributed and where it reaches its maximum value. The first time that FEA was used for orthopaedic biomechanics was in 1972 to evaluate human bone stresses (Brekelmans, et al., 1972). At the moment FEA is being used widely in industry and the research environment. Strain gauge results are also used to validate them.

Mechanical testing when compared to FEA is more expensive and time consuming. Under this method, a specific point is considered using strain gauges, or on the outer layer of the structure, as in photoelasticity, whilst FEA is less invasive, cheaper and faster to analyse. Moreover, it offers analysis for a wide range of prostheses designs. It also demonstrates the full effects of stress over the structure with varying patient situations.

There have been major improvements since then in creating more precise models of humans. The relationship between bone resorption and stress shielding around hip stem was discovered using FE modelling in 1991. It was also elicited that by using flexible stems, the stress shielding around the stem will decrease. However, the proximal interface stresses go up. In addition, high proximal interface stresses can result in interface debonding and micromotion (Huiskes, et al., 1992).

Moreover, it was determined that the reduction of stress regarding stress shielding causes 50 % of mass bone reduction after 4 to 7 years after operation (Sumner & Galante, 1992).

Many studies have been carried out on the relationship between material flexibility and bone resorption. These have demonstrated that as the flexibility of the material increases the bone resorption will decrease. Similar results were obtained when solid stems were replaced with more flexible hollow stems (Boby, et al., 1990).

2.7.1 ABAQUS Software

ABAQUS/CAE 6.14-1 was used in this research, which is software suitable for FEA and computer-aided engineering. It was originally released in 1978. ABAQUS. Abaqus/CAE, Abaqus/Standard, Abaqus/Explicit, Abaqus/CFD and Abaqus/Electromagnetic are the five core software products.

Abaqus/CAE is a complete Abaqus environment that provides a simple, consistent interface for creating, submitting, monitoring, and evaluating results from Abaqus/Standard and Abaqus/Explicit simulations (ABAQUS/CAE USER'S GUIDE, 2014). There are different modules needed to be completed before simulation, with each defining a logical aspect of the modelling process. For example, the geometry and material properties can be determined as well as a mesh generated. When these modules are completed, the model is built from which Abaqus/CAE generates an input file submitted to the Abaqus/Standard or Abaqus/Explicit analysis product (ABAQUS/CAE USER'S GUIDE, 2014). The analysis product performs the analysis, sends information to Abaqus/CAE to allow for monitoring of the progress of the job, and generates an output database. Finally, the visualisation module of Abaqus/CAE (also licensed separately as Abaqus/Viewer) can be used to read the output database and view the results of the analysis. Abaqus/Viewer provides graphical display of Abaqus finite element models and results, being incorporated into Abaqus/CAE as the visualisation module (ABAQUS/CAE USER'S GUIDE, 2014).

2.7.2 Material properties

The material properties for bone are complex and it is hard to define the interface relation between the implant and the bone. Consequently, the material property of the bone has been simplified in many studies (Ramos & Simoes, 2006). That is, cancellous bone has been assumed as being homogeneous for simplicity, but bone is non-linear, heterogeneous and anisotropic. Most researchers have specified bone as a linear elastic material in FEA. This material property is rational when bone is under non-impact loading (Biewener, 1992).

However, bone material properties can differ significantly from one location to another. Furthermore, the microstructural organisation of the bone affects its stiffness and strength in both the cancellous and cortical bone. This usually results in different stiffness and strength characteristics in various directions known as anisotropy (Biewener, 1992). The two most popular anisotropic material models for bone are transverse isotropy (five independent material constants) and orthotropy (nine independent material constants) (Biewener, 1992). In contrast, isotropy has two independent material constants: Young's modulus, E and Poisson's ratio, ν . As an example, Haversian cortical bone from the diaphysis of a long bone is specified as a transversely isotropic material. Sometimes, cancellous bone is specified as an orthotropic material due to its directional material behaviour (Biewener, 1992).

Different studies have used different Poisson's ratios and Young's moduli. This is exemplified in work undertaken by Walker et al. in 2000, who used Young's moduli and Poisson's ratio in three orthogonal directions for cortical bone as follows: $E_1 = 20$ GPa, $E_2 = 13.4$ GPa, $E_3 = 12$ GPa and $\nu_1 = 0.24$, $\nu_2 = 0.22$, $\nu_3 = 0.38$. $E = 1$ GPa and $\nu = 0.3$ were assigned as the material property for cancellous bone and it was assumed to be isotropic (Walker, et al., 2000).

2.7.3 Mesh element type and size

It is up to the user to decide, firstly, whether to use a 1D, 2D or 3D representation. In the real world, all structures are three dimensional, but simple stress analyses can be made for approximation. Furthermore, the physics of the problem can help users in choosing the right type of element (Biewener, 1992). Moreover, opting for meshing in FEA settings and choosing the element size as well type is down to the user. In biomechanics, using 1D representation is not sufficient, but a two dimensional demonstration can be suitable. That is, sometimes, deformation and stress occur mainly in a specific direction. Hence, analysing the stress and strain in such a direction is very effective. A similar principle applies when analysing the structure in 2D; however, in biomechanics these situations rarely occur (Biewener, 1992).

Meshing is a process where the model is divided into nodes and elements. These elements can be linear or quadratic. Linear is where the elements have two nodes per side and with quadratic there are three (Biewener, 1992). A fine mesh increases the simulation time and accuracy when compared to a coarse one. Tetrahedral elements are usually the number one

choice when it comes to meshing as they are automatically generated and they also provide high quality mesh due to their shape (Chang , et al., 2001).

The number of equations and calculations in FEA increases when the interpolation order increases. Moreover, the time and accuracy of the simulation is enhanced by increasing the interpolation order. Interpolation order could add extra nodes between two ends of elements. Elements are divided into three different categories (simplex, complex and multiplex) based on their interpolating function (Biewener, 1992).

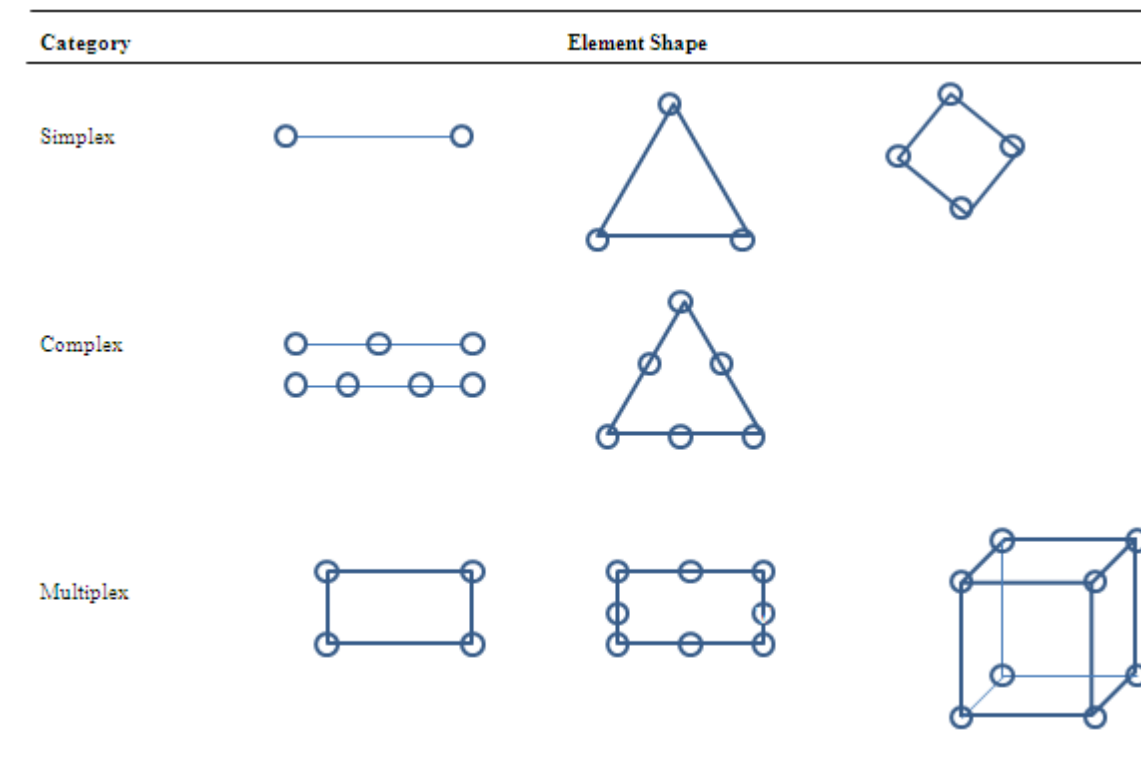


Figure 2-20 Illustration of simplex, complex and multiplex elements (Fagan, 1992)

As it is demonstrated in Figure 2-20, simplex elements have polynomials with constant and linear terms, with their nodes being positioned at the corners. Complex elements have the same shape as simplex ones, but with more nodes, whereas higher order interpolation polynomials are used in complex elements, which are the same as multiplex ones. However, multiplex elements have their sides parallel to the coordinate system (Fagan, 1992). The linear eight-node brick and the quadratic twenty-node one are the most used 3D elements (Biewener, 1992).

FEA subdivides the whole geometry into fine elements and applies boundary conditions as well as load variables across the model by distributing them along the elements, one by one (Fagan, 1992). The deformation of the elements should not be excessive as it causes false

results. There are a few methods for controlling deformation of the elements and checking whether they are reliable. As shown in the Figure 2-21, the first, is the ratio of the longest side of an element to the shortest. The second, is the measure of skew and taper to quantify element distortion. In addition, the internal angles of the elements can also be used as a way of assessing element distortion. Triangular elements should have angles near 60° and the corner of the rectangular elements should be close to 90° (Fagan, 1992).

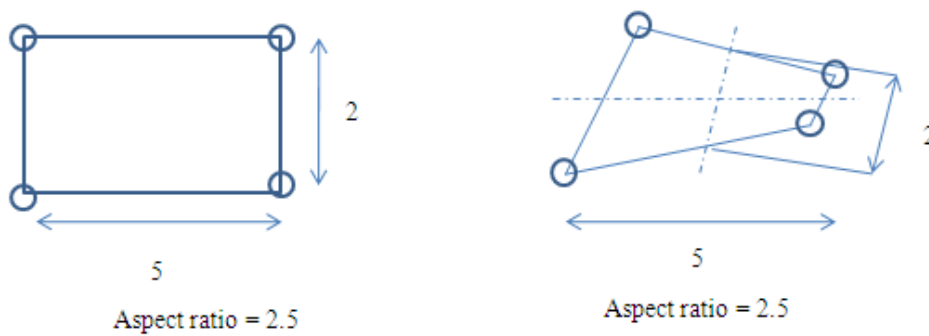


Figure 2-21 Two rectangular elements with the same aspect ratio with different behaviours (Fagan, 1992)

The effect of mesh density in bonded and debonded cemented hip implants was studied by Stolk et al. in 1998, when it was observed that the former are not sensitive to mesh density, but the debonded cemented implants showed high sensitivity to this (Stolk, et al., 1998).

In other studies on the mesh, two typical element types on the femur have been compared, with the typical elements being hexahedral (8 and 20 node bricks) and tetrahedral (4 and 10 node tetrahedrons). The obtained results from these two elements were von-Mises stresses and principal strains. These results were also compared to theoretical von-Mises stress distribution. In sum, tetrahedral elements demonstrated closer results to the theoretical ones, whilst hexahedral elements appeared to be more steady (Ramos & Simoes, 2006).

2.7.4 Modelling the interface between bone and implant

Defining the interface between the bone and implant is very important due to its role in passing the load through the two. There are elements in bone and implant that are not always connected and another type of element is needed to reach load transfer across the interface, which is particularly significant when an uncemented implant is used. Uncemented implants form a fibrous interface between the bone and implant. There are two issues that result in loosening of the prosthesis, one is by wear particles in bone osteolysis and other is a fibrous

tissue formation process (Pioletti, et al., 1999). There are no biological factors illuminated for the fibrous interface (Fernandes, et al., 2002). In some studies, it has been suggested that the mechanical environment of the bone cells is more effective in causing the fibrous tissue than wear particles (Aspenberg & Herbertsson, 1996). Some other factors may play a role in formation of fibrous material, such as hydrostatic compression (Skripitz & Aspenberg, 2000), fluid pressure (Van der Vis, et al., 1998) and fluid flow velocity (Yuan, et al., 2000).

There are ways of defining the interface between bone and the implant. In the FE software, parameters have been developed to describe the interface between the two. Moreover, in some studies, laws have been created to model the dynamic behaviour of the tissues around implants (Nuno & Amabili, 2002) and in some cases a series of bone-implant interface parameters were set (Fernandes, et al., 2002). There are many parameters for defining non-linear behaviour in FE software. Parameters such as contact elements are node to node, node-to-surface and surface-to-surface. Node-to-surface or surface-to-surface, which are usually selected for bone-implant interface due to their accuracy (Viceconti, et al., 2000). In the current study, fully bonded and friction contact are defined at the interface between bone and the implant.

A study 2001 demonstrated that parameters, such as convergence tolerance and contact stiffness are important in the precision of finite element results (Bernakiewicz & Viceconti, 2001).

2.7.5 Applying boundary conditions such as muscle loads and constraints

One of the other steps before simulation is applying boundary conditions and loads to the components. For example, when designing parts of the skeletal system, loads that exist during the gait cycle are usually joint, ligament and musculotendon forces. The constraints in FEA are controlled by defining displacement for the models in terms of the nodal behaviour and controlling it. These displacements will cause stress in the nodes. For instance, a rigid body means that displacement is zero in any direction. In addition, selection of the constraint should be carefully defined as this may result in artefact stress (Biewener, 1992). For implant-bone simulation, it is crucial to apply load at the centre of the femur head. There are various conditions when applying load. That is, loads on the implant will differ with walking, fast walking, downstairs walking, stair climbing and so on. Bergmann et al. (2001) calculated parameters for boundary conditions for different activities (Bergmann, et al., 2001). Figure 2-22 shows different direction of forces and moments on the femur, which are useful when

applying load and boundary conditions for FEA. Figure 2-24 demonstrates the average of the contact forces for different activities, which can be used to simulate the hip analysis for each of them.

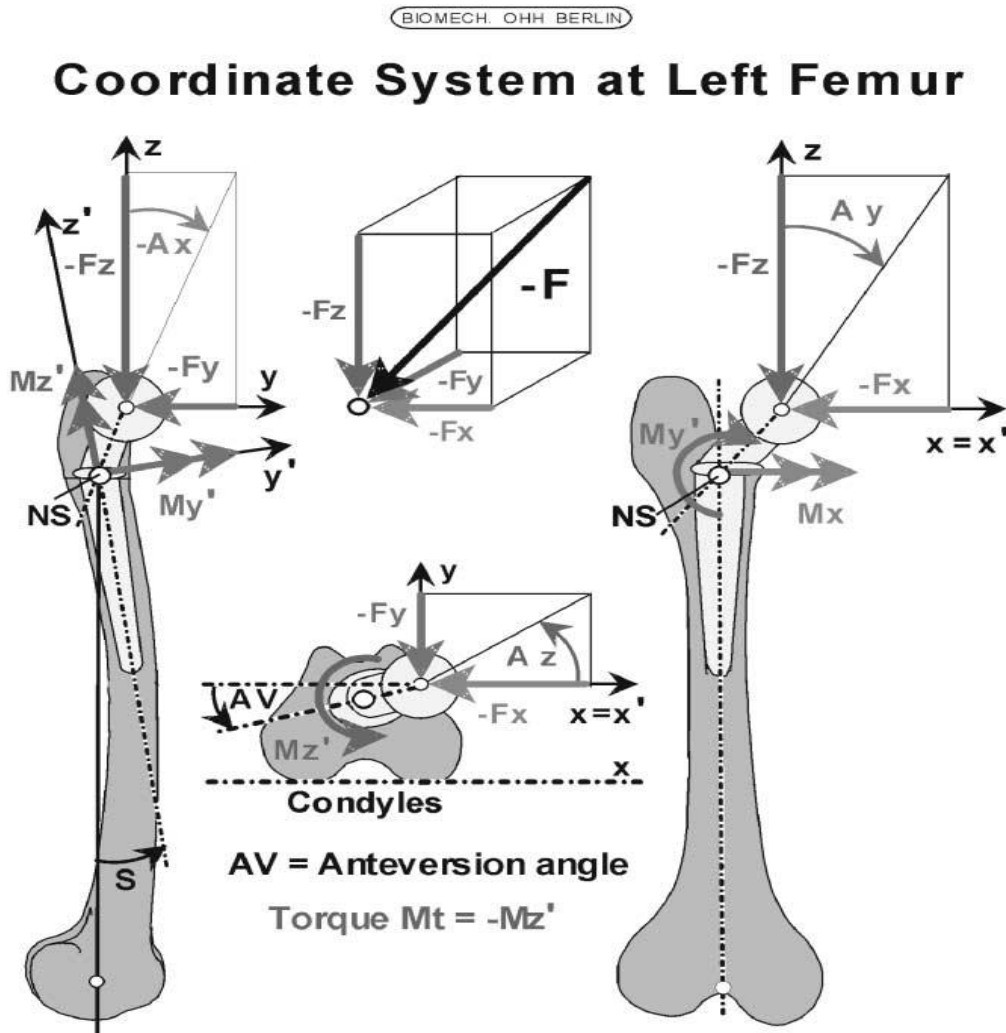


Figure 2-22 The force components in x, y, z directions. The axis x is parallel to the dorsal contour of the femoral condyles in the transverse plane and z is parallel to the idealised midline of the femur (Bergmann, et al., 2001)

Muscle load plays an important role in joint movement. Results have shown that the internal joint load reduces by 50% when compared to models that ignore the effect of muscle load (Duda, et al., 1997). Cristofolini et al. (1995) also studied the impact of muscles on the femur. Specifically, they looked at the impact of each muscle group on the femur in relation to axial and hoop strains. Furthermore, this study also showed the significant impact of muscle loads, especially the three glutei (Cristofolini, et al., 1995). For another study, in 1997, an FE model of a femur was developed to look at the stresses and strains for all thigh muscles and the joint contact forces involved. Four phases of a gait cycle were considered in this study. It was shown that, by having all the thigh muscles attached, the surface strains were closer to in vivo

recordings. The difference existed in results, were reduced to 5% when having adductors added to a loading regime (Duda, et al., 1997).

The importance of the muscles' role was also established by Stolk et al., who investigated the minimum number of muscle forces needed for pre-clinical tests in a cementless THR. The highest effect of the muscles on joint load is when they abduct. That is, of all the forces created by the different muscles, the abductors had the most significant impact (Stolk, et al., 2001). In sum, by having the hip joint contact force and all the muscle forces, especially the abductors, more sufficient results can be obtained that are closer to in-vivo recordings. Figure 2-23 displays the muscles of the hip.

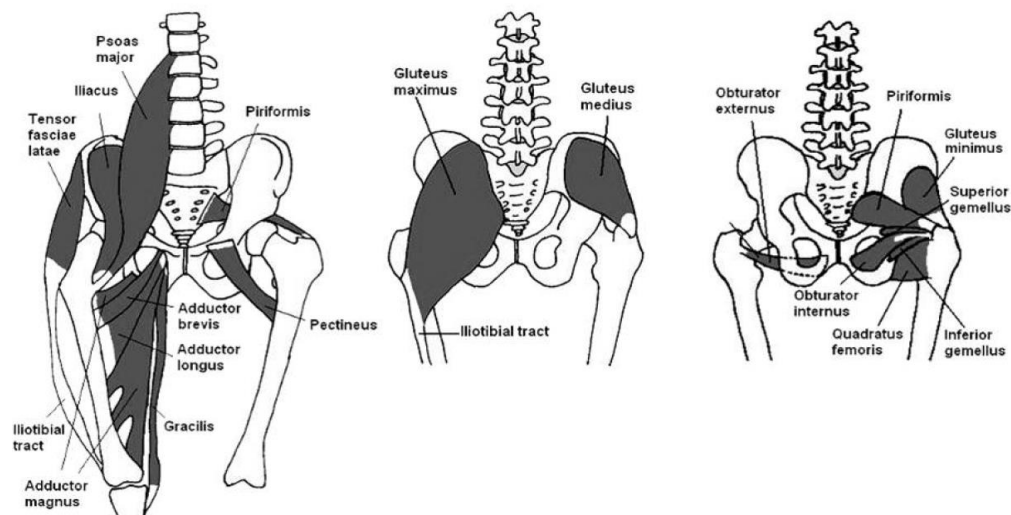


Figure 2-23 Muscles of the hip (González, 2009)

Constrained rigid body motion and defining the degree of freedom have an important effect on FE simulation in that they control the behaviour of the nodes. Defining the constraints and degrees of freedom at the nodes in the mid diaphysis (Easley, et al., 2007) or nodes on the distal condyles (Polgár , et al., 2003) is a common criterion.

Speirs et al. applied five different load conditions in FEA on a femur and compared them with a physiological model to study the effect of different load and boundary conditions on the bone. The results showed that the model with every muscle force applied is close to the physiological reality. Also, it was elicited that the mid-diaphysis constrained model has lower strain and the distally constrained model has higher strain on the femur compare to the physiological one (Speirs, et al., 2007).

Hence, choosing the constraints plays an important role in FE simulation, which has previously been largely ignored. Studies thus need to be conducted to estimate the best constraints to use and to analyse the sensitivity of the output regarding the constraints.

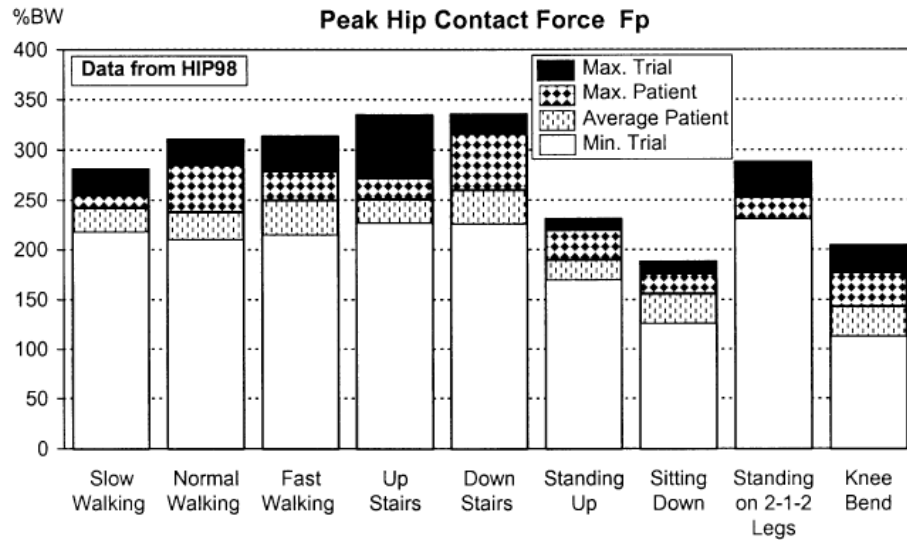


Figure 2-24 Average, minimum and maximum values for hip contact force (Bergmann, et al., 2001)

A study in 2007 considered three different cases under various displacement constraints to avoid rigid body motion as shown in figure ... in the first two cases, all three nodes were fully constrained at the mid-diaphysis or distal condyles, respectively similar to previous studies. The third case, node constraints were chosen to approximate joint constraints at the knee and hip: a node at the knee centre was selected to be constrained in three translational degrees of freedom (DOFs). The node at the hip contact where the force for instance was applied, was constrained in two DOFs in a way that this node could only deflect along an axis towards the knee centre. The sixth node to be constrained was on the distal lateral epicondyle to prevent any rigid body motion of the model around the hip-knee axis (Speirs, et al., 2007).

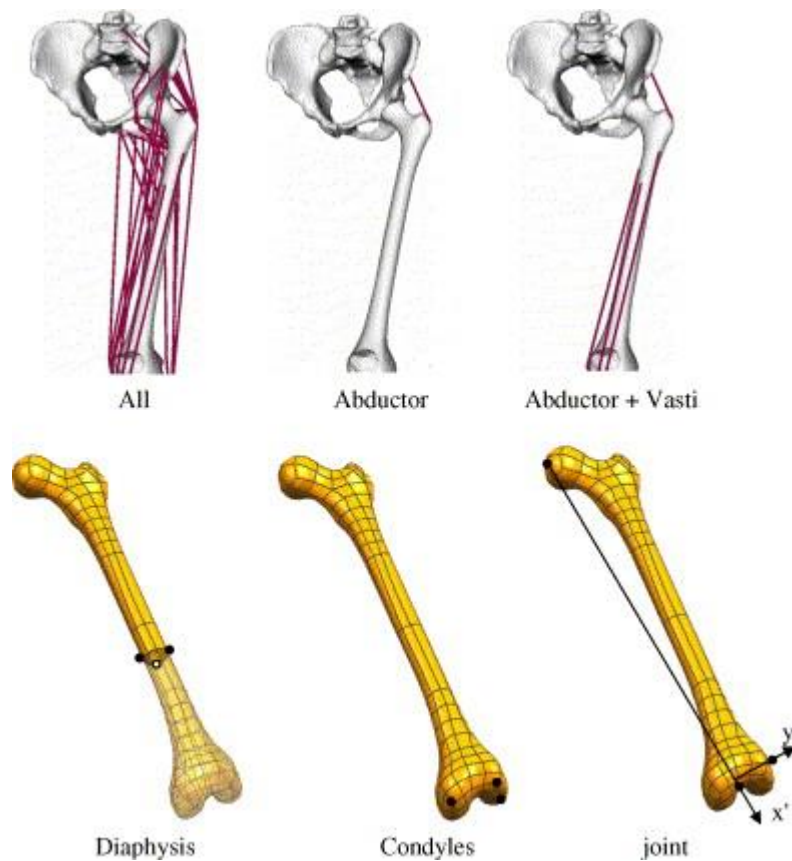


Figure 2-25 Top: muscle sets included in the analysis. Bottom: oblique view of the femur solid model showing the location of node constraints for each configuration (Speirs, et al., 2007)

The total deflection of the femur depended significantly on the applied boundary conditions (fig2). A significant posterior and medial deflection of the hip centre was observed up to 15 and 11 mm, respectively in the cases A to D. Whereas in case E, deflection occurred in the distal direction which made the femoral shaft to bow laterally. In addition, the deflection magnitude of the latter case was less than 2 mm under human gait loads, in comparison to the other cases which were 8-19 mm. A follower hip contact force caused reduction in deflections to between 6 and 7.5 mm (Speirs, et al., 2007).

In the case E, when the shaft bending was examined in the local distal coordinate system, a displacement of 2.5 mm at the mid-shaft and 3.2 mm at the femoral head were observed.

When the bending of the shaft was tested in the local distal coordinate system, a displacement of 2.5 mm at the mid-shaft and 3.2 mm at the femoral head were determined (case E). This compared to 5.8 mm at the femoral head for case D (Speirs, et al., 2007).

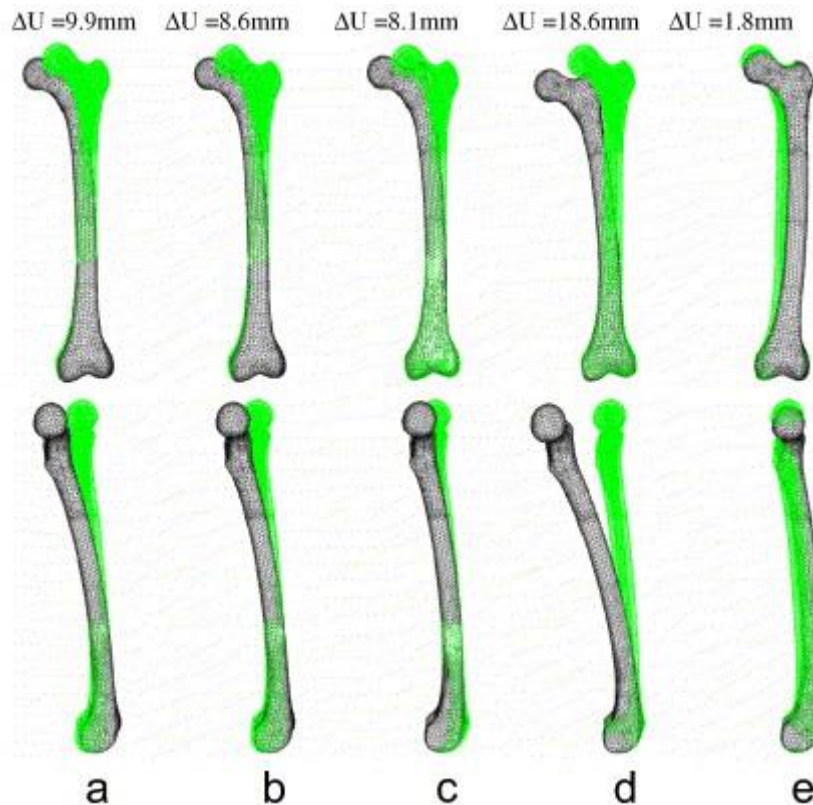


Figure 2-26 Deflected femur (solid) under walking loads in the anterior (top) and medial (bottom) views compared to the undeflected shape (outline) (Speirs, et al., 2007)

The contact pressure goes up when a wedge-shaped implant is fixed, but, friction coefficients is measured under constant contact pressure. Plastic deformation and abrasion of the bone while implantation is taking place are hardly reported, although they state the effective interference, by decreasing the nominal interference between implant and bone cavity (Damm, Morlock, & Bishop, 2015). In a study in 2015 Analysed radial forces during simulated implantation and explantation of angled porous and polished implant surfaces against trabecular specimens, to define the corresponding friction coefficients. The effective interference after implantation was defined by analysing permanent deformation. For porous surface structure that was tested, the friction coefficient primarily augmented while normal contact stress during implantation was increasing, however, it reduced at higher contact stresses. For a lower porosity surface, the friction coefficient augmented with normal contact stress during implantation, however, it did not attain the peak magnitude measured for rougher surface. For the polished surface, the friction coefficients were independent of normal contact stress and lower in comparison to the porous surfaces. Friction coefficients for pull-out were slightly lower in comparison to push-in for the porous surfaces, but not for the polished surface. For the porous surfaces, the efficacious interference was 30% of the nominal interference (Damm, Morlock, & Bishop, 2015).

2.7.6 Solution

The computer time that is essential for simulation completion depends upon the number of nodes and degrees of freedom per node. The property of data format, element definitions, adequacy of the boundary conditions and the appropriateness of the material properties are checked by the FE program (Biewener, 1992).

2.7.7 Validation of results

The validation of any FEA results comprises an assessment of two distinct issues: model validity and model accuracy. The validity of the model in FEA depends on geometry, loads, material properties, interface and the boundary conditions. The closer the definitions of these are to the real structure, the more reliable and valid results can be obtained. The accuracy of the model in FEA can be assured by a convergence test once a valid model has been defined (Biewener, 1992). This test comprises refinement of the mesh, which can be accomplished either by decreasing the size of the elements or increasing the number of nodes and elements in important areas. The purpose of mesh refinement is to increase the precision of the results and in order to minimise the effect of the mesh on the simulation, its size should be refined. That is, its size should be refined until the simulation result is not affected significantly. In other words, the mesh size of a model has a direct relationship with the results and hence, mesh refinement should reach a level such that these are not affected significantly (Fagan, 1992). Figure 2-27 shows how errors occur in results due to unsuitable mesh choice. As can be seen, when a combination of linear variation and quadratic variation is used, this causes a gap in the model. The suggestion for sorting out this problem is to use either transition elements or to impose a constraint equation on the mid-side nodes (Fagan, 1992).

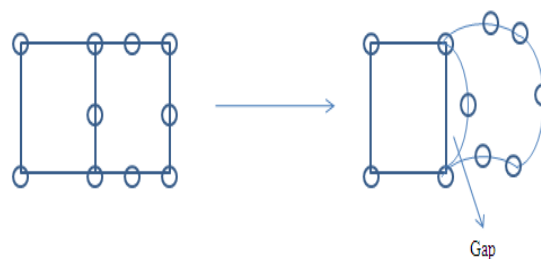


Figure 2-27 Unacceptable element combinations (Fagan, 1992)

2.7.8 Interpretation of the results

The visualisation of results is known as the first step of the interpretation process. The displacements, stresses and strains within the structure of hard tissue biomechanics are the main variables when analysing a model. Stress or strain on a surface or plane of a model is visualised by contour and fringe plots. In addition, the graphical vision of displacements is usually analysed by looking at the mesh in the deformed configuration (Biewener, 1992). The stress and strain when studying biomedical results can be overestimated in FEA. Finally, the results in FEA can be used to understand the mechanical behaviour of the model in general.

2.8 Conclusion

The surface finish of a hip implant is important due to the interaction between the bone and the implant. There have been so many studies aimed at demonstrating the advantages of a polished femoral stem over a matt surface. Regarding which, it has been elicited that in the same cases a matt surface failed earlier than polished, such as with the Exeter and Iowa stem (Howie, et al., 1998).

The current materials used in biomedical engineering cannot compete with the material properties of bone (Thielen, et al., 2009). The main biomedical metals used for medical applications are stainless steel, Co alloys and Ti alloys (Niinomi, 2008); (Karanjai, et al., 2007).

As it was explained, one type of biomaterials extensively used are titanium alloys, which are exceptionally known for failure previous to Cobalt chrome and stainless steel. Furthermore, the reason is that titanium is sensitive to fracture corrosion. Femoral stems manufactured using titanium alloys have certain concerns, and titanium articulating surfaces are no longer recommended for biomedical applications (Zhang, 2009).

One of the most important failure aspects that all implants face is stress shielding. The higher the rigidity of the implant, the more chance of getting bone resorption, as the implant will transfer a smaller amount of load to the bone (Bitsakos, et al., 2005). Rigid stems show greater stress shielding than flexible ones and the latter have demonstrated less bone resorption (Sumner & Galante, 1992). Titanium compared to all the alloys used in THR is the most suitable due to its low modulus and high fatigue strength. Whilst stiff stems result in bone resorption, flexible ones decrease it, if the interface bond is strong. It can be concluded that flexible stems are the solution to bone resorption, but it may also result in increased loosening rates (Huiskes, et al., 1992). If the stiffness of an implant decreases, an increase in

load transfer from the femoral stem to the proximal femur will occur, which will result in a decrease in the stress shielding (Diegel, et al., 1989). Implant stiffness depends on the implant material and its cross sections.

There have been studies investigating what factors could lead to stress shielding reduction.

In a study in 1990, a hollowed stem prosthesis using FEM was worked on and it was discovered that a hollowed structure reduces the stress peak below the end of the prosthesis. In addition, in the proximal cortical bone, stress is increases about 20% (Mattheck, et al., 1990). In other research, the data for 40 patients who had had their hip replaced with a hollow structure implants were analysed. The results obtained from their clinical records after one year, showed adequate improvements and no thigh pain had been reported, which was attributed to the increased elasticity and better stem fitting (Schmidt & Hackenbroch, 1994).

A study in 2001, was focused on optimising a hollow structure stem to decrease stress shielding and also decreasing the maximum stress in the cement. In this research, the inner diameter was the variable and cement stress defined as the design constraint. The obtained results were compared with a solid structure stem, but the implant was only cylindrical with simple boundary conditions. The stem with the hollow structure showed an increase in proximal bone stress of about 15% and this was 32% for the case with high strength cement (Gross & Abel, 2001).

Regarding another approach in 2001, a new thin mid-stem design was introduced, which was aimed at improving the stability of the implant within the femur. Another variable in this design is the distant from distal end which is demonstrated below. These variables help to increase load transfer by decreasing the cross-sectional area of the stem (Chang , et al., 2001).

A study in 2007 demonstrated how topology optimisation is to achieve the best design to distribute stress within a fixed body, while boundary conditions are applied. Optimised implants have been more successful in passing the load onto the femur to decrease the stress shielding when compared to traditional femoral stems (Ridzwan, et al., 2007).

There have been two approaches regarding the relation between porosity and Young's modulus such that when the former goes up, the latter will decrease. In these studies, the cellular implant had a structure like a spongy bone and it acted nearly like a solid femoral stem. The cellular implant demonstrated a rise in the load-transfer mechanism in comparison

to the solid one. Hence, it was concluded that metal foams will lead to a longer period before stress shielding happens (Rahman & Mahamid, 2002); (Smith, et al., 2012).

Finally, honeycomb geometries were added to the stem designs in new THR implants. These geometries were analysed using the finite element method and the auxetic stems showed a reduction in the stress shielding effect (Sanami, 2015).

As the above studies have shown, stress shielding is a major problem and that reducing Young's modulus could solve the issue. One of the ways to reduce the young modulus is to have a porous structure.

3 Research Method

As discussed in the previous chapter, titanium is the bench mark material used in biomedical fields due to its outstanding strength despite having a low modulus. Previous studies have worked on optimising the design of implants with different materials to reduce stress shielding.

For this study, a new structure for implants, such as stainless steel, to mimic titanium, has been developed. The structure was applied to stainless steel due to its abundance and its price. This could be ideal for third world countries and also people with lower budgets for their hip replacement. The idea is doable based on 3D printing capability and the new structure also reduces stress shielding rapidly.

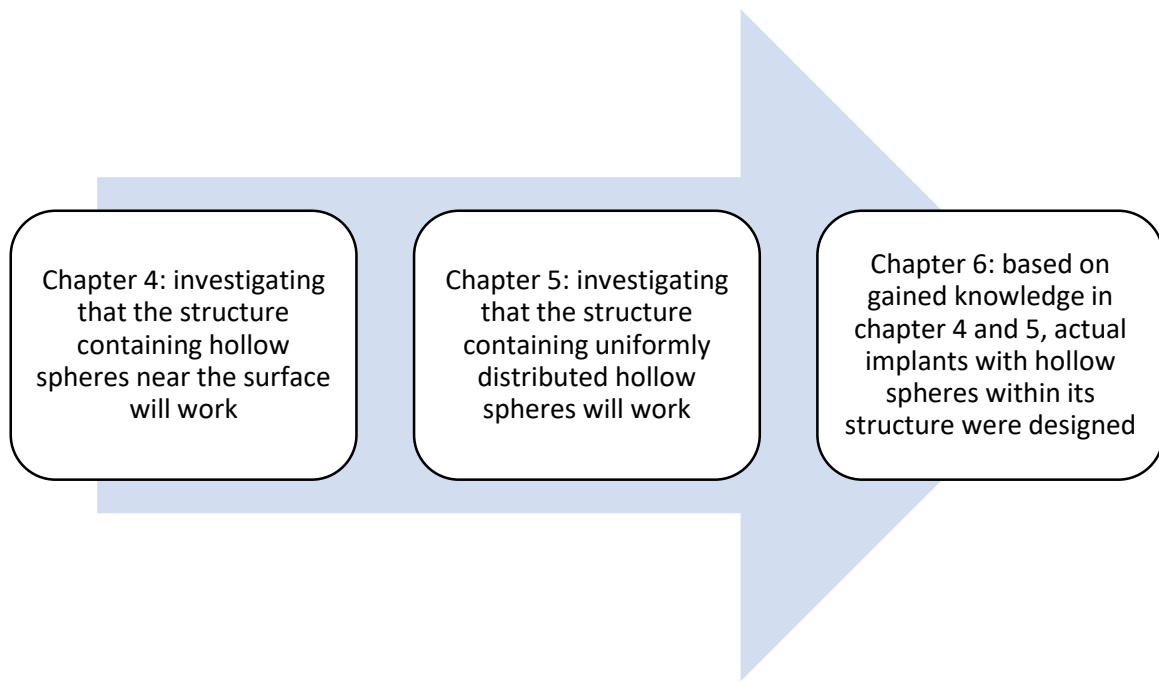


Figure 3-1 Schematic view of the logics behind each chapter of this thesis

This chapter contains summary of the structure of this study conducted to achieve the objectives of the thesis. Figure 3-1 provides an outline of chapters four, five and six. These chapters are conducted to approve the reduction in stress shielding post placing hollow spheres within the implant. These improving steps led to the optimum design. Initially, hollow spheres creation in the actual implant resulted in failure due to the high number of elements, which made the problem unsolvable. Another problem faced was regarding the meshing, whereby the spheres could not be recognised by the Abaqus meshing module. Hence, different software (3-matic) was used to tackle the issue. In addition, creating implant samples containing spheres of various sizes and at different places was not easy to program. Finally, to distinguish the optimum case practically, printing implant samples would have been expensive. Consequently, cylinder samples were created to investigate the impact of hollow spheres within a structure. In regards to the idea, two chapters were dedicated to discussing these effects in localised and uniformly distributed phases.

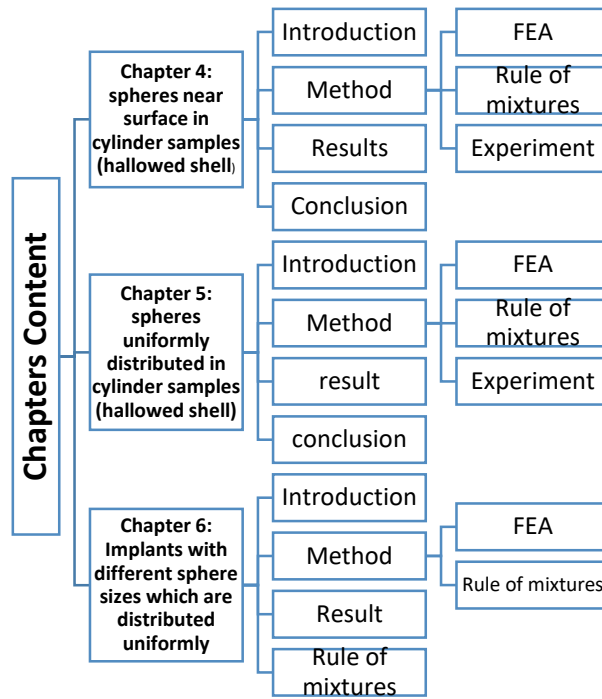


Figure 3-2 Contents of the chapters for this thesis

Figure 3-2 displays how the chapters are structured to achieve the aim of thesis. Each contains an introduction, methods and results, with each making a specific contribution to achieving this aim. The purpose of chapter 4 is to prove that structures containing hollow spheres close to their surface (hollow shell) reduce stress shielding. This was accomplished by the increase that occurred in the load transfer. The aim for chapter 5 is to investigate how structures containing uniform distributed hollow spheres will behave. This was pursued by comparing the reduction of Young’s modulus with the samples containing close to surface hollow spheres. Finally in chapter 6, these design characteristics are implemented on femoral implants to investigate the effect of hollow spheres in the hip prostheses field.

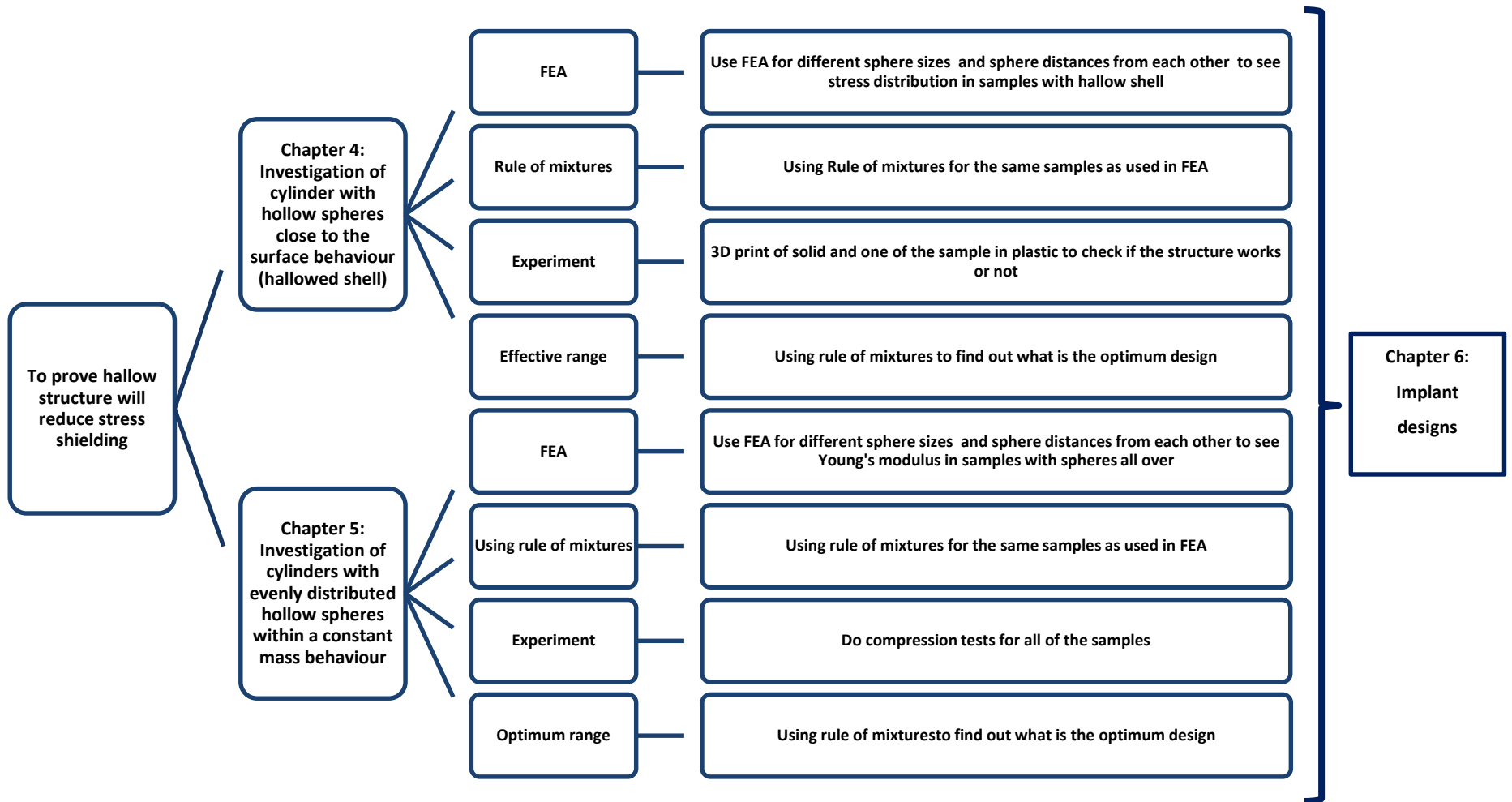


Figure 3-3 Summary of chapters 4 and 5

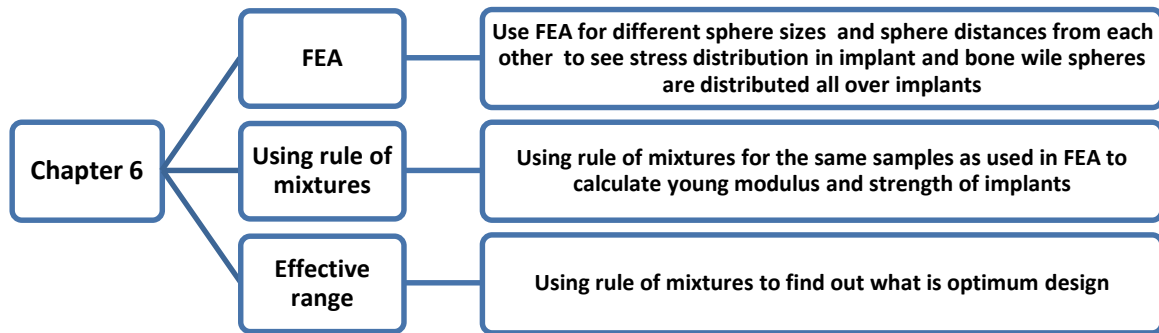


Figure 3-4 Summary of chapter 6

The first approach was to investigate the effect of localised hollow spheres near the surface. The samples were created in Solidworks as cylindrical objects. The idea was applied to a smaller scale due to the high number of elements when the actual implant contained spheres. Firstly, the cylindrical models containing spheres near their surface were analysed using FEA. That is, a cylindrical solid design with bone specifications was used as bone in FEA. The rule of mixtures was also used for these cylindrical samples (only for the shell area) to calculate the strength and Young's modulus. The best cases of these samples and a solid one were then 3D printed in plastic using the machines at the University. A compression test was carried out to ascertain whether the idea also works on a structure. The second approach was to use ASTM Standards to design the samples and try to distribute hollow spheres uniformly throughout the structure. The cylindrical models containing uniformly distributed hollow spheres were simulated using FEA. The rule of mixtures was used, because FEA could not be accomplished due to the high number of elements. The rule of mixtures was also used to estimate how much volume could be extracted from the model without weakening the structure and it was also utilised to calculate the Young's modulus of each specimen. Then, the samples were 3D printed using stainless steel for a compression test, which Figure 3-3 summarises. The final approach was to add hollow spheres to the actual implant to investigate the outcome of this new structure. FEA was applied and the rule of mixtures to calculate the Young's modulus. Figure 3-4 provides a summary of chapter 6.

The following criteria are a summary of the main methods used in the empirical chapters of this study, with, as aforementioned, each chapter containing its own objectives and aim. Hence, they include their separate methods and results.

3.1 Rule of mixtures

Having established that meshing in the presence of small hollow spheres generates over 15,000,000 elements, conventional approach FEA proved to be impossible, and in fact mesh generation failed to operate. Due to this, the only way to conduct this research is to resort to the rule of mixtures. As a part of this research, the rule of mixtures was used to work out the volume fraction for the specimens in this study. That is, the models were considered to be composite and the rule of mixtures aided the estimation of the volume that could be extracted. It was also deployed to work out the Young's modulus. In the analysis chapters, the rule of mixtures was also used as comparison element alongside the computational and experimental analysis.

3.2 Finite element method

Finite element analysis (FEA) was used to ascertain, computationally, how the stress distributes over a structure containing hollow spheres. It was also used to obtain stress-strain graphs of the specimens and to see how much stress was transferred to the bone.

In order to understand the impact of hollow spheres within a structure, the FEA method was applied to the samples containing localised hollow spheres near the surface, samples having uniformly distributed hollow spheres and actual implants. When designing the specimens including hollow spheres, three main variables were taken into consideration for the analysis: sphere size, the distance from the surface and the distance from each other.

3.3 Compression test

A compression test was applied to two sets of samples. The samples were printed in plastic, with the hollow spheres were placed near the surface. Those that had uniformly distributed hollow spheres were sintered and printed in stainless steel. The compression test was applied to obtain strain by strain gauges in the plastic samples. Then, the results were converted into stress to analyse the stress differences at the surface of the samples, as provided in chapter 4. Whilst a compression test was applied to stainless steel specimens to obtain the compression modulus and stress-strain curve in chapter 5. Moreover, this was undertaken to ascertain the differences between the various sphere specifications in a mass.

4 Investigation of cylinder with hollow spheres close to the surface behaviour

This chapter includes details of the applied materials, calculations, meshing strategies, different composite scenarios and the simulations that helped to analyse models. SolidWorks 2014 SP 4.0 was used to create the samples in this chapter. These samples were designed cylindrically with similar height and radius; however, their internal structures differ. Then, Abaqus/CAE 6.14-1 was used to analyse imported 3-D models by finite element analysis and the results were obtained using the Abaqus result module. This chapter also provides details of the calculations using the rule of mixtures, which were obtained using PTC Mathcad 3.1. Furthermore, details of the compression test that was applied to two samples are included in this chapter.

4.1 Introduction

The aim of this chapter, is to develop the idea of having hollow voids near the surface (outer layer) of the samples, as shown schematically in the Figure 4-1, so as to reduce the localised Young's modulus. This chapter basically focuses on weakening the structure at the bone-cylinder interface to reduce stiffness at the skin. This chapter also focuses on verifying whether a hollow sphered structure near the surface will decrease stress shielding. In addition, it also identifies the best configuration in terms of the sphere size and distribution within the mass. Having a reduced Young's modulus will improve displacement, for as this increases, more stress will transfer onto the surrounding area, which in this study is bone. The purpose of having the spheres near to the surface is to transfer the stress to the surrounding areas to reduce stress shielding, whilst at the same time having a solid centre so as to

maintain the strength of the structure. Furthermore, having empty spheres near to the surface will help the stress inserted to be distributed evenly to the surrounding bone. FEA, the rule of mixtures and experiments were used to investigate these effects under specific load. In sum, this chapter is set out to evaluate whether these hollow structures decrease stress shielding by altering the size and distribution of spheres. The spheres in each sample have been placed uniformly in each row close to the surface.

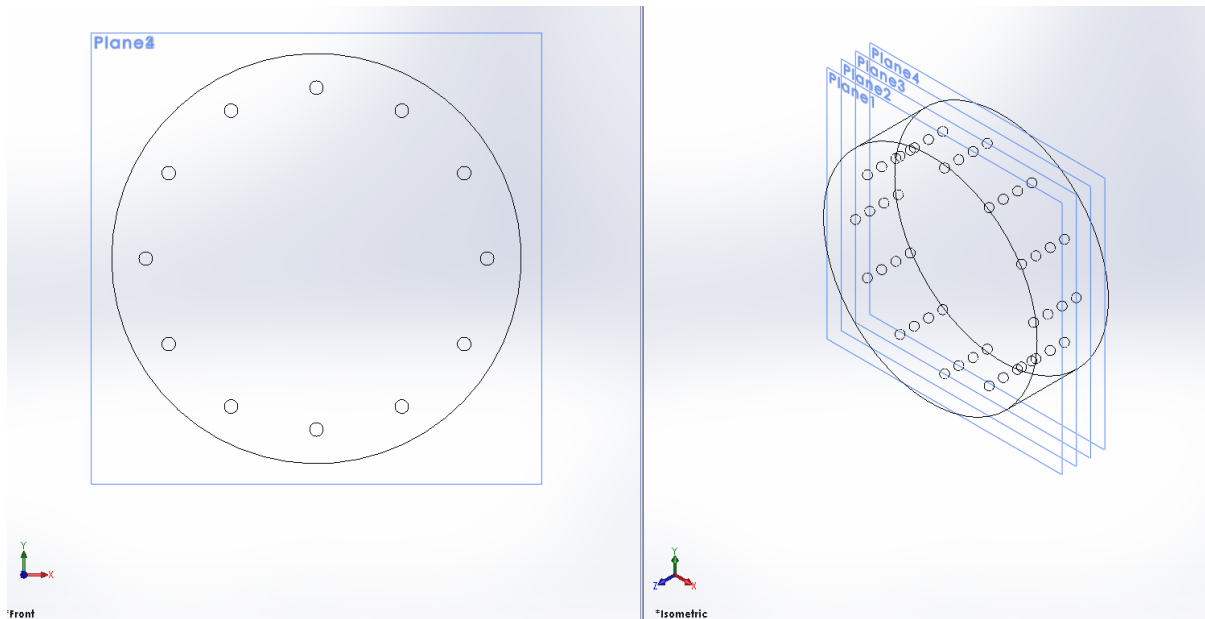


Figure 4-1 Schematic view of a hollow shell cylinder

4.2 Study of 3-dimensional designs

Cylindrical samples with a radius of 30mm and height of 20mm were created. As shown in Figure 4-2, the outer layer of the cylinder contains empty spheres, whilst the centre of the cylinders is solid with a radius of 20 mm. Previous studies (Chait, 1971); (Tuninetti, et al., 2012); (Fan, et al., 2017); (Auvray, et al., 2016); (Khan, et al., 2014); (Williams & Gamonpilas, 2008) have mentioned that the size of samples does not have any impact on the modulus for a compression test. Furthermore, these studies have defined an aspect ratio between the height of the sample and its diameter to be from 0.3-3. Several cases were defined based on the distance from the surface, distance from each other as well as the number and size of spheres. These parameters were defined to see the effect of them on the Young's modulus of an implant as well as stress in the bone and implant.

The first case involved considering different gaps vertically between the spheres. In one scenario, 4mm was the difference in distance between the spheres, whilst in the other it was

5mm. In addition, in this condition, one cylinder had one more layer of spheres than the other one.

The gap between the centre of the spheres and the surface of the wall was the second case to be modelled. Two scenarios were defined, one with a 2mm gap and the other with one of 5mm gap. Furthermore, the outer layer of the cylinders differed in both scenarios.

The number of spheres or different gaps between spheres horizontally was another case that was investigated. In one example, each layer consisted of 24 spheres, whilst for the other, there were 12. Finally, the last condition modelled was sphere size, with the radius of the spheres in the first case being 1mm and the other it was 2mm. Table 4-1 summarises the different cases according to the hollow sphere distributions and size that are studied in this chapter.

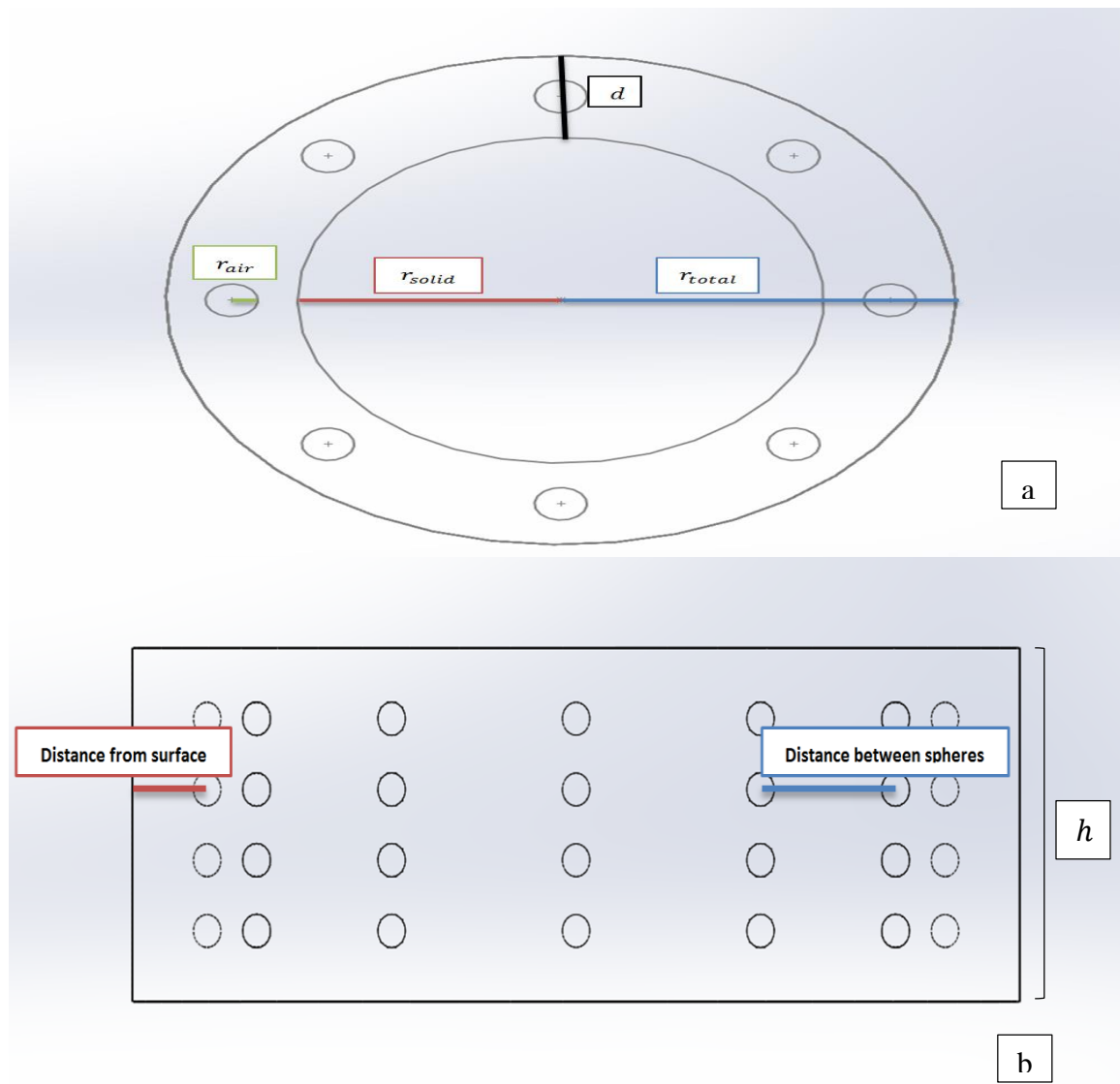


Figure 4-2 Hollow shell cylinder views a) defined parameters; b) examples of hollow shell cylinder dimensions

Table 4-1 Various designs used for this chapter based on distribution and sphere size

Different cases	Size of spheres (r_{air}) mm	No of Spheres (n)	Width of hollow spheres close to surface (d)	Distance from each other vertically	Distance from surface (mm)
Sample 1	1	4x24	10 mm	4 mm	3
Sample 2	1	3x24	10 mm	5 mm	3
Sample 3	1	3x24	10 mm	5 mm	2
Sample 4	1	3x24	10 mm	5 mm	5
Sample 5	1	3x24	10 mm	5 mm	3
Sample 6	1	3x12	10 mm	5 mm	3
Sample 7	1	3x24	10 mm	5 mm	5
Sample 8	2	3x24	10 mm	5 mm	5
Experimental sample	1	4x12	10 mm	4 mm	5

4.3 Method

4.3.1 Rule of mixtures

Various composite properties of composite materials can be predicted using a weighted mean technique known as the *rule of mixtures*. It is introduced to calculate Young's modulus and the strength of the composite materials. That is, the rule of mixtures is a calculation method to work out mechanical and physical properties of composites using the matrix and fibre mechanical and physical properties. These calculations are based on an even distribution of fibres within a uniformed matrix. In addition, the matrix is a solid, homogenous alloy with no additional material, as demonstrated in Figure 4-3. In the current chapter, the outer region is where the rule of mixtures is used, and this region is designed starting with radius = 20 mm to outer radius, 30 mm. Having established that meshing in the presence of small hollow spheres generates over 15,000,000 elements, conventional approach FEA proved to be impossible, and in fact mesh generation failed to operate. Due to this, the only way to conduct this research is to resort to the rule of mixtures.

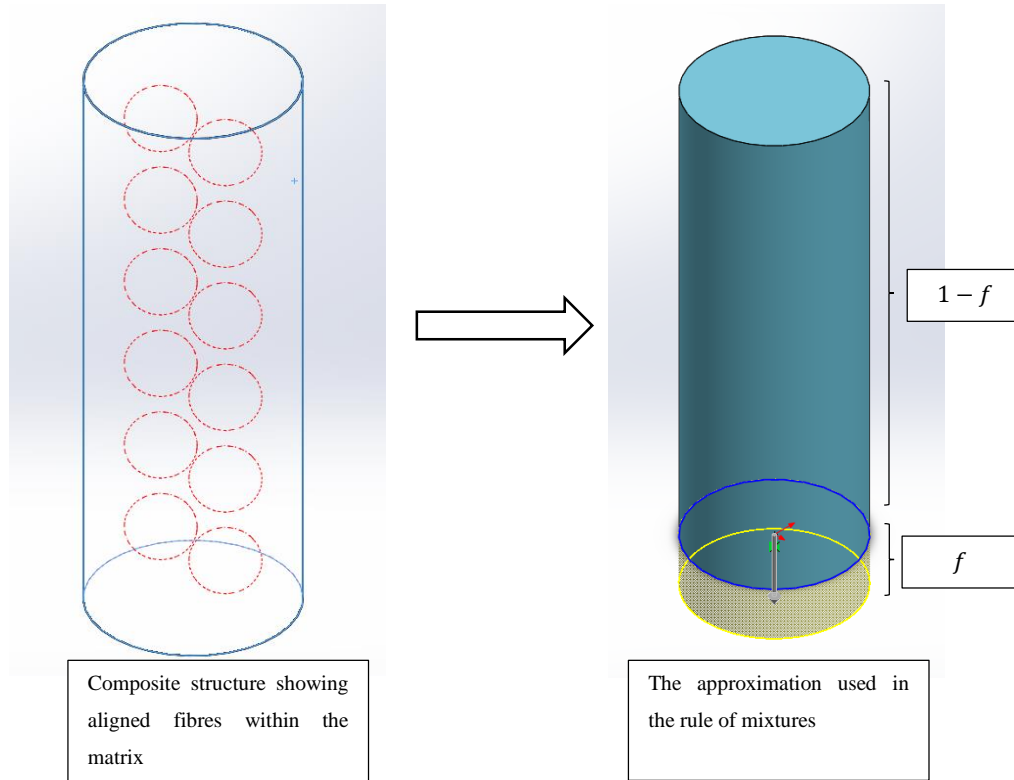


Figure 4-3 The matrix and fibres in the composite materials

Composite stiffness can be predicted using a micro-mechanics approach termed the rule of mixtures. The two main derivation from elastic modulus in rule of mixtures are the upper bound and the lower bound. For this study, upper bound was used and the derivation is demonstrated in detail.

Fibres are evenly distributed within the matrix that is free of voids. Completed bonding between fibres and matrix are achieved and applied loads are either parallel or normal to the fibre direction. Fibres and matrix behave as linearly elastic materials. For effective reinforcement, the particles should be small and uniformly distributed within the matrix.

4.3.1.1 Upper bound

Imagine a composite structure under uniaxial tension σ_{∞} . If the structure is to stay intact, the strain of the fibres, ε_f must be similar to the strain of the matrix, ε_m . Therefore, invoking hooke's law for uniaxial tension gives

$$\frac{\sigma_f}{E_f} = \varepsilon_f = \varepsilon_m = \frac{\sigma_m}{E_m} \quad (1)$$

Where σ_f and E_f are the stress and elastic modulus for the fibre and E_m and σ_m are for the matrix. Considering stress to be a force per unit area, a force balance gives that

$$\sigma_\infty = f\sigma_f + (1 - f)\sigma_m \quad (2)$$

If the assumption is that the composite structure behaves as a linear-elastic material, i.e, invoking hooke's law $\sigma_\infty = E_c\varepsilon_c$ for elastic modulus of the composite and strain of the composite, equation 1 and 2 could be combined to achieve

$$E_c\varepsilon_c = fE_f\varepsilon_f + (1 - f)E_m\varepsilon_m \quad (3)$$

Finally, due to all the strains being equal to each other, the overall elastic modulus of the composite could be demonstrated as

$$E_c = fE_f + (1 - f)E_m \quad (4)$$

4.3.1.2 Lower Bound

When the composite material is loaded perpendicular to the fibres, assuming that all the stresses $\sigma_\infty, \sigma_f, \sigma_m$ are equal. The total strain in the composite is distributed between the materials in a way that

$$\varepsilon_c = f\varepsilon_f + (1 - f)\varepsilon_m \quad (5)$$

The overall modulus in the material is then presented by

$$E_c = \frac{\sigma_\infty}{\varepsilon_c} = \frac{\sigma_f}{f\varepsilon_f + (1 - f)\varepsilon_m} = \left(\frac{f}{E_f} + \frac{1 - f}{E_m}\right)^{-1} \quad (6)$$

Since $\sigma_f = E\varepsilon_f, \sigma_m = E\varepsilon_f$.

The rule of mixtures is used for composite materials to calculate Young's modulus, according to equation 7 (Cambridge, 2015). In this study upper bound was used for the proposed structure.

$$E_c = fE_f + (1 - f)E_m \quad (7)$$

Where:

$f = \frac{V_f}{V_f + V_m}$ is the volume fraction of the fibres

E_f is the material property of the fibres

E_m is the material property of the matrix

4.3.2 FEA Simulation

There are many ways to create a part in ABAQUS/CAE. It could be imported from design software, it could be imported as a meshed part from an ABAQUS input file or as an output database. It can also be created, using the tools available in the parts module. This section shows the development of 3D models to enhance hip implant design. Eight different cylinders were created with various internal composite structures and the parameters used to design the samples are explained.

Abaqus is powerful finite element analysis (FEA) software extensively used for linear/nonlinear structures, CFD models, electromagnetic models and standard/explicit model simulations. It is also widely used for various applications, such as the industrial, biomedical, automotive and aerospace domains. FEA allows for the development of new ideas with new structures or analysing existing components. It converts complex geometries into subdivisions and mathematical equations are used to solve problems. Meshing involves creating elements that are subdivided in geometrical sections for simulation and the sum of these elements forms an entire geometry that needs to be analysed. The size and types of these elements are usually selected by the user depending on accuracy of the solution. Coarse meshing converts the components into larger elements, whilst fine meshing transforms them into smaller ones.

A group of nodes creates an element, and the sum of the elements builds a complex geometry. The interactions between nodes create a nodal solution and the interactions between the elements generate an elemental solution, because of the implemented boundary conditions. FEA is an important technique, not least because time and cost can be saved when compared to laboratory set-ups. Moreover, FEA produces flexible and precise results as well.

The parts were imported from SolidWorks after being meshed in 3-matic for this study.

4.3.2.1 Cylinder Modelling

Prior to adding spheres to the actual implant, spheres were added to several cylinders with a radius of 30 millimetres and height 20 millimetres. Various scenarios were defined for these cylinders to investigate the impact of this structure. Different distances from each other, different distance from surface and sphere sizes were examined and allocated to the cylinders.

These models were created in SolidWorks 2014 and they were meshed using 3-matic 10. They were exported from 3-matic into Abaqus using inp format to analyse using finite element. In addition, these cylinders were assembled with an empty cylinder as bone in SolidWorks. Surface meshing was applied in 3-matic as it was compatible with Abaqus and it could be transferred into volumetric mesh in Abaqus. These conversions appeared to provide higher accuracy especially with more complex geometries.

First, a cylinder with hollow spheres was created to see if the concept of stress distribution would work. This achievement led to creating more samples with different conditions as a composite in the same volume. The cylinder dimensions, the height and radius were chosen randomly to see how the concept reacts under the same volume with various composite structures on a smaller scale. The parameters that were changeable in the samples were not observable from outside, these being: spheres radius, sphere distances from each other vertically and horizontally as well as their gap from the wall surface. These factors were changed to find out the optimum sphere positions in a cylindrical environment.

Running simulation for these samples required material properties that needed to be assigned in Abaqus. It contains different modules to assign the material properties to the objects, which include: the part module, the property module, the assembly module, the step module, the interaction module, the load module, the mesh module, the optimisation module, the job module and the sketch module. Each module is designed for a specific area of the objects to be looked at and assigned their right properties.

In the property module, the material property for each part is defined, including: density, Young's modulus, ultimate tensile strength and Poisson's ratio, which are inserted for each part.

4.3.2.2 Cylinder material

Three different material properties have been used for running the simulations. The mechanical properties used in simulations for two cylinders and bone are listed in Table 4-2.

Table 4-2 Mechanical properties of common biomaterials (Sabatini & Goswami, 2008)

Material	Elastic modulus (GPa)	Ultimate tensile strength (Mpa)	Poisson's ratio	Density (g/cm³)
Ti6Al4V	114	900	0.32	4.4
316L SS	200	1000	0.3	7.9
Cortical bone	20	130	0.3	2.0

4.3.2.3 Cylinders boundary conditions

Assignment of material properties in FEA is an important step, which defines the characteristics of the solid components to be analysed. These cylinders were assembled into an empty cylinder acting as a foam material and the material property of the bone was assigned to this material. Pressure was exerted on the top surface of the cylinders with a magnitude of 5 MPa. Then, the sample was pinned at the bottom of the bone type material.

4.3.2.4 Force and pin area

Figure 4-4 shows where the stress was exerted and where the model was pinned. The figure also demonstrates the pinned area, which is at the bottom of the empty cylinder.

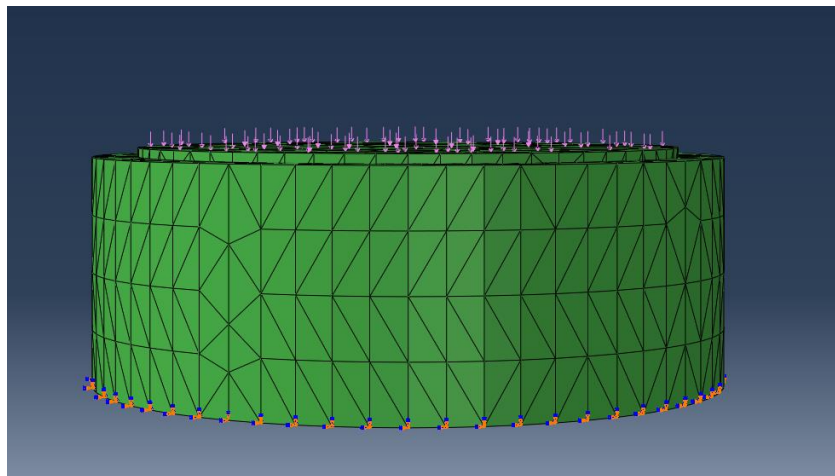


Figure 4-4 Force and pin area

4.3.2.5 Cylinder mesh accuracy

These models were imported into Abaqus from 3-matic, where they had been surface meshed and then, they were into volumetric mesh. These simulations were performed as explicit dynamic analysis. As the mesh density increases, the time to solve the problem increases and fine mesh yields very accurate results. Furthermore, small element size will also increase the complexity of the FE models. The right element size must be selected base on how complex the component is and choosing the appropriate one will result in obtaining accurate outcomes and saving as much computing time as possible.

There have been numerous studies on finite element analysis performance with different element size and types. One study concluded that as the curve and surface boundary of a higher-order element can precisely approximate the boundary, the calculation accuracy accomplished by a hexahedral element is higher than a tetrahedral. Furthermore, by increasing the number of nodes, the calculation accuracy of model analysis also increases (Liu, et al., 2011). In another approach, the performance of linear and quadratic tetrahedral elements and hexahedral ones in different structural problems was analysed. It was concluded that the accuracy of the results were the same for both types of elements (Raut, 2012).

4.3.3 Experiment to validate the FEA results

Two cylinders were printed using ABS plastic in the University's 3D printing lab. One cylinder contained hollow spheres close to the surface and the other one was solid. ABS stands for Acylonitrile Butadiene Styrene, which is an oil-based plastic; it is a strong material that is widely used in various industries, for it has good structural integrity. The experiment was carried out to compare and contrast stress-strain graphs of hollow shell structures with solid ones. Furthermore, these tests were carried out to justify the structure.

These two samples were tested using Instron machine for compression tests, as shown in Figure 4-5. A strain gauge was attached to each cylinder to calculate the strain and the stress inserted into the surrounding areas.



Figure 4-5 Compression machine used to carry out stress-strain tests

As explained in subsection 2.6.3, Fused deposition modelling (FDM) was used to model both, solid and hollow shell cylinders. Figure 4-6 shows the ABS samples after being printed using the Fused deposition modelling (FDM) technique.



Figure 4-6 ABS models of solid and hollow shell cylinders

4.4 Results

4.4.1 Results of the rule of mixtures

In this study, the rule of mixtures was used as the structure was assumed to be composite. The metals are the matrix and the hollow spheres are assumed to be fibre. The rule of mixtures was used to calculate the Young's modulus and strength of the structures.

$$E_{steel} = 200 \text{ Gpa}, \sigma_{steel} = 1000 \text{ MPa}$$

where, E_{steel} is the Young's modulus of steel and σ_{steel} is its strength.

$$E_{air} = 0.14 \text{ MPa} \approx \text{Zero}, \sigma_{air} \approx 0 \text{ MPa}$$

where, E_{air} is the Young's modulus of the spheres and σ_{air} is their strength.

where, r_{air} is the radius of a sphere:

$$r_{total} = 30 \text{ mm}, h = 20 \text{ mm}$$

Figure 4-2 shows all of the above parameters schematically.

$$V_{air} = \frac{4}{3} \pi \cdot r_{air}^3 \cdot n \quad (8)$$

Where, V_{air} is the volume of the spheres and n is their number.

$$V_{total} = Area_{shell} \cdot h \quad (9)$$

$$f = \frac{V_{air}}{V_{total}} \quad (10)$$

Where, f is the function:

$$E_c = f \cdot E_{air} + (1 - f) \cdot E_{steel} \quad (11)$$

$$\sigma_c = f \cdot \sigma_{air} + (1 - f) \cdot \sigma_{steel} \quad (12)$$

The equations for Young's modulus and strength were applied according to the rule of mixtures, which is shown in equation 11 and 12.

Table 4-1 demonstrates the different conditions under which the cylinders were calculated with the rule of mixtures. Table 4-3 shows the calculated outcomes for Young's modulus and strength for all the specimens. The results of the calculations show that if the total sphere volume increases then the Young's modulus and strength are reduced. Hence, there is an optimum volume of voids that can reduce stress shielding in the bone regardless of weakening of the strength.

In the first scenario, the vertical distance between each sphere was considered; in one case 4mm and the other one 5mm, with the former providing the better results.

Another scenario was to consider the distance from the centre of each sphere to the wall surface of the cylinder for one case when the space was 2mm and the other when it was 5mm. That further away from the wall surface proved to have superior performance.

A further condition that was considered was the number of spheres within the cylinder; in one case this was 36, whilst in the comparator it was 72. Whilst there was not much difference in the results of these two conditions, the structure with 36 spheres did perform slightly better.

Sphere size is the last scenario to be looked at in this section, with one cylinder consisting of spheres with 1mm radius and one with 2mm ones. The cylinder which contained the smaller spheres was a better performer when compared that with larger spheres.

Table 4-3 Calculation results according to the rule of mixtures

Different cases	E_c (GPa)	σ_c (MPa)
Sample 1	197.44	987.2
Sample 2	198.08	990.4
Sample 3	196.51	982.54
Sample 4	198.8	990.4
Sample 5	198.33	991.66
Sample 6	198.51	992.59
Sample 7	198.8	990.4
Sample 8	184.64	923.2
Experimental sample	198.72	993.6

4.4.2 Finite element analysis

To find out that how the stress transfers from an implant to bone, FEA was run and in this section, the results of this simulation are presented.

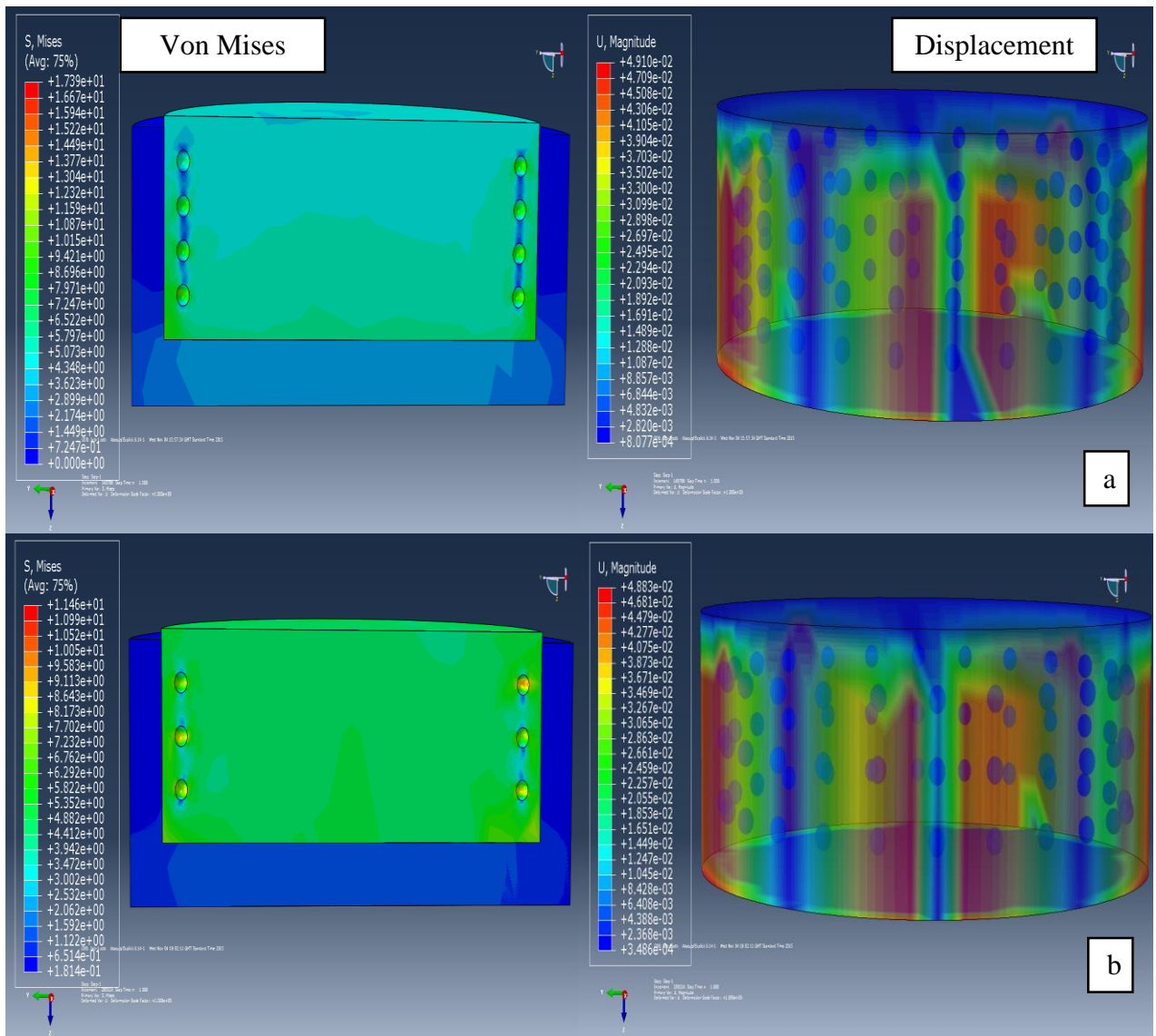


Figure 4-7 Von Mises stress and displacement for different distance from each other vertically: a) 4mm; b) 5mm

Figure 4-7 a shows Von Mises stress distribution and displacement when spheres are at a distance from each other of 4mm vertically, whereas Figure 4-7 b shows this distance as being 5mm. The stress transferred into the bone through sphered samples is greater in the 4mm hollow sphered shell cylinder than in the 5 mm one. The load-transferred onto the bone for the sample containing closer spheres is between 1.45-2.34 MPa, whereas in the other case it is 1.1 MPa. The displacement in Figure 4-7 a is also slightly higher than in Figure 4-17 b. As the displacement increases, the load-transfer onto the bone will also increase. Figure 4-7 a performs slightly better due to its closer distanced spheres and an extra layer of them. The maximum displacement occurring in Figure 4-7 a is 0.049 mm, whilst it is 0.048 mm in Figure 4-7 b.

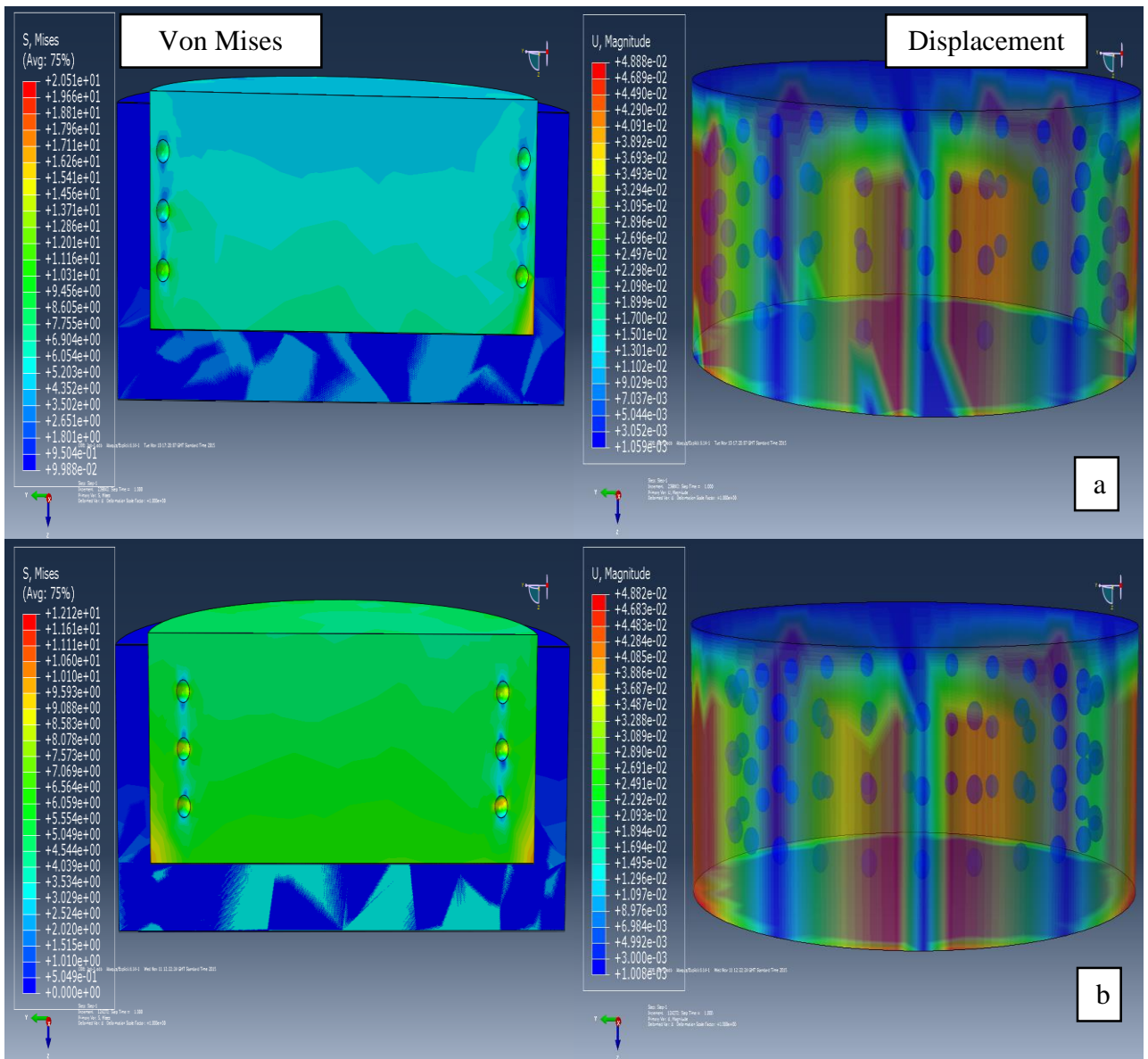


Figure 4-8 Von Mises stress and displacement for different distance from the side-surface: a) 2mm; b) 5mm

Figure 4-8 shows the differences between the two scenarios where the spheres were placed at different distance from the side-surface, with Figure 4-8 illustrating when this was 2mm, whilst Figure 4-8 b demonstrates when it was 5mm. The stress transferred to the bone is higher in Figure 4-8 a in comparison to Figure 4-8 b. As shown in Figure 4-8 a, the Von Mises stress level transferred onto the bone is approximately between 1-2.65 MPa, whereas in Figure 4-8 b, it is between 1-2 MPa. Furthermore, Figure 4-8 a shows that larger stress is being carried by the bone, the displacement of which is also slightly larger in this figure when compared to Figure 4-8 b. Figure 4-8 a portrays a maximum displacement as 0.04888 mm, whilst that of Figure 4-8 b is 0.04882 mm. The larger the displacement, the more load will be transferred onto the bone.

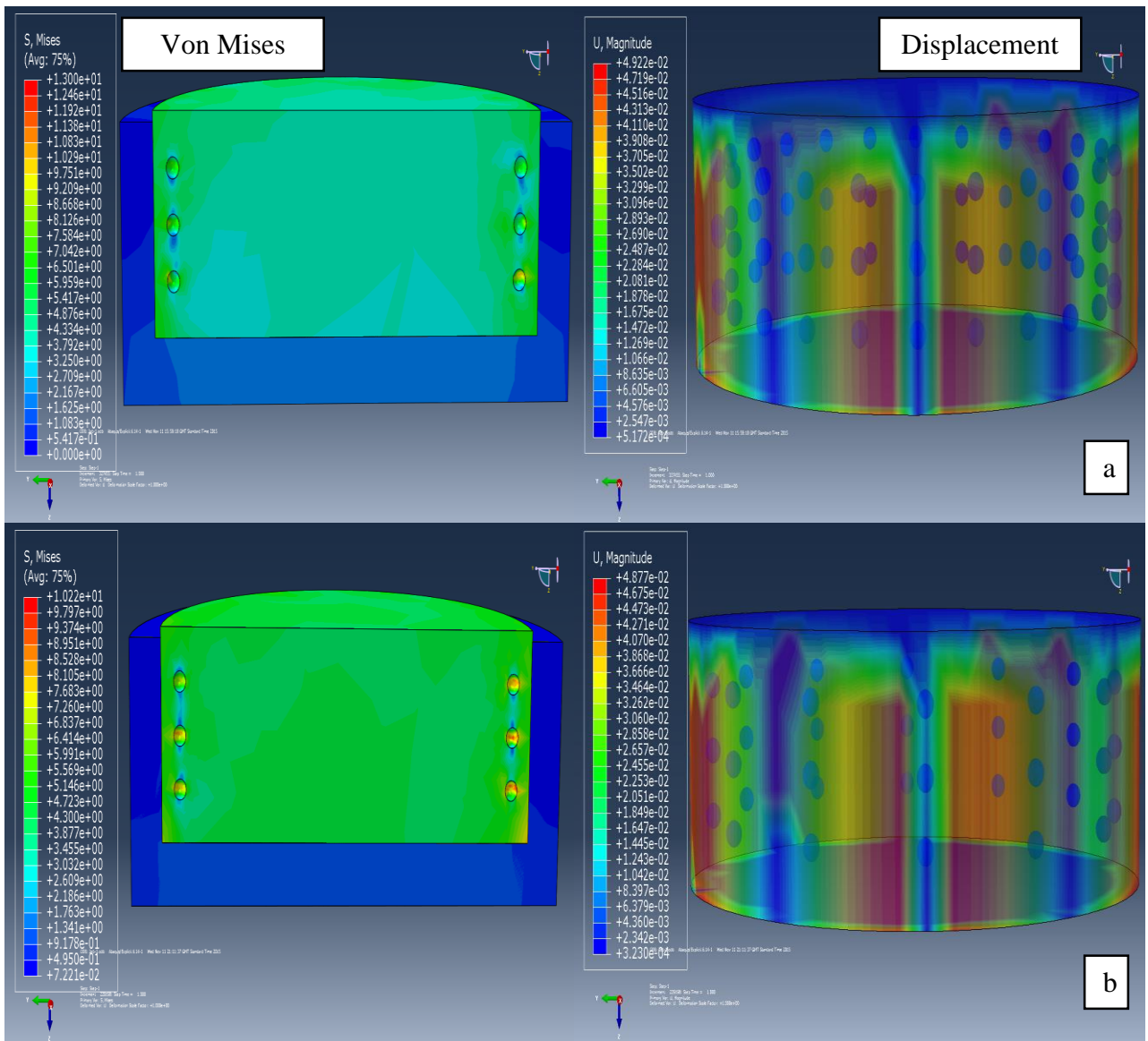


Figure 4-9 Von Mises stress and displacement for different numbers of spheres in each row (different distance horizontally): a) 24 spheres; b) 12 spheres

Figure 4-9 demonstrates different numbers of spheres placed in each row or a difference in their horizontal distance. Figure 4-9 a shows the case with 24 spheres in each row and Figure 4-9 b shows 12. The stress-transfer appears to be slightly higher in the cylinder with more spheres. Furthermore, Figure 4-9 a shows a clear distribution of stress to the sides, with a range of between 1.08-2.1 MPa but Figure 4-9 b demonstrates slightly smaller stress being transferred, i.e. 0.9-1.3 MPa. These differences could be due to the number of spheres and their distance from each other. Figure 4-9 a also portrays a larger displacement compared to Figure 4-9 b. In addition, the maximum displacement for the sample with more spheres is 0.0492 mm and for the one with fewer spheres, this is 0.0487 mm.

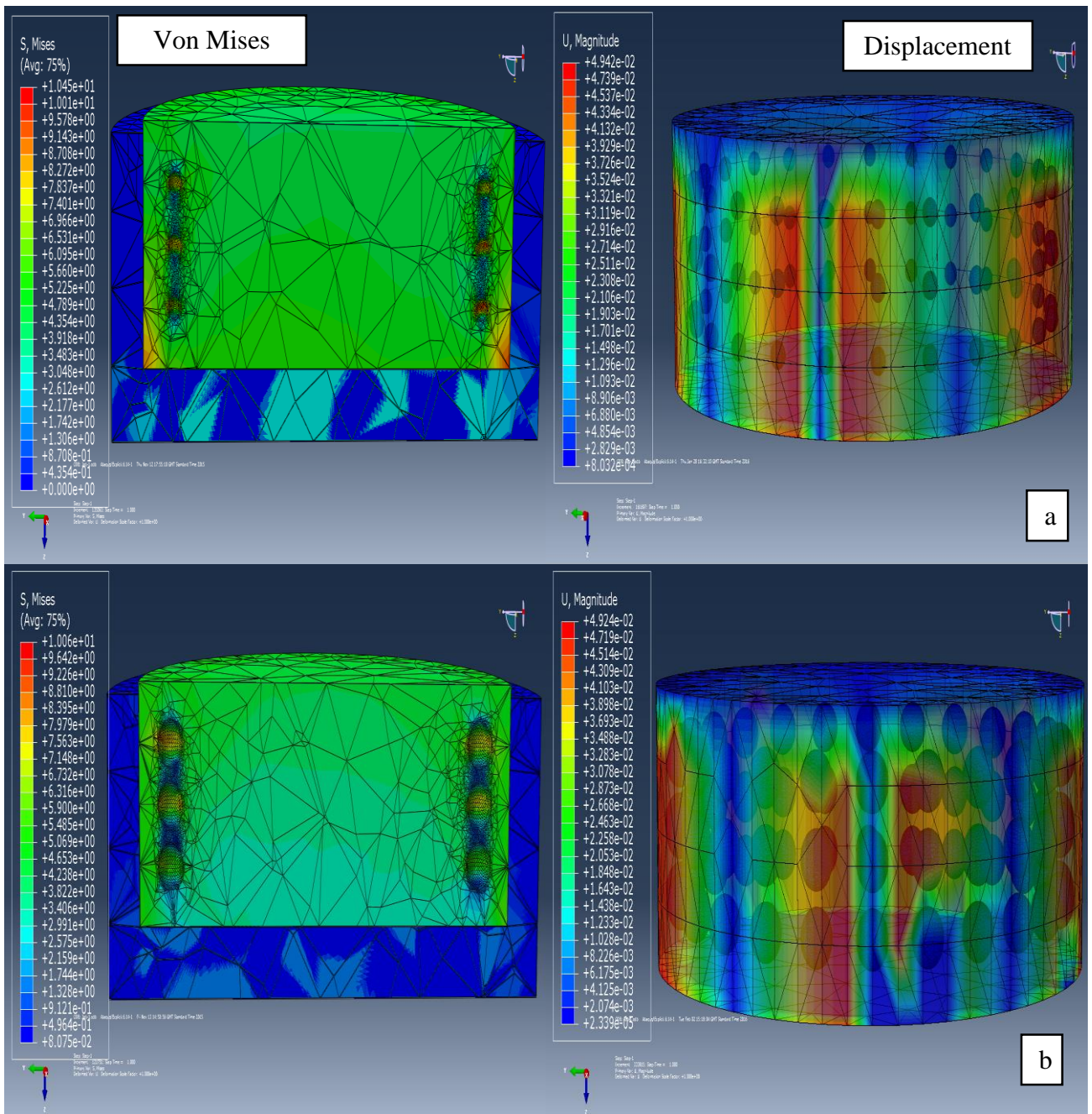


Figure 4-10 Von Mises stress and displacement for different sphere radius sizes: a) 1mm; b) 2mm

Figure 4-10 shows Von Mises stress distribution and displacement for different sphere sizes. Figure 4-10 a portrays the specimen containing spheres with 1mm radius, Figure 4-10 b shows the case containing spheres modelled with 2mm radius. The stress-transferred into the bone is slightly greater in the sample containing spheres with 1 mm radius that containing spheres with 2 mm radius. In addition, it can be observed from Figure 4-10 that the load-transfer is almost similar in both cases, with approximately just 0.39 MPa difference in their maximum Von Mises stress. The displacement is also very similar for the two cases, Figure 4-10 a showing a marginally larger displacement of 0.018 mm.

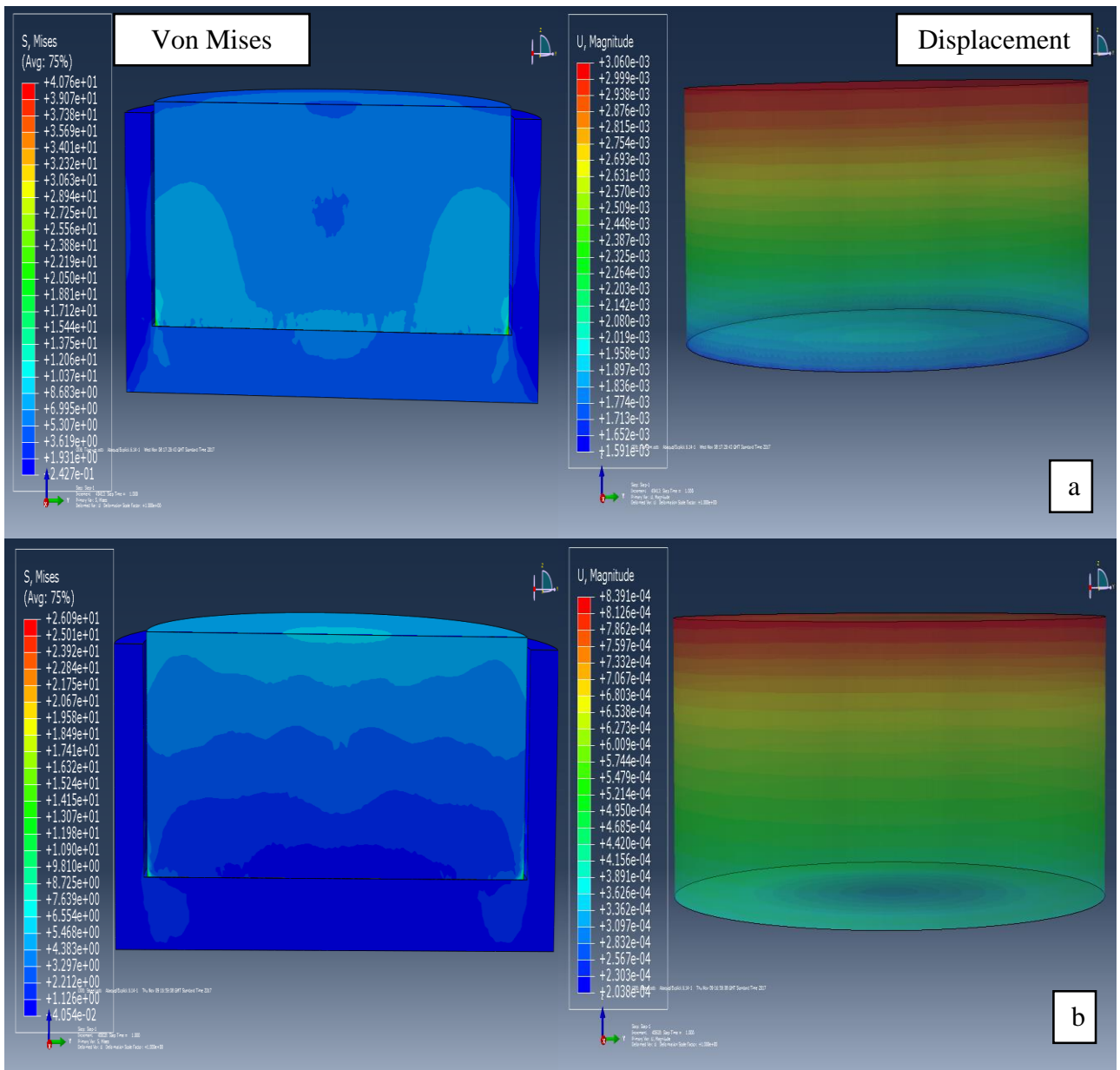


Figure 4-11 Von Mises stress and displacement of solids: a) titanium; and b) stainless steel

Figure 4-11 shows one similar case with different material properties. Figure 4-11 a shows titanium's behaviour, whilst Figure 4-11 b illustrates that of stainless steel and the stress passed on to the bone is higher in titanium cylinder. Moreover, the stress in the cylinder itself is lower in the titanium one. It can be observed that the Von Mises stress transferred onto the bone in Figure 4-11a is between 4 and 5.3 MPa, whereas in Figure 4-11b, it is between 1-2.2 MPa. The maximum displacement occurring in the titanium sample is 0.00306 mm, which is larger than that for stainless steel, at 0.000839 mm.

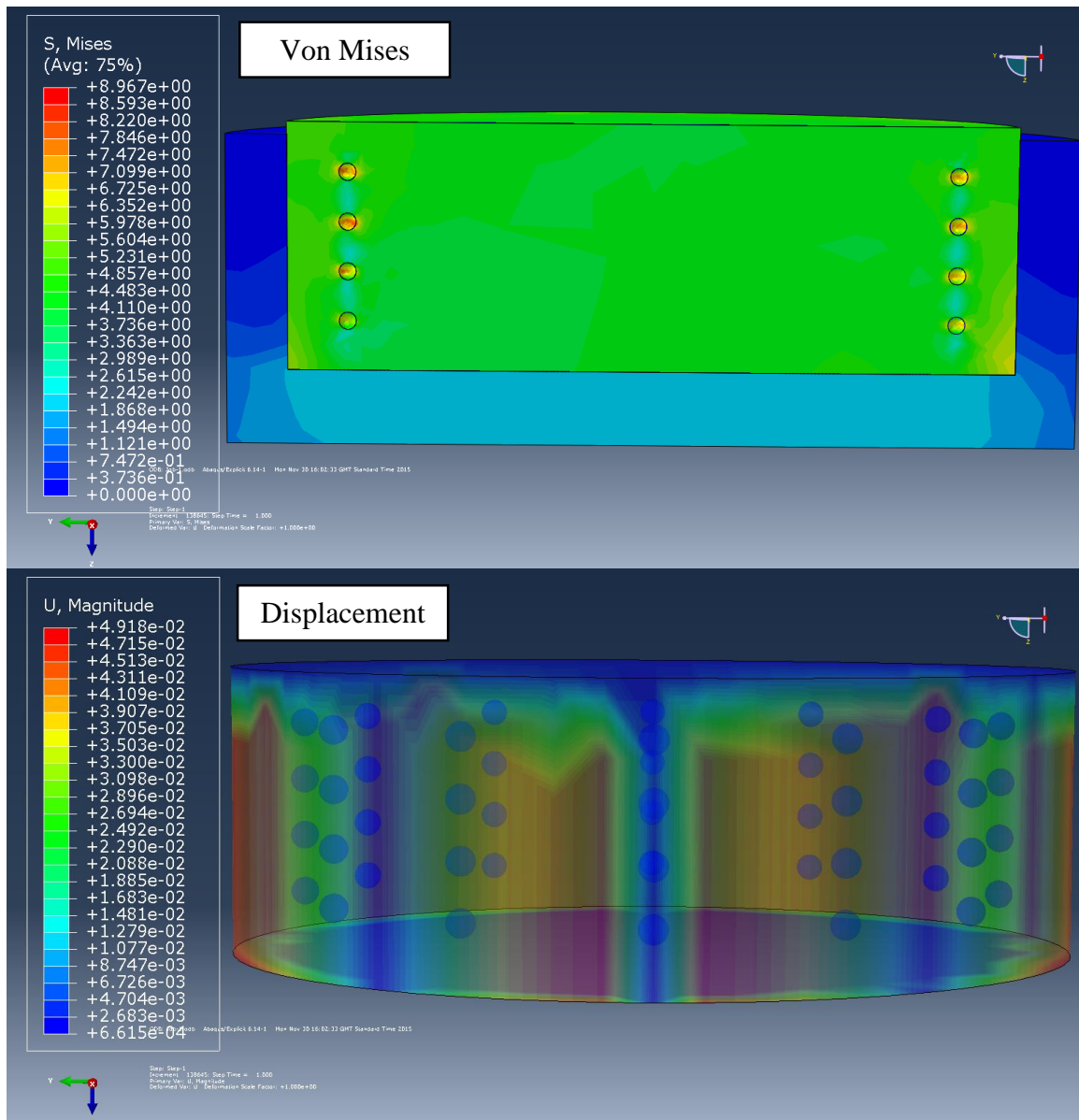


Figure 4-12 Von Mises stress and displacement for the experiment case

Figure 4-12 shows the Von Mises stress and displacement for the experiment case, which is the experimental sample, printed containing hollow spheres. The displacement for the experiment case is larger than that for solid stainless steel. That is, the maximum displacement occurring in the latter case is 0.000839 mm, whilst in the experimental case containing hollow spheres this is 0.05 mm. The load-transfer onto the bone is also larger in sphered sample Figure 4-12 when compared to the solid stainless steel structure. The stress in the bone in experimental sample is between 2 and 3 MPa, whereas it is between 1 and 2.2 MPa in the solid stainless steel sample.

Table 4-4 summarises the results of FEA based on Von Mises stress distribution in the bone and cylinders. It is shown that the Von Mises stress reduces in comparison to the solid one;

however, it is still higher than for titanium. In addition, the results indicate that the stress at the bone-implant interface increases more compared with solid stainless steel, but this is still lower than for titanium. Furthermore, it can be observed that having hollow spheres within a structure close to its surface would appear to reduce its Young's modulus and stress shielding through an increase in load-transfer.

Table 4-4 Von Mises stress results for the different study cases

Different cases	Cylinder conditions	Bone (MPa)	Bone near cylinder (MPa)	Cylinder (MPa)
Sample 1	4mm	1.45-2.34	2.8-3.9	10-15
Sample 2	5mm	1.1	1.59	6-11
Sample 3	2mm	1-2.65	2.65-3.5	10-15
Sample 4	5mm	1-2	2-4	7-12
Sample 5	3x24	1	1.7	7-13
Sample 6	3x12	1	1.7	4-10
Sample 7	1mm	0.8-2	2-4	6-10
Sample 8	2mm	1.1-1.7	1.7-2.5	3-10
Sample 9	Titanium	2-4	4-5.3	3.6-7
Sample 10	S Steel	0.05-1	1.1-2.2	4.3-10
Experimental sample		2-3	2.24	6-9

One case, which was a combination of other cases, was modelled as the experiment specimen. It was printed using 3D plastic lab to indicate whether the experimental results confirm that the hollow structure has a greater impact on Young's modulus compared to the completely solid model.

4.4.3 Compression Results

Figure 4-13 demonstrates the stress-strain graph obtained from the experimental results. These cylinders were sintered and printed using ABS material. A solid and a hollow shell cylinder were printed to go through a compression test and Figure 4-13 indicates that the gradient of stress over strain is higher for the solid structure than for the hollow shell structure.

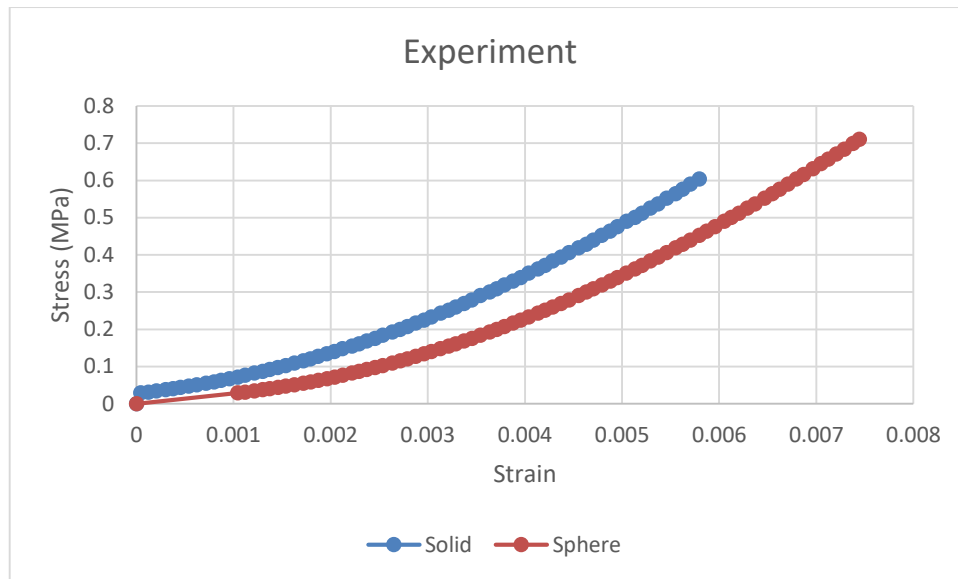


Figure 4-13 Stress-strain graph of solid and hollow spheres close to the surface of the structure

4.5 Minimising stress shielding by changing the volumetric ratio

To conclude, this chapter has shown that having hollow spheres close to the surface reduces Young's modulus and the stiffness. Moreover, there is an optimal amount of hollow spheres to be created for a Young's modulus reduction, for exceeding that amount will result in weakening the structure. Furthermore, having hollow spheres in the outer layer of the cylinder (close to the surface) will also increase the load-transfer to the surrounding bone. However, the centre of the cylinder remains solid and stiff. As a result, the hollow spheres are distributed everywhere within the volume uniformly in the next chapter, as this could result in a lower Young's modulus throughout the structure. In addition, having uniformly distributed hollow spheres within a closed volume with no solid centre could increase load-transfer onto the bone.

So, there is no exact number to put forward as number of spheres, distance from the wall, distance from each other and sphere size. However, there is a relationship between all of these parameters. f could be calculated as a function of a composite Young's modulus by using equation 11, which is named as f_1 , as demonstrated in equation 13. In addition, f could also be calculated as a function of composite strength by using equation 12, which is named as f_2 , as shown in equation 14. If the Young's modulus of stainless steel (200 GPa) is reduced to that of titanium (114 GPa), then the outcome of equation 13, i.e. f_1 , must be 0.4. However, the strength of the material also decreases rapidly and thus, equation 14 is useful to determine how much strength reduction is appropriate for composites. 900 MPa was chosen

as the ultimate tensile strength for composites due to titanium's strength. A study in 2016 mentioned that, the stress applied to hips when climbing down is 312 MPa (Colic, et al., 2016). In another approach in 2007, when a part is under cyclic load, such as the hip, a safety factor is suggested, which is between 2.5 and 2.9 (Sivasankar, 2007). If the safety factor is multiplied by the cyclic load, the outcome will approximately be 900 MPa and hence, σ_c was considered to be this value for this study.

$$f_1 = \frac{E_c - E_{steel}}{E_{air} - E_{steel}} \quad (13)$$

$$f_2 = \left(\frac{\sigma_c - \sigma_{steel}}{\sigma_{air} - \sigma_{steel}} \right) \quad (14)$$

where, σ_c is assumed to be 900 MPa

$$\sigma_c = 900 \text{ MPa}, \sigma_{steel} = 1000 \text{ MPa}, \sigma_{air} \approx 0 \text{ MPa}$$

$$f_2 = \left(\frac{900 - 1000}{-1000} \right) = 0.1 \quad (15)$$

According to equations 10 and 15, the relationship between the volume of a sphere and that of a composite are as follows:

If f is replaced with f_2 , which is 0.1 in equation 16, then:

$$\frac{V_{air}}{V_{toall}} = 0.1 \quad (16)$$

Equation 16 shows the ratio between the extracted volume and total volume, which is 10% of the latter. In order to have a general view of the effective parameters, such as r_{air} , d , h and etc., the relationships between them were defined, which came of use when designing the samples.

A relationship that can be obtained from equation 16, is that between the radius of a sphere and their number. It is shown in equations 17 and 18 how this relationship is calculated.

$$\frac{\frac{4}{3}(3.14)(r_{air}^3) \cdot n}{3.14(20)(30^2 - 20^2)} = 0.1 \quad (17)$$

$$n = \frac{3000}{4r_{air}^3} \quad (18)$$

$$n(r_{air}) = 750r_{air}^{-3} \quad (19)$$

At the beginning of this chapter, hollow spheres were added to see if the stress shielding can be reduced. There was no theoretical logic to run simulation at the start of this chapter, neither was mesh creation of so many samples as it was time consuming. Later in this chapter, the only way to conduct this research and overcome the mentioned issues, was to use rule of mixtures. Moreover, rule of mixtures was also used to determine volume fraction of the samples. In this part, relationships between geometrical parameters of the samples were created to have a better understanding for future designs. Equation 19 was used to define the relationship between the radius of spheres and their number. Figure 4-14 is the curve drawn based on equation 19, and also helped to visualise equation 19. It also shows how the relationship between these two parameters work instead of setting $r_{air} = 1, 2, 3, \dots$ and calculating n .

According to Figure 4-14, which shows the relationship between the number of spheres and their radius, if the radius decreases to less than 1 mm, then, the number of them should be increased significantly. However, if the radius of the spheres increases to 2mm or more, the number of them stays steady and hence, any size between 1 and 2 mm will be more effective.

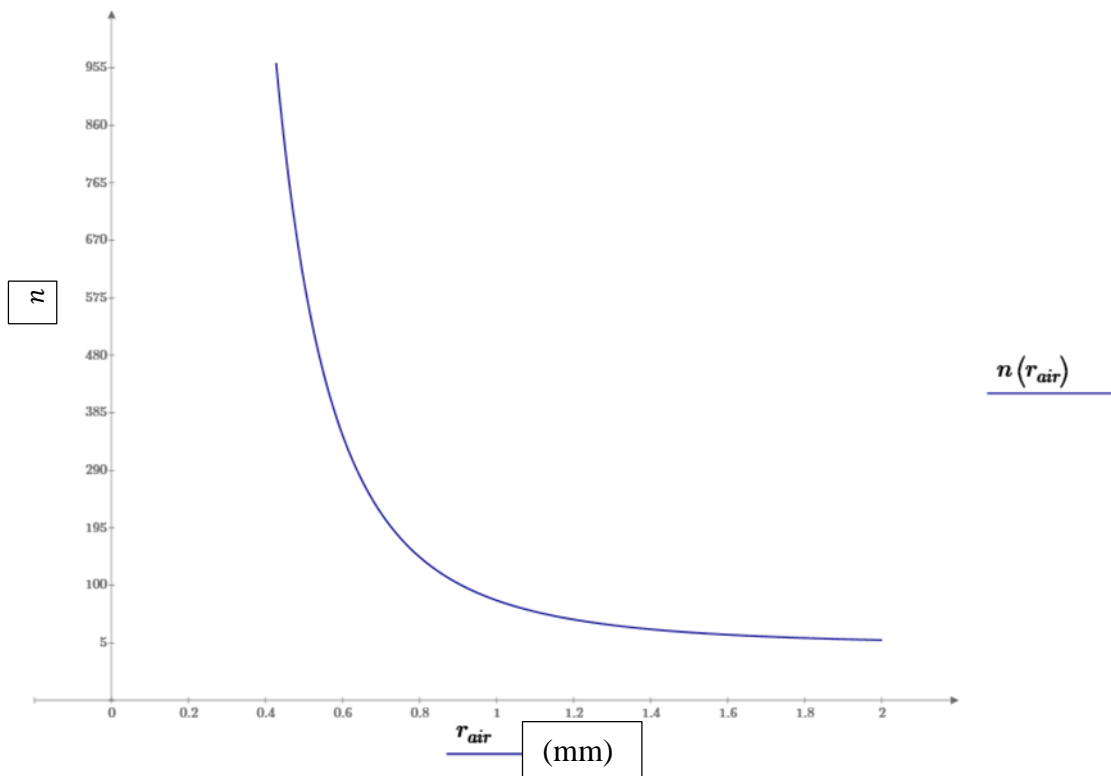


Figure 4-14 The relationship between the radius of the spheres in (mm) and their number

Another relationship that can be obtained from equation 16, is that between hollow shell thickness and the height of the cylinder. Based on equation 19, if the radius of the spheres is 1mm, the number of them will be 750. Equations 20 and 21 show how the relationship between hollow shell thickness (d) and the height of the cylinder (h) is calculated.

$$\frac{\frac{4}{3}(3.14)(1^3)(750)}{(3.14)(h)(r_{all} + r_{solid})(r_{all} - r_{solid})} = 0.1 \quad (20)$$

$$\frac{1000}{(h)(60 - d)(d)} = 0.1 \quad (21)$$

As it was mentioned earlier in this part, relationships between geometrical parameters of the samples were created to have a better understanding for future designs. Equation 21 was used to define the relationship between the hollow shell thickness and the height of the cylinder. Figure 4-15 is the curve drawn based on equation 21, and also helped to visualise equation 21. It also shows how the relationship between these two parameters work instead of setting $d = 1, 2, 3, \dots$ and calculating h .

Figure 4-15 demonstrates the relationship between hollow shell thickness and the height of the cylinders. The results prove that as the hollow shell decreases, the height of the cylinders increases, until this increase and thickness become steady. It can also be observed that when the thickness reaches 3 mm, the height stays almost steady with a minor gradient. The curve provides a general idea about the relationship between d and h , if r_{air} is 1 mm, which could well be also of use when designing the structure.

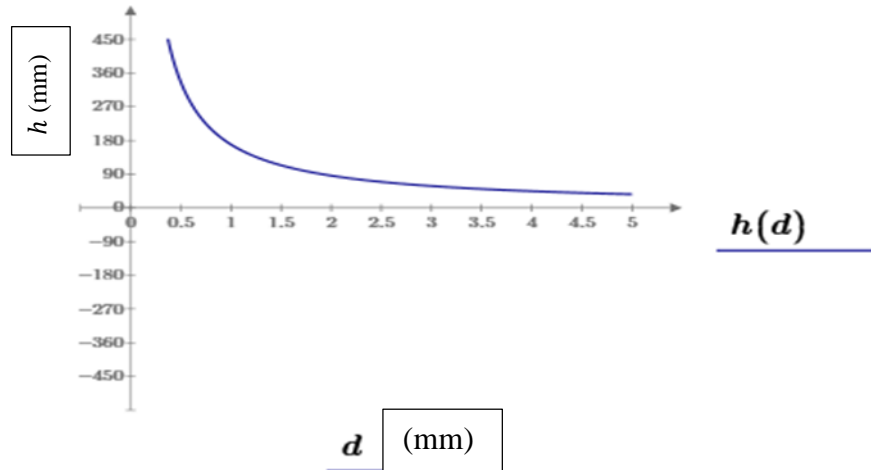


Figure 4-15 The relationship between hollow shell thickness (mm) and the height of the cylinder (mm)

Furthermore, another relationship can be concluded is between the number of spheres and the radius of cylinder, from equation 16. The radius of a sphere is 1 mm and the height of the cylinder is considered to be 20 mm in this relationship. Equations 22 and 23 show how the relationship between the number of spheres and the radius of cylinder is calculated.

$$\frac{\frac{4}{3}(3.14)(1^3) \cdot n}{(3.14)(20)(r^2)} = 0.1 \quad (22)$$

$$n(r) = 1.5r^2 \quad (23)$$

As it was mentioned earlier in this part, relationships between geometrical parameters of the samples were created to have a better understanding for future designs. Equation 23 was used to define the relationship between the number of spheres and radius of the cylinder. Figure 4-16 is the curve drawn based on equation 23, and also helped to visualise equation 23. It also shows how the relationship between these two parameters work instead of setting $r = 1, 2, 3, \dots$ and calculating n .

Figure 4-16 demonstrates the association between the number of spheres and the radius of the cylinder, which reveals that as the radius increases, the number of spheres goes up as well. As the radius increases, the size of sample also gets larger, which makes the volume larger. The larger the total volume, the more that needs to be extracted.

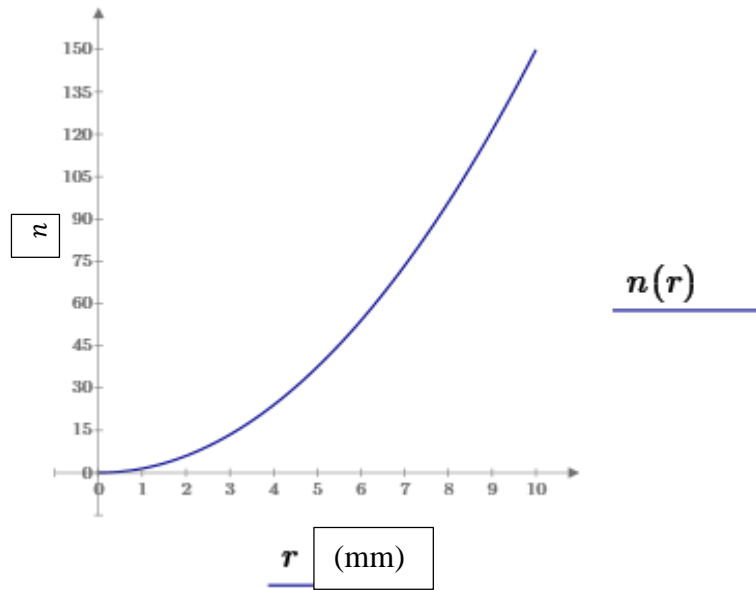


Figure 4-16 Relationship between the number of spheres and radius of the cylinder (mm)

From equation 16, another relationship can be found between the hollow shell thickness and the radius of the cylinder. Based on equation 19, if the radius of the spheres is 1mm, then their number will be 750. Equations 24-27 provide the calculations for this relationship.

$$\frac{\frac{4}{3}(3.14)(1^3)(750)}{3.14(20)(r_{all} + r_{solid})(r_{all} - r_{solid})} = 0.1 \quad (24)$$

$$\frac{\frac{3}{4}(3.14)(750)}{(3.14)(20)(2r_{all} - d)(d)} = 0.1 \quad (25)$$

$$(2r_{all} - d)(d) = 500 \quad (26)$$

$$r(d) = \frac{500}{2d} + \frac{d}{2} \quad (27)$$

As it was mentioned earlier in this part, relationships between geometrical parameters of the samples were created to have a better understanding for future designs. Equation 27 was used to define the relationship between the radius of the shell and radius of the cylinder. Figure 4-17 is the curve drawn based on equation 27, and also helped to visualise equation 27. It also shows how the relationship between these two parameters work instead of setting $d = 1, 2, 3, \dots$ and calculating r .

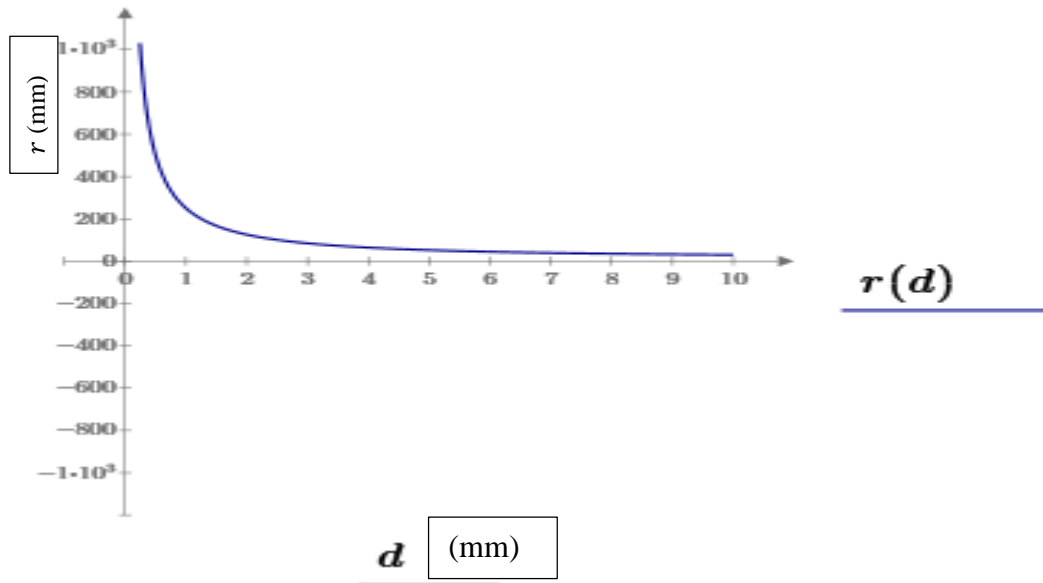


Figure 4-17 Relationship between hollow shell thickness (mm) and radius of the cylinder (mm)

Figure 4-17 shows the relationship between the hollow shell thickness and the radius of the cylinder, illustrating how as the thickness of the hollow shell decreases, so too does the radius of the cylinder. However, it remains steady after 10mm. It can also be observed that when the thickness increases the radius of the cylinder decreases.

These relationships have been defined in this section to obtain an overall view of the effective parameters on this particular structure. However, the mathematical equations remain the same. For example, the number of spheres is proportionally related to $750r_{air}^{-3}$ in equation 19. If the dimensions of the structure change, the constant number 750 will change as well. However, the number of spheres will still have a proportional relationship with r_{air}^{-3} .

4.6 Conclusion

This chapter has demonstrated that having hollow spheres in a solid volume reduces Young's modulus. However, the reduction is not considerable. Moreover, the hollow shell structure improves the stress at the cylinder-bone interface, but this improvement is not significant. As the extracted volume is similar in all the cases, FEA results visualisation were almost similar. However, the sphered samples were not as sufficient as titanium, but better than solid stainless steel. Moreover, the samples 1 and 3 demonstrated larger stress-transfer into the surrounding bone, the stress in sample 1 is 3.9 MPa and in sample 3 is 3.5 MPa. Whereas, the stress in solid titanium is 5.3 MPa, and in solid stainless steel is 1 MPa. To conclude, it is

observed that in sample 1, the spheres are closer to each other in terms of their horizontal distance, and the spheres are closer to the surface in sample 3. Therefore, closer spheres to each other and surface result in larger stress-transfer into the surroundings. In the next chapter, uniformly distributed hollow sphered structure behaviour within a constant mass is investigated in depth.

5 Investigation of cylinders with evenly distributed hollow spheres within a constant mass behaviour

In this chapter, details about materials, meshing strategies, and the different loading conditions that were applied to the samples for analysis, are provided. SolidWorks 2014 SP 4.0 was used to design the samples for FEA analysis, which were based on ASTM standards and previous study (Sugimoto, et al., 2017); (ASTM E9, 2000). In this chapter, metal 3D printing is also discussed, which was used to create samples to run compression tests on. Twelve different cylinders were designed in SolidWorks for stress analysis in order to see the difference in stress distribution over a constant volume. The compression test was also applied to the samples and the rule of mixtures was used to measure Young's modulus and the strength of each sample.

5.1 Introduction

The height and diameter used in this chapter were obtained from the standard (ASTM E9, 2000) and previous study (Sugimoto, et al., 2017) for the compression testing. This standard states that test specimens must be cylindrical. Specifically, based on this standard, the height and diameter were modelled as 38 mm and 12 mm, respectively. In the previous chapter, the spheres were only created close to the surface and the results obtained showed the transfer of stress onto the bone. However, the load-transfer was not significant, which led to the work for this chapter having hollow spheres spread evenly throughout the structure. That is, the aim of this chapter is to develop the idea of having hollow voids throughout the samples distributed uniformly close to the surface, as shown in Figure 5-1, to reduce the Young's modulus. Reducing this, will reduce the stiffness of the materials and the less this is, the more

deformation occurs and more stress is transferred to the surrounding area. FEA, the rule of mixtures and experiments were used to find out about the effects of hollow voids on Young's modulus.

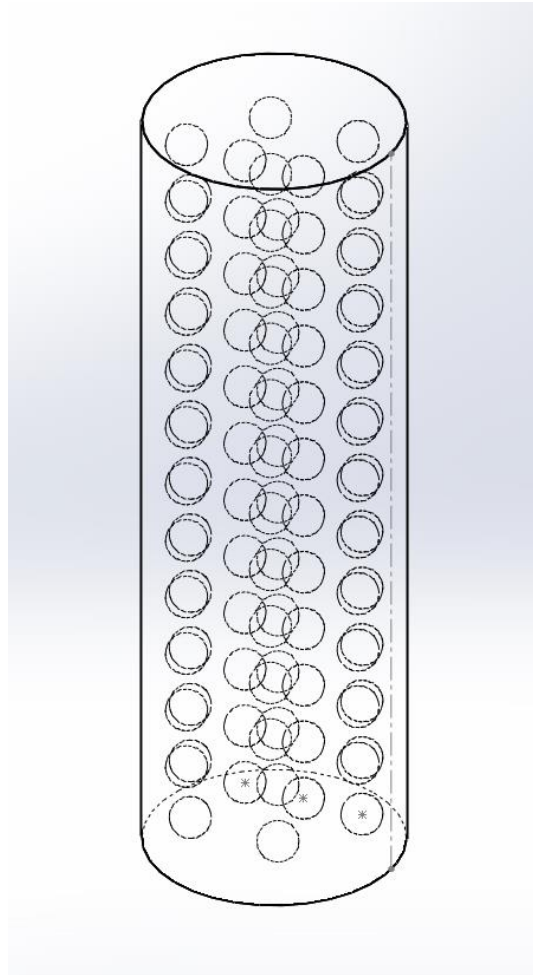
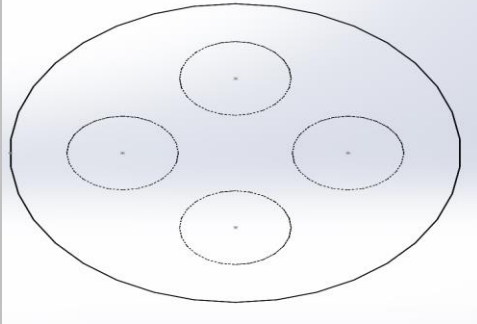
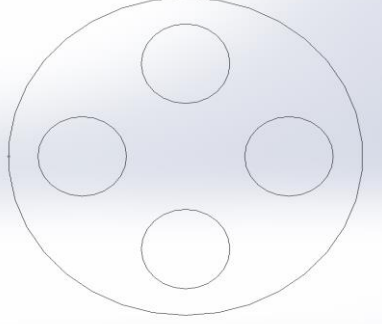
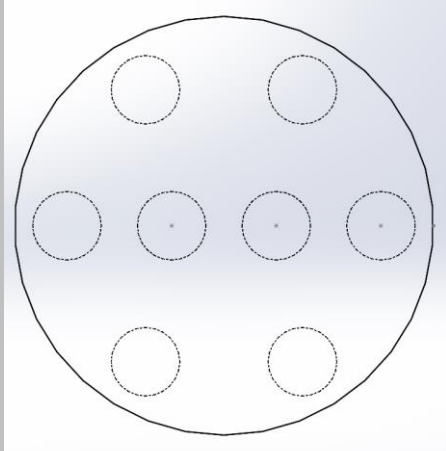
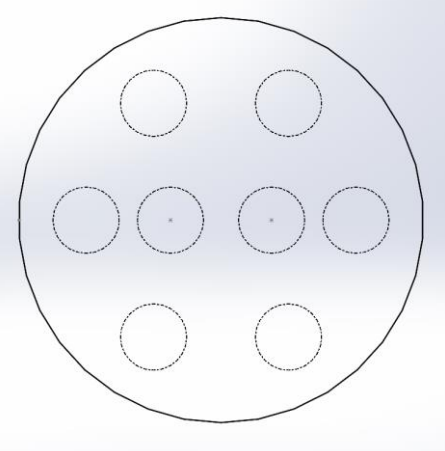
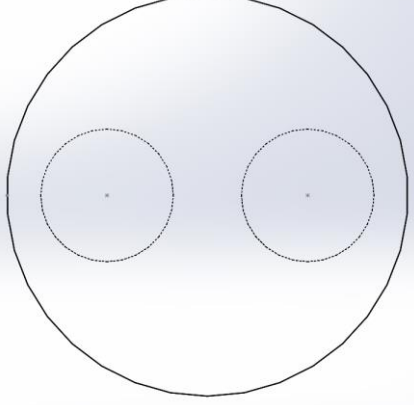
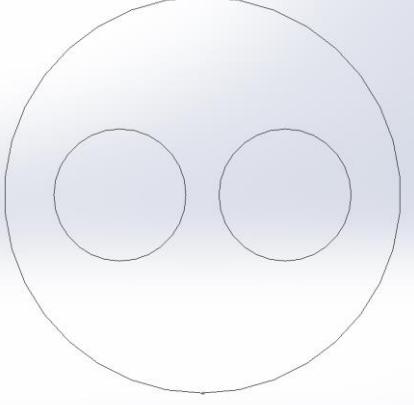


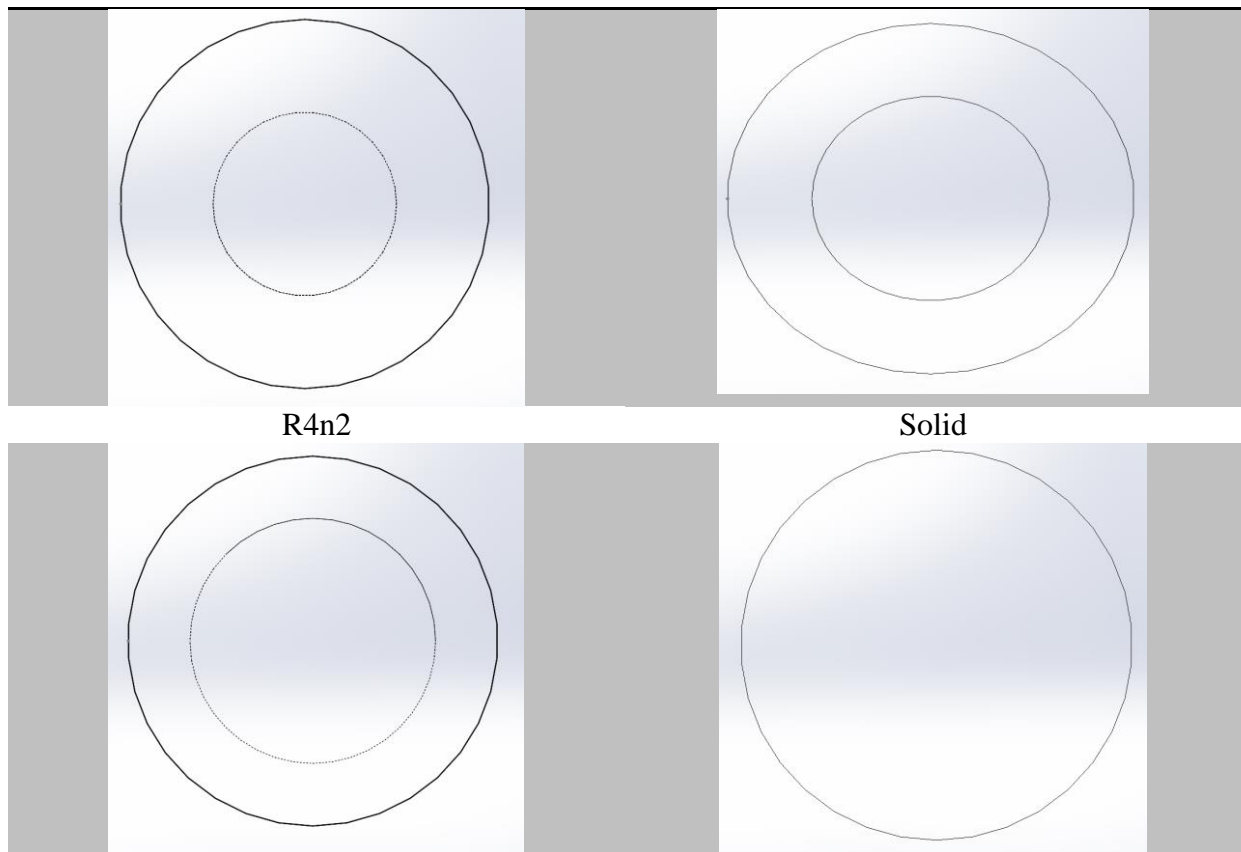
Figure 5-1 Uniformly hollow sphere in the cylinder samples

5.2 Study of 3-dimensional designs

The dimensions used to model these cylinders were obtained from the ASTM standards and previous study (Sugimoto, et al., 2017), with the height being 38 mm and the radius 6 mm. The hollow spheres were evenly distributed in identical volumes to consider different scenarios. There were twelve different scenarios precisely analysed using computational and experimental methods. Table 5-1 illustrates a plan view of each sphered cylinder, which has been modelled based on their distance from each other and from the cylinder side surface as well as the sphere sizes.

Table 5-1 Twelve samples of hollow cylinders

<p>R1.5n32</p> 	<p>R1.5n32/2</p> 
<p>R1n96</p> 	<p>R1n96/2</p> 
<p>R2</p> 	<p>R2n12/2</p> 
<p>R3n4</p>	<p>R3.5n3</p>



5.3 Method

5.3.1 Rule of mixtures

As explained in subsection 4.3.1, the rule of mixtures was used to calculate the Young's modulus and strength of the composite. These were calculated using equations 10, 11 and 12, according to the volume of cylinders. Having established that meshing in the presence of small hollow spheres generates over 15,000,000 elements, conventional approach FEA proved to be impossible, and in fact mesh generation failed to operate. Due to this, the only way to conduct this research is to resort to the rule of mixtures. The rule of mixtures is applied to the whole mass for this chapter.

5.3.2 FEA simulation

FEA was used to analyse twelve different porous cylindrical models. These differences pertained to the sphere sizes, their distance from wall surface and their distance from each other. In addition, the spheres were distributed evenly in these specimens to find out how they would affect the stress distribution over a controlled volume. SolidWorks 2014 SP 4.0 was used to model the parts and they were exported into CREO for FEA. The aim of the

numerical approach was to evaluate stress on the outer surfaces through different internal structural designs in a controlled volume.

5.3.2.1 Cylinder modelling

As aforementioned, there are twelve different models used in this chapter that were designed based on standards. The dimensions for the main structure (diameter and height) were obtained from these, with the porous structure or hollow spheres being the variable in the specimens. Two of the specimens have a different kind of porous structure, the first contains four hollow cylinder within a constant volume, whilst the second one has four hollow ellipsoids, demonstrated in Figure 5-2. The reason to have these two designs along with other specimens was to have a design where no debris is left inside and the other one containing four hollow ellipsoids was to try larger voids and their effects in comparison to hollow spheres. The four hollow ellipsoid example was termed new design/1, whilst with four cylindrical holes was named new design/2.

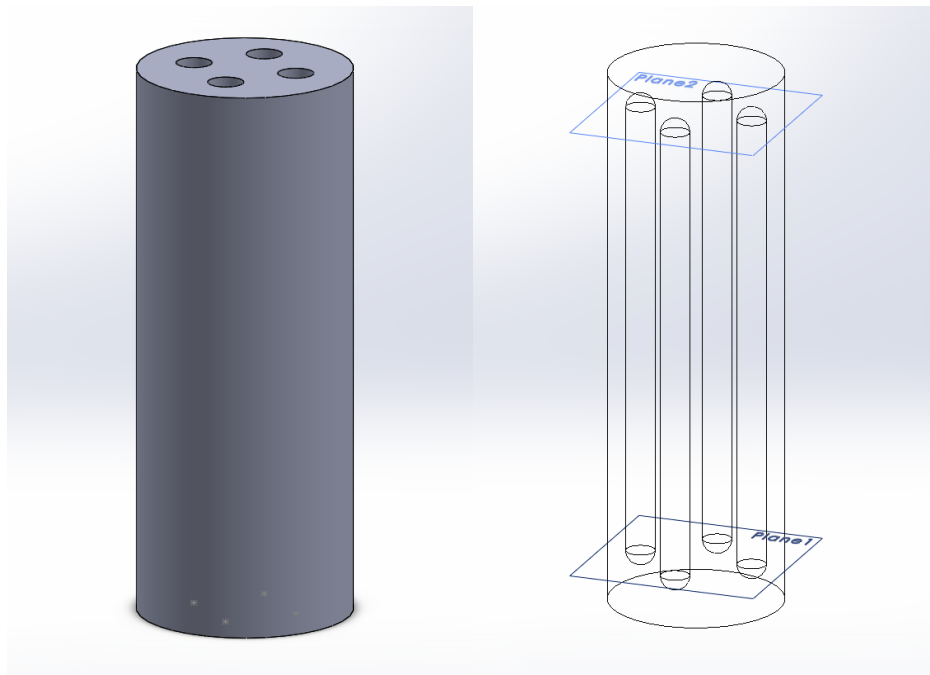


Figure 5-2 The other two specimens with different porous structures

5.3.2.2 Cylinder material

The material used for this work was only stainless steel with the properties illustrated in Table 4-2 (Sabatini & Goswami, 2008).

5.3.2.3 Cylinder boundary condition

The boundary condition was applied in CREO using stainless steel properties. Figure 5-3 shows where the force was applied and where the specimen was pinned. Regarding which, all the specimens were pinned at the bottom of the cylinder, which was set due to the standards of the compression test condition for metals. A force of 10 KN was inserted at the top of each specimen vertically to see how the hollow spheres affected stress distribution within the structure.

5.3.2.4 Force and pin area

As it is shown in Figure 5-3, the force and pinned area of cylinders are similar to the chapter three conditions. Loads can be defined in many forms, such as displacements, forces, pressures, velocities, thermal, gravity etc. They are defined at certain time intervals depending on the situation. That is, the results are recorded at given time durations by defined sub steps in finite element analysis. The force is applied to simulate the strains that are caused and also to investigate the stress distribution. As abovementioned, a force of 10 KN was applied in the Y direction to the top surface of the cylinders. After the load was applied, static analysis was selected based on desired simulation characteristics. Figure 5-3 shows the pin and force area in the cylinder.

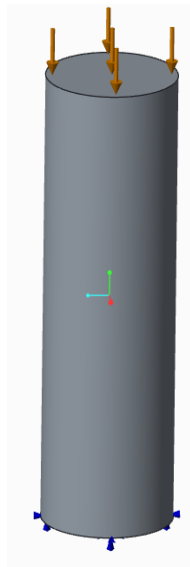


Figure 5-3 Pin and force area of the hollow cylinder

5.3.2.5 Cylinder mesh accuracy

The twelve samples were modelled in SolidWorks as CreoPart (.prt) format and were imported into CREO for meshing and FEA. As the complexity of objects increases, the chances for a perfect FEA decreases. The volumetric mesh used for these samples was

tetrahedral and this meshing helps to divide objects into smaller elements for FEA. The accuracy of the mesh was checked based on the stress-mesh size to achieve precise results.

5.3.3 Experiment to validate the FEA results

All the samples were printed to carry out a compression test for modulus and strength measurements, with the weight, diameter and height of each being measured for calculation purposes.

5.3.3.1 3-D model

As mentioned in the subsection 2.6.8, the Direct metal laser sintering (DMLS) technique was used to print these hollow sphere cylinders.

5.3.3.2 Samples measurements

Samples weights were measured by scale to confirm the reduction in mass when containing hollow spheres. The height and diameter of the samples were also measured by a digital Vernier caliper to calculate their volume. Table 5-2 displays the mass and dimensions of the samples.

Table 5-2 Weight and dimension of the samples measured by scale and a digital Vernier caliper

<i>Samples</i>	<i>Mass (g)</i>	<i>r (mm)</i>	<i>h (mm)</i>	<i>Vol (mm³)</i>
<i>New design/1</i>	34	6.113	38.16	4479.887
<i>New design/2</i>	32	6.13	38.13	4501.297
<i>R1.5n32</i>	34	6.1183	38.096	4480.132
<i>R1.5n32/2</i>	34	6.143	38.113	4518.393
<i>R1n96</i>	34	6.13	38.11	4498.936
<i>R1n96/2</i>	34	6.1283	38.116	4497.148
<i>R2n12</i>	34	6.126	38.116	4493.773
<i>R2n12/2</i>	34	6.13	38.14	4502.477
<i>R3.5n3</i>	34	6.125	38.14	4495.135
<i>R3n4</i>	33	6.1283	38.126	4498.328
<i>R4n2</i>	33.6	6.1316	38.143	4505.182
<i>Solid</i>	35	6.1316	38.126	4503.174

5.3.3.3 Compression test

A compression test was applied to all the samples under the same conditions at room temperature. Figure 5-4 demonstrates one of the samples between the compression anvils. The stress-strain graphs were extracted from the tests for each sample. Furthermore, compression modulus and ultimate compression stress were obtained from the tests, the results of which were compiled in a stress-strain graph.



Figure 5-4 One of the samples between compression anvils

5.4 Results

5.4.1 Results of the rule of mixtures

Table 5-3 demonstrates the results of the Young's modulus and strength after calculations based on the rule of mixtures. As it can be observed, the Young's modulus of all the samples containing spheres was less than for the solid structure. The volume of cylinders is similar and the extracted volume of each sample is approximately the same, these volume extractions being based on equation 16. As Table 5-3 shows, f is between 0.09-0.12. Furthermore, Table 5-3 proves that the Young's modulus of all of the sphered cylinders is approximately similar due to the f values. Hence, this shows that the size of spheres and how far they are positioned from each other or the surface do not affect the Young's modulus according to the rule of mixtures.

Table 5-3 Calculation results for different hollow cylinder designs

<i>samples</i>	<i>Number of sphere</i>	<i>Radius of sphere (mm)</i>	<i>Volume of cylinder (mm³)</i>	<i>Volume of sphere(mm³)</i>	<i>f</i>	<i>E (GPa)</i>	<i>Strength (Mpa)</i>
<i>Solid cylinder</i>	0	0	4295.52	0	0	200	1000
<i>R1n96</i>	96	1	4295.52	401.92	0.093567251	181.28	906.43
<i>R1n96/2</i>	96	1	4295.52	401.92	0.093567251	181.28	906.43
<i>R1.5n32</i>	32	1.5	4295.52	452.16	0.105263158	178.94	894.73
<i>R1.5n32/2</i>	32	1.5	4295.52	452.16	0.105263158	178.94	894.73
<i>R2n12</i>	12	2	4295.52	401.92	0.093567251	181.28	906.43
<i>R2n12/2</i>	12	2	4295.52	401.92	0.093567251	181.28	906.43
<i>R3</i>	4	3	4295.52	452.16	0.105263158	178.94	894.73
<i>R3.5</i>	3	3.5	4295.52	538.51	0.125365497	174.92	874.63
<i>R4</i>	2	4	4295.52	535.893	0.124756335	175.04	875.24
<i>samples</i>	<i>Number of sphere</i>	<i>Radius of sphere (mm)</i>	<i>Volume of cylinder (mm³)</i>	<i>Volume of hollow (mm³)</i>	<i>f</i>	<i>E (GPa)</i>	<i>Strength (Mpa)</i>
<i>New design/1</i>	None	N/A	4295.52	416.7	0.097	180.59	902.99
<i>New design/2</i>	None	N/A	4295.52	475.34	0.11	177.86	889.34

5.4.2 Finite element analysis

The Von Mises stress and displacement of the samples are presented in this section. Figure 5-5 shows the stress distribution and displacement in the solid stainless steel cylinder. Figure 5-5 a demonstrates that the Von Mises stress is very low on the side surfaces in comparison to the bottom of the structure. Specifically, it is between 43.83 and 68.33 MPa, whilst at the bottom, it ranges from 190-215 MPa. Figure 5-5 b shows the displacement and the maximum is 0.016 mm.

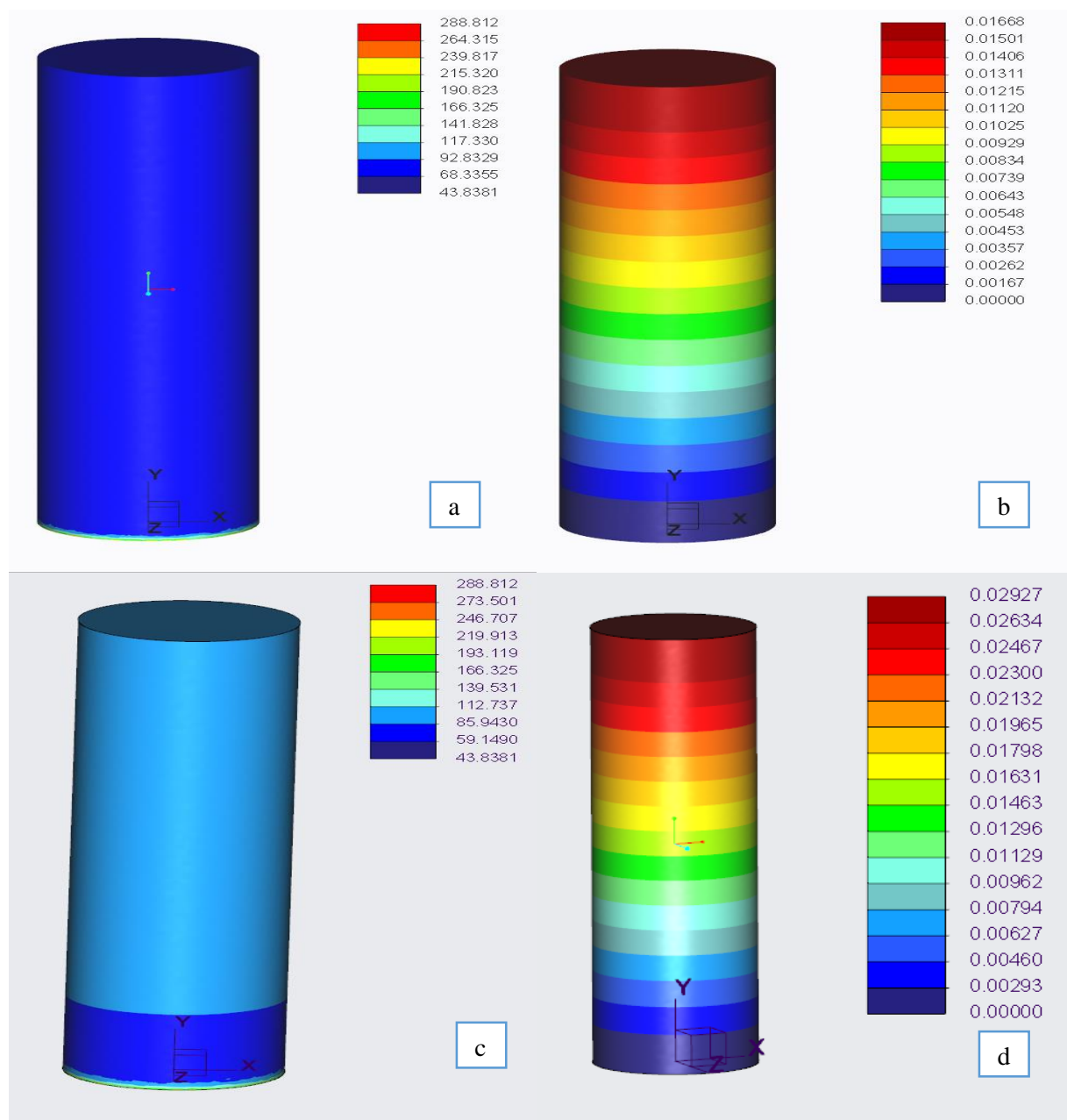


Figure 5-5 Solid stainless steel FEA results: a) von Mises stress distribution (MPa); b) displacement (mm) Solid Titanium FEA results; c) von Mises stress distribution (MPa); d) displacement (mm)

Figure 5-5 c shows the stress distribution and Figure 5-5 d displays the displacement in solid titanium. It can be seen that displacement is higher than for solid stainless steel, whilst the stress distribution is lower.

Figure 5-6 demonstrates the stress distribution and displacement in uniformly distributed 1 mm radius spheres within the cylinder. Figure 5-6 a shows von Mises stress distribution, where it can be observed that the range is between 80 and 120 MPa close to the surface. Around the hollow spheres, higher stress is found as it is concentrated and this reduces as the surface is reached. Hence, the hollow spheres within the structure create localised stress concentration. Figure 5-6 b demonstrates displacement, in which it can be seen that the maximum displacement is 0.019 mm, this being 0.003 mm greater than for the solid structure.

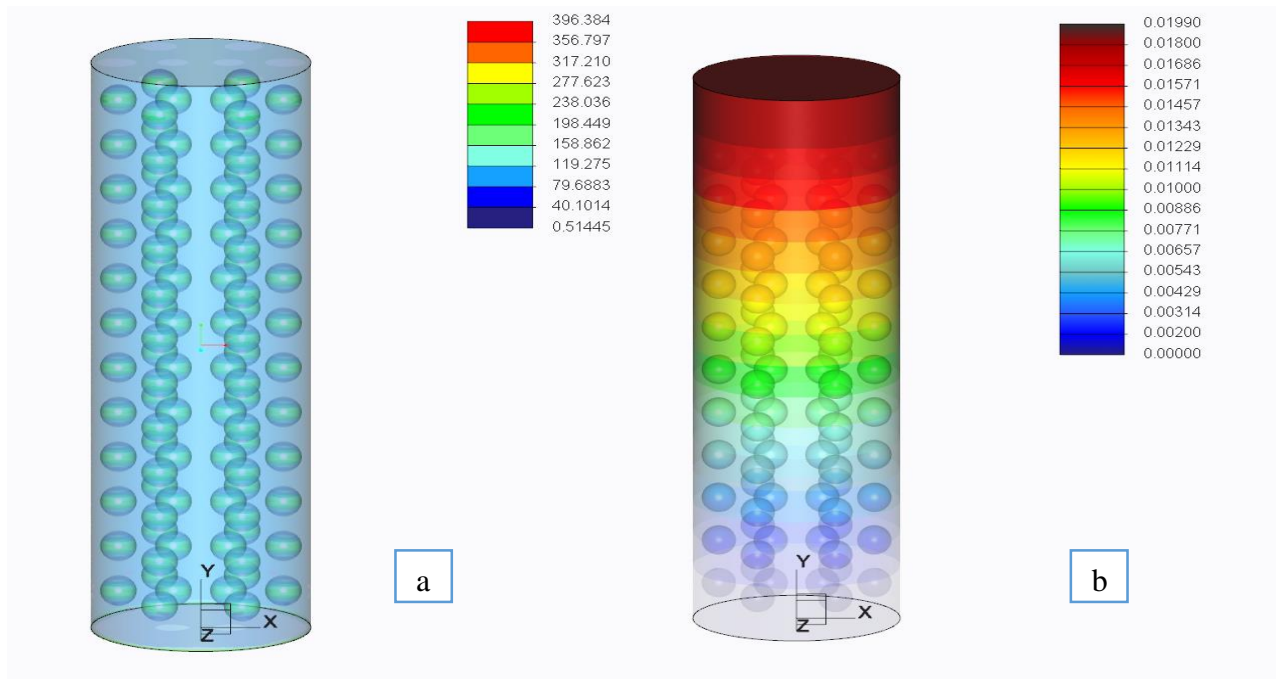


Figure 5-6 R1 FEA results: a) von Mises stress distribution (MPa); b) displacement (mm)

Figure 5-7 also shows the computational results for a cylinder containing spheres with a 1 mm radius. The difference is the hollow spheres' distance to the surface, which is further in this case. In addition, the stress distribution and displacement are shown in the figure, with the stress distribution range being between 80 and 120 MPa near the surface. Around the hollow spheres, higher stress appears, as it is concentrated and diminishes as it reaches the surface. Hence, it is evidenced that hollow spheres within the structure create localised stress concentration. The displacement shown is approximately similar to Figure 5-6 b, which is

still greater than for solid stainless steel and larger displacement causes more load-transfer to the surrounding area.

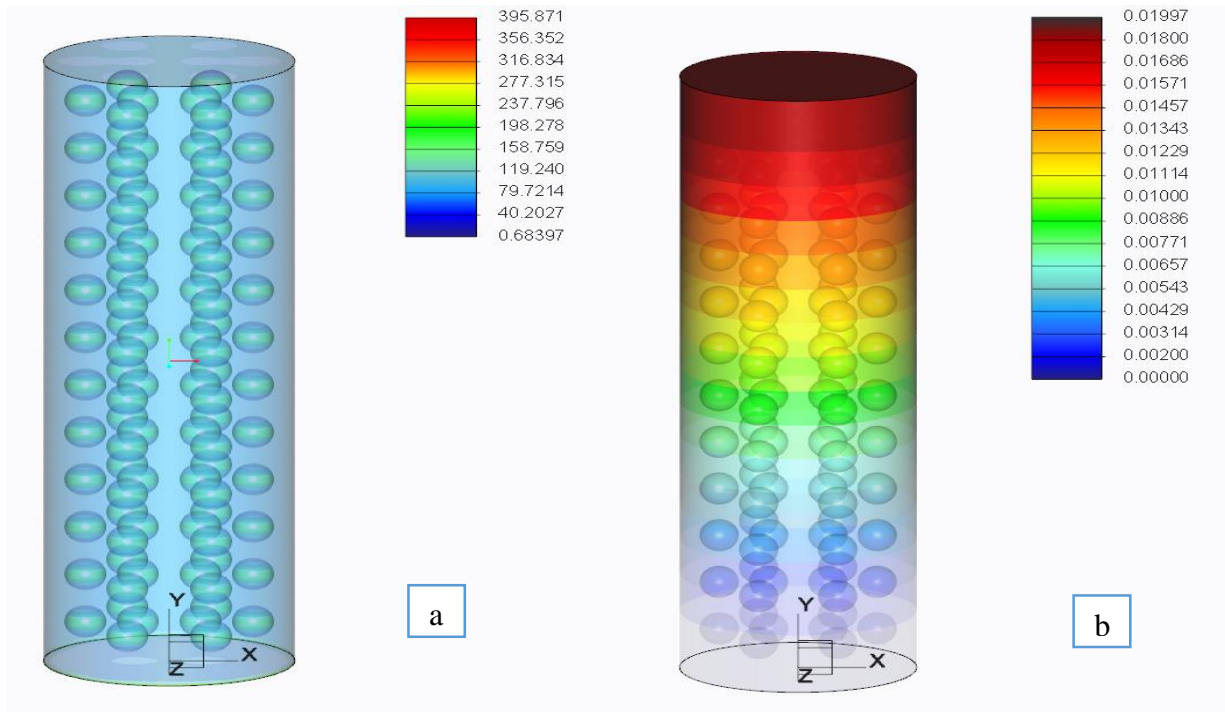


Figure 5-7 R1/2 FEA results: a) von Mises stress distribution (MPa); b) displacement (mm)

Figure 5-8 displays the stress distribution and displacement for a cylinder containing uniformly distributed spheres with 1.5 mm radius. In Figure 5-8 a, the stress distribution is between 96 and 127 MPa close to the surface, which is similar to the stress distribution of the samples containing spheres with 1mm radius at this location. Around the hollow spheres, higher stress appears as it is concentrated, which reduces as it reaches the surface. That is, the hollow spheres within the structure create localised stress concentration. The stress concentration near the spheres is also lower than for the samples with a 1 mm radius. Figure 5-8 b displays the displacement, which is 0.020 mm and it is larger in comparison with that of the samples containing spheres with 1mm radius.

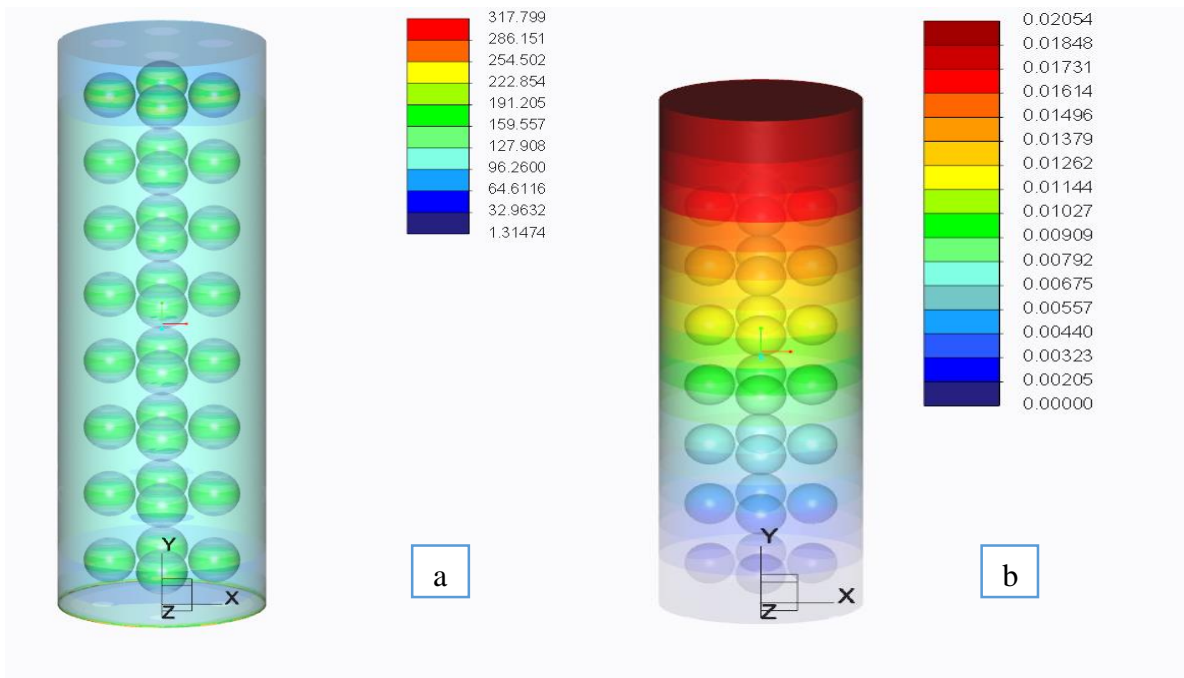


Figure 5-8 R1.5 FEA results: a) von Mises stress distribution (MPa); b) displacement (mm)

Figure 5-9 also indicates the stress distribution and displacement in uniformly distributed 1.5 mm radius spheres in a cylinder. The difference in this case to the previous case is the hollow spheres distance to the surface, which is closer. Figure 5-9 a demonstrates the stress distribution range, which ranges from 100-126 MPa near the surface. This is similar to the stress distribution range for the cases containing hollow spheres with 1 mm radius at that location. Around the hollow spheres, higher stress appears as it is concentrated, which reduces as it reaches the surface. That is, the hollow spheres within the structure create localised stress concentration. The stress concentration near the spheres is also lower than for the samples with a 1 mm radius and maximum displacement is almost the same as that in Figure 5-8 b, with the latter being slightly larger.

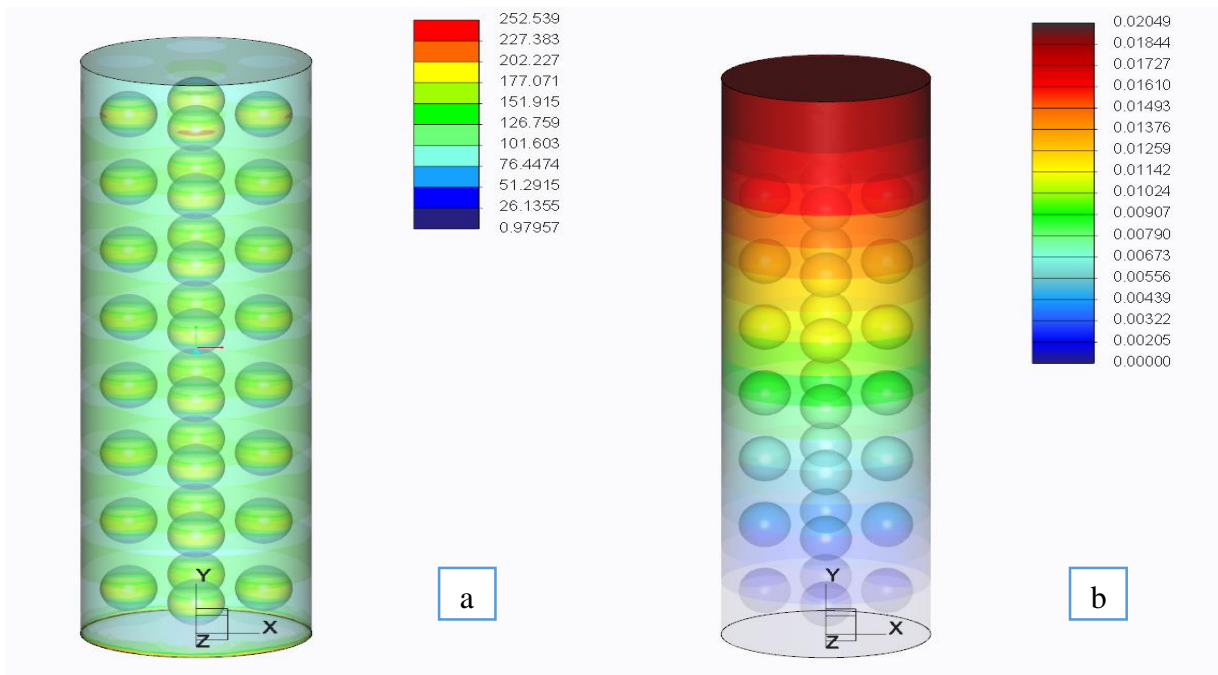


Figure 5-9 R1.5/2 FEA results: a) von Mises stress distribution (MPa); b) displacement (mm)

Figure 5-10 displays the stress distribution and displacement in evenly distributed 2mm radius spheres within a cylinder. Figure 5-10 a shows a stress distribution range that is between 94 and 126 MPa close to the surface. Around the hollow spheres, higher stress can be seen as it is concentrated, which reduces as it reaches the surface. That is, the hollow spheres within the structure create localised stress concentration. Furthermore, the stress concentration near spheres is also lower than the samples with 1 mm and 1.5 mm radius. It can be observed that hollow spheres cause the stress to be distributed evenly. Figure 5-10 b demonstrates displacement within the specimen and the maximum occurring is 0.02 mm, which is slightly larger than the sample containing hollow spheres with 1 mm radius.

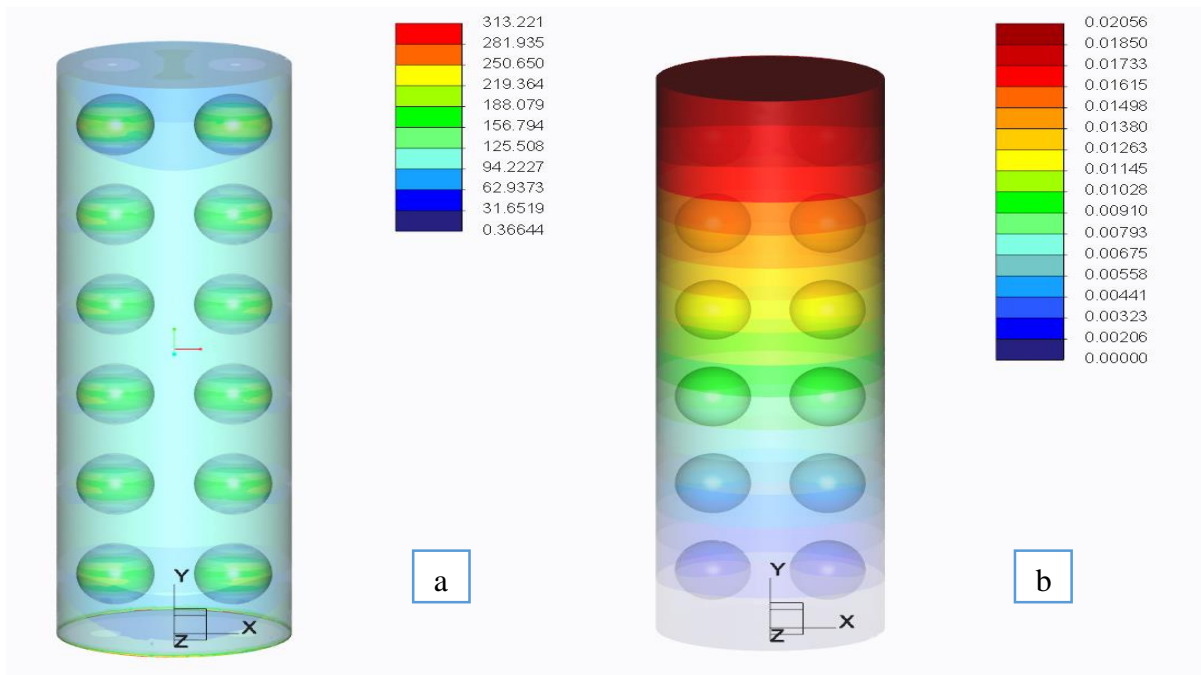


Figure 5-10 R2 FEA results: a) von Mises stress distribution (MPa); b) displacement (mm)

Figure 5-11 demonstrates the stress distribution and displacement in another cylinder containing equally distributed spheres with 2 mm radius. The difference to the previous sample is in the spheres distance from the surface, which is further away and they are closer to each other. The stress distribution in Figure 5-11 a is between 92 and 130 MPa near the surface. Around the hollow spheres, higher stress appears as it is concentrated, which reduces as it reaches the surface. Therefore, the hollow spheres within the structure create localised stress concentration. The stress concentration near the spheres is also lower than for the samples with 1 mm and 1.5 mm radius. The maximum displacement in Figure 5-11 b is 0.02 mm, which is slightly smaller than the previous sample. Hence, the larger the displacement, the greater load-transfer onto the surrounding object.

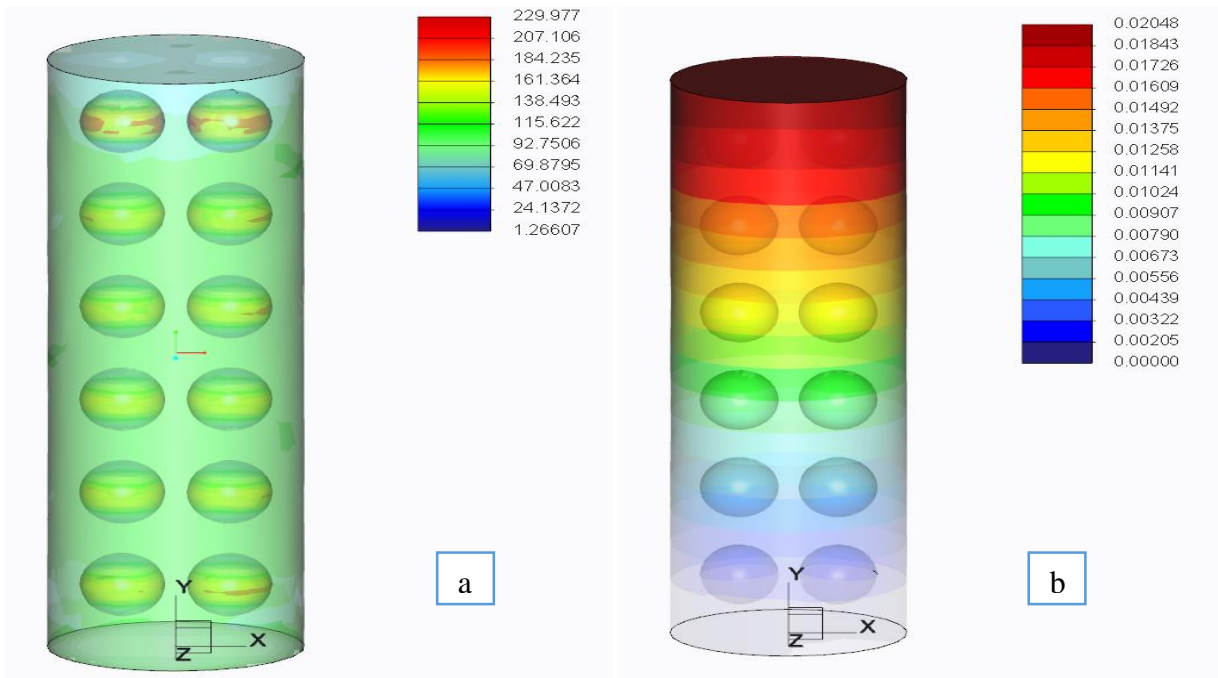


Figure 5-11 R2/2 FEA results: a) von Mises stress distribution (MPa); b) displacement (mm)

Figure 5-12 displays the stress distribution and displacement within a cylinder, where spheres with 3 mm radius are distributed evenly. Figure 5-12 a shows the stress distribution and Figure 5-12 b displays displacement for this case. There are precisely four hollow spheres placed at even gaps from each other. The stress distribution range is between 107 and 134 MPa close to the surface. In addition, the stress concentration close to the spheres is smaller than for the samples with 1 mm, 1.5 mm and 2 mm radius. The maximum displacement is 0.021 mm, which is bigger than for all the previous samples so far discussed.

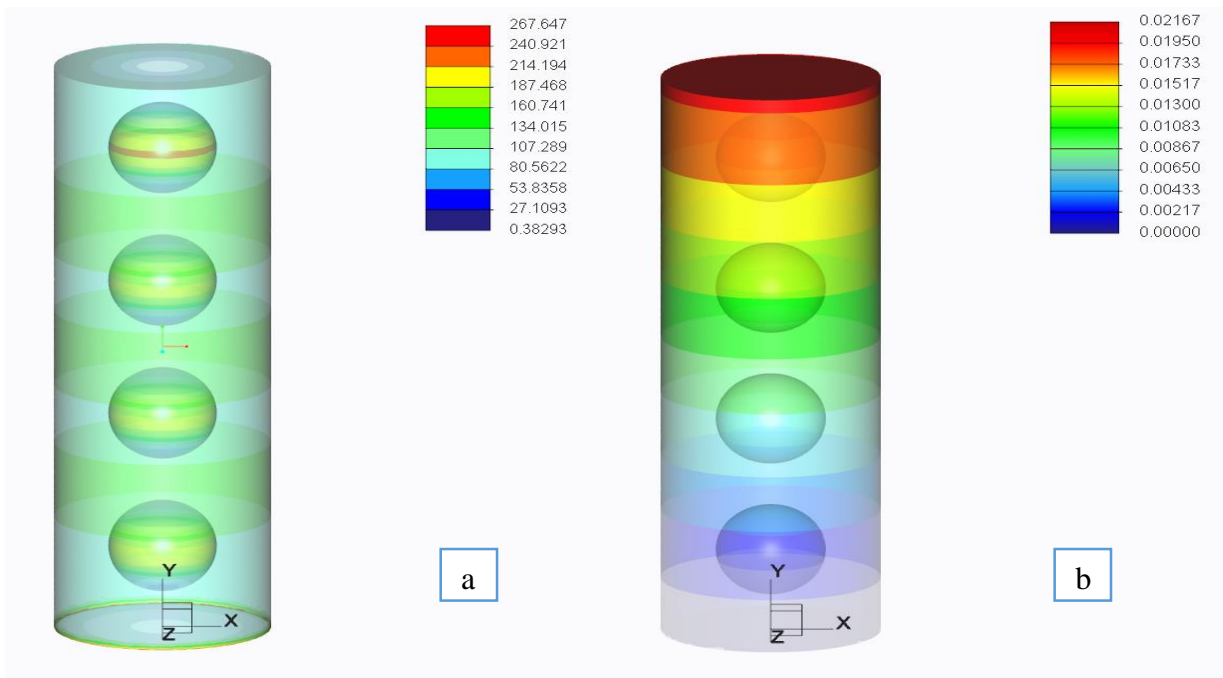


Figure 5-12 R3 FEA results: a) von Mises stress distribution (MPa); b) displacement (mm)

Figure 5-13 demonstrates the simulation for a cylinder that contains spheres with 3.5 mm radius. In addition, it shows the stress distribution and displacement within the specimen. There are exactly three hollow spheres within the cylinder. As it can be observed, the stress distribution ranges from 107 to 134 MPa close to the surface of the cylinder, which is approximately in the same range as for the sample containing 3 mm radius spheres. Moreover, the stress concentration close to the spheres is smaller than for the samples with 1 mm, 1.5 mm, 2 mm and 3 mm radius. The maximum displacement is 0.022 mm, which is slightly larger than for the previous sample.

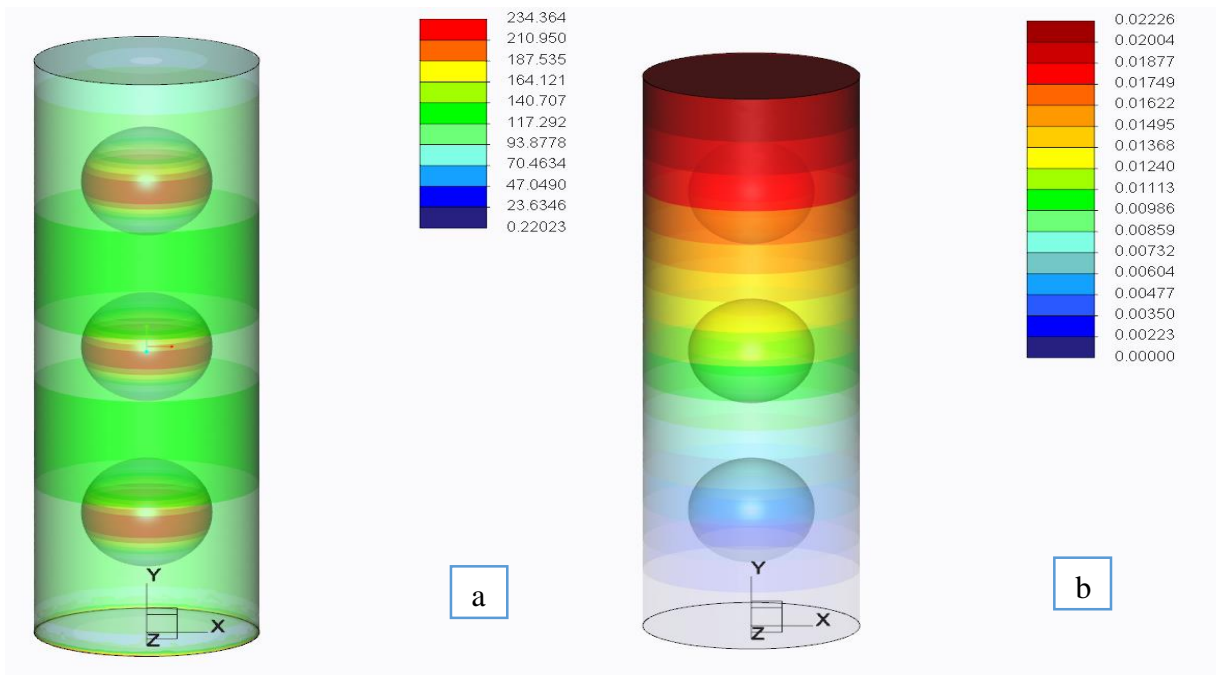


Figure 5-13 R3.5 FEA results: a) von Mises stress distribution (MPa); b) displacement (mm)

Figure 5-14 shows the stress distribution and displacement for a cylinder containing spheres with 4 mm radius and there are precisely two hollow spheres placed evenly within the structure. Figure 5-14 a displays how the stress is distributed within the structure and this is between 88.44 and 140 MPa close to the surface of the cylinder. Furthermore, the magnitude is slightly higher than in Figure 5-13 a, which contains hollow spheres with 3.5 mm radius. In addition, the stress concentration close to the spheres is smaller than for the samples with 1 mm, 1.5 mm and 2 mm radius. Figure 5-14 b shows displacement and the maximum value is 0.022 mm, which is again slightly higher than with the previous case.

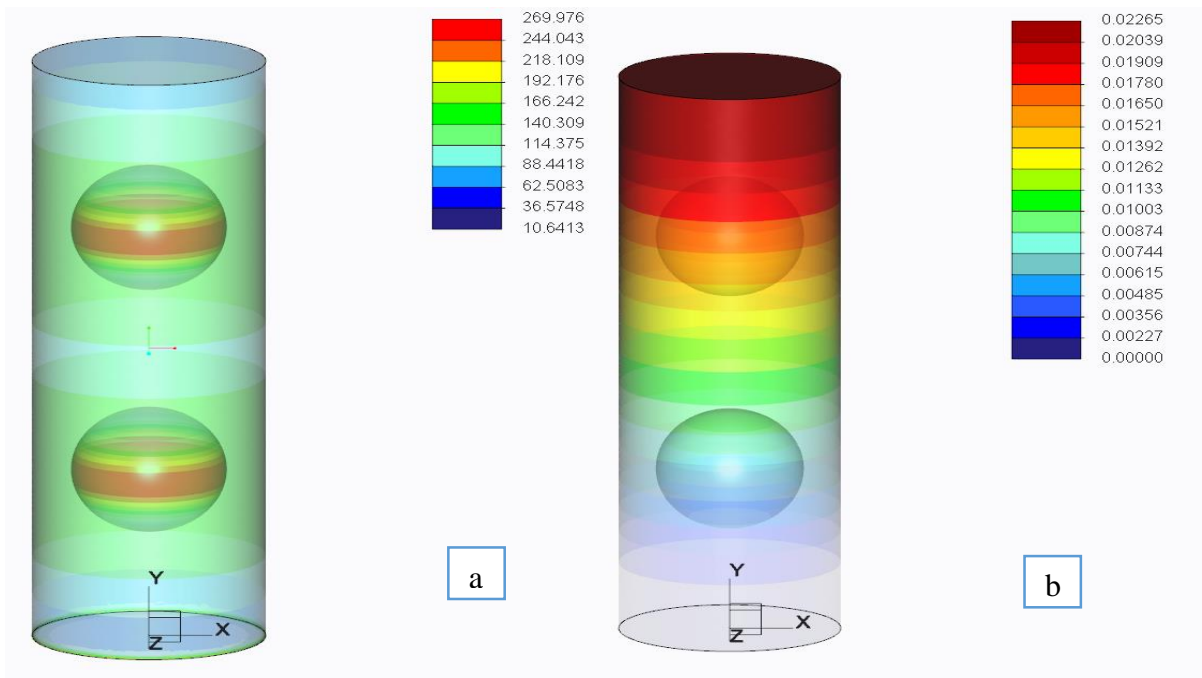


Figure 5-14 R4 FEA results: a) von Mises stress distribution (MPa); b) displacement (mm)

Figure 5-15 demonstrates the stress distribution and displacement for a cylinder with a hollow cylinder within. This case has four cylindrical holes within the same volume as the other cases. The stress distribution range is between 81.87 and 123.68 MPa, whilst the maximum displacement is 0.018 mm.

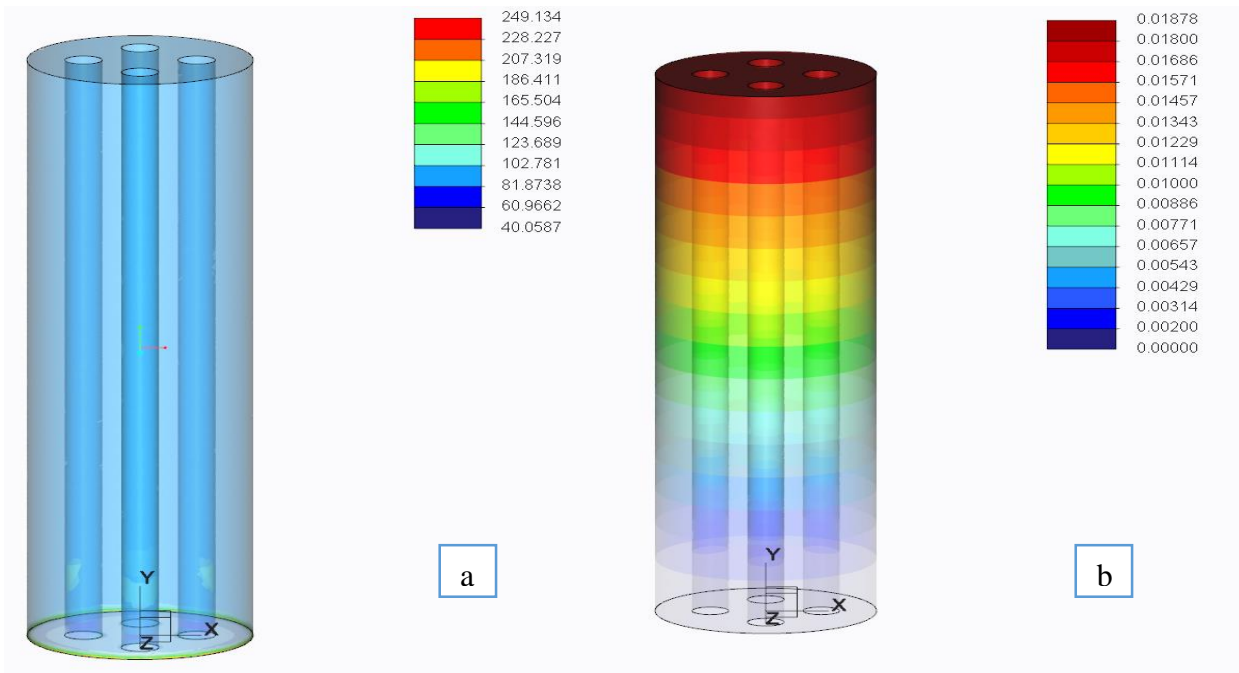


Figure 5-15 FEA results for four cylindrical holes (new design/2): a) von Mises stress distribution (MPa); b) displacement (mm)

Figure 5-16 shows the stress distribution and displacement for a cylinder containing four hollow ellipsoids within the mass. Figure 5-16 a displays stress distribution, whilst Figure 5-16 b shows displacement. The stress distribution ranges from 99.39-164.67 MPa and the maximum displacement is 0.018 mm.

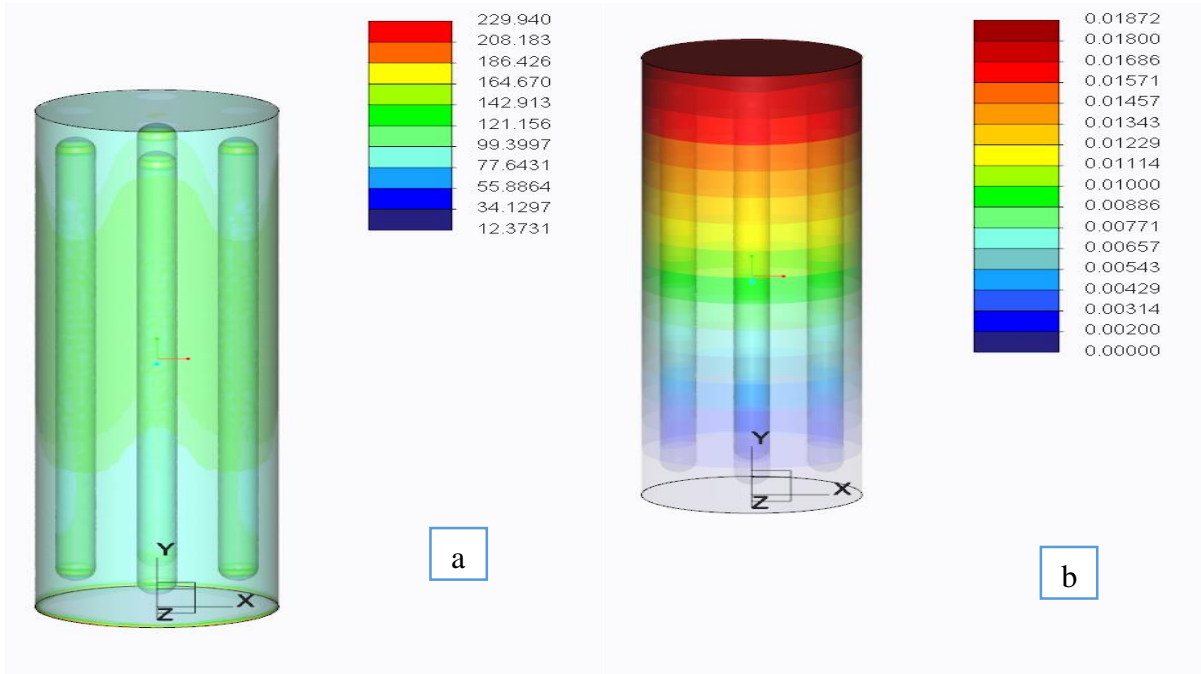


Figure 5-16 FEA results for four hollow ellipsoids (new design/1): a) von Mises stress distribution (MPa); b) displacement (mm)

Figure 5-5 to Figure 5-16 show the stress distribution and displacement under a compression force to measure Young's modulus and displacement. The displacement of the specimens remains approximately similar between 0.018-0.022 mm due to the similar volume extraction from the solid stainless steel. The specimens containing spheres with 1, 1.5 and 2 mm radius have two different designs each, with the difference being the distance to the side surface of the cylinders to the spheres. Their analysis has elicited that the samples containing spheres closer to the side surface have lower stress compared to those closer to each other. Moreover, the other two cylinders that have different designs without hollow spheres have less stress distribution. In addition, the size of sphere affects the stress concentration near to it and the larger it is, the lower the stress concentration close to the surface. However, once the size of sphere reaches 4 mm, the stress concentration remains constant, being also similar to those with a 3 mm and 3.5 mm radius. The stress close to the surface remains approximately similar in all of the hollow sphered samples and the size of spheres also affects the displacement in, i.e. the bigger the size of the sphere is, the higher is the displacement.

Therefore, it will result in higher load-transfer onto the bone to decrease the effect of stress shielding.

The simulation results show the displacement of samples when a 10 KN force is applied. The Young's modulus of each model has been calculated using their stress and strain. Stress is force divided by the area and strain is displacement over the height.

Table 5-4 Finite element results for sphered cylinders

Samples	<i>Displacement (mm)</i>	<i>Force applied (N)</i>	<i>E (GPa)</i>
<i>Solid</i>	0.01668	10000	201
<i>R1</i>	0.0199	10000	169
<i>R1/2</i>	0.01997	10000	168
<i>R1.5</i>	0.02053	10000	164
<i>R1.5/2</i>	0.02049	10000	164
<i>R2</i>	0.02043	10000	164
<i>R2/2</i>	0.02048	10000	164
<i>R3</i>	0.02167	10000	155
<i>R3.5</i>	0.02226	10000	151
<i>R4</i>	0.02265	10000	148
<i>New design/1</i>	0.01871	10000	179
<i>New design/2</i>	0.01876	10000	179

Table 5-4 demonstrates the results of Young's modulus in FEA. As can be observed, a reduction occurs in this modulus when spheres are included within the volume when compared to the solid model. Furthermore, as the size of spheres increases, the reduction in Young's modulus is greater. These finite element results also prove that the distance of the spheres from each other and the surface do not make a big difference in the outcome.

5.4.3 Compression results

The results obtained from experimental and manual measurements are represented in Table 5-5. The weight of the samples is calculated using equations 10 and 16. V_{air} was replaced by $V_{all} - V_{samples}$ and as is known, volume is density multiplied mass. Table 5-5 also displays how the mass reductions in the calculated and experimental results are approximately similar and that the samples containing spheres weigh less than the solid one. Furthermore, it is also

shown that the UTS_C of the samples containing spheres are approximately similar to each other, that for solid stainless steel being just slightly higher. However, the reduction is significant in the cylinder containing spheres with 4 mm radius. It can also be observed that the E_C magnitude in the samples containing spheres is smaller compared to the solid one. In addition, E_C in the samples containing spheres is almost similar; however, the reduction in sphere size of radius 4 mm is significant. Furthermore, the compression modulus for the samples pertaining to new designs (two samples) is similar to that of the solid sample.

Table 5-5 Experimental results for hollow cylinders

<i>Samples</i>	<i>Weight of sample/g (experiment)</i>	<i>Weight of sample/g (calculation)</i>	<i>UTS_C(MPa)</i>	<i>E_C(GPa)</i>
<i>New design/1</i>	32	35.56	530.77	42.99
<i>New design/2</i>	34	35.39	510.73	45.68
<i>R1n96</i>	34	30.75	453.61	41.05
<i>R1n96/2</i>	34	30.75	476.02	43.52
<i>R1.5n32</i>	34	30.36	499.78	40.24
<i>R1.5n32/2</i>	34	30.36	497.88	41.68
<i>R2n12</i>	34	30.75	506.40	38.98
<i>R2n12/2</i>	34	30.75	500.92	39.40
<i>R3n4</i>	33	30.36	494.24	39.91
<i>R3.5n3</i>	34	29.68	448.07	37.93
<i>R4n2</i>	33.6	29.70	402.76	35.15
<i>Solid</i>	35	33.93	574.30	45.03

5.5 Minimising stress shielding by changing the volumetric ratio

To conclude, this chapter has demonstrated that having evenly distributed hollow cylinders decreases Young's modulus and stiffness. There is certain number of spheres that can be created based on total volume that avoids weakening the structure. In addition, an excessive number of spheres, i.e. beyond the optimum, will result in failure of the structure. In this chapter, spheres are evenly distributed in cylinders and an exact number of spheres and the distance from each other and surface could not be defined. However, there is a relationship between all of these factors, as presented in section 4.5 equation 16.

A relationship that can be obtained from equation 16, is that between the radius of a sphere and their number. This relationship is worked out using the equations 28, 29 and 30 using the rule of mixtures.

$$\frac{\frac{4}{3}(3.14)(r_{air}^3) \cdot n}{3.14(38)(6^2)} = 0.1 \quad (28)$$

$$n = \frac{410}{4r_{air}^3} \quad (29)$$

$$n(r_{air}) = 102r_{air}^{-3} \quad (30)$$

As it was mentioned earlier in this part, relationships between geometrical parameters of the samples were created to have a better understanding for future designs. Equation 30 was used to define the relationship between the radius of sphere and their number. Figure 5-17 is the curve drawn based on equation 30, and also helped to visualise equation 30. It also shows how the relationship between these two parameters work instead of setting $r_{air} = 1, 2, 3, \dots$ and calculating n .

According to Figure 5-17, if the radius of a sphere goes down to 0.9 mm or smaller, significant numbers should be added to the cylinder based on equation 16. However, if the radius reaches 3 mm or larger, the number of spheres will be approximately constant, with a slight gradient. As the radius of spheres increases, their volume increases accordingly, which results in a significant reduction in their total number. On the other hand, as the radius gets smaller, their individual volume also decreases, which leads to a rapid increase in the total number of spheres. Hence, spheres sizes could differ from 0.9 to 3 mm to achieve the most effective outcome.

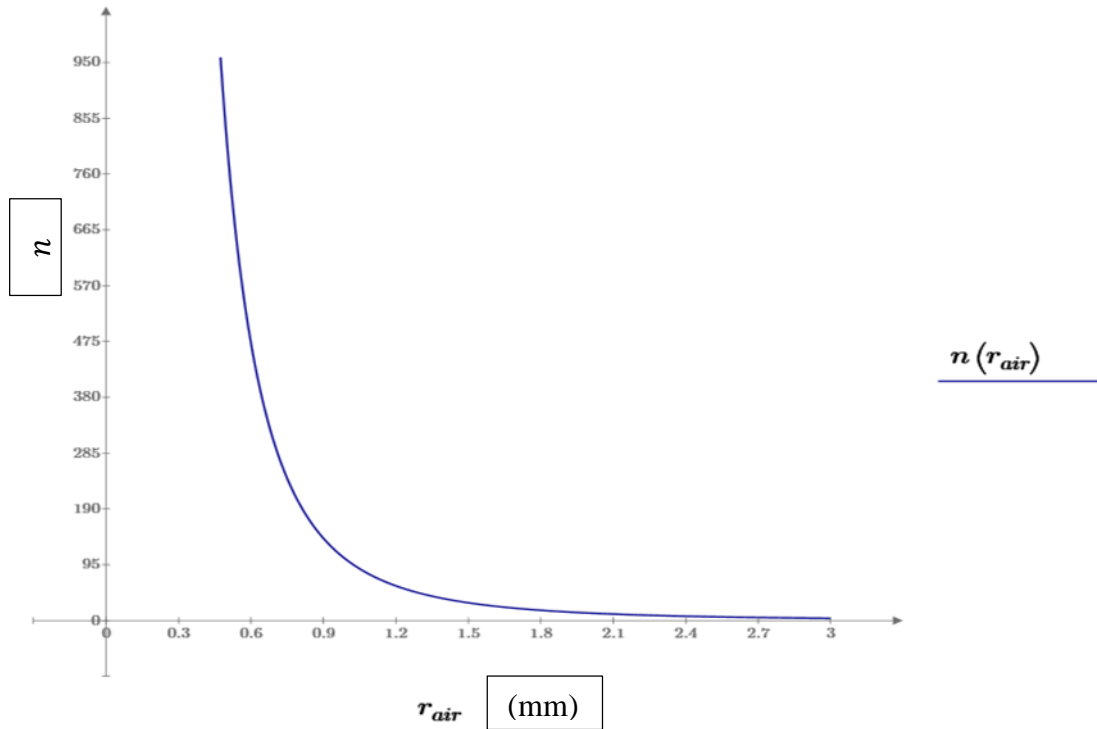


Figure 5-17 The relationship between the radius of spheres (mm) and their number

There could be another relationship concluded as that between the number of spheres and the radius of the cylinder when $r_{air} = 1 \text{ mm}$ and below, is the calculation for this relationship.

$$\frac{\frac{4}{3}(3.14)(1) \cdot n}{(3.14)(38)(r^2)} = 0.1 \quad (31)$$

$$n(r) = \frac{11.4r^2}{4} \quad (32)$$

As it was mentioned earlier in this part, relationships between geometrical parameters of the samples were created to have a better understanding for future designs. Equation 32 was used to define the relationship between the number of sphere and the radius of the cylinder. Figure 5-18 is the curve drawn based on equation 32, and also helped to visualise equation 32. It also shows how the relationship between these two parameters work instead of setting $r = 1, 2, 3, \dots$ and calculating n .

Figure 5-18 demonstrates the relationship between the number of spheres and the radius of a cylinder. The graph shows as the radius increases, the number of spheres goes up as well. When the radius of the cylinder increases, the total volume of the object also increases

rapidly. This will result in a vast increase in total number of hollow spheres. Based on equation 16, as the number in the denominator (total volume) gets larger, the numerator (extracted volume) must increase as well.

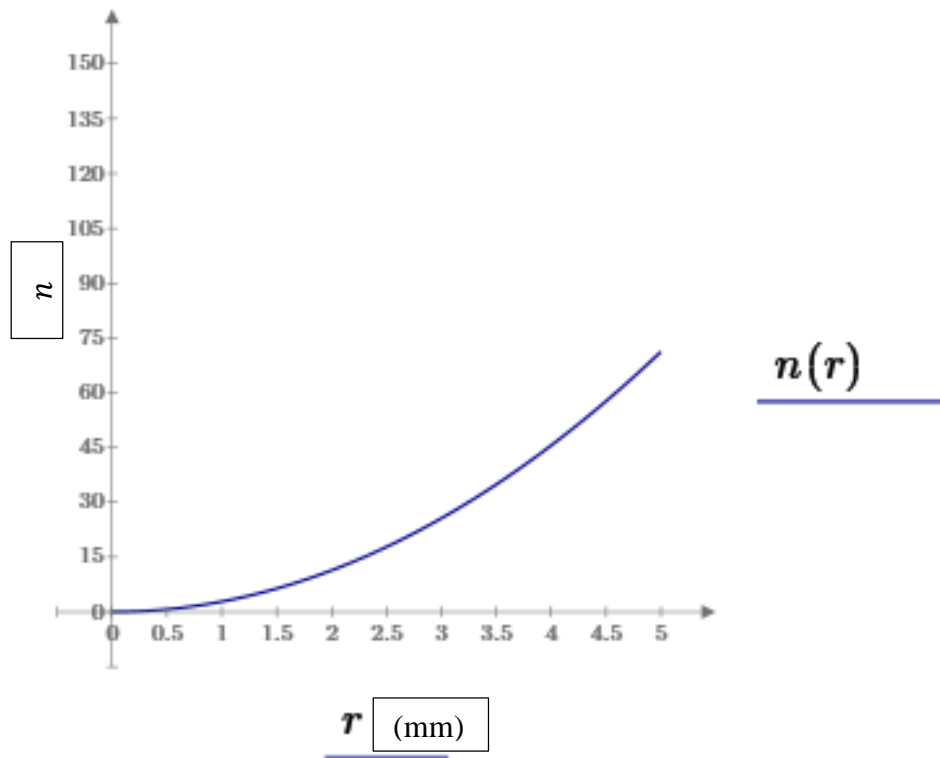


Figure 5-18 Relationship between the number of spheres and the radius of the cylinder (mm)

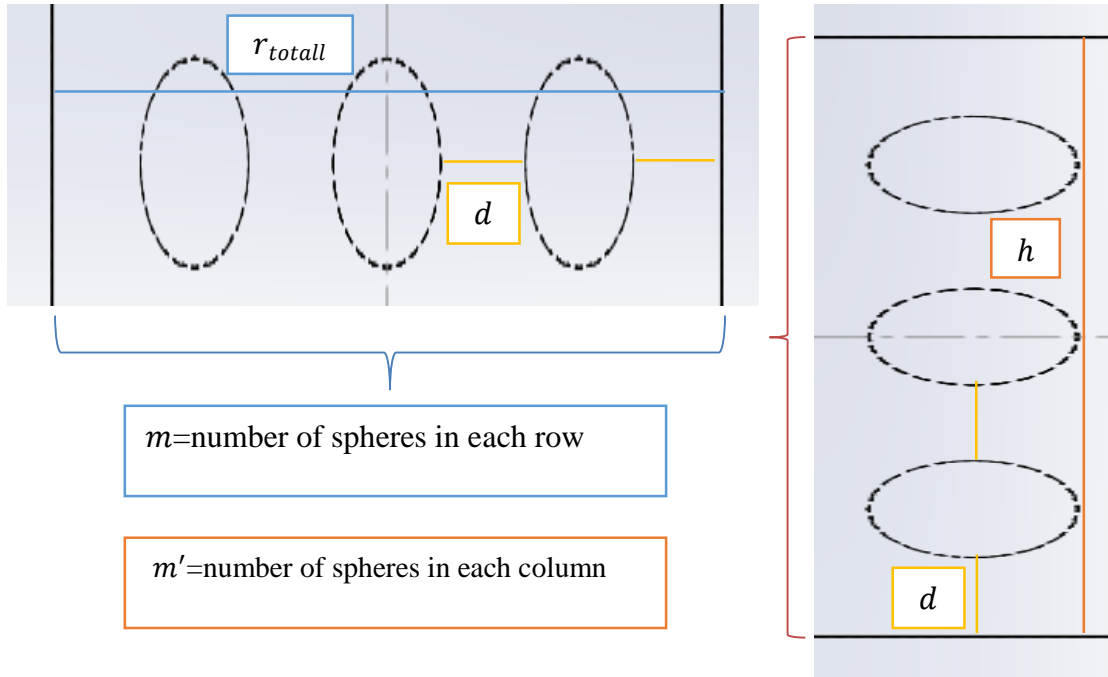


Figure 5-19 Parameter of a cylinder with 38mm height and 6mm radius

Figure 5-19 demonstrates the number of spheres in a row and a column that were used in calculations.

$$(2r_{air} + d)m = 2 \cdot 3.14(r_{all} - d - r_{air}) \quad (33)$$

where, m is the number of spheres in a row, if $2r_{air} + 2d > r_{all}$

$$m = \frac{2 \cdot 3.14(r_{all} - d - r_{air})}{2 \cdot r_{air} + d} \quad (34)$$

where, m is the number of spheres in a row, if $2r_{air} + 2d < r_{all}$

$$m = \frac{2 \cdot 3.14(r_{all} - d - r_{air})}{2 \cdot r_{air} + d} + \frac{2 \cdot 3.14(d + r_{air})}{2 \cdot r_{air} + d} = \frac{2 \cdot 3.14(r_{all} - d - r_{air} + d + r_{air})}{2 \cdot r_{air} + d} \quad (35)$$

$$h = (2 \cdot r_{air} + d) \cdot m' + d \quad (36)$$

where, m' is the number of spheres in a column

$$m' = \frac{h - d}{2 \cdot r_{air} + d} \quad (37)$$

$$m \cdot m' = n \quad (38)$$

In equation 38, n can be replaced by equation 30, $r_{all} = 6mm$, $h = 38mm$, m' could be replaced by equation 37 and m can be replaced by equation 34 for $2r_{air} + 2d > r_{all}$.

$$\left(\frac{2 \cdot 3.14 \cdot (r_{all} - d - r_{air})}{2r_{air} + d}\right) \cdot \left(\frac{h - d}{2r_{air} + d}\right) = 102r_{air}^{-3} \quad (39)$$

$$\left(\frac{2 \cdot 3.14 \cdot (6 - d - r_{air})}{2r_{air} + d}\right) \cdot \left(\frac{38 - d}{2r_{air} + d}\right) = 102r_{air}^{-3} \quad (40)$$

$$\left(\frac{(2 \cdot 3.14 \cdot (6 - d - r_{air})) \cdot (38 - d)}{(2r_{air} + d)^2}\right) = 102r_{air}^{-3} \quad (41)$$

Equation 41 shows the relationship between r_{air} and d , if $2r_{air} + 2d > r_{all}$.

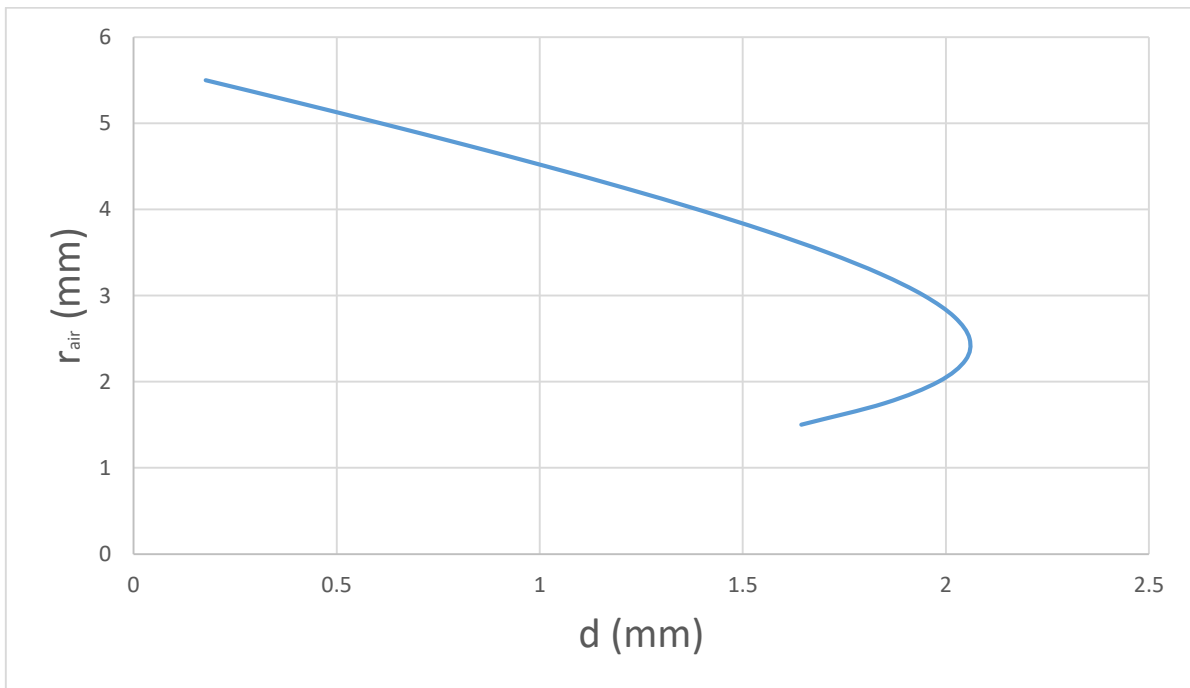


Figure 5-20 Relationship between r_{air} and d when $2r_{air} + 2d > r_{all}$

Figure 5-20 displays relationship between r_{air} and d when $2r_{air} + 2d > r_{all}$. It can be observed that, as the radius of the hollow spheres increases to 2.25 mm, their distance from each other will go up to 2.10 mm. However, this distance decreases when the radius of the spheres gets to being larger than 2.25 mm. Figure 5-20 provides an overview of the relationship between d and r_{air} when the hollow spheres are spread uniformly.

In equation 38, n can be replaced by equation 30, $r_{all} = 6\text{mm}$, $h = 38\text{mm}$, m' can be replaced by equation 37 and m can be replaced by equation 35 for $2r_{air} + 2d < r_{all}$.

$$\left(\frac{2 \cdot 3.14 \cdot (r_{all} - d - r_{air} + d + r_{air})}{2r_{air} + d}\right) \cdot \left(\frac{h - d}{2r_{air} + d}\right) = 102r_{air}^{-3} \quad (42)$$

$$\left(\frac{2 \cdot 3.14 \cdot 6}{2r_{air} + d}\right) \cdot \left(\frac{38 - d}{2r_{air} + d}\right) = 102r_{air}^{-3} \quad (43)$$

$$\left(\frac{1431 - 38d}{(2r_{air} + d)^2}\right) = 102r_{air}^{-3} \quad (44)$$

Equation 44 shows the relationship between r_{air} and d in a hollow sphered cylinder, if $2r_{air} + 2d < r_{all}$.

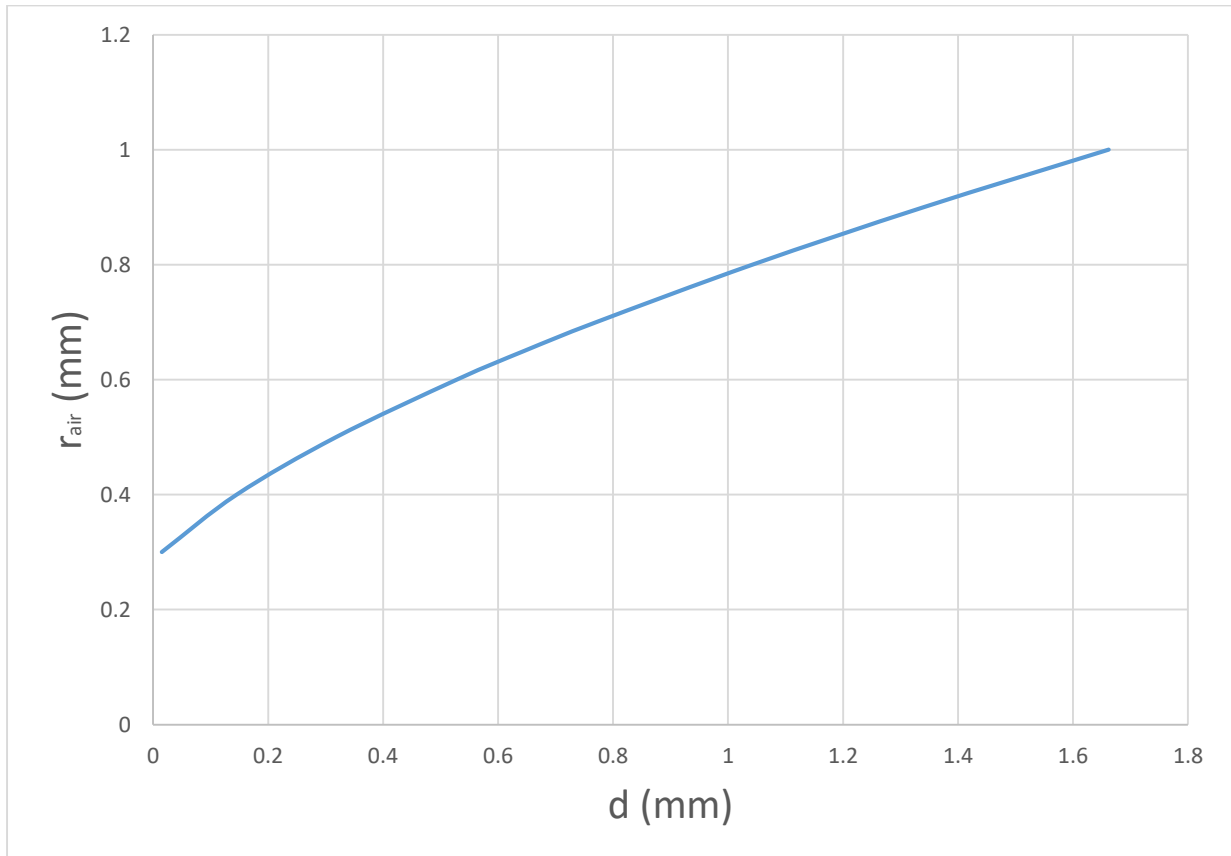


Figure 5-21 Relationship between r_{air} and d when $2r_{air} + 2d < r_{all}$

Figure 5-21 demonstrates the relationship between r_{air} and d when $2r_{air} + 2d < r_{all}$. Figure 5-21 displays that as the radius of the hollow spheres increases, their distance of hollow spheres from each other will increase accordingly. Furthermore, it gives an overview of the

relationship between r_{air} and d when the hollow spheres are spread uniformly and $2r_{air} + 2d < r_{all}$.

As it was mentioned earlier in this part, relationships between geometrical parameters of the samples were created to have a better understanding for future designs. Equations 41 and 44 were used to define the relationship between the radius of the spheres and their distance. Figure 5-20 and Figure 5-21 are the curve drawn based on equations 41 and 44, and also helped to visualise equations 42 and 44. It also shows how the relationship between these two parameters work instead of setting $r_{air} = 1, 2, 3, \dots$ and calculating d . Moreover, these two figures demonstrate as r_{air} increases from 0.3 mm to 2.25 mm, their distance (d) also increases. Their distance (d) starts to decrease once the radius of spheres, r_{air} enlarges more than 2.25 mm.

5.6 Conclusion

In conclusion, this chapter has presented the designs and results for cylinders with hollow spheres being distributed evenly in a controlled mass. Regarding the results, these prove that samples with hollow spheres have a smaller Young's modulus in comparison to solid samples. Experimental results showed that as the radius of hollow spheres increases, the compression modulus for the sphered sample decreases, but, titanium compression modulus is still the lowest. The compression modulus for solid titanium is 30 GPa and for solid stainless steel is 45 GPa. However, it is 35 GPa for sphered samples, which is smaller than solid stainless steel and larger than solid titanium. The FEA results also displayed that the Young's modulus for hollow sphered samples decrease depending on the size of the hollow spheres, the larger the size of hollow spheres, the more the reduction in the Young's modulus is observed. In addition, the Young's modulus for solid titanium is 114 GPa, Solid stainless steel is 200 GPa and hollow sphered sample is 148 GPa. The rule of mixtures displayed similar reduction in all hollow sphered samples Young's modulus, 175 GPa, due to the constant extracted volume from all the samples. Finally, it can be concluded that having hollow spheres uniformly distributed within a mass is better towards the aim of this study. In the next chapter, the behaviour of uniformly distributed hollow sphered stainless steel implants is investigated and compared with solid stainless steel and titanium structure.

6 Investigation of hollow sphered implant behaviour

6.1 Introduction

Finite element analysis (FEA) is a powerful tool for measuring the biomechanical changes that occur during routine everyday activities. Stress distribution and displacement can be obtained by applying FEA. Having a model that can facilitate accurate analysis of the complex biomechanical behaviour of the human gait cycle is crucial for this project, particularly regarding hip implants, due to their load-carrying in daily activities.

In this chapter, a hollow spheres structure is used for actual hip implants, according to the knowledge obtained from previous chapters. Five different implants with two different materials were modelled, namely titanium and stainless steel. The internal structure for stainless steel contained hollow spheres with various sizes in each case. The samples were designed by adding 1 mm, 1.5 mm and 2 mm hollow spheres for the different cases. These models were simulated using Abaqus and the results were compared. The rule of mixtures was also used to determine the relationships between the effective factors. The aim was to decrease the Young's modulus to an effective level to reduce stress shielding. It was also the intention to identify a material that is much cheaper than titanium, which by altering the internal structure, could biomechanically behave close to titanium.

The purpose of modelling these internal structure on the same stem body was to compare the stress distribution and displacement under pressure. The stress distribution and displacement were analysed by using finite element method.

6.2 Methodology

In this section, two methods are described in depth. Finite element analysis and the rule of mixtures are used to analyse the designed models comprehensively.

6.2.1 FEA analysis

6.2.1.1 Part module

The actual implant was designed in solidworks 2014; Figure 6-1 shows the dimensions used to design hip stem. Two solid hip stems and five different hip stems containing various sphere sizes within the stem were modelled. These stems were then fitted inside a bone shaped component, as shown in Figure 6-5. The stems were designed and assembled in SolidWorks 2014, and then, the components were exported into 3-matic Research 10 to apply a surface mesh. Furthermore, they were saved as “Inp” format for transfer into Abaqus/CAE 6.14 for FEA. In addition, volumetric mesh and boundary condition and interface were applied to the models in Abaqus.

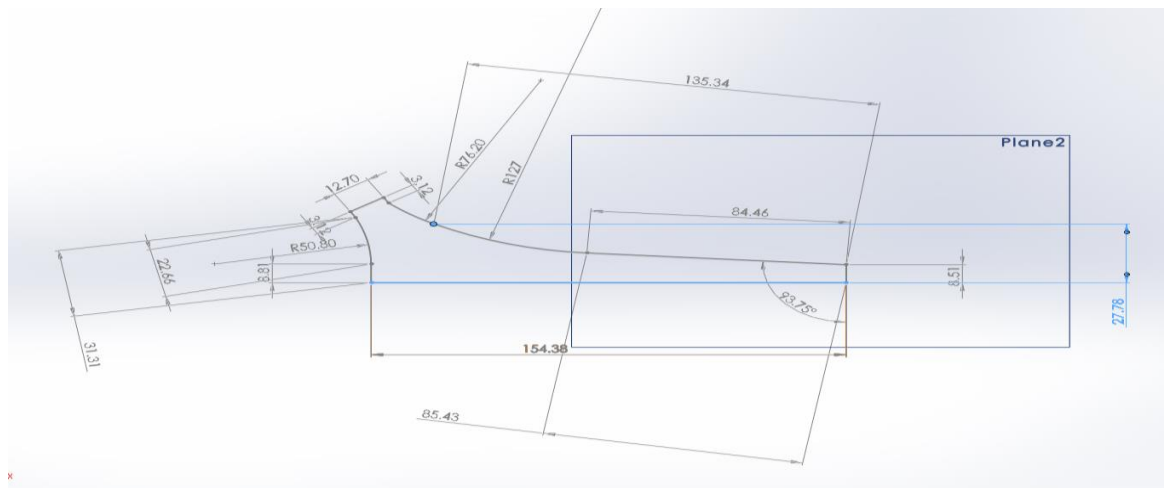


Figure 6-1 Hip stem dimensions

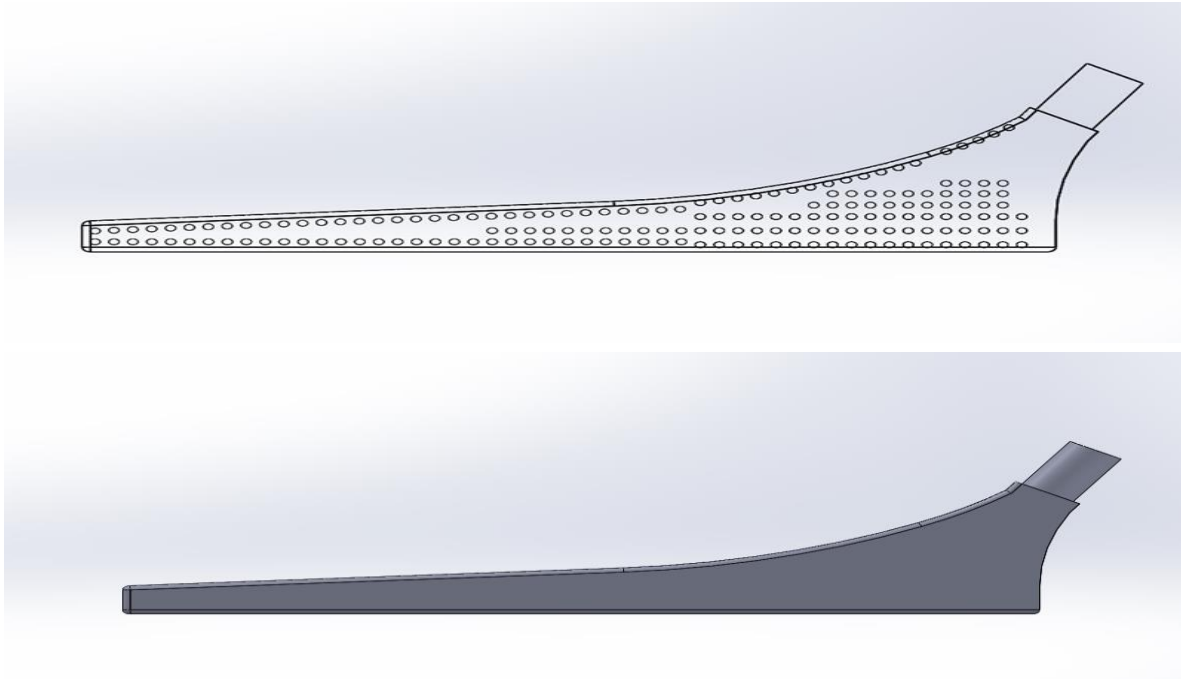


Figure 6-2 Wireframe vs shaded view of the stem

As it was explained in section 4.5, a study in 2016 mentioned that the stress applied to the hips when climbing down is 312 MPa (Colic, et al., 2016). In another approach in 2007, a part under cyclic load, such as a hip, a safety factor of between 2.5 and 2.9 was suggested (Sivasankar, 2007). If the safety factor is multiplied by the cyclic load, the outcome will approximately be 800-900 MPa and hence, in equation 14, σ_c was considered to be within this range. Therefore, in equation 15, f_2 will be between 0.1 to 0.2, which makes the total volume of the hollow spheres between 0.1 and 0.2 of the total implant volume.

Designing implants with spheres was accomplished by creating five different hollow sphered implant models. Three out of the five were designed according to equation 16, where only 10% of the total volume was extracted based on rule of mixtures. Specifically, the stems with different sphere sizes are as follows; hollow spheres implant with 1mm radius spheres; hollow sphere implant with 1.5mm radius spheres; and hollow sphere implant with 2mm radius spheres. The other two hollow sphere implants, containing spheres with 1.5 mm and 2 mm radius are not designed according to the equation 16. In addition, the total volume of spheres is more than one tenth of the total implant volume and Table 6-1 shows the sample dimensions. As demonstrated in Figure 6-2, the spheres are modelled evenly close to the surface of the stem. Table 6-2 displays all designed implants except for the one containing spheres with 1 mm radius which is shown in Figure 6-2. As the sphere size enlarges, the

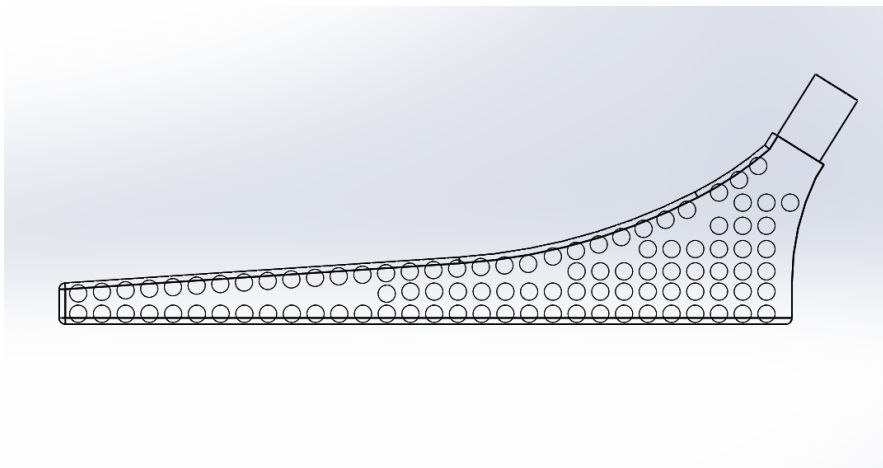
number of spheres decreases. The rule of mixtures was used for calculating the input number of spheres within the stem. This mathematical method was explained in detail in chapter 4.

Table 6-1 Implant samples information

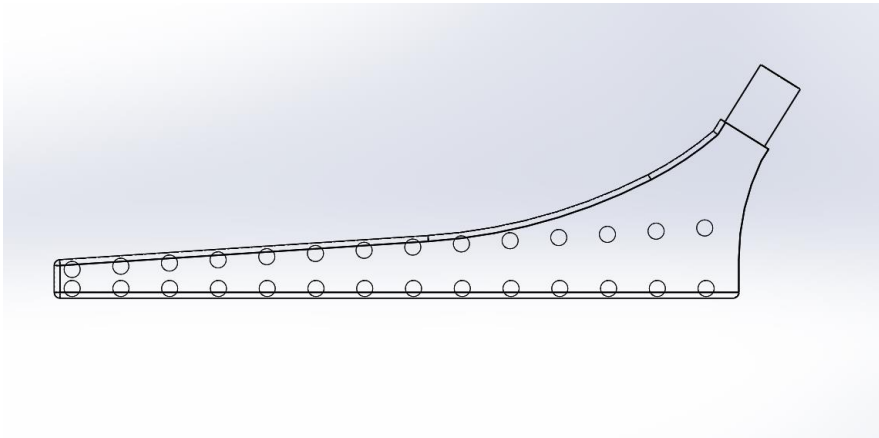
Samples	Radius of the spheres	Number of spheres	Calculation based on equation 16
Hollow Stainless Steel R1	1	416	Yes
Hollow Stainless Steel R1.5 limited	1.5	123	Yes
Hollow Stainless Steel R1.5 unlimited	1.5	299	No
Hollow Stainless Steel R2 limited	2	56	Yes
Hollow Stainless Steel R2 unlimited	2	196	No
Solid Stainless Steel	None	None	N/A
Solid Titanium	None	None	N/A

Table 6-2 Schematic view of the designed implants with 2 mm and 1.5 mm sphere radius

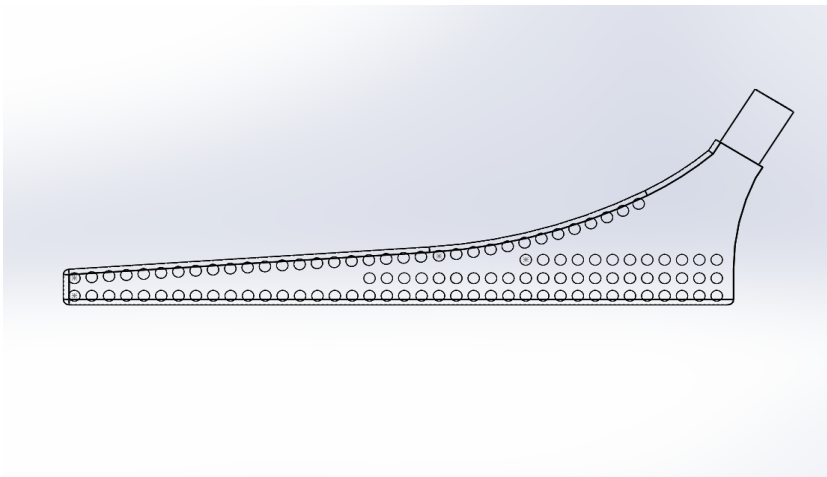
Implant containing spheres with 2 mm radius (unlimited)



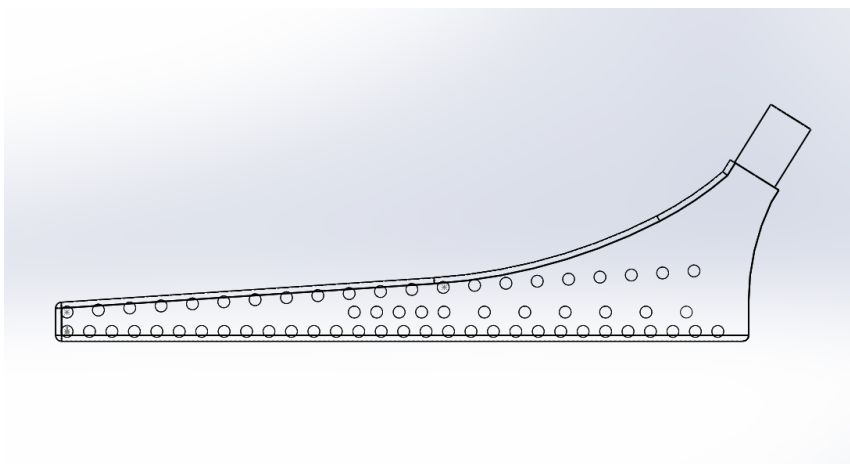
Implant containing spheres with 2 mm radius (limited)



Implant containing spheres with 1.5 mm radius (unlimited)



Implant containing spheres with 1.5 mm radius (limited)



A 3D model of the bone was created in SolidWorks and the implants placed in the bone using the assembly command in SolidWorks. Figure 6-3 shows the modelling for the bone used in

this chapter that was inspired from studies conducted on finite element analysis of hip stem designs (Spinelli, et al., 2012); (Bennett & Goswami, 2008).

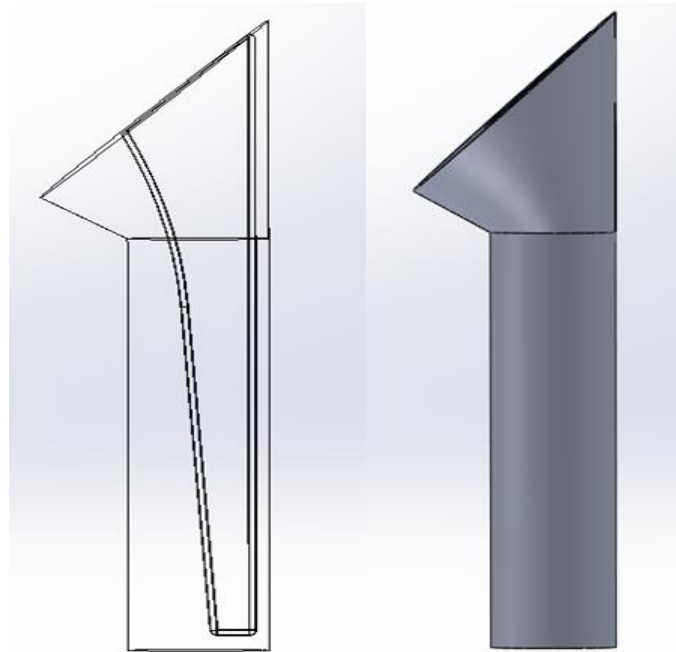


Figure 6-3 Wireframe vs shaded view of the bone shaped design

6.2.1.2 Property module

The main constituent of the skeletal system is bone, which is different in rigidity and hardness to the connective tissues. This rigidity and hardness comes from inorganic salts impregnating the matrix, which contain collagen fibres, a large range of non-collagenous proteins and minerals. Figure 6-4 shows a schematic diagram of bone material.

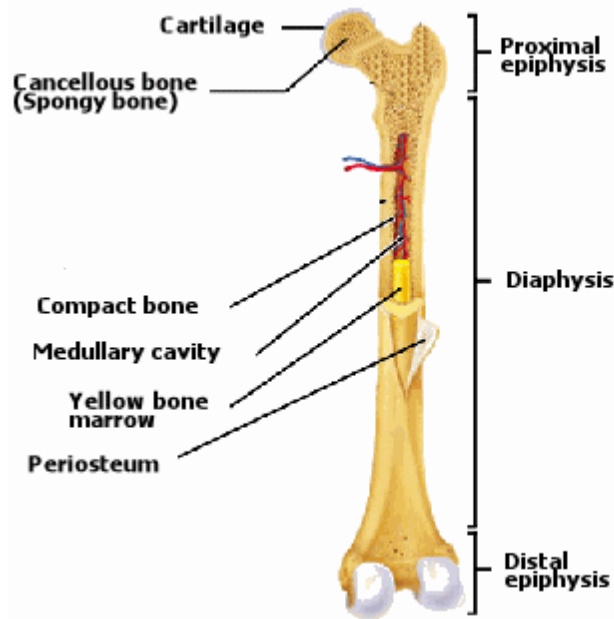


Figure 6-4 Schematic diagram of bone material

In this study, bone was assumed to be an isotropic for computational efficiency and linear elastic material (Geraldes & Phillips, 2014). The values inserted for material properties for bone are show in Table 4-2 (Sabatini & Goswami, 2008). The material properties used in this study were taken as estimations and the actual manufacturing material properties could be slightly higher or lower than those used in this research.

In this study, a titanium alloy (Ti6Al4V) and low-carbon type 316 stainless steel (316L SS) were the alloys used for FEA. The properties of these two materials are listed in Table 4-2. Five different hip stems were designed, being modelled as a linear, homogeneous and isotropic material (Singh & Harsha, 2014); (Anguiano-Sanchez, et al., 2016).

The materials used for this section are the titanium alloy, 316L stainless steel and cortical bone as described in subsection 4.3.2.2. Titanium on its own has poor mechanical properties, but it is biocompatible. Alloyed with aluminium (Al), vanadium (V) and niobium (Nb), as mainly Ti6Al4V and Ti6Al7Nb, it is mainly suitable for uncemented femoral stem production. In addition, the mechanical properties of titanium alloys will improve, whereas the biocompatibility will reduce due to the toxic elements, such as aluminium and vanadium. On the other hand, the weak shear strength and wear resistance of titanium alloys have affected the usage of them in biomedical fields (Long & Rack, 1997) and the metal is also very expensive.

6.2.1.3 Implant boundary condition

To conduct FEA, all parameters must be defined. That is, boundary conditions, initial conditions and material properties need to be assigned for FEA as it is very important and effective.

In this study, Abaqus/explicit was set to run simulations on the samples, which is capable of handling non-linear behaviour and is a strong software capable of solving many problems involving contact interaction between many bodies.

FEA provides multiple set of contact behaviour options to specify the non-linear behaviour at the interface. The contact surfaces of the femoral stem and femur were defined as surface-to-surface contact to increase the accuracy of the results. These parameters are defined for objects having large interfaces, such as femur and stem. In similar studies to the current one, either node-to-node or node-to-surface or surface-to-surface are defined, which are more precise (Viceconti, et al., 2000); (Mann , et al., 1995).

6.2.1.4 Force and pin area

The mathematical aspect of this chapter shows how the spheres react to the applied loads and constraints. Loads can be assigned in many forms, such as displacements, forces, pressures, velocities, thermal, gravity etc. The load application is defined by the load steps at certain time intervals and the results are recorded at these given time durations in static analysis. Pressure was applied to the implants, as shown in Figure 6-5, which were pinned at the distal and proximal epiphysis. Specifically, pressure was applied at an angular direction on femoral stem with a magnitude of 86.34 MPa (Bennett & Goswami, 2008); (Sabatini & Goswami, 2008). The distal epiphysis was pinned for the boundary condition, that is the distal end of the femur (Dudaa, et al., 1998).

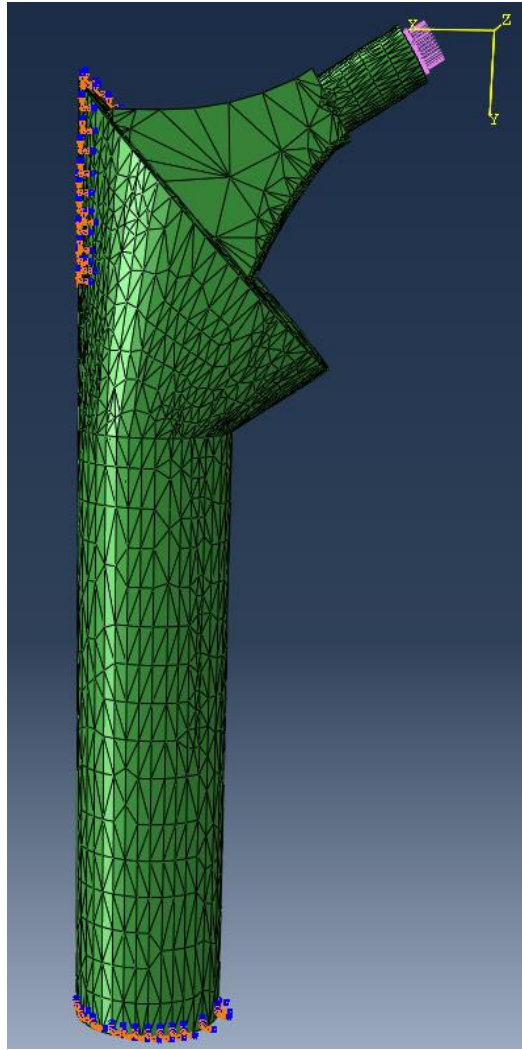


Figure 6-5 Force and pin area

6.2.1.5 Implant mesh accuracy

The bodies are converted into volumetric mesh prior to the simulation. As the radius of spheres decreases, the mesh elements on the implants have to be smaller to create those spheres as accurately as possible. Meshing must be uniform and refinement can be used for sharp edges and to ensure the integrity of mesh, it must be as fine as possible. In the present study, the maximum number of elements reached was 5,271,103. These values relate to the implant containing spheres with 1 mm radius, which increases the number of elements and nodes in that mass. To achieve a complete volumetric mesh, the surface mesh imported previously from 3-matic software converts into volumetric mesh in Abaqus (from triangular to tetrahedral elements). The volumetric mesh was verified using some defined parameters, such as the mesh aspect ratio and an analysis check was accomplished to check the mesh quality. Figure 6-6 shows a view of mesh in Abaqus.

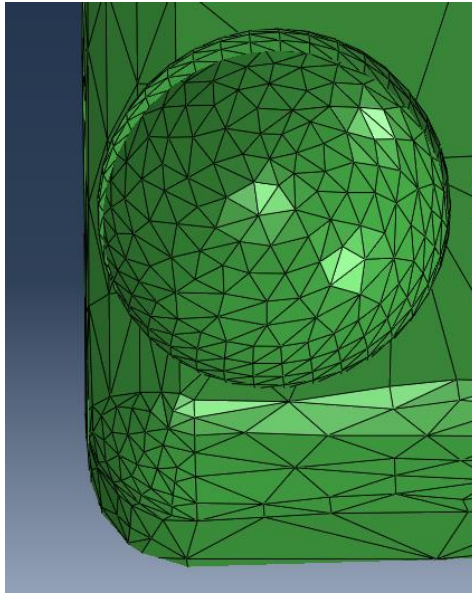


Figure 6-6 Mesh of the implant

6.2.2 Rule of mixtures

The calculation for the implant was carried out according to equation 16 for 3 hollow samples as explained in Table 6-1. As described in the chapter 4, there should be a limited number of hollow spheres in a mass.

$$f = \frac{\left(\frac{4}{3} \cdot \pi r^3 \cdot n\right)}{volume_{implant}} \quad (45)$$

$$f = \frac{\left(\frac{4}{3} \cdot \pi r^3 \cdot n\right)}{20665.15} \quad (46)$$

$$f = 0.0002r^3 \cdot n \quad (47)$$

$$f = 0.1 \quad (48)$$

$$0.1 = 0.0002r^3 \cdot n \quad (49)$$

$$500 = r_{air}^3 \cdot n \quad (50)$$

There were two other designs containing unlimited spheres with 1.5 and 2 mm radius, which were not based on the equation 16. Equations 11 and 12 were used to calculate the Young's modulus and UTS of these structures.

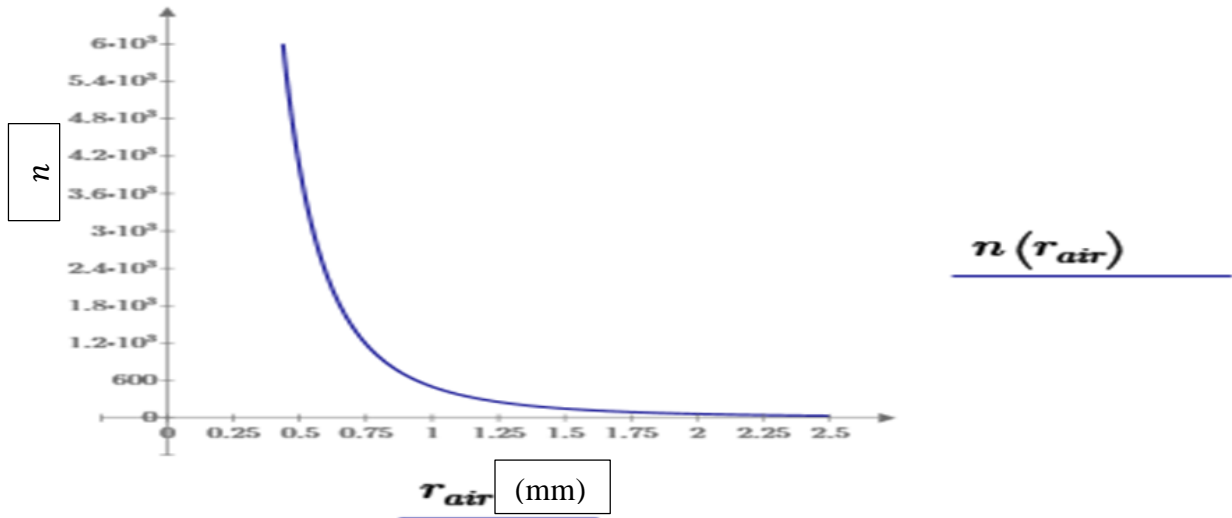


Figure 6-7 Relationship between the number of spheres in an implant and their radius (mm)

In this part, relationships between geometrical parameters of the samples were created to have a better understanding for future designs. Equation 50 was used to define the relationship between the number of spheres in an implant and their radius. Figure 6-7 is the curve drawn based on equation 50, and also helped to visualise equation 50. It also shows how the relationship between these two parameters work instead of setting $r_{air} = 1, 2, 3, \dots$ and calculating n .

Figure 6-7 shows the relationship between the number of spheres in an implant and their radius. The X axis is the radius of spheres in mm and Y axis displays their number. If the radius of sphere decreases to under the 1 mm, then their number increases significantly. However, when the radius of the spheres increases to 3mm or more, their number stays almost steady and hence, any size between 1 and 3 mm will be more effective.

6.3 Implant finite element results

Figure 6-8 shows the von Mises stress of solid stainless steel in bone, implant and as an assembly. As can be observed in Figure 6-8 a, the stress distribution in bone is between 0.5 and 3 MPa. Figure 6-8 c displays the stress distribution within the solid implant, where it can be seen that the range is 10.01-20 MPa and that the maximum stress is at the distal end of the implant. Figure 6-8 b shows the transferred stress from the implant onto the bone.

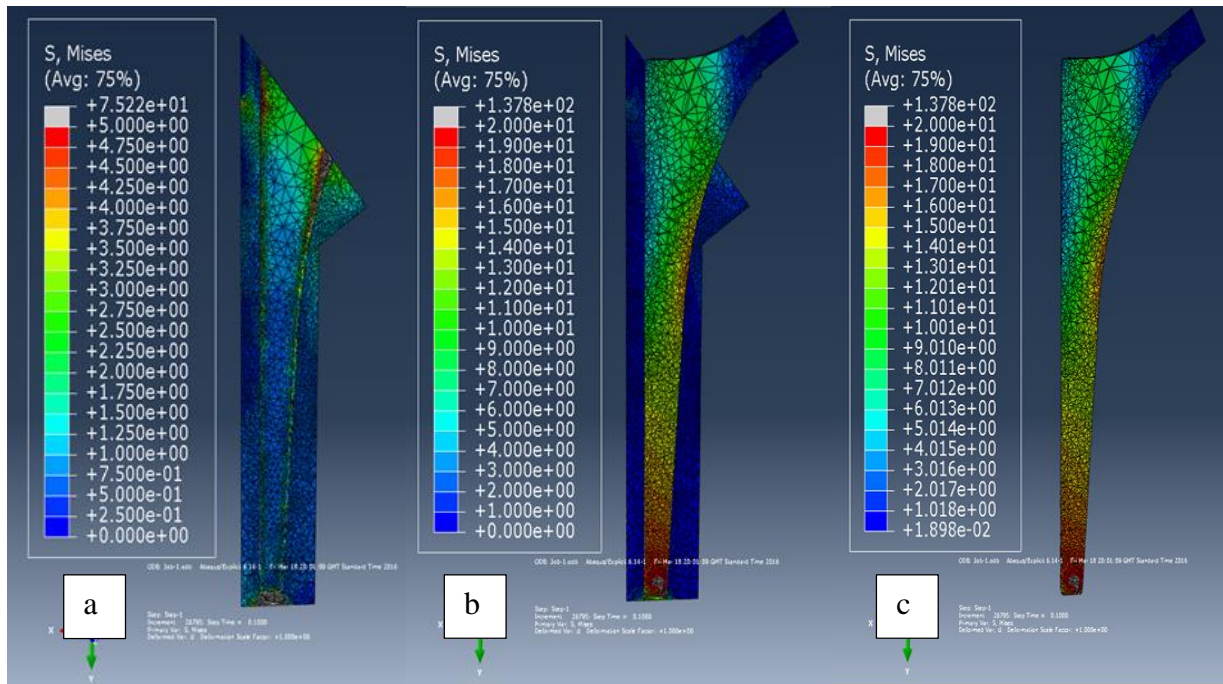


Figure 6-8 Von Mises stress for solid stainless steel: a) bone; b) bone and implant; c) implant

Figure 6-9 shows the von Mises stress of solid titanium in bone, implant and as an assembled model. Figure 6-9 a demonstrates stress distribution in the bone, which varies from 1.00 to 4.00 MPa. As can be observed, this is distributed more evenly in the titanium sample in comparison to the solid stainless steel. Figure 6-9 c displays the stress distribution in the solid titanium implant, with the range being 8.01-18 MPa, which is smaller than for stainless steel, meaning that more stress has gone onto the bone. Figure 6-9 b shows the bone and the implant as assembled objects and the stress transferred onto the bone from the implant.

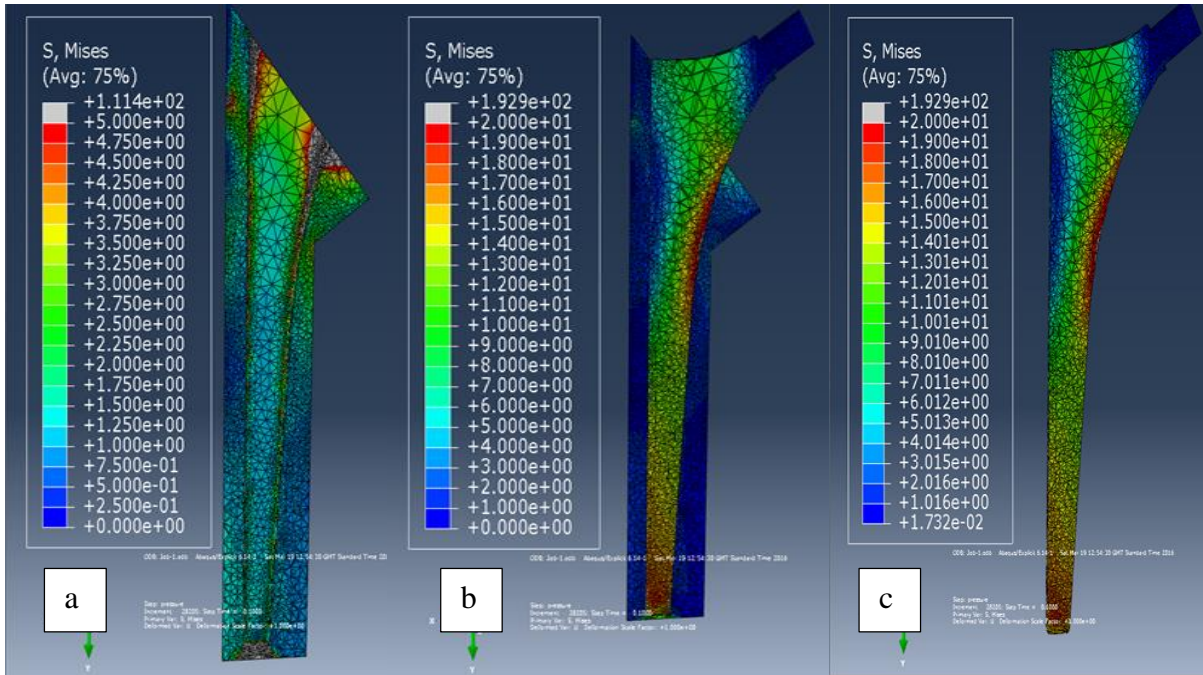


Figure 6-9 Von Mises stress for solid titanium: a) bone; b) bone and implant; c) implant

Figure 6-10 displays the von Mises stress for stainless steel containing spheres with 1 mm radius in three different states. This sample contains the greatest number of spheres of all the specimens. Figure 6-10 a demonstrates the stress distribution in bone, which is between 0.75 and 3.25 MPa and so, is larger than that in solid stainless steel. Figure 6-10 c displays the stress distribution in the implant containing hollow spheres with 1 mm radius, where it can be seen that the range of stress is between 8.01 and 19 MPa. In addition, Figure 6-10 b shows the stress distribution when the implant and bone are assembled and how the stress is transferred. Figure 6-10 b also confirms that the stress close to the hollow spheres is greater; however, more stress is transferred onto the bone in comparison to the solid structure. It can also be observed that where hollow spheres do not exist, the stress is lower, but, the stress in implant is still larger compared to that in bone.

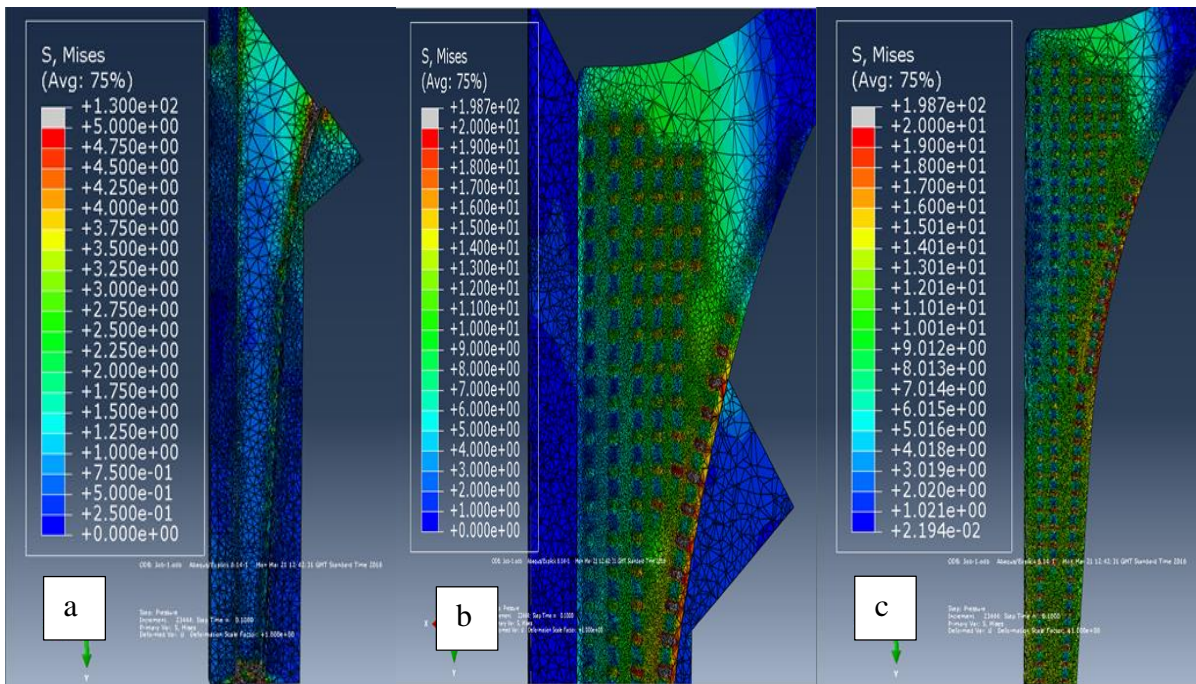


Figure 6-10 Von Mises stress in implant containing spheres with 1mm radius: a) bone; b) bone and implant; c) implant

Figure 6-11 demonstrates the von Mises stress of a stainless steel implant containing unlimited hollow spheres with 1.5 mm radius in three different situations. The stress distribution within bone is between 0.75 and 4 MPa, as demonstrated in Figure 6-11 a, which is larger than in the solid structure case. Figure 6-11 c displays the stress distribution in an implant containing hollow spheres with 1.5 mm, being created unlimitedly, i.e. not based on equation 16. The range is between 8.04 and 18.01 MPa, which is smaller in comparison to the solid stainless steel implant. Moreover, Figure 6-11 b displays the stress distribution when assembled and how the stress is transferred. Figure 6-11 b also confirms that the stress close to the hollow spheres is greater; however, more stress is transferred onto the bone in comparison to the solid structure. It can also be observed that where hollow spheres do not exist, the stress is lower, but the stress in the implant is still larger compared to the stress in bone.

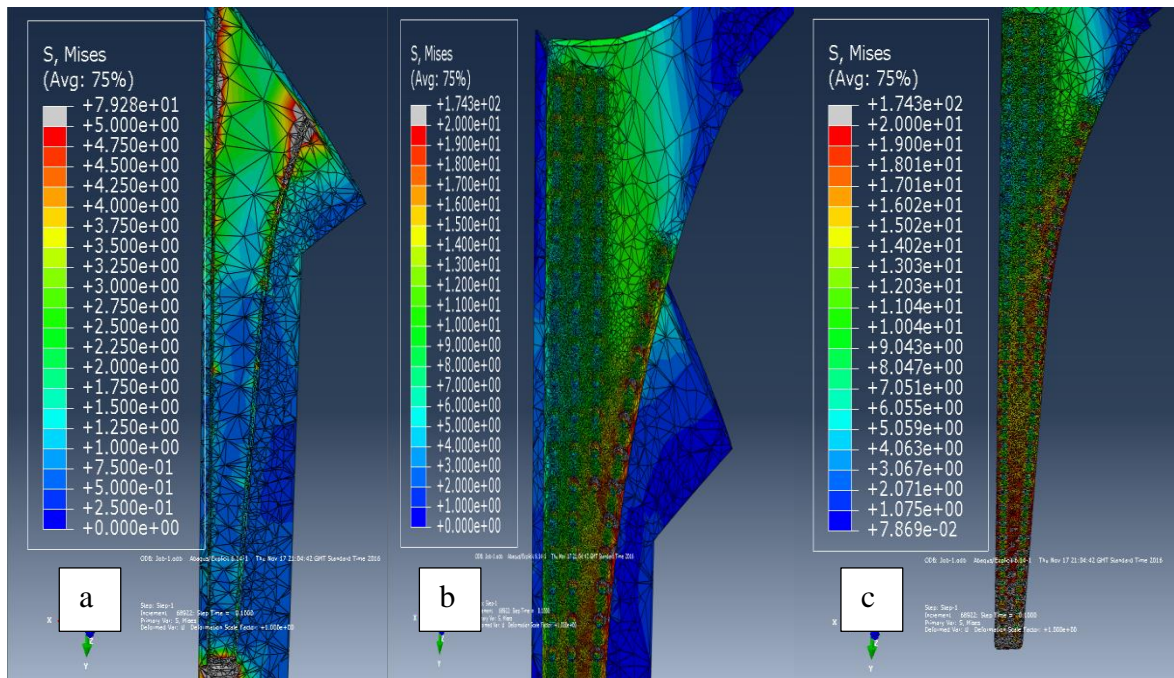


Figure 6-11 Von Mises stress in an implant containing unlimited hollow spheres with 1.5mm radius: a) bone; b) bone and implant; c) implant

Figure 6-12 shows the von Mises stress for a stainless steel implant that has limited spheres with 1.5 mm radius. The hollow spheres have been created based on equation 16 in this sample, with only 10 % of the total volume of the implant having been extracted. Figure 6-12 a shows the stress distribution in bone, which ranges from 2.5 to 4 MPa and this is larger than for the solid stainless steel sample. Figure 6-12 c displays the von Mises stress in the actual implant, which is from 8.06 to 17.01 MPa and this is smaller than for the solid stainless steel structure. Figure 6-12 b shows how the stress is transferred when they are both assembled. Figure 6-12 b also confirms that the stress close to the hollow spheres is greater; however, more stress is transferred onto the bone in comparison to the solid structure. It can also be observed that where hollow spheres do not exist, the stress is lower, but, the stress in the implant is still larger compared to that in bone.

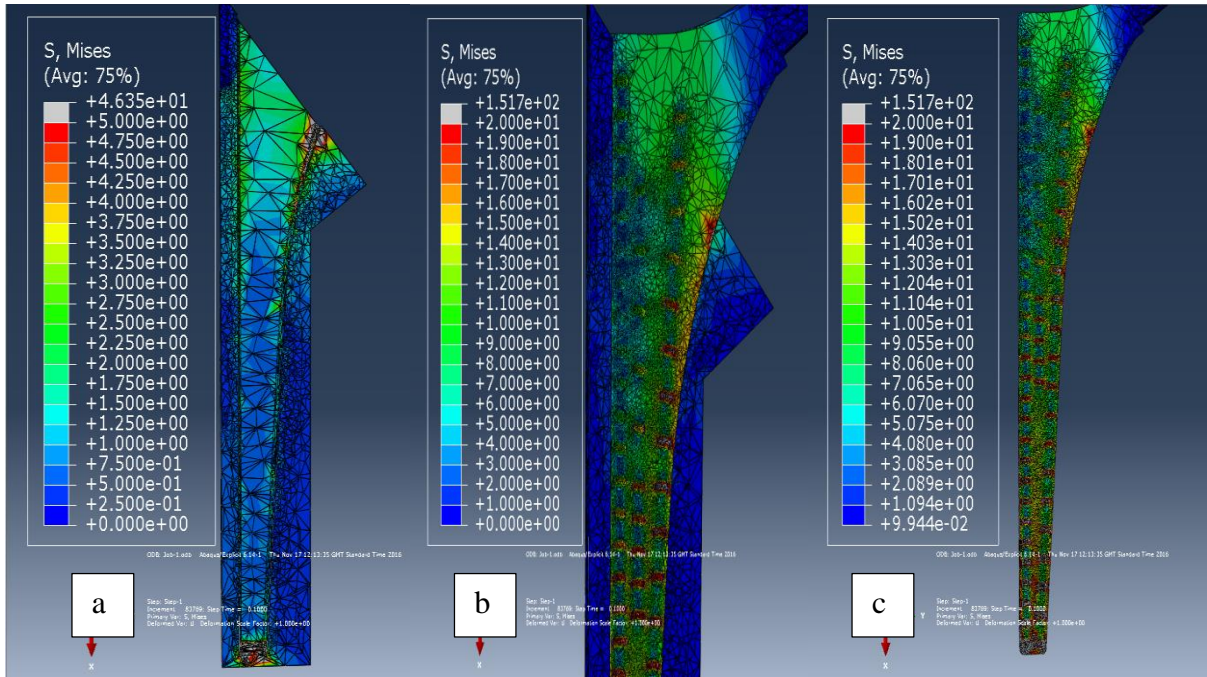


Figure 6-12 Von Mises stress in an implant containing limited spheres with 1.5mm radius: a) bone; b) bone and implant; c) implant

Figure 6-13 displays the von Mises stress for a stainless steel implant that holds limited hollow spheres with 2 mm radius in three different states. The hollow spheres were added based on equation 16 and as their size increases, the number of them decrease, accordingly. Figure 6-13 a displays stress distribution within the bone and this ranges from 1.25 to 3.75 MPa, which is slightly higher than for the solid structure. Figure 6-13c demonstrates the stress distribution in the implant and it can be observed that it is in the range of 9.03-17.01 MPa, which is smaller than for solid stainless steel. Figure 6-12 b displays the stress in assembled form. It also confirms that the stress close to the hollow spheres is greater; however, more is transferred onto the bone in comparison to the solid structure. It can also be observed that where hollow spheres do not exist, the stress is lower, but the stress in implant is still larger compared to that in bone.

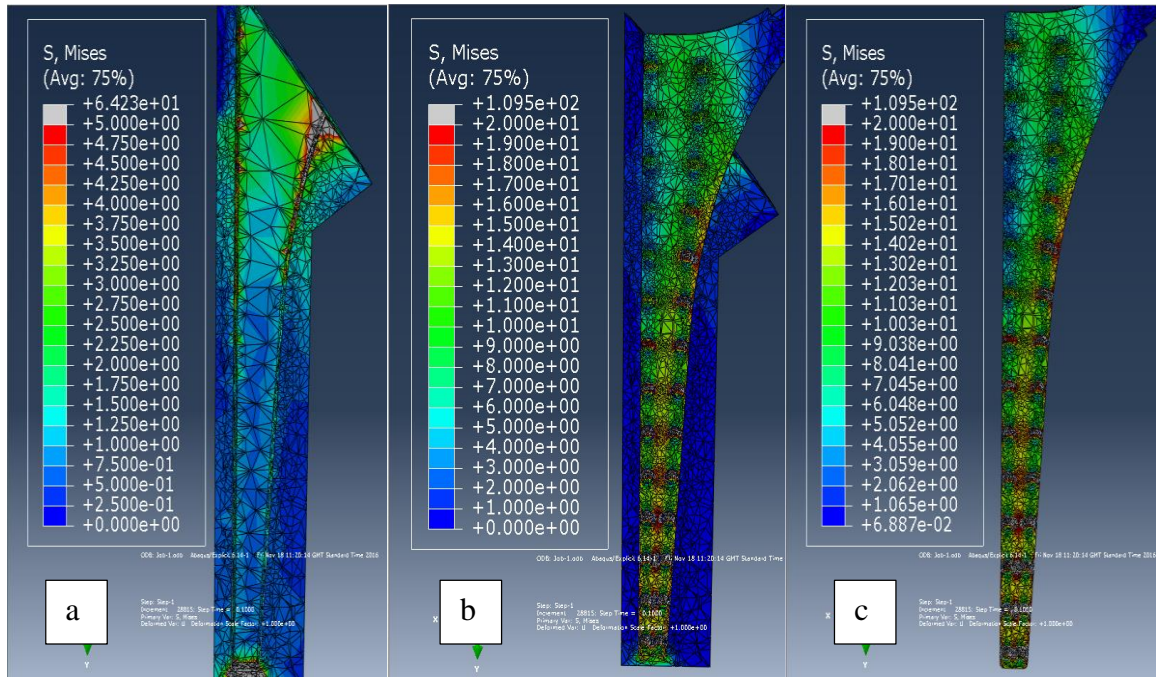


Figure 6-13 Von Mises stress in an implant containing limited spheres with 2mm radius: a) bone; b) bone and implant; c) implant

Figure 6-14 demonstrates the von Mises stress for a stainless steel implant that has unlimited hollow spheres with 2 mm radius in three various situations. The stress distribution within bone is between 1.75 and 4 MPa as shown in Figure 6-14 a, which is larger than for the solid structure case. Figure 6-14 c displays the stress distribution in an implant containing hollow spheres with 1.5 mm radius, being created unlimitedly, i.e. not based on equation 16. The stress distribution range is between 8.04 and 18.01 MPa, which is smaller than that for the solid stainless steel implant. Figure 6-14 b displays the stress distribution when assembled and how the stress is transferred. It also confirms that the stress close to the hollow spheres is greater; however, more stress is transferred onto the bone than with the solid structure. It can also be observed that where hollow spheres do not exist, the stress is lower, but the stress in the implant is still larger compared to that in bone.

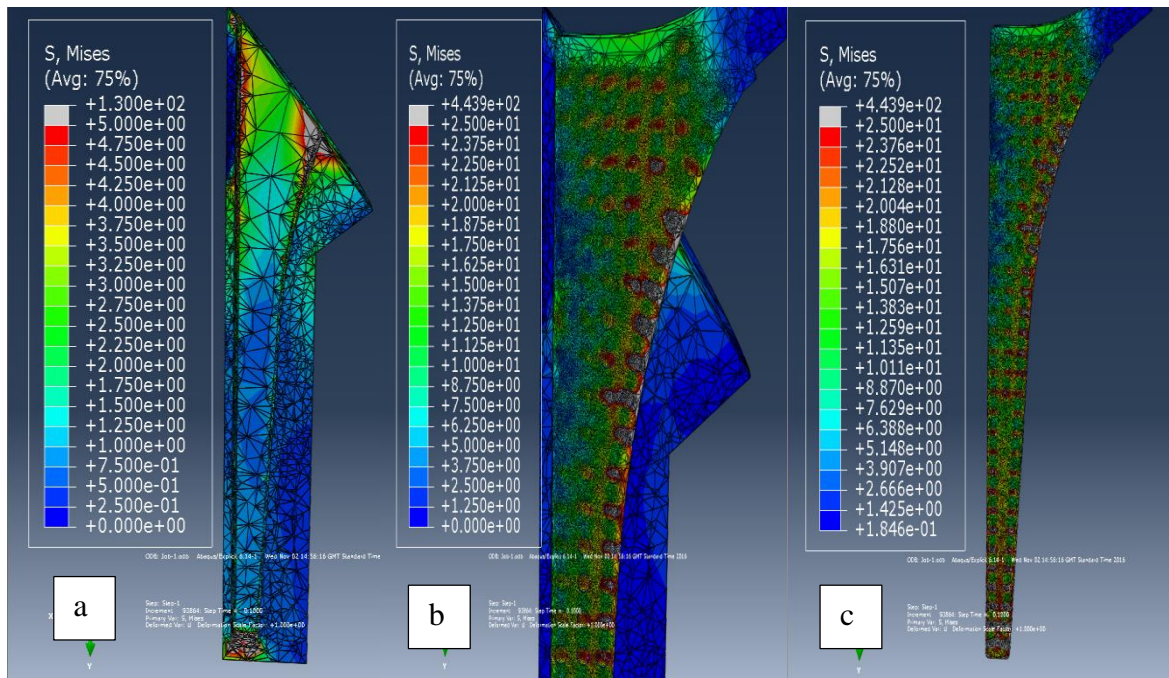


Figure 6-14 Von Mises stress in an implant containing unlimited spheres with 2mm radius: a) bone; b) bone and implant; c) implant

Figure 6-8 to Figure 6-14 display the stress distribution in bone and implants with different materials and structures. That in implants containing hollow spheres, is lower than for solid stainless steel, but it is still higher than with a titanium implant. The stress distribution in bone for the samples containing hollow spheres is greater than for solid stainless steel; however, it is still lower than the titanium sample. The highest stress in bone occurs with the implant that contains hollow spheres of 2 mm radius and this is similar to that for the titanium implant. There are two separate designs for the implants that contain hollow spheres of 1.5 and 2 mm radius. That is, in one case the spheres are added based on the total volume, i.e. they are limited, whilst in the other they are added unlimitedly. The implants with limited hollow spheres have a higher stress distribution in bone when compared to the unlimited hollow spheres implants.

Table 6-3 displays the results of the calculations for the implants. These outcomes are entirely based on the total volume of the spheres. The implants containing spheres with 1 mm, 1.5 mm and 2 mm radius, which are limited, have the same Young's modulus and strength. This is less than for solid stainless steel, but higher than for titanium.

Furthermore, the Young's modulus and stiffness of the implant containing unlimited spheres of 2 mm radius, is lower than that with the unlimited 1.5 mm ones due to its higher extracted volume. The Young's modulus for the unlimited samples is less than for solid stainless steel,

but higher than for titanium. However, the strength of the unlimited samples is less than for both solid stainless steel and titanium.

Table 6-3 Results of calculations for the implants

<i>samples</i>	<i>Young modulus (GPa)</i>	<i>Strength (MPa)</i>	<i>f</i>
<i>R1</i>	182	910	0.09
<i>R1.5 limited</i>	182	910	0.09
<i>R1.5 unlimited</i>	160	800	0.2
<i>R2 limited</i>	180	900	0.1
<i>R2 unlimited</i>	140	700	0.3
<i>Solid Stainless Steel</i>	200	1000	1
<i>Solid Titanium</i>	114	900	N/A

6.4 Conclusion

To summarise, the implant samples with uniformly distributed spheres reduce the Young's modulus of stainless steel. Moreover, these spheres also have a direct effect on reducing the stress shielding by transferring more stress onto the supporting bone than the solid models. Moreover, the hollow sphered implant improves the stress at the implant-bone interface. FEA results showed as the size of hollow spheres enlarges, the amount of stress transferred onto the bone also increases. The implant containing hollow spheres with the size of 2 mm was as sufficient as titanium in terms of transferring stress to the bone. The stress in hollow sphered implant with the size of 2 mm is 4 MPa and in solid stainless steel implant is 3 MPa and in solid titanium is 4 MPa.

7 Discussion and Conclusion

In this chapter, a summary of all of the previous chapters is provided. A final conclusion is also made and future possible studies that could be carried out are proposed.

7.1 Discussion

In chapter 4, hollow spheres close to the surface were designed with consideration of different specifications in order to reduce stress shielding in bone. A reduction in the Young's modulus was observed when hollow spheres of air were added to the solid mass. Reduction of the modulus leads to higher stress being transferred onto the bone in comparison to the solid model. Theoretically, according to the rule of mixtures, the volume of hollow spheres has a relationship with the Young's modulus: the greater the number of hollow spheres created, the smaller that of the implant. As the extracted volume is similar in all cases, the Young's modulus will reduce to a similar magnitude as well regardless of sphere size and distance from each other and wall surface. Figure 7-1 displays finite element analysis for hollow spheres close to the surface and the solid structure. At each node, the stress is compared and as is shown, the stress in bone for the solid structure is less than for the hollow sphered structure. This provides evidence that a hollow structure can lead to less stress shielding.

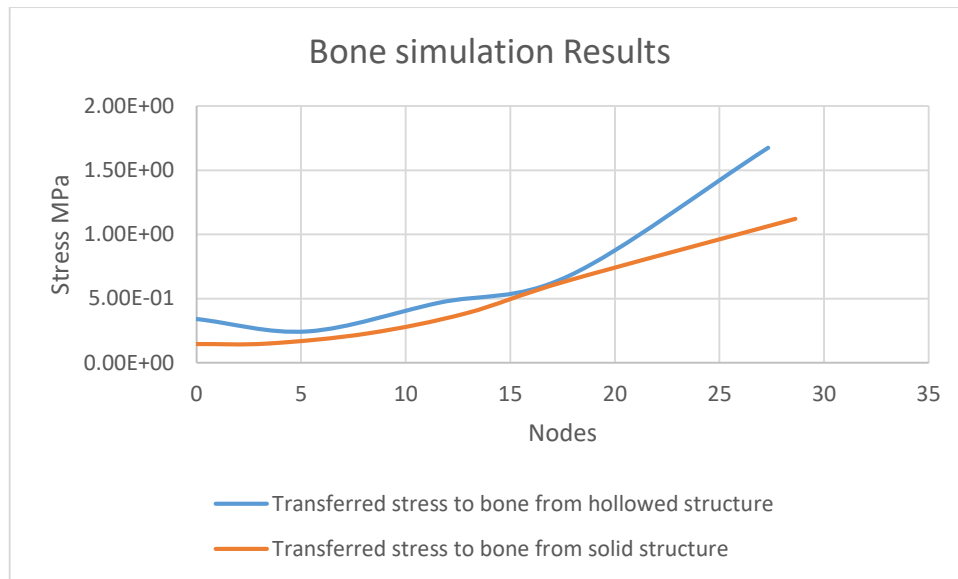


Figure 7-1 Transferred stress to bone from two specimens

Table 7-1 displays Young’s modulus for different samples obtained from computational, experimental and rule of mixtures results. These results were obtained from chapter 5, where hollow spheres were distributed evenly within the objects. There is a relationship between the extracted volume and the Young’s modulus of the sample; the greater the volume of hollow spheres, the smaller that of the implant will be. As has been mentioned before, regardless of the sphere configuration, the Young’s modulus will reduce based on how much volume is extracted. However, there is an optimum number and size for spheres, as explained in chapter 4 too, thereby obtaining the most effective outcome. The Young’s modulus calculated for solid structures using a computational method and the rule of mixtures is similar. Moreover, the computational results for hollow sphered samples are lower in comparison to the calculation of their modulus due to the effect of the sphere size and their position. Whilst regarding the rule of mixtures, the extracted volume is always similar, which results in approximately the same outcomes. However, a reduction in the Young’s modulus is observed in cylinders containing spheres when compared to the solid structure. The computational and rule of mixtures results also show that increasing the size of spheres will cause more reduction in the Young’s modulus.

For the experimental results shown in Table 7-1, the compression modulus was measured and that for hollow structure cylinders decreased. However, the modulus for new design 2 increases when compared to hollow sphered structures and remain approximately similar to

the solid structure. The modulus for new design 1 decreases compared to the solid structure, which could be due to uneven extracted volume.

Table 7-1 Comparison of the modulus in different samples for computational, the rule of mixtures and experimental results

Samples	<i>E (Rule of mixtures)</i> <i>GPa</i>	<i>E (FEA) GPa</i>	<i>E_c (Experiment) GPa</i>
<i>Solid stainless steel</i>	200	200	45.03
<i>R1</i>	181.28	169	41.05
<i>R1/2</i>	181.28	168	43.52
<i>R1.5</i>	178.94	164	40.24
<i>R1.5/2</i>	178.94	164	41.68
<i>R2</i>	181.28	164	38.98
<i>R2/2</i>	181.28	164	39.40
<i>R3</i>	178.94	155	39.91
<i>R3.5</i>	174.92	151	37.93
<i>R4</i>	175.04	148	35.15
<i>New design/1</i>	177	179	42.99
<i>New design/2</i>	180	203	45.68

Table 7-2 demonstrates the percentage reduction in the compression modulus in comparison to the solid model. The reduction observed in the rule of mixtures results is approximately 10% in all of the hollow spheres samples due to the constant volume extraction. However, the reduction of this modulus for the FEA results is much greater, being 15-26% for hollow spheres and about 10% for new designs 1 and 2. The decrease of it for the experimental values is much smaller than with the rule of mixtures and FEA results, which range from 1.5% - 21% for the structures with hollow spheres, whilst these values increase for new designs 1 and 2. In sum, the experimental results confirm a drop in compression modulus for hollow sphered cylinders, but not in the new design samples. Moreover, as the size of the spheres increases, the modulus reduction will increase in comparison to the samples with smaller spheres. With the last two cylinders (new design 1 and 2) that contain hollow cylinders within their structure, one being open ended and the other closed, were assumed to be composites in the calculation and FEA analysis. However, experimental outcome for the new design 2 demonstrates otherwise, whereby it mimics solid stainless steel. This is due to it

not having a hollow structure within the volume and thus, could not be counted as a composite material.

Table 7-2 Percentage reduction in Young's modulus compared to the solid model

Samples	<i>E (calculation)</i>	<i>E (FEA)</i>	<i>E_c (Experiment)</i>
<i>R1</i>	9.35%	15.92%	8.83%
<i>R1/2</i>	9.35%	16.41%	3.35%
<i>R1.5</i>	10.52%	18.4%	10.62%
<i>R1.5/2</i>	10.52%	18.4%	7.43%
<i>R2</i>	9.35%	18.4%	13.42%
<i>R2/2</i>	9.35%	18.4%	12.49%
<i>R3</i>	10.52%	22.88%	11.36%
<i>R3.5</i>	12.5%	24.87%	15.76%
<i>R4</i>	12.47%	26.36%	21.93%
<i>New design/1</i>	11.5%	10.94%	4.51%
<i>New design/2</i>	10%	-1.5%	-1.45%

Figure 7-2 displays the stress distribution in implants for titanium, solid stainless steel and hollow spheres with 1 mm radius. As is observed, the stress in the implant containing hollow spheres is lower than that for solid stainless steel, but slightly lower for titanium. Figure 7-3 displays the stress distribution for these three specimens in their surrounding bone. It is demonstrated that the stress in bone increases in the hollow sphered sample (radius of 1 mm) in comparison to the solid one, whilst a reduction is observed when this is compared to the titanium sample. The stress transferred onto the bone for solid stainless steel is between 0.5-1 MPa, for hollow sphered sample is 1.5-3 MPa and for solid titanium is 2-4 MPa. Moreover, these values prove the advantage of hollow sphered structure over solid stainless steel. Figure 7-2 and Figure 7-3 provide evidence of a reduction of stress shielding in hollow sphered stainless steel implants in comparison to the solid structure. However, the titanium sample is still slightly better than the hollow sphered implant. Nevertheless, it should be stressed that stainless steel is much cheaper than titanium, whilst also being more available. Hence, this could be an option for the NHS to cut down the cost of implant production and also be made available for poor people, all over the world, who cannot afford the current expensive implants.

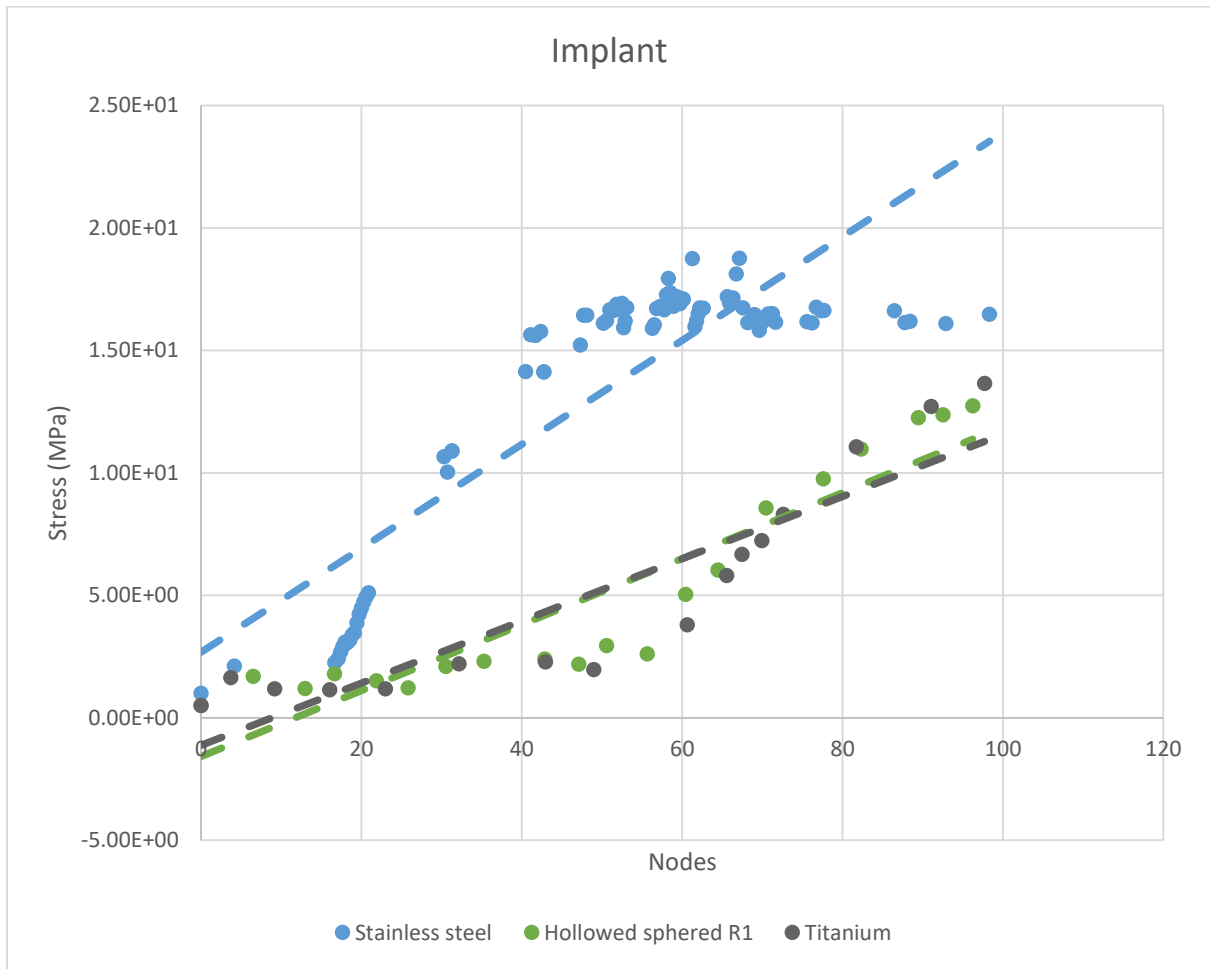


Figure 7-2 Stress distribution in implants for titanium, stainless steel and hollow structure sample

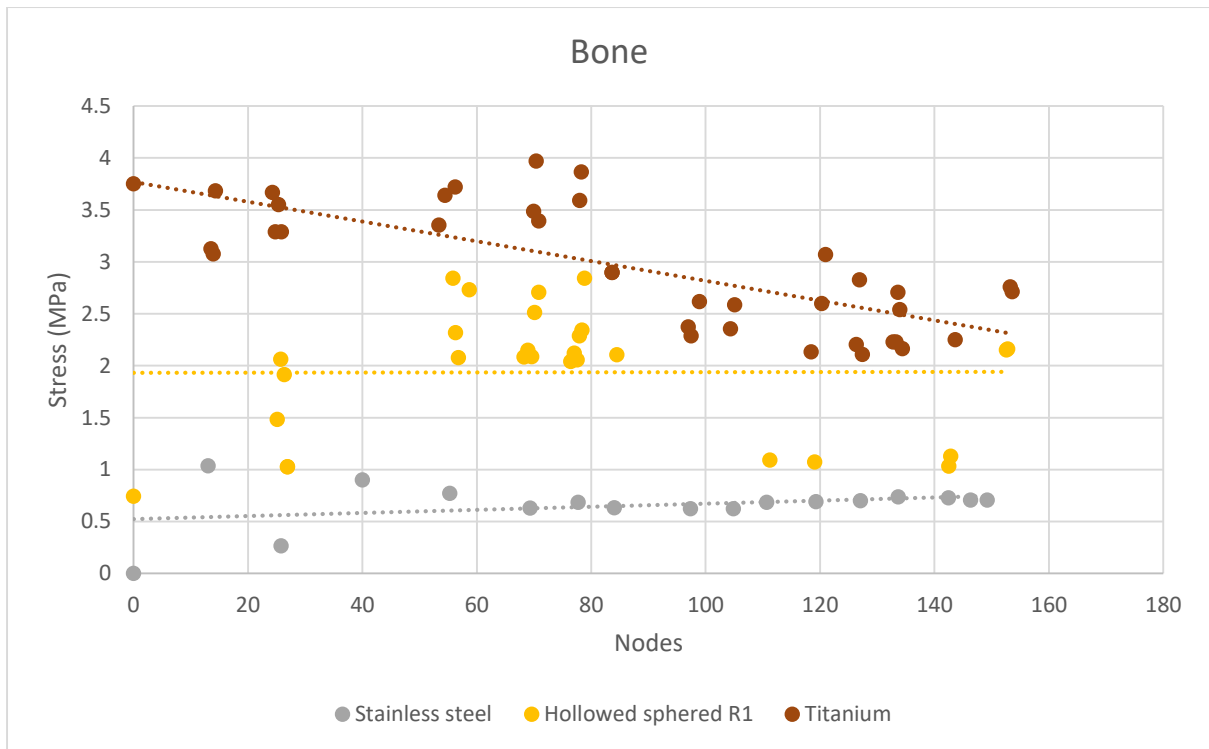


Figure 7-3 Stress distribution in bone for titanium, stainless steel and hollow structure sample

Figure 7-4 displays the stress transferred onto the bone from implants at different nodes. The R1 ($f=0.09$) has the lowest stress-transfer onto the bone among other samples. As can be observed, the bone in the titanium sample is carrying more stress in comparison to the stainless steel samples containing hollow spheres, such as for R1 ($f=0.09$), R1.5 ($f=0.09$) and R2 ($f=0.3$). On the other hand, the implants containing R1.5 ($f=0.2$) and R2 ($f=0.1$) hollow spheres transferred more stress onto the bone compared to the titanium sample, which can be seen in Figure 7-4. The best outcome and the most stress transferred, is for the R2 ($f=0.1$) implant, where the maximum stress approximately reaches 25 MPa. As can be seen, the samples containing larger spheres transfer more stress than those with smaller spheres, which is due to the lower stress concentration that the former have. Moreover, when the size of the spheres is larger, more volume can be extracted. It was also mentioned in subsection 6.2.1.1 that f should be between 0.1 and 0.2, whilst the stress distribution is lower for R2 ($f=0.3$) than for R2 ($f=0.1$). Having a hollow sphered structure helps to reduce the Young's modulus, which leads to an increase in displacement and hence, results in more stress transfer.

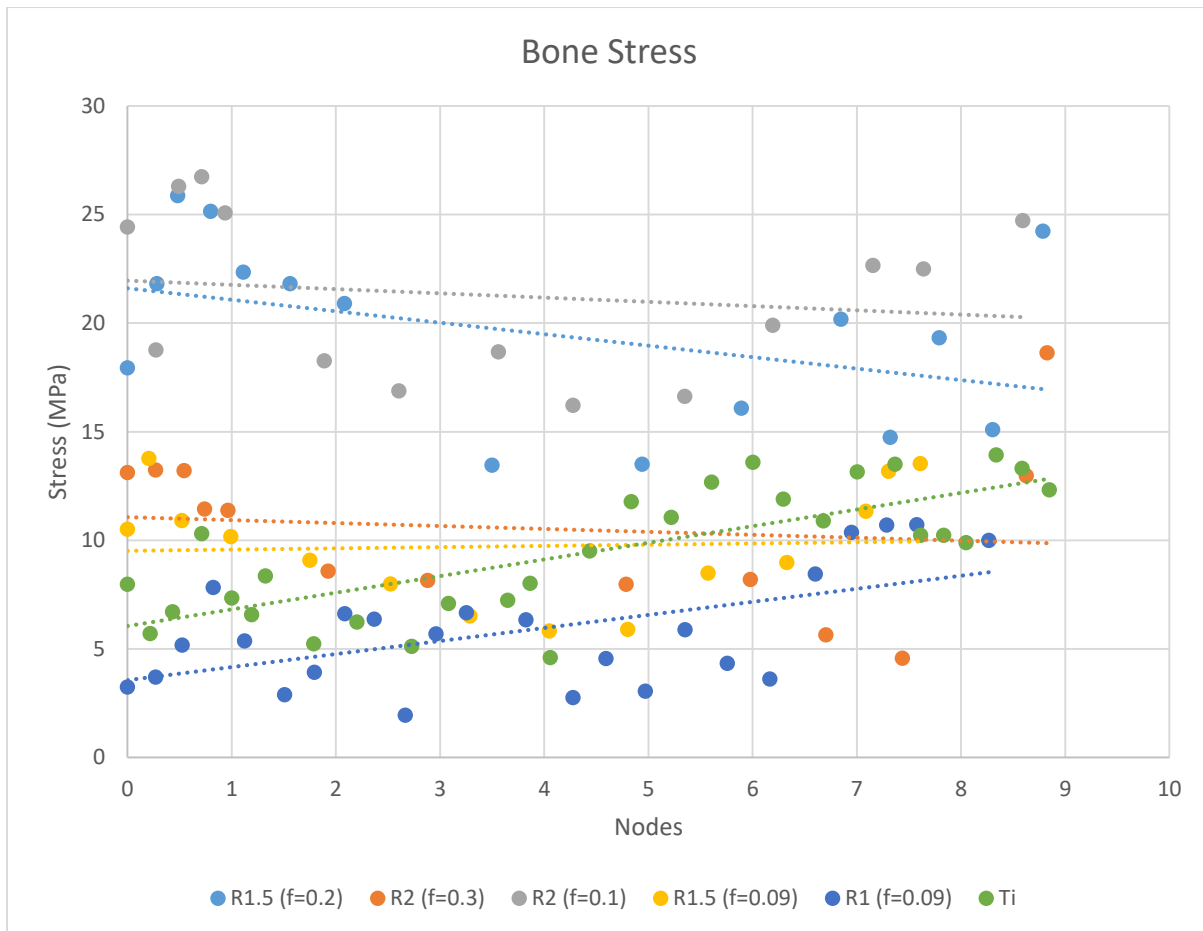


Figure 7-4 Stress distribution in bone for titanium and stainless steel implants containing different hollow sphere sizes

7.2 Final Conclusion

For this study, finite element stress analysis of the femoral stem in a hip joint prostheses has been carried out by considering the design of hollow sphere structures. The design geometric parameters were the size of spheres, number of spheres as well as their distance from each other and the surface. It was found that the new structure introduced in this study can decrease the Young's modulus, thereby leading to stress shielding reduction. According to these designs, an optimum zone was identified for an optimal outcome, which can reduce the maximum stresses significantly and enhance the mechanical properties of the femoral stem. Moreover, it was also found that these can only be sintered and printed for production.

- It was found that by accommodating one tenth hollow spheres of the total volume within traditional solid stems, stress shielding can be reduced in the femur.
- This study outcomes have demonstrated that the mechanical stiffness of sphered implants is lower in comparison to solid implants, thus leading to the claim that it will be potentially more beneficial in terms of reducing stress shielding and bone loss.

- A hollow sphered structure reduces the Young's modulus of the model, thus resulting in stress shielding reduction. This reduction is proportional to the volume of the pores, for instance, if one tenth of the total volume is extracted; the Young's modulus is also reduced by 10%.
- A hollow sphered stainless steel implant is an option for replacing an expensive and limited titanium implant, as it correlates with titanium's mechanical properties.
- Hollow sphered samples close to the surface demonstrated 3.5 Mpa stress-transfer into the surrounding bone. Whereas, the stress in solid titanium is 5.3 MPa, and in solid stainless steel is 1 Mpa.
- The compression modulus for solid titanium is 30 GPa and for solid stainless steel is 45 GPa. However, it is 35 GPa for sphered samples in uniformly distributed hollow sphered samples. In addition, the Young's modulus for solid titanium is 114 GPa, Solid stainless steel is 200 GPa and hollow sphered sample is 148 GPa.
- The average stress transferred to the cortical bone is: 1.5-3 MPa for titanium; 1-2 MPa for solid Stainless steel; 1.2-2.5 MPa for a stainless steel implant containing hollow spheres.

7.3 Recommendations for future works

- Use the structure in different applications, such as aerospace and the automotive industry.
- Extend the simulations carried out in this study to include anisotropic materials.
- This structure can be applied to titanium implants as well.
- Conduct the experimental analysis to validate the finite element modelling results for the actual implants.
- Improvement in 3D modelling production is required as there is a little powder debris remaining inside each sphere.
- Study the micromotions of hollow sphered implants in depth.
- Study the effect of sphered geometry on the cemented type of hip prostheses.

Bibliography

Feldt, C. E., 2011. *STRESS SHIELDING MINIMIZED IN FEMORAL HIP IMPLANTS: A FINITE ELEMENT MODEL OPTIMIZED BY VIRTUAL COMPATIBILITY*, Orlando, Florida: University of Central Florida.

3D printing from scratch, 2017. *3Dprintingfromscratch*. [Online] Available at: <http://3dprintingfromscratch.com/common/types-of-3d-printers-or-3d-printing-technologies-overview/> [Accessed 26 April 2017].

3trpd, 2015. *Metal Additive Manufacturing (AM) using Direct Metal Laser Sintering (DMLS)*. [Online] Available at: <https://www.3trpd.co.uk/dmls.htm> [Accessed 27 April 2017].

ABAQUS/CAE USER'S GUIDE, 2014. *SIMULIA*. [Online] Available at: http://abaqus.software.polimi.it/v6.14/pdf_books/CAE.pdf [Accessed 01 03 2017].

Alvarado, J., Maldonado, R., Marxuach, J. & Otero, R., 2003. *BIOMECHANICS OF HIP AND KNEE PROSTHESES*, Puerto Rico Mayaguez: Applications of Engineering Mechanics in Medicine, GED – University of Puerto Rico Mayaguez .

Anguiano-Sanchez, J. et al., 2016. Influence of PEEK Coating on Hip Implant Stress Shielding: A Finite Element Analysis. *Comput Math Methods Med*.

Anon., 2014. *BBC Biology*. [Online] Available at: http://www.bbc.co.uk/bitesize/standard/biology/the_body_in_action/movement/revision/3/ [Accessed 21 03 2017].

Anthony, P. P., Gie, G. A., Howie, C. R. & Ling, R. S., 1990. Localised endosteal bone lysis in relation to the femoral components of cemented total hip replacements. *Journal of Bone and Joint Surgery*, 72–B(6), p. 971–979.

Ashby, M., Gibson, L., Wegst, U. & Olive, R., 1995. The mechanical-properties of natural materials. *Proc R Soc London Ser A – Math Phys Sci*, Volume 450, pp. 123-140.

Aspenberg, P. & Herbertsson, P., 1996. Periprosthetic bone resorption. Particles versus movement. *J Bone Joint Surg Br*, 78(4), pp. 641-646.

ASTM E9, 2000. *Standard Test Methods of Compression Testing of Metallic Materials at Room Temperature*, West Conshohocken: American Society for Testing and Materials.

Auvray, C., Lafrance, N. & Bartier, D., 2016. Elastic modulus of claystone evaluated by nano-/micro-indentation tests and meso-compression tests. *Journal of Rock Mechanics and Geotechnical Engineering*, Volume 9, pp. 84-91.

Bagge, M., 2000. A model of bone adaptation as an optimization process. *J. Biomechanics*, 33(11), pp. 1349-1357.

Balla, V. K., Bodhak, S., Bose, S. & Bandyopadhyay, A., 2010. Porous tantalum structures for bone implants: Fabrication, mechanical and in vitro biological properties. *Acta Biomaterialia*, pp. 3349-3359.

Barfeie, A., Wilson, J. & Rees, J., 2015. Implant surface characteristics and their effect on osseointegration. *Br Dent J*, 218(5), pp. 1-9.

Barrack, R. L., 2003. Dislocation after total hip arthroplasty: implant design and orientation. *J Am Acad Orthop Surg*, 11(2), pp. 89-99.

Bennett, D. & Goswami, T., 2008. Finite element analysis of hip stem designs. *Materials & Design*, 29(1), pp. 45-60.

Bergmann, G. et al., 2001. Hip contact forces and gait patterns from routine activities. *Journal of Biomechanics*, Volume 34, pp. 859-871.

Bernakiewicz, M. & Viceconti, M., 2001. The role of parameter identification in finite element contact analyses with reference to orthopaedic biomechanics applications. *Journal of Biomechanics*, Volume 35, pp. 61-67.

Biegler, F. B. et al., 1995. Effect of porous coating and loading conditions on total hip femoral stem stability. *J Arthroplasty*, 10(6), pp. 839-847.

Biewener, A. A., 1992. *Structures and Systems, a practical approach*. New York, USA: Oxford University Press.

- Bitsakos, C., Kerner, J., Fisher, I. & Amis, A. A., 2005. The effect of muscle loading on the simulation of bone remodelling in the proximal femur. *Journal of Biomechanics*, 38(1), p. 133–139.
- Black, J. & Hastings, G. W., 1998. *Handbook of Biomaterials Properties*. 1st ed. London, UK: Chapman and Hall.
- Bobyn, J. et al., 1990. The effect of stem stiffness on femoral bone resorption after canine porous-coated total hip arthroplasty. *Clin Orthopaedics*, Volume 261, pp. 196-213.
- Boyle, C. & Yong, K., 2011. Comparison of different hip prosthesis shapes considering micro-level bone remodeling and stress-shielding criteria using three dimensional design space topology optimization. *Journal of Biomechanics*, 44(9), p. 1722–1728.
- Branemark, P. I., 1983. Osseointegration and its experimental background. *The Journal of Prosthetic Dentistry*, 50(3), pp. 399-410.
- Brekelmans, A. W., Poort, W. H. & Slooff, J. T., 1972. A new method to analyse the mechanical behaviour of skeletal parts. *Acta Orthopaedic Scandinavian*, 43(5), pp. 301-317.
- Brown, J. A., Vendra, L. J. & Rabiei, A., 2010. Bending Properties of Al-Steel and Steel-Steel Composite Metal Foams. *Metallurgical and Materials Transactions A*, 41(11), p. 2784–2793.
- Callaghan, J. J. et al., 2000. Charnley total hip arthroplasty with cement. Minimum twenty-five-year follow-up. *Journal of Bone and Joint Surgery Am*, 82(4), pp. 487-497.
- Cambridge, U. O., 2015. *Derivation of the rule of mixtures and inverse rule of mixtures*. [Online]
Available at: https://www.doitpoms.ac.uk/tlplib/bones/derivation_mixture_rules.php
[Accessed 26 06 2017].
- Cansizoglu, O., 2008. *Mesh Structures with Tailored Properties and Applications in Hip Stems*, s.l.: North Carolina State University.
- Chait, R., 1971. *FACTORS INFLUENCING THE STRENGTH DIFFERENTIAL OF HIGH STRENGTH STEELS*, Watertown, Massachusetts: MATERIALS TESTING DIVISION.

- Chang , P. et al., 2001. Design and analysis of robust total joint replacements: finite element model experiments with environmental variables. *Journal of Biomechanical Engineering*, Volume 123, pp. 239-246.
- Chen, W.-P. et al., 2004. Comparison of Stress Shielding among Different Cement Fixation Modes of Femoral Stem in Total Hip Arthroplasty– A Three-Dimensional Finite Element Analysis. *Journal of Medical and Biological Engineering*, pp. 183-187 .
- Colic, K. et al., 2016. Finite element modeling of hip implant static loading. *Procedia Engineering*, Volume 149, pp. 257-262.
- Cristofolini, L., Viceconti, M., Toni, A. & Giunti, A., 1995. Influence of thigh muscles on the axial strains in a proximal femur during early stance in gait. *Journal of Biomechanics*, 28(5), pp. 617-624.
- Damm, N. B., Morlock, M. M. & Bishop, N. E., 2015. Friction coefficient and effective interference at the implant-bone interface. *Journal of Biomechanics*, pp. 3517-3521.
- Dattani, R., 2007. Femoral osteolysis following total hip replacement. *Postgrad Med J*, 83(979), p. 312–316.
- Decking, R., Puhl, W., Simon, U. & Claes, L. E., 2006. Changes in strain distribution of loaded proximal femora caused by different types of cementless femoral stems. *Clinical Biomechanics*, 21(5), p. 495–501.
- Diegel, P. D., Daniels, A. U. & Dunn, H. K., 1989. Initial effect of collarless stem stiffness on femoral bone strain. *J. Arthroplasty*, 4(2), p. 173–178.
- Dudaa, G. N. et al., 1998. Influence of Muscle Forces on Femoral Strain Distribution. *Journal of Biomechanics* , 31(9), p. 841—846.
- Duda, G. N., Schneider, E. & Chao, E. Y., 1997. Internal forces and moments in the femur during walking. *Journal of biomechanics*, 30(9), pp. 933-941.
- Easley, S. K. et al., 2007. Finite element-based probabilistic analysis tool for orthopaedic applications. *Computer methods and programs in Biomedicine*, 85(1), pp. 32-40.
- Eldridge, D. et al., 2014. Outcome of Porous Tantalum Acetabular Components for Paprosky Type 3 and 4 Acetabular Defects. *The Journal of Arthroplasty*, 29(6), p. 1318–1322.

- El-warrak, A. O. et al., 2004. An experimental animal model of aseptic loosening of hip prostheses in sheep to study early biochemical changes at the interface membrane. *BMC Musculoskelet Disord*, Volume 5, pp. 1-13.
- Engh, A. C. et al., 2002. Extensively porous-coated femoral revision for severe femoral bone loss * * * *: Minimum 10-year follow-up. *The Journal of Arthroplasty*, 17(8), pp. 955-960.
- Engh, C. A. & Bobyn, J. D., 1988. The influence of stem size and extent of porous coating on femoral bone resorption after primary cementless hip arthroplasty. *Clinical orthopaedics and related research*, Volume 231, pp. 7-28.
- Engh, C., Bobyn, J. & Glassman, A., 1987. Porous-coated hip replacement. The factors governing bone ingrowth, stress shielding, and clinical results. *J Bone Joint Surg Br*, Volume 69, pp. 45-55.
- English, R., Ashkanfar, A. & Rothwell, G., 2015. A computational approach to fretting wear prediction at the head–stem taper junction of total hip replacements. *Wear*, Volume 338-339, p. 210–220.
- Fagan, M. J., 1992. *Finite Element Analysis, Theory and Practice*. illustrated, reprint ed. Harlow: Longman Scientific & Technical.
- Fan, X. G. et al., 2017. Friction assessment in uniaxial compression test: A new evaluation method based on local bulge profile. *Journal of Materials Processing Technology*, Volume 243, pp. 282-290.
- Fernandes, P. R., Folgado, J., Jacobs, C. & Pellegrini, V., 2002. A contact model with ingrowth control for bone remodelling around cementless stems. *Journal of Biomechanics*, 35(2), p. 167–176.
- Fernandes, R. P., Folgado, J., Jacobs, C. & Pellegrini, V., 2002. A contact model with ingrowth control for bone remodeling around cementless stems. *Journal of Biomechanics*, Volume 35, pp. 167-176.
- Fratzl, P. & Weinkamer, R., 2007. Nature’s hierarchical materials. *Progress in Materials Science*, 52(8), p. 1263–1334.
- Friedl, O. et al., 2008. Experimental Investigation of Mechanical Properties of Metallic Hollow Sphere Structures. *Metallurgical and Materials Transactions B*, 39(1), p. 135–146.

- Geetha, M., Singh, A. K., Asokamani, R. & Gogia, A. K., 2009. Ti based biomaterials, the ultimate choice for orthopaedic implants – A review. *Progress in Materials Science*, 54(3), pp. 397-425.
- Geraldes, D. M. & Phillips, A. T. M., 2014. A comparative study of orthotropic and isotropic bone adaptation in the femur. *Int J Numer Method Biomed Eng*, 30(9), p. 873–889.
- Gillies, R. M. et al., 2002. The influence of design parameters on cortical strain distribution of a cementless titanium femoral stem. *Medical Engineering & Physics*, 24(2), pp. 109-114.
- Glyn-Jones, S., Gill, H. S., McLardy-Smith, P. & Murray, D. W., 2004. Roentgen stereophotogrammetric analysis of the Birmingham hip resurfacing arthroplasty. A two-year study.. *J Bone Joint Surg Br*, 86(2), pp. 172-176.
- Goad, M. E. & Goad, D. L., 2002. Biomedical Devices and Biomaterials. In: W. M. Haschek, M. A. Rousseaux & M. A. Wallig, eds. *Handbook of Toxicologic Pathology*. San Diego: Academic Press Harcourt Science and Technology, pp. 459-477.
- Goldstein, S. A., 1987. The mechanical properties of trabecular bone: dependence on anatomic location and function. *J Biomech*, pp. 1055-1061.
- González, C. D., 2009. *Probabilistic finite element analysis of the uncemented total hip replacement*, Southampton: University of Southampton ePrints Soton.
- Gough, J. & Downes, S., 2001. Osteoblast cell death on methacrylate polymers involves apoptosis. *J Biomed Mater Res*, Volume 57, pp. 497-505.
- Gross, S. & Abel, E. W., 2001. A finite element analysis of hollow stemmed hip prostheses as a means of reducing stress shielding of the femur. *Journal of Biomechanics*, 34(8), pp. 995-1003.
- Hallab, N. J. et al., 2005. Lymphocyte responses in patients with total hip arthroplasty. *J Orthop Res*, 23(2), pp. 384-391.
- Henriques, V. A. R. et al., 2010. Production of Ti–13Nb–13Zr alloy for surgical implants by powder metallurgy. *Journal of Materials Science*, 45(21), p. 5844–5850.
- Howie, J. R., Middleton, R. G. & Costi, K., 1998. Loosening of matt and polished cemented femoral stems. *Journal of bone and joint surgery*, 80–B(4), p. 573–576.

- Huiskes, R., 1990. The various stress patterns of pressfit ingrown and cemented femoral stems. *Clin Orthop*, pp. 261-270.
- Huiskes, R., Verdonschot, N. & Nivbrant, B., 1998. Migration, stem shape, and surface finish in cemented total hip arthroplasty. *Clinical Orthopaedics and Related Research*, 355(10), p. 103–112.
- Huiskes, R., Weinans, H. & van Rietbergen, B., 1992. The relationship between stress shielding and bone resorption around total hip stems and the effects of flexible materials. *Clin Orthop Relat Res*, Volume 274, pp. 124-134.
- Hussein, M. A., Mohammed, A. S. & Al-Aqeeli, N., 2015. Wear Characteristics of Metallic Biomaterials: A Review. *Materials*, 8(5), pp. 2749-2768.
- Jee, W., 2001. Integrated bone tissue physiology: anatomy and physiology. In: S. Cowin, ed. *Bone Mechanics*. Boca Raton: CRC press, pp. 1-34.
- Jeffers, J. et al., 2007. Cement mantle fatigue failure in total hip replacement: experimental and computational testing. *Journal of Biomechanics*, Volume 47, p. 1525–1533.
- Jergesen, H. E. & Karlen, J. W., 2002. Clinical outcome in total hip arthroplasty using a cemented titanium femoral prosthesis. *J. Arthroplasty*, 17(5), p. 592–599.
- Jinno, T., Kirk, S., Morita, S. & Goldberg, V., 2004. Effects of Calcium Ion Implantation on Osseointegration of Surface-Blasted Titanium Alloy Femoral Implants in a Canine Total Hip Arthroplasty Model. *The Journal of Arthroplasty*, 19(1), pp. 102-109.
- Joshi, M. G., Advani, S. G., Miller, F. & Santare, M. H., 2000. Analysis of a femoral hip prosthesis designed to reduce stress shielding. *Journal of Biomechanics*, 33(12), p. 1655–1662.
- Kaplan, R. B., 1994. *Open cell tantalum structures for cancellous bone implants and cell and tissue receptors*. United States of America, Patent No. US 5282861 A.
- Karanjai, M. et al., 2007. Development of titanium based biocomposite by powder metallurgy processing with in situ forming of Ca–P phases. *Materials Science and Engineering: A*, 447(1-2), pp. 19-26.
- Katti, K. S., 2004. Biomaterials in total joint replacement. *Colloids and Surfaces B: Biointerfaces*, 39(3), p. 133–142.

Kelmanovich, D., Parks, M. L., Sinha, R. & Macaulay, W., 2003. Surgical Approaches to Total Hip Arthroplasty. *JOURNAL OF THE SOUTHERN ORTHOPAEDIC ASSOCIATION*, 12(2), pp. 90-94.

Kennon, R. E. et al., 2003. Total hip arthroplasty through a minimally invasive anterior surgical approach. *J Bone Joint Surg Am*, pp. 39-48.

Kernozek, T. W. & Willson, J. D., 2015. *iKNOWLEGDE*. [Online] Available at: <http://clinicalgate.com/gait-2/> [Accessed 21 03 2017].

Khan, A. S., Balzer, J. E., Wilgeroth, J. M. & Proud, W. G., 2014. *Aspect ratio compression effects on metals and polymers*. London, Institute of Shock Physics, Imperial College.

LaPorte, D., Mont, M. & Hungerford, D., 1999. Proximally porouscoated ingrowth prostheses: limits of use. *Orthopedics*, Volume 22, pp. 1161-1162.

Lawrence, K. J., 1980. Anisotropy of Young's modulus of bone. *Nature*, Volume 283, p. 106–107.

Liu, W., Gheni, M. & Yu, L., 2011. Effect of Mesh Size of Finite Element Analysis in Model Analysis for Periodic Symmetric Struts Support. *Key Engineering Materials*, Volume 462-463, pp. 1008-1012.

Long, M. & Rack, H. J., 1997. Titanium alloys in total joint replacement—a materials science perspective. *Biomaterials*, p. 1621—1639.

Lozynsky, A. J., Sedlacek, R. C. & O'Connor, D. O., 1996. *Quantification of bone loss in the proximal femur after cemented total hip replacement using DEXA on autopsy retrieved specimens*, s.l.: Proceedings of American Academy of Orthopaedic Surgeons 1996 Annual Meeting-Scientific Program, Paper No. 532.

Mann, K. A., Bartel, D. L., Wright, T. M. & Burstein, A. H., 1995. Coulomb frictional interfaces in modelling cemented total hip replacements, a more realistic model. *Journal of Biomechanics*, 28(9), pp. 1067-1078.

Matassi, F. et al., 2013. Porous metal for orthopedics implants. *Clin Cases Miner Bone Metab*, p. 111–115.

- Mattheck, C., Vorberg, U. & Kranz, C., 1990. Effects of hollow shaft endoprosthesis on stress distribution in cortical bone. *Biomed Eng*, Volume 35, pp. 316-319.
- Mattheck, C., Vorberg, U. & Kranz, C., 1990. Effects of hollow shaft endoprosthesis on stress distribution in cortical bone. *Biomed Tech*, 35(12), pp. 316-319.
- Meek, R. M. et al., 2008. Late Dislocation after Total Hip Arthroplasty. *Clin Med Res*, 6(1), pp. 17-23.
- Mittra, E., Rubin, C. & Qin, Y., 2005. Interrelationship of trabecular mechanical and microstructural properties in sheep trabecular bone. *Journal of Biomechanics*, Volume 38, pp. 1229-1237.
- Moreau, M. et al., 1998. Free radicals and side products released during methylmethacrylate polymerization are cytotoxic for osteoblastic cells. *J Biomed Mater Res*, Volume 40, pp. 124-31.
- Muriel, J., Sánchez Roa, A., Barona Mercado, W. & Sánchez Sthepa, H., 2009. STEEL AND GRAY IRON FOAM BY POWDER METALLURGICAL SYNTHESIS. *Supl Rev Latinoam Metal Mater*, S1(4), pp. 1435-1440.
- National joint registry, 2016. *NJR Stats Online*. [Online] Available at: <http://www.njrcentre.org.uk/njrcentre/LinkClick.aspx?fileticket=QkZM7sN-HpA%3D&portalid=0> [Accessed 22 August 2017].
- Nelson, C. L., 2002. Cemented femoral revision: technique and outcome. *American Journal of Orthopedics*, Volume 31, pp. 187-189..
- Niespodziana, K., Jurczk, K. & Jurczk, M., 2008. THE SYNTHESIS OF TITANIUM ALLOYS FOR BIOMEDICAL APPLICATIONS. *Rev. Adv. Mater. Sci*, Volume 18, p. 236–240.
- Nigg, B. & Herzog, W., 1999. *Biomechanics of the Musculo-Skeletal System*. Chichester: John Wiley & Sons.
- Niinimäki, T., Junila, J. & Jalovaara, P., 2001. A proximal fixed anatomic femoral stem reduces stress shielding. *International Orthopaedics*, Volume 25, p. 85–88.

NIINOMI, M., 2002. Recent metallic materials for biomedical applications. *Metallurgical and Materials Transactions A*, Volume 33, pp. 477-486.

Niinomi, M., 2008. Metallic biomaterials. *J Artif Organs*, 11(3), pp. 105-110.

Nikolaus, P., Charles, K. & Tong, J., 2007. Fatigue failure in the cement mantle of a simplified acetabular replacement model. *International Journal of Fatigue*, Volume 29, p. 1245–1252.

NJRR, A., 2017. *Australian Orthopaedic Association National Joint Replacement Registry*.

[Online]

Available at: <https://aoanjrr.sahmri.com/hips>

[Accessed 19 07 2017].

Nuno, N. & Amabili, M., 2002. Modelling debonded stem-cement interface for hip implants: effect of residual stresses. *Clinical Biomechanics*, Volume 17, pp. 41-48.

Ohidul Alam, M. & Haseeb, A. M., 2002. Response of Ti–6Al–4V and Ti–24Al–11Nb alloys to dry sliding wear against hardened steel. *Tribology International*, 35(6), pp. 357-362.

Park, J. & Lakes, R. S., 2007. *Biomaterials an Introduction*. 3rd ed. Berlin/Heidelberg, Germany: Springer.

Patel, N. R. & Gohil, P. P., 2012. A Review on Biomaterials: Scope, Applications & Human Anatomy Significance. *International Journal of Emerging Technology and Advanced Engineering*, 2(4), pp. 91-101.

Pearson, O. M. & Lieberman, D. E., 2004. The aging of Wolff's "law": ontogeny and responses to mechanical loading in cortical bone. *Am J Phys Anthropol*, Volume 125, p. 63–99.

Pierce, M. C., Bertocci, G. E., Vogeley, E. & Moreland, M. S., 2004. Evaluating long bone fractures in children: a biomechanical approach with illustrative cases. *Child Abuse & Neglect*, Volume 28, p. 505–524.

Pioletti, P. D. et al., 1999. The cytotoxic effect of titanium particles phagocytosed by osteoblasts. *Journal of Biomedicine and Materials Research*, Volume 46, pp. 399-407.

- Polgár , K. et al., 2003. Strain distribution within the human femur due to physiological and simplified loading: finite element analysis using the muscle standardized femur model. *Institute of mechanical engineers*, 217(3), pp. 173-189.
- Puolakka, T. J. et al., 2001. The Finnish Arthroplasty Register: report of the hip register. *Acta Orthop Scand*, 72(5), pp. 433-441.
- Rahman, A. & Mahamid, M., 2002. *Functionally graded cellular metal alloys for joint implants*. Columbia University, New York, Proceedings of the 15th ASCE Engineering Mechanics Conference.
- Ramos, A. & Simoes, A. J., 2006. Teta hedral versus hexahedral finite elements in numerical modeling of the proximal femur. *Medical Engineering & Physics*, 28(9), pp. 916-924.
- Ramos, A. & Simoes, A. J., 2006. Teta hedral versus hexahedral finite elements in numerical modeling of the proximal femur. *Medical Engineering & Physics*, 28(9), pp. 916-924.
- Ramsden, J. J. et al., 2007. The Design and Manufacture of Biomedical Surfaces. *CIRP Annals - Manufacturing Technology*, 56(2), pp. 687-711.
- Ratner, B. D., Hoffman, A. S., Schoen, F. J. & Lemons, J. E., 1996. *Biomaterials Science: An Introduction to Materials in Medicine*. California, USA: ACADEMIC PRESS.
- Raut, P., 2012. Impact Of Mesh Quality Parameters On Elements Such As Beam, Shell And 3D Solid In Structural Analysis. *International Journal of Engineering Research and Applications*, 2(6), pp. 99-103.
- Registry, N. J., 2017. *NJR Stats Online*. [Online] Available at: <http://www.njrcentre.org.uk/njrcentre/Healthcareproviders/Accessingthedata/StatsOnline/NJRStatsOnline/tabid/179/Default.aspx> [Accessed 19 07 2017].
- Ribeiro, A. L. et al., 2009. Mechanical, physical, and chemical characterization of Ti–35Nb–5Zr and Ti–35Nb–10Zr casting alloys. *J Mater Sci Mater Med*, 20(8), pp. 1629-1636.
- Ridzwan, M. I. Z. et al., 2007. Problem of Stress Shielding and Improvement to the Hip Implant Designs: A Review. *Journal of Medical Sciences*, Volume 7, pp. 460-467.

- Roesler, H., 1987. The history of some fundamental concepts in bone biomechanics. *J Biomech*, Volume 20, p. 1025.
- Ryan, G., Pandit, A. & Apatsidis, D. P., 2006. Fabrication methods of porous metals for use in orthopaedic applications. *Biomaterials*, pp. 2651-2670.
- Sabatini, A. L. & Goswami, T., 2008. Hip implants VII: Finite element analysis and optimization of cross-sections. *Materials & Design*, 29(7), p. 1438–1446.
- Sabatini, A. L. & Goswami, T., 2008. Hip implants VII: Finite element analysis and optimization of cross-sections. *Materials & Design*, 29(7), pp. 1438-1446.
- Sanami, M., 2015. *AUXETIC MATERIALS FOR BIOMEDICAL APPLICATIONS*, Bolton: University of Bolton.
- Sanami, M., Ravirala, N., Alderson, K. & Alderson, A., 2014. Auxetic materials for sports applications. *ScienceDirect*, Volume 72, p. 453 – 458.
- Sancez-Sotelo, J., Berry, D. & Harmsen, S., 2002. Long-term results of use of a collared matte-finished femoral component fixed with secondgeneration cementing techniques, a fifteen-year-median follow-up study. *J Bone Jt Surg*, Volume 84, pp. 1636-1641.
- Sarmiento, A. & Gruen, T. A., 1985. Radiographic analysis of a low-modulus titanium-alloy femoral total hip component. Two to six-year follow-up. *J Bone Joint Surg Am*, 67(1), pp. 48-56.
- Savilahti, S., Myllyneva, I., Pajamaki, K. & Lindholm, T., 1997. Survival of Lubinus straight (IP) and curved (SP) total hip prostheses in 543 patients after 4–13 years. *Arch Orthop Trauma Surg*, Volume 116, pp. 10-13.
- Scheerlinck, T. & Casteleyn, P. P., 2006. The design features of cemented femoral hip implants. *Journal of Bone and Joint Surgery*, 88(11), p. 1409–1418.
- Schmidler, C., 2016. *healthpages.org*. [Online] Available at: <http://www.healthpages.org/surgical-care/hip-joint-replacement-surgery/> [Accessed 22 03 2017].
- Schmidt, J. & Hackenbroch, H., 1994. The Cenos hollow stem in total hip arthroplasty: first experiences in a prospective study. *Arch Orthop Trauma Surg*, 113(3), pp. 117-120.

- Semlitsch, M. & Willert, H. G., 1980. Properties of implant alloys for artificial hip joints. *Medical and Biological Engineering and Computing*, 18(1), p. 511–520.
- Sevilla, P., Aparicio, C., Planell, J. A. & Gil, F. J., 2007. Comparison of the mechanical properties between tantalum and nickel–titanium foams implant materials for bone ingrowth applications. *Journal of Alloys and Compounds*, 439(1-2), pp. 67-73.
- Singh, S. & Harsha, A. P., 2014. *Analysis of Femoral Components of Cemented Total Hip Arthroplasty*, Uttar Pradesh, India: Indian Institute of Technology (Banaras Hindu University).
- Sivasankar, M., 2007. *Failure Analysis Of Hip Prosthesis*, Guwahati: Indian Institute Of Tchnology Guwahati.
- Skipitz, R. & Aspenberg, P., 2000. Pressure-induced periprosthetic osteolysis: a rat model. *J Orthop Res*, 18(3), pp. 481-484.
- Smith, B. H. et al., 2012. Steel foam for structures: A review of applications, manufacturing and material properties. *Journal of Constructional Steel Research*, Volume 71, pp. 1-10.
- Sood, M., 2013. *arthritisresearchuk*. [Online] Available at: <http://www.arthritisresearchuk.org/arthritis-information/arthritis-today-magazine/159-winter-2013/the-challenge-of-revision-hip-replacement-surgery.aspx> [Accessed 9 January 2017].
- Sotereanos, N. & Engh, C., 1995. Cementless femoral components should be made from cobalt chrome. *Clin Orthop*, Volume 313, p. 146–153.
- Speirs, A. D., Heller, M. O., Duda, G. N. & Taylor, W. R., 2007. Physiologically based boundary conditions in finite element modelling. *Journal of Biomechanics*, pp. 2318-2323.
- Speirs, A. D. et al., 2007. Influence of changes in stem positioning on femoral loading after THR using a short-stemmed hip implant. *Clinical Biomechanics*, 22(4), pp. 431-439.
- Spinelli, L. d. F. et al., 2012. Femoral stem-bone interface analysis of logical uncemented stem. *Rev. Bras. Eng. Bioméd*, Volume 28, pp. 238-247.
- Steven, H., Weeden, M. D., Robert, H. & Schmidt, M. D., 2007. The Use of Tantalum Porous Metal Implants for Paprosky 3A and 3B Defects. *The Journal of Arthroplasty*, 22(6), pp. 151-155.

Stolk, J., Verdonshot, N. & Huiskes, R., 1998. *Sensitivity of failure criteria of cemented total hip replacements to finite element mesh density*. Toulouse, France, European Society of Biomechanics.

Stolk, J., Verdonshot, N. & Huiskes, R., 2001. Hip joint and abductor muscle forces adequately represent in vivo loading of a cemented total hip reconstruction. *Journal of Biomechanics*, Volume 34, pp. 917-926.

Sugimoto, K.-i., Hojo, T. & Mizuno, Y., 2017. Torsional Fatigue Strength of Newly Developed Case Hardening TRIP-Aided Steel. *Metals*, 7(9).

Sumner, D. R. & Galante, J. O., 1992. Determinants of stress shielding - design, materials, interface. *Clin Orthop*, Volume 274, pp. 202-206.

Sumner, D. R. & Galante, J. O., 1992. determinants of stress shielding design versus materials versus interface. *Clin Orthopaed Related Res*, Volume 274, pp. 202-212.

Surin, H. B., 2005. *stress shielding effect of the shaft component*. [Online] Available at: http://www.bananarepublican.info/Stress_shielding.htm [Accessed 26 01 2017].

Teoh, S. H., 2000. Fatigue of biomaterials: a review. *International Journal of Fatigue*, 22(10), pp. 825-837.

Thielen, T. et al., 2009. Development of a reinforced PMMA-based hip spacer adapted to patients' needs. *Medical Engineering & Physics*, Volume 31, p. 930–936.

trip4care.com, 2014. *trip4care.com*. [Online] Available at: <http://trip4care.com/the-high-cost-of-hip-replacement/> [Accessed 20 April 2017].

Tuninetti, V., Gilles, G., Péron-Lührs, V. & Habraken, A. M., 2012. Compression Test for Metal Characterization using Digital Image Correlation and Inverse Modeling. *Procedia IUTAM*, Volume 4, pp. 206-214.

Van der Vis, H. et al., 1998. Fluid pressure causes bone resorption in a rabbit model of prosthetic loosening. *Clin Orthop Relat Res*, Volume 350, pp. 201-208.

- Viceconti, M. et al., 2000. Large-sliding contact elements accurately predict levels of bone-implant micromotion relevant to osseointegration. *Journal of Biomechanics*, Volume 33, pp. 1611-1618.
- Walker, P. et al., 2000. Stability and bone preservation in custom designed revision hip stems. *Clin Orthop Relat Res*, Volume 373, pp. 164-173.
- Walowit, J. A. et al., 1997. The analysis, design, and testing of a blood lubricated hydrodynamic journal bearing. *ASAIO J*, 43(5), pp. 556-9.
- Weinans, H., Huiskes, R. & Grootenboer, H. J., 1992. Effects of material properties of femoral hip components on bone remodeling. *J Orthop Res*, 10(6), pp. 845-853.
- Weinans, H., Sumner, D. R., Igloria, R. & Natarajan, R. N., 2000. Sensitivity of periprosthetic stress-shielding to load and the bone density-modulus relationship in subject-specific finite element models. *Journal of Biomechanics*, 33(7), pp. 809-817.
- Wennerberg, A., Albrektsson, T. & Jimbo, R., 2015. *Implant Surfaces and Their Biological and Clinical Impact*. 1st ed. Berlin/Heidelberg, Germany: Springer-Verlag.
- Wennerberg, A., Albrektsson, T. & Jimbo, R., 2015. *Implant Surfaces and Their Biological and Clinical Impact*. 1st ed. Berlin : Springer Berlin Heidelberg.
- whiteclouds, 2015. *Direct Metal Laser Sintering (DMLS)*. [Online] Available at: <https://www.whiteclouds.com/3dpedia-index/direct-metal-laser-sintering-dmls> [Accessed 27 April 2017].
- Willert, H. G., Bertram, H. & Buchom, G. H., 1990. Osteolysis in alloarthroplasty of the hip: the role of bone cement fragmentation. *Clinical Orthopaedics & Related Research*, Volume 258, pp. 108-121.
- Williams, D., 1990. An Introduction to Medical and Dental Materials. In: D. Williams, ed. *Concise Encyclopedia of Medical & Dental Materials*. Oxford, UK: Pergamon Press, p. xvii–xx.
- Williams, J. G. & Gamonpilas, C., 2008. Using the simple compression test to determine Young's modulus, Poisson's ratio and the Coulomb friction coefficient. *International Journal of Solids and Structures*, 45(16), pp. 4448-4459.

Yongtae, J. & Kuiwoon, C., 2010. Design of patient-specific hip implants based on the 3D geometry of the human femur. *Advances in Engineering Software*, Volume 41, pp. 537-547.

Yuan, X., Ryd, L. & Huiskes, R., 2000. Wear particle diffusion and tissue differentiation in TKA implant fibrous interfaces. *J Biomech*, 33(10), pp. 1279-1286.

Zhang, H., 2009. *The Influence of Stem Design and Fixation Methods on the Lifetime of Total Hip Replacement*, Huddersfield: University of Huddersfield.

Appendix

Appendix A

A.1 Mathcad rules of mixture relationship for chapter 4

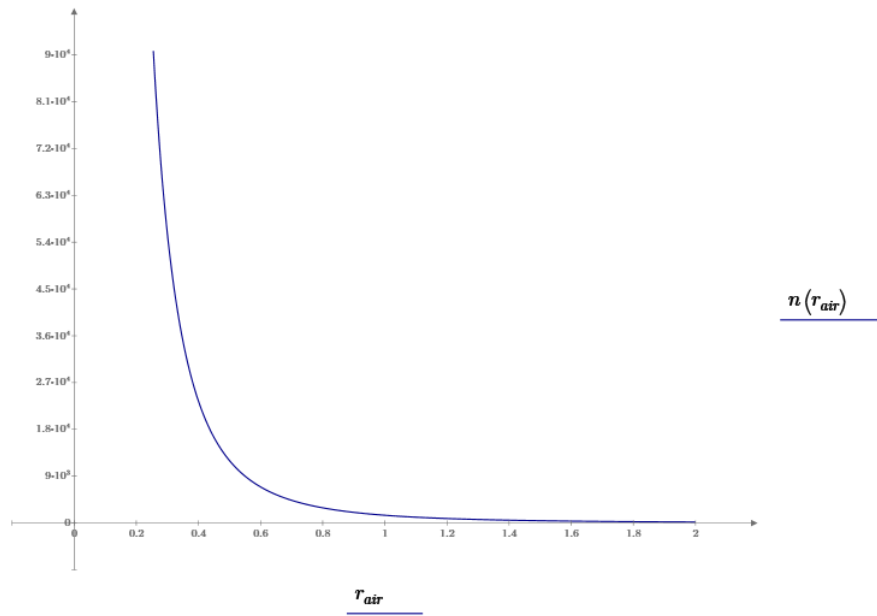


Figure A1: Relationship between radius of spheres (mm) and number of spheres for $f=0.2$

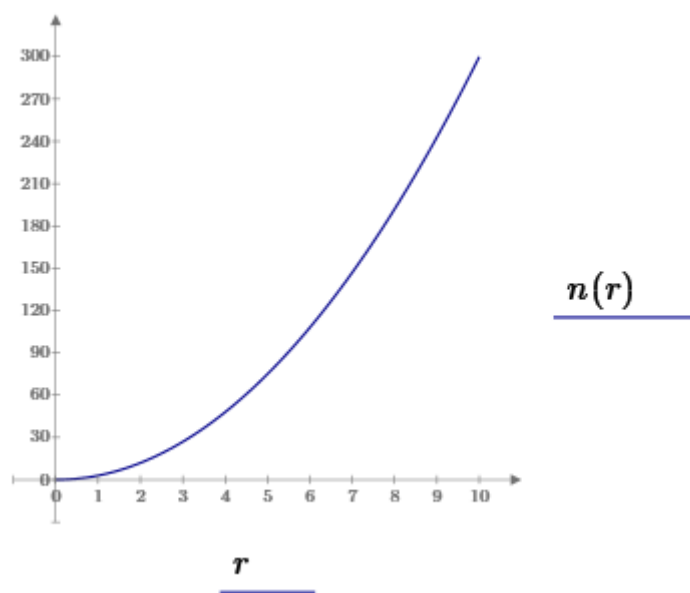


Figure A2: Relationship between number spheres and radius of the cylinder (mm) for $f=0.2$

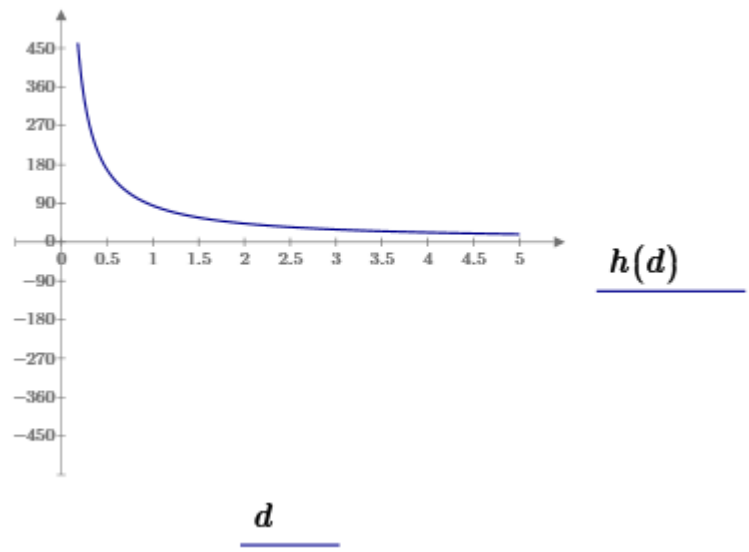


Figure A3: Relationship between hollow shell thickness (mm) and the height of the cylinder for $f=0.2$

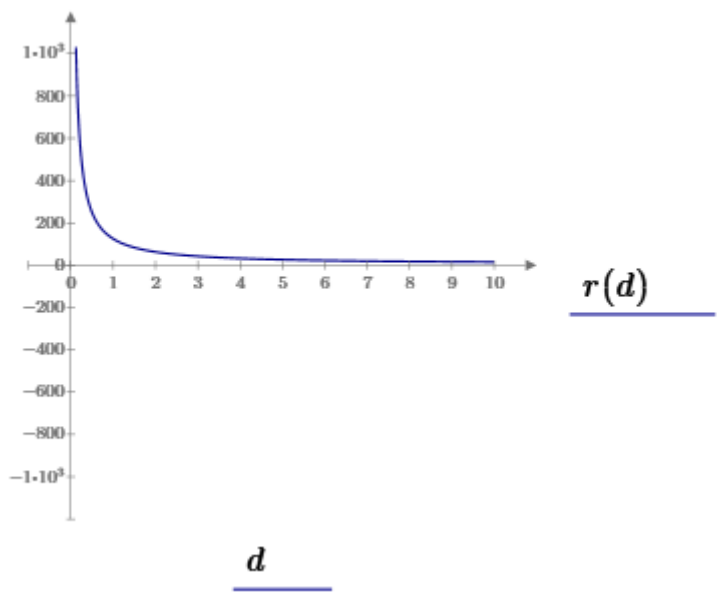


Figure A4: Relationship between radius of shell (mm) and radius of the cylinder for $f=0.2$

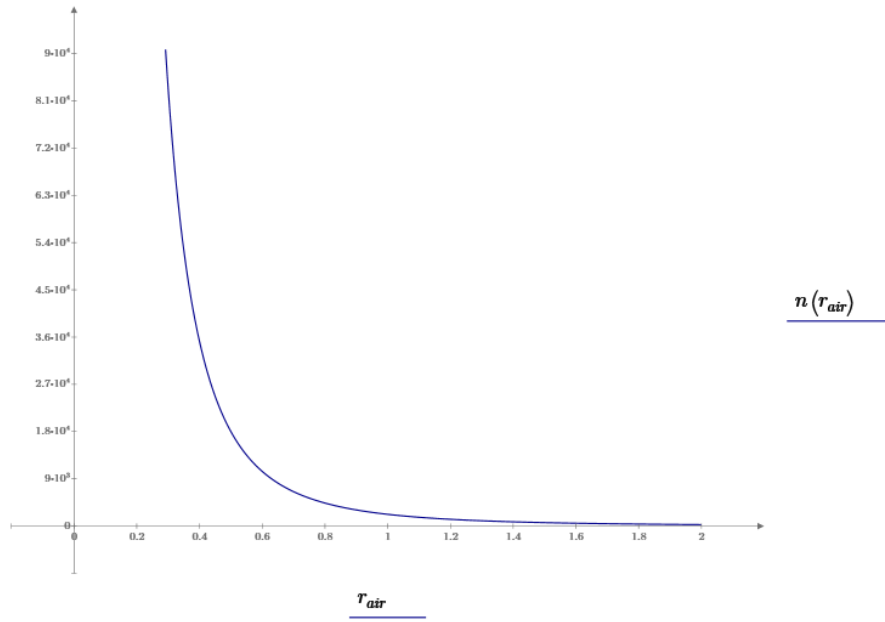


Figure A5: Relationship between radius of spheres (mm) and number of spheres for $f=0.3$

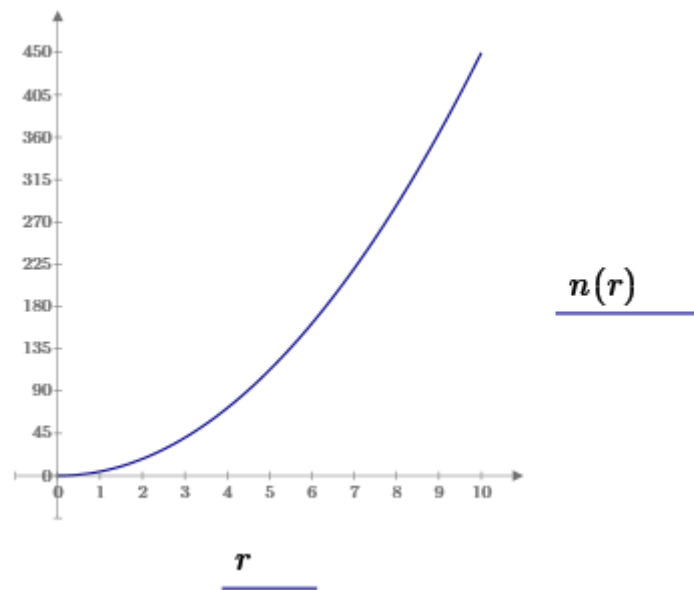


Figure A6: Relationship between number spheres and radius of the cylinder (mm) for $f=0.3$

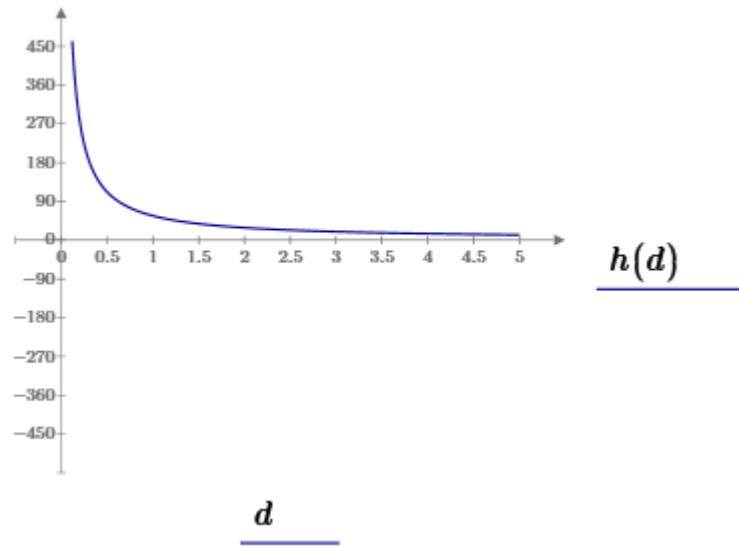


Figure A7: Relationship between hollow shell thickness (mm) and the height of the cylinder for $f=0.3$

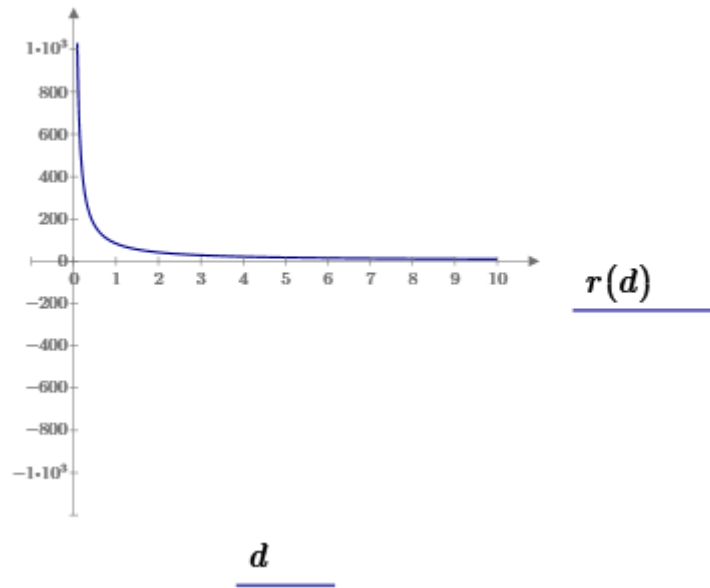


Figure A.8: Figure A4: Relationship between radius of shell (mm) and radius of the cylinder for $f=0.3$

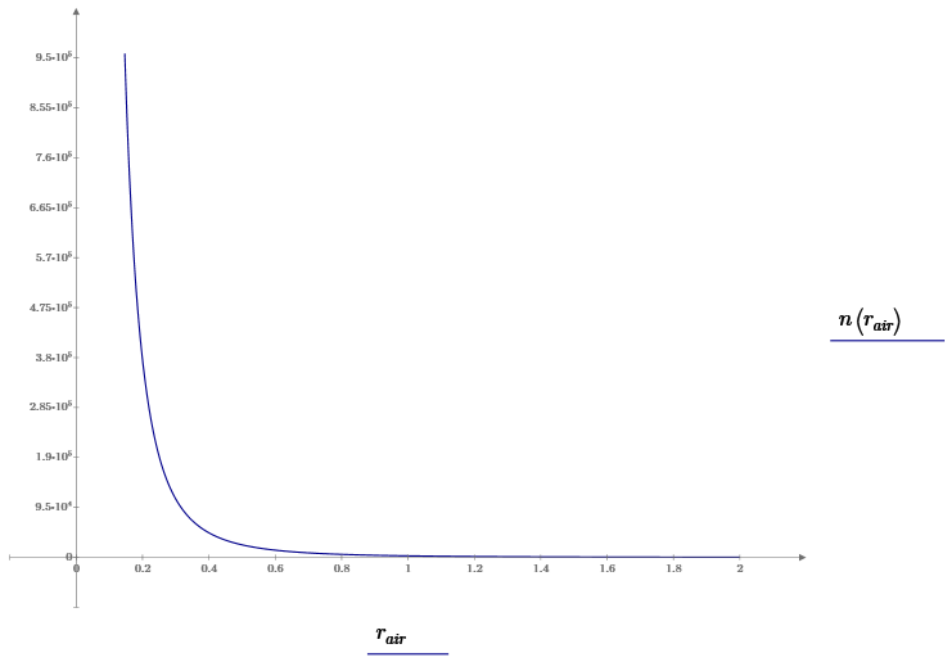


Figure A9: Figure A5: Relationship between radius of spheres (mm) and number of spheres for $f=0.4$

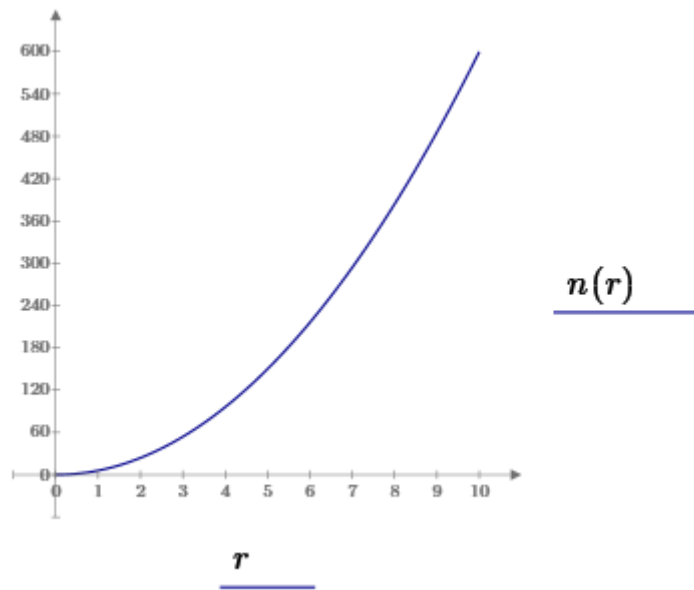


Figure A9: Relationship between number spheres and radius of the cylinder (mm) for $f=0.4$

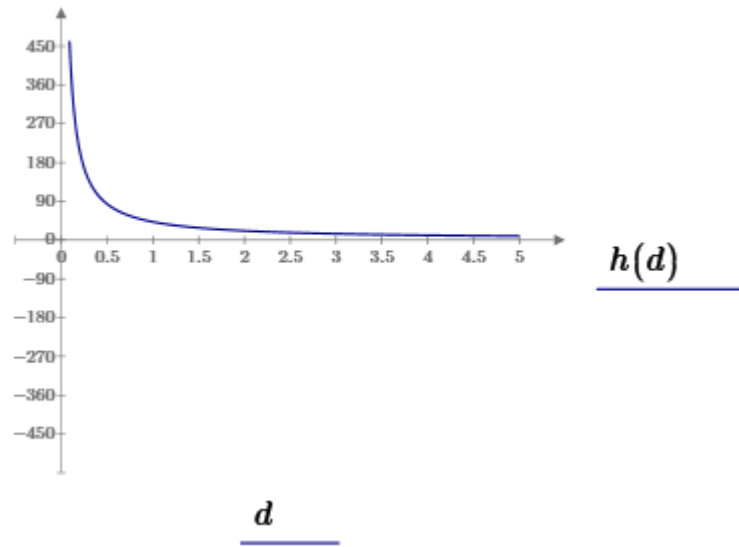


Figure A9: Relationship between hollow shell thickness (mm) and the height of the cylinder for $f=0.4$

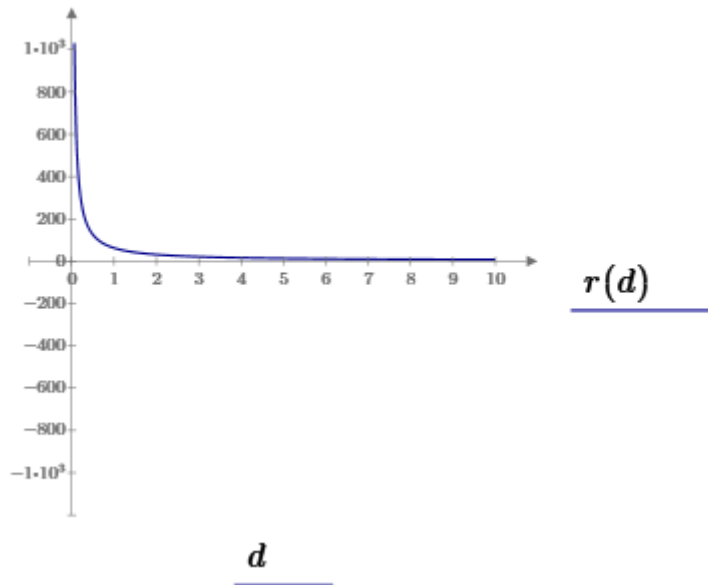
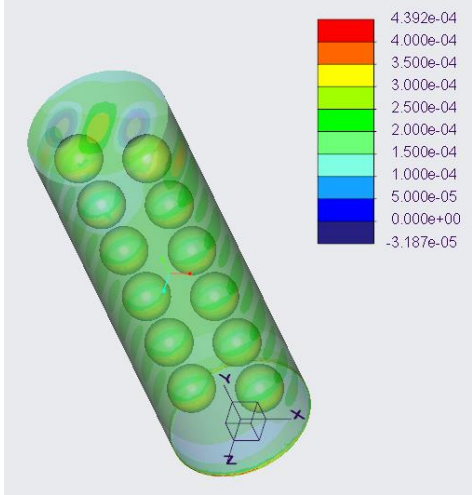
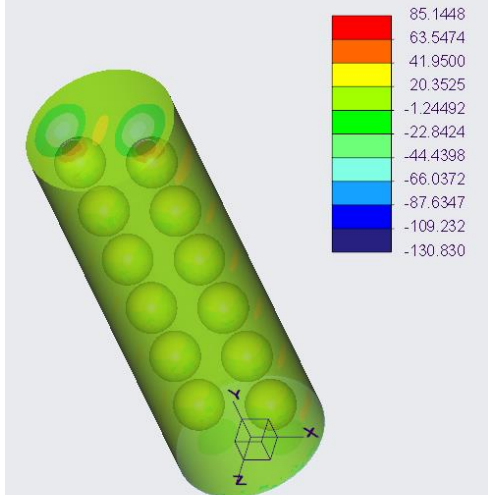
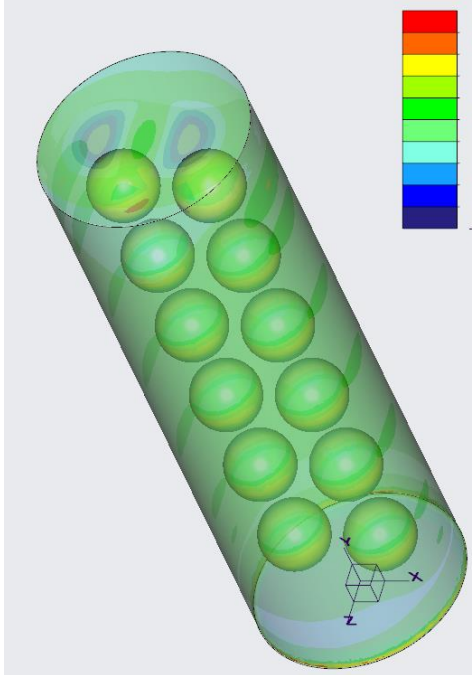
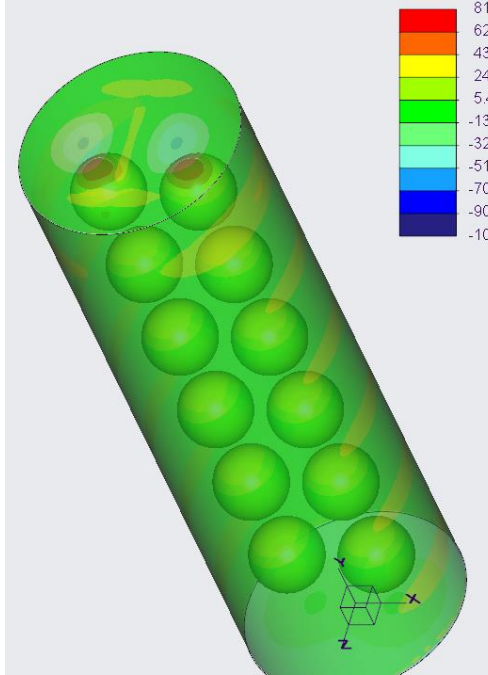


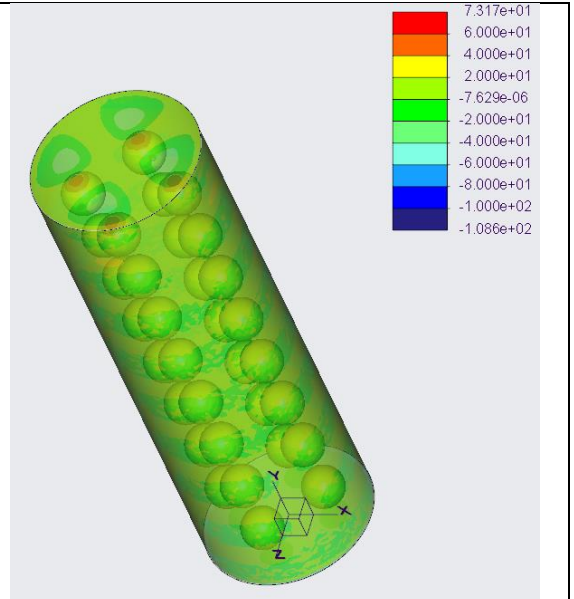
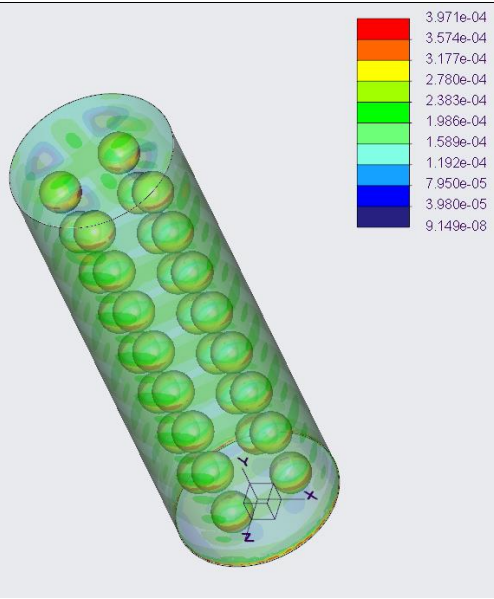
Figure A9: Figure A4: Relationship between radius of shell (mm) and radius of the cylinder for $f=0.4$

Appendix B

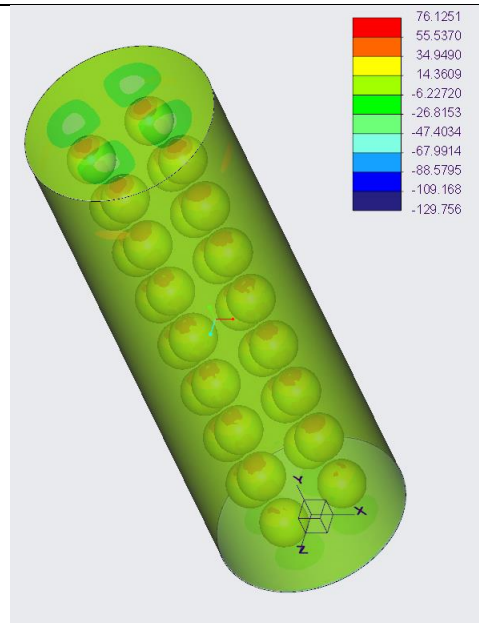
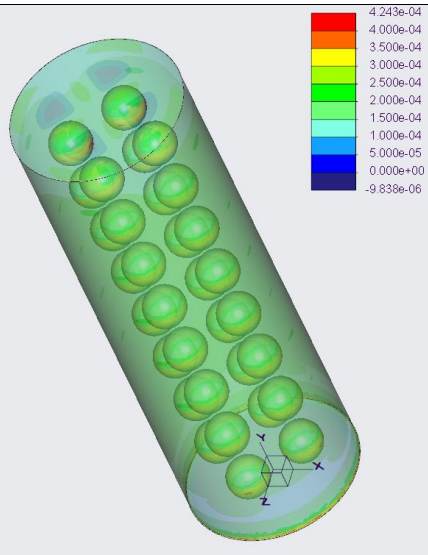
B.1 Maximum principle stress and strain for chapter 5 samples

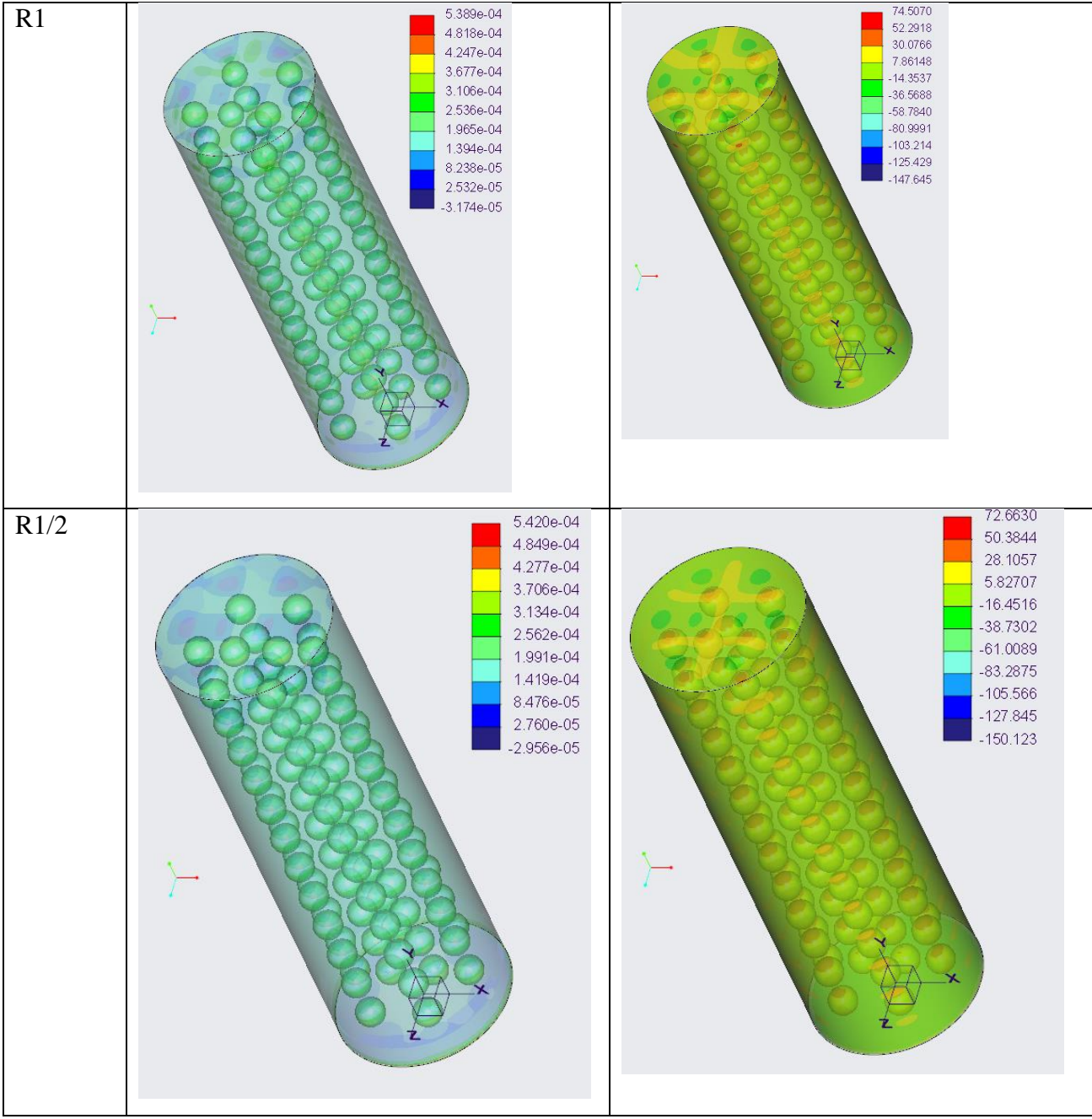
	Max principal strain	Max principal stress (MPa)
R2	 <p>4.392e-04 4.000e-04 3.500e-04 3.000e-04 2.500e-04 2.000e-04 1.500e-04 1.000e-04 5.000e-05 0.000e+00 -3.187e-05</p>	 <p>85.1448 63.5474 41.9500 20.3525 -1.24492 -22.8424 -44.4398 -66.0372 -87.6347 -109.232 -130.830</p>
R2/2	 <p>4.293e-04 4.000e-04 3.500e-04 3.000e-04 2.500e-04 2.000e-04 1.500e-04 1.000e-04 5.000e-05 0.000e+00 -3.294e-05</p>	 <p>81.8749 62.7684 43.6619 24.5555 5.44899 -13.6575 -32.7640 -51.8704 -70.9769 -90.0834 -109.190</p>

R1.5/2

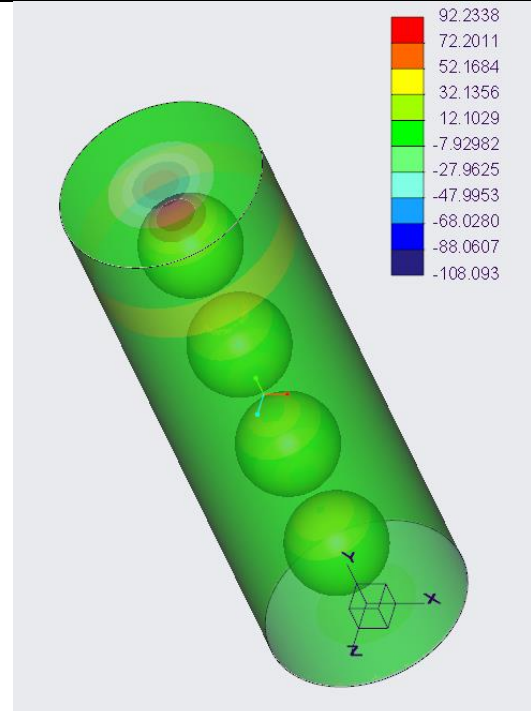
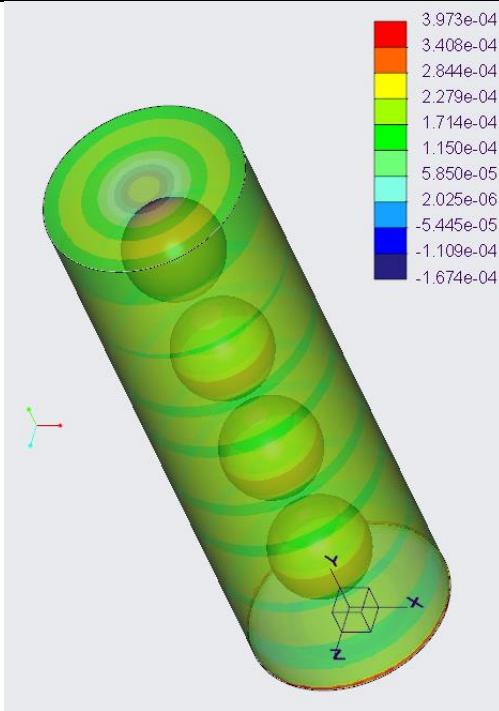


R1.5

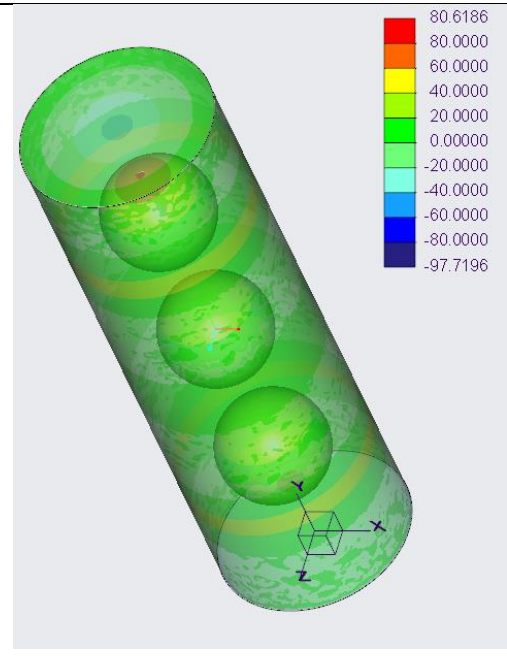
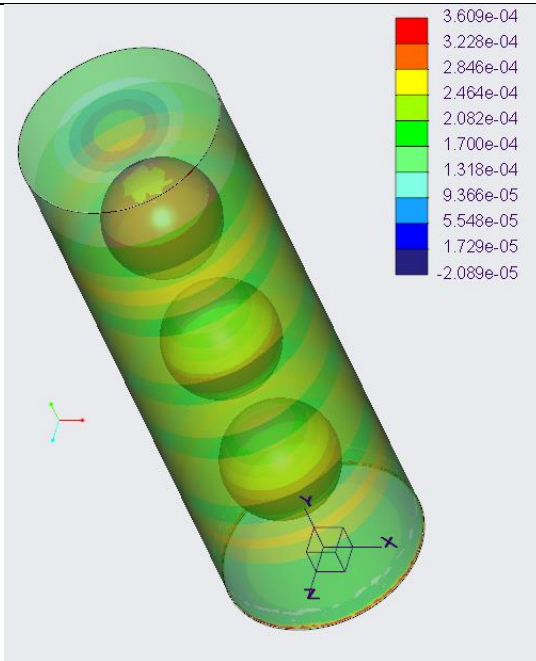


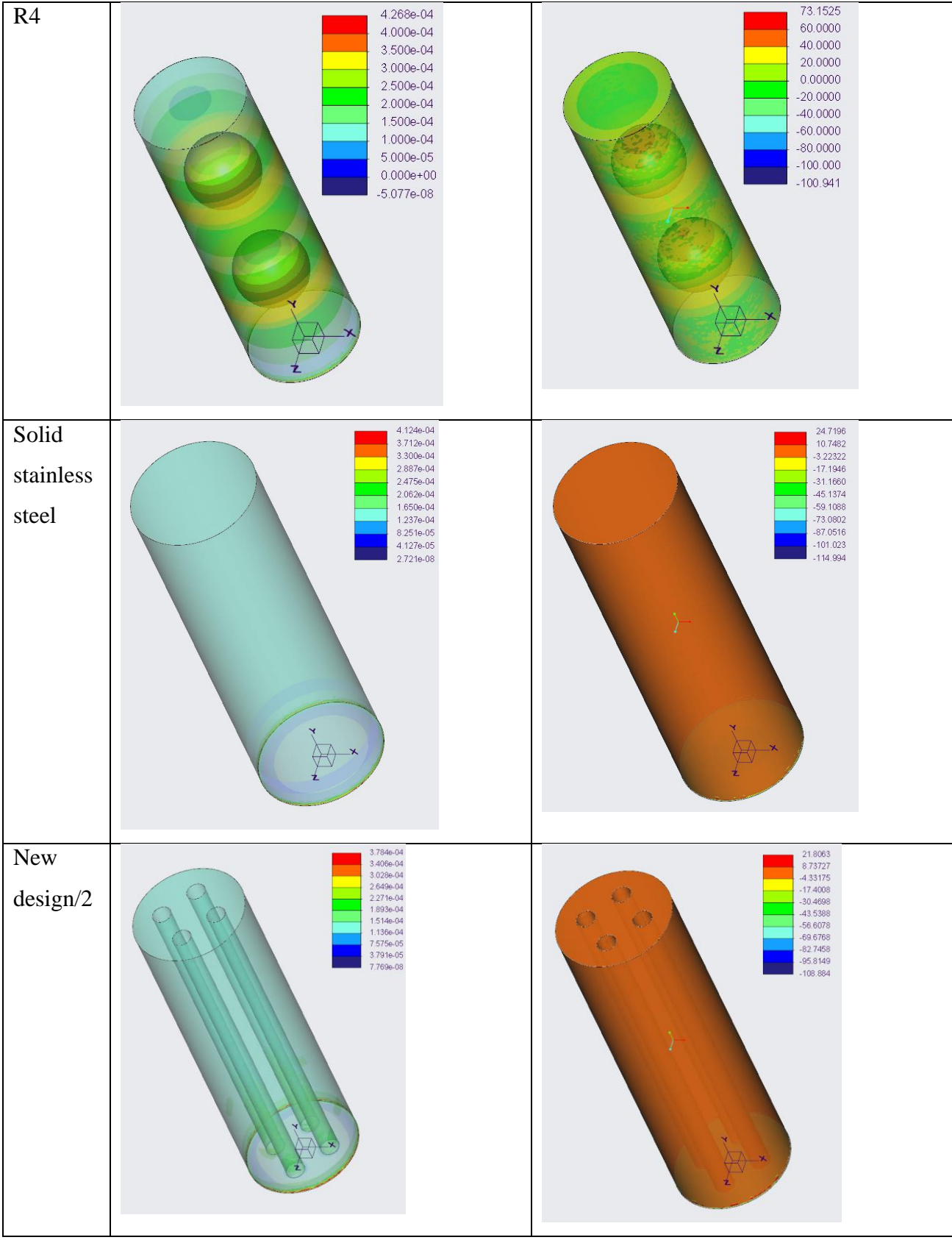


R3



R3.5





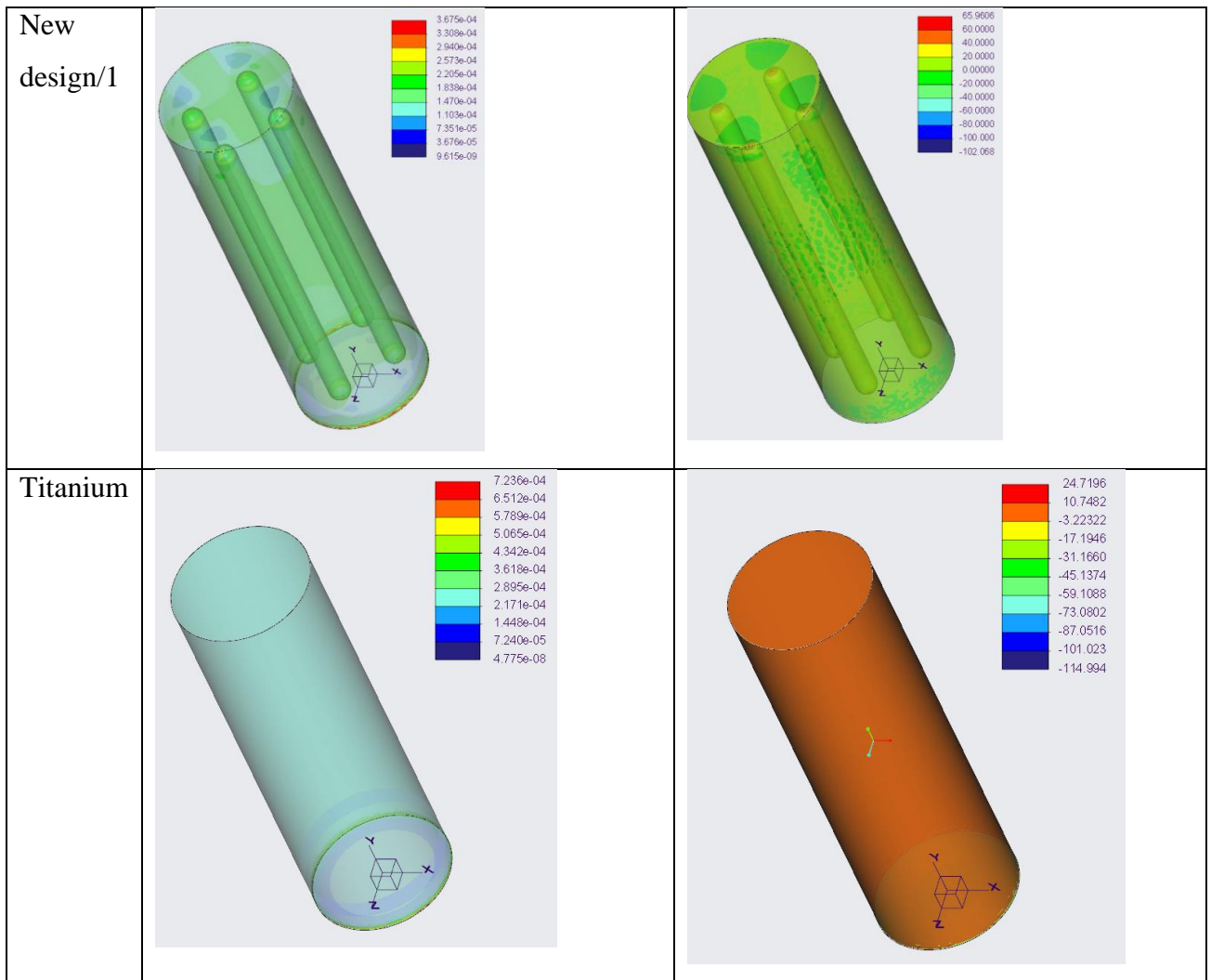


Table B1: Maximum principle stress and strain for chapter 5 samples

B.2 Experimental results of Stress-Strain graphs for chapter 5 samples

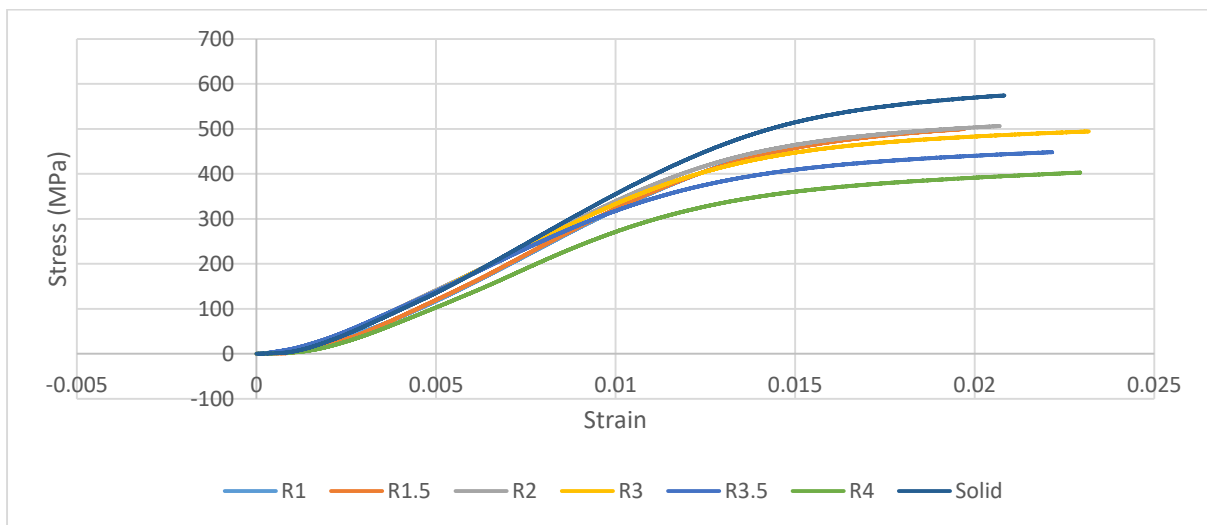


Figure B2: Experimental results for solid and hallowed spheres samples

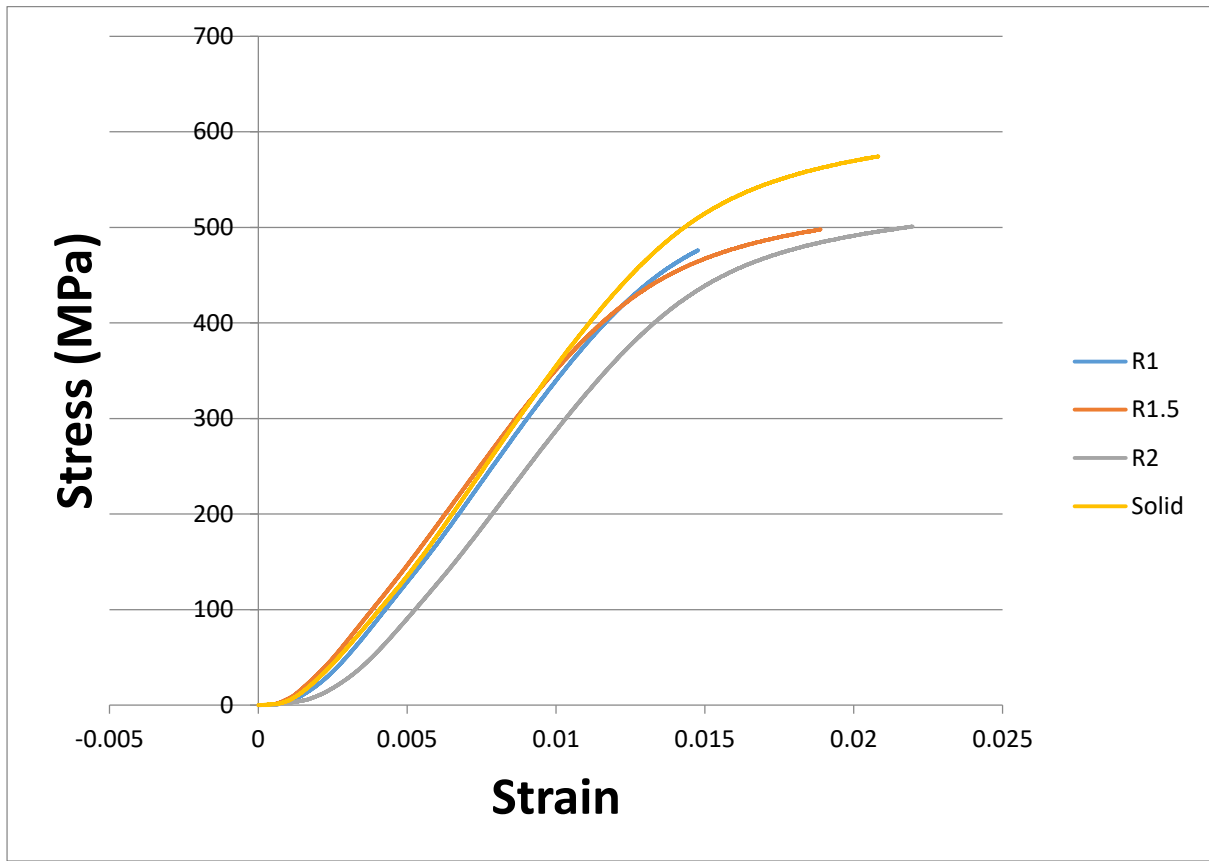


Figure B3: Experimental results for solid and hallowed spheres samples

B.3 Mathcad rules of mixture relationship for chapter 5

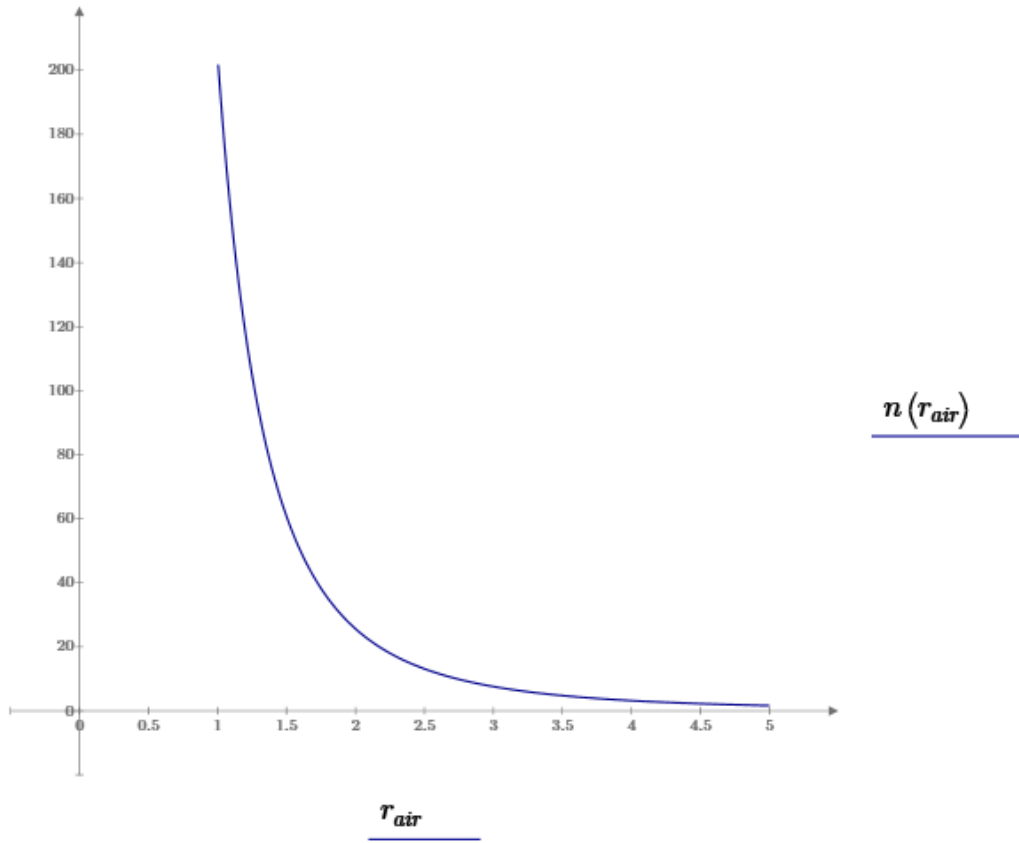


Figure B4: Relationship between radius of spheres (mm) and number of spheres for $f=0.2$

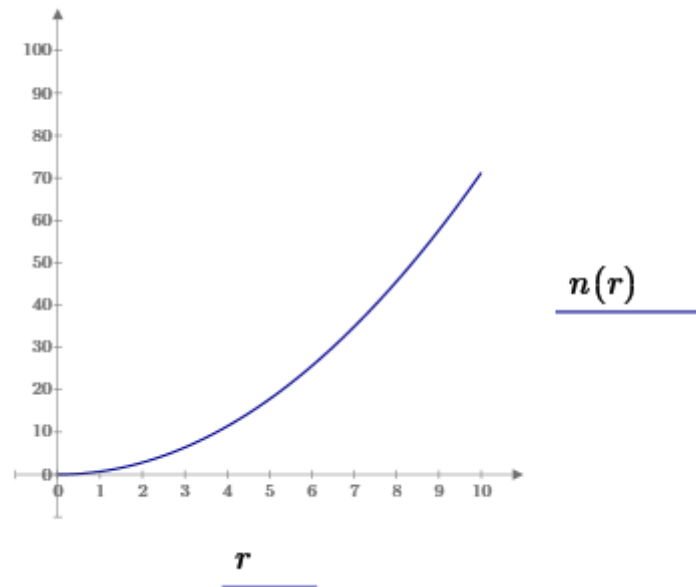


Figure B5: Relationship between radius of samples (mm) and number of spheres for $f=0.2$

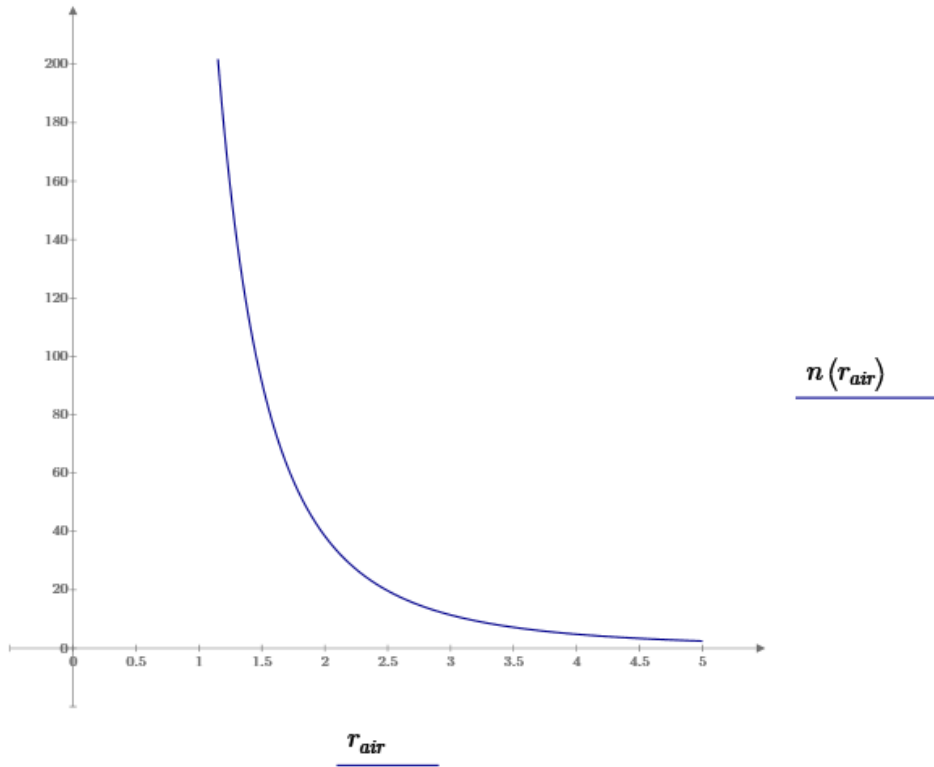


Figure B6: Relationship between radius of spheres (mm) and number of spheres for $f=0.3$

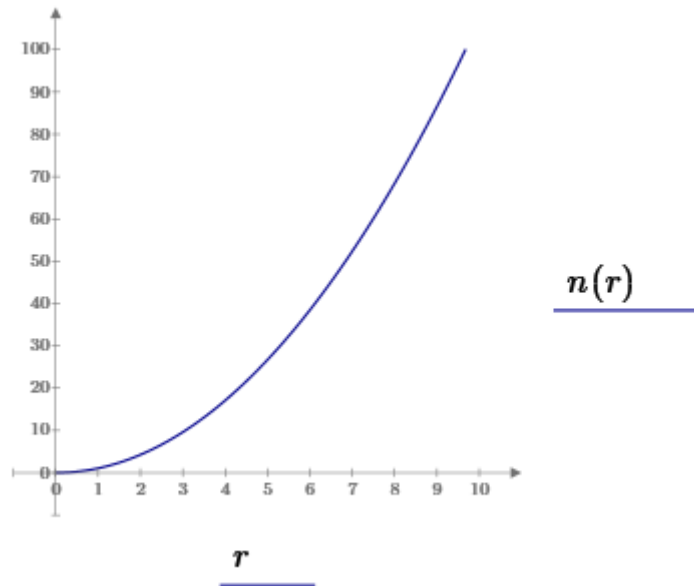


Figure B7: Relationship between radius of samples (mm) and number of spheres for $f=0.3$

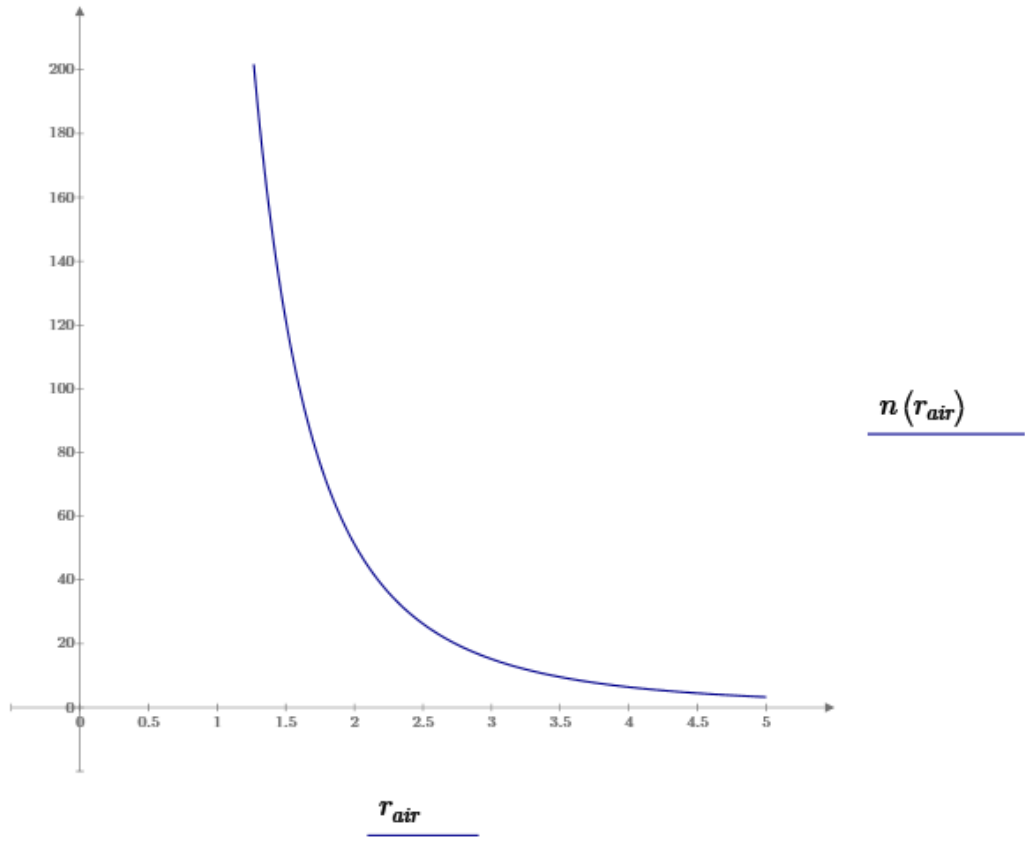


Figure B8: Relationship between radius of spheres (mm) and number of spheres for $f=0.4$

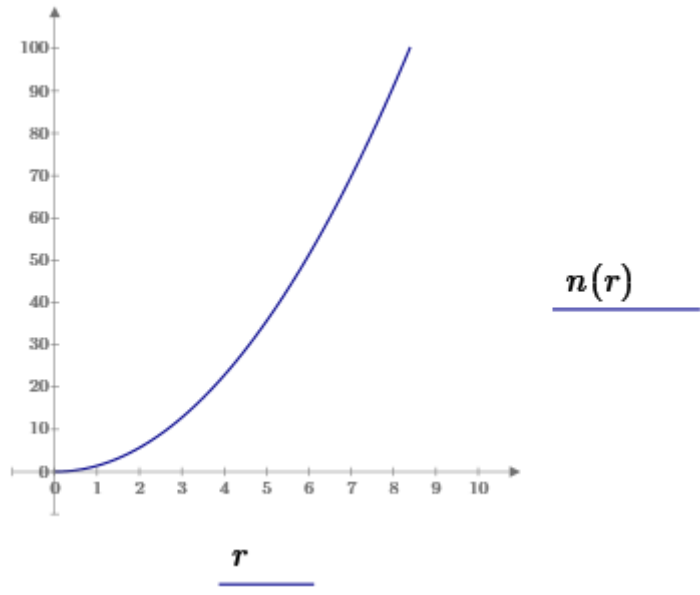
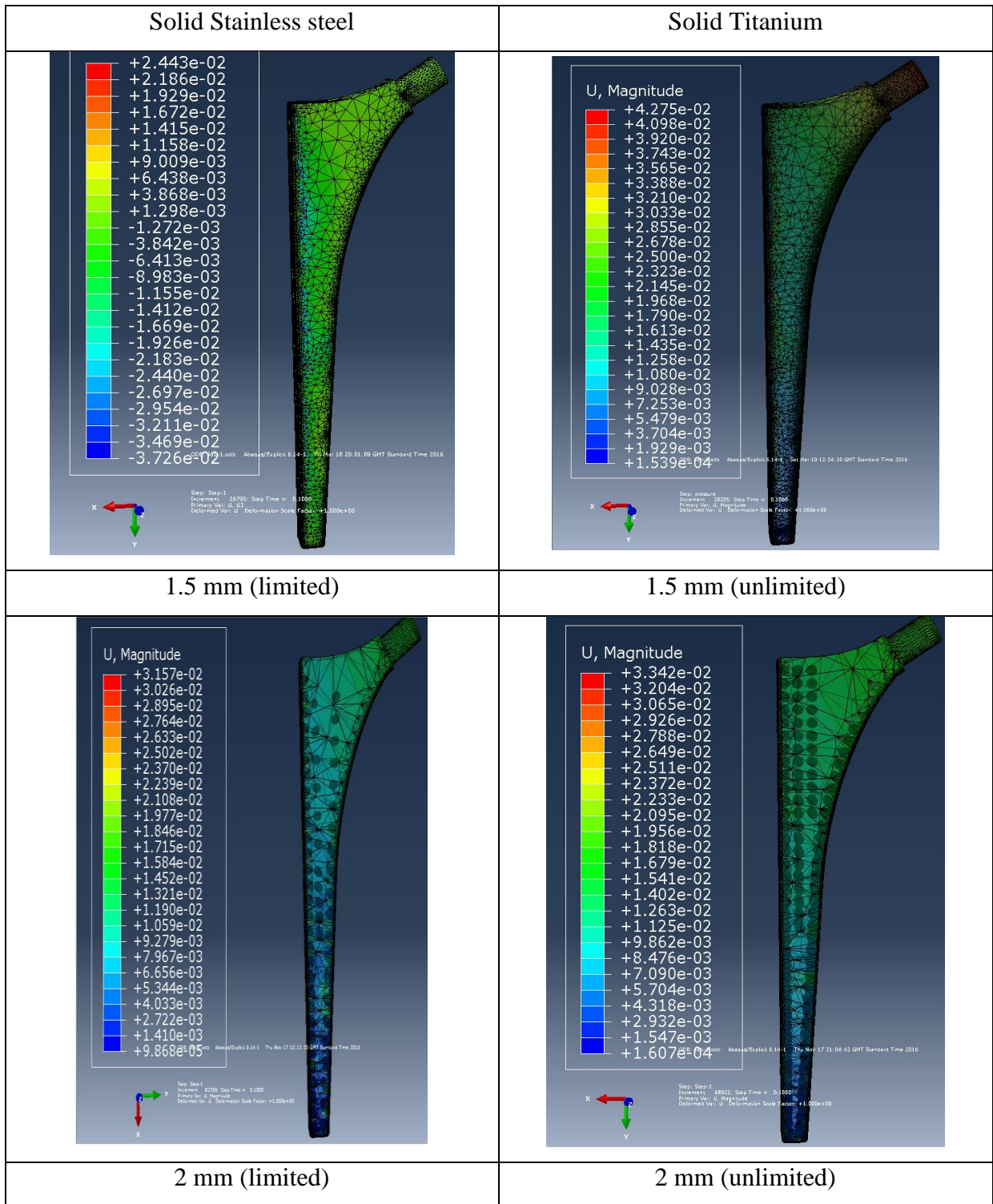
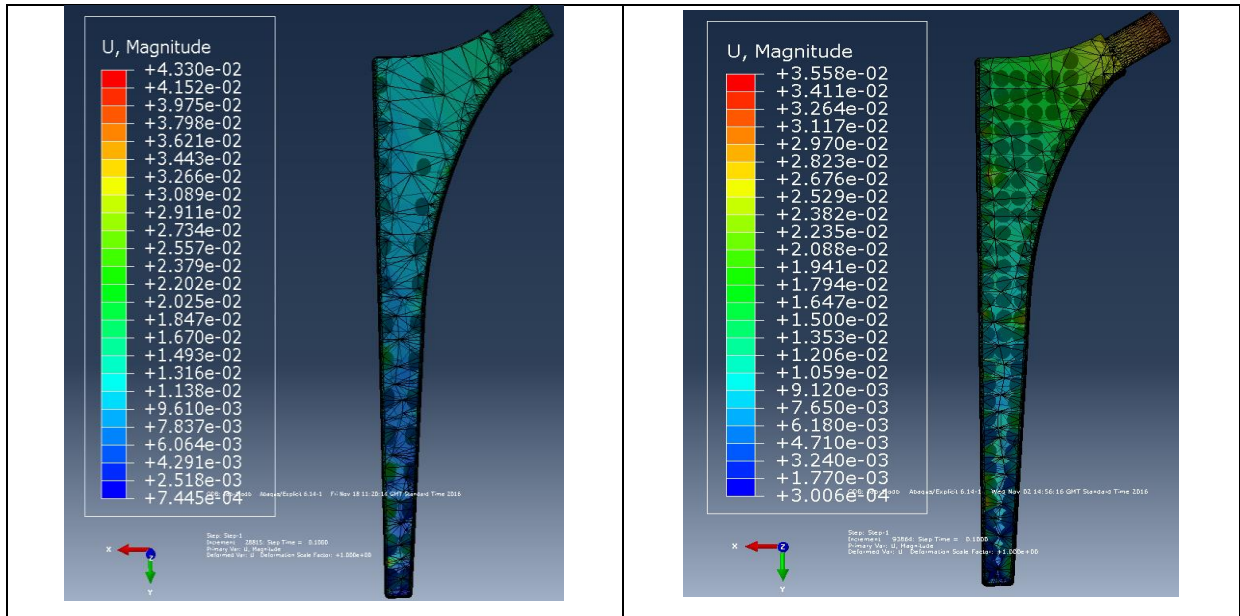


Figure B9: Relationship between radius of samples (mm) and number of spheres for $f=0.4$

Appendix C

C.1 Displacement results in FEA for different implant for chapter 6





1 mm

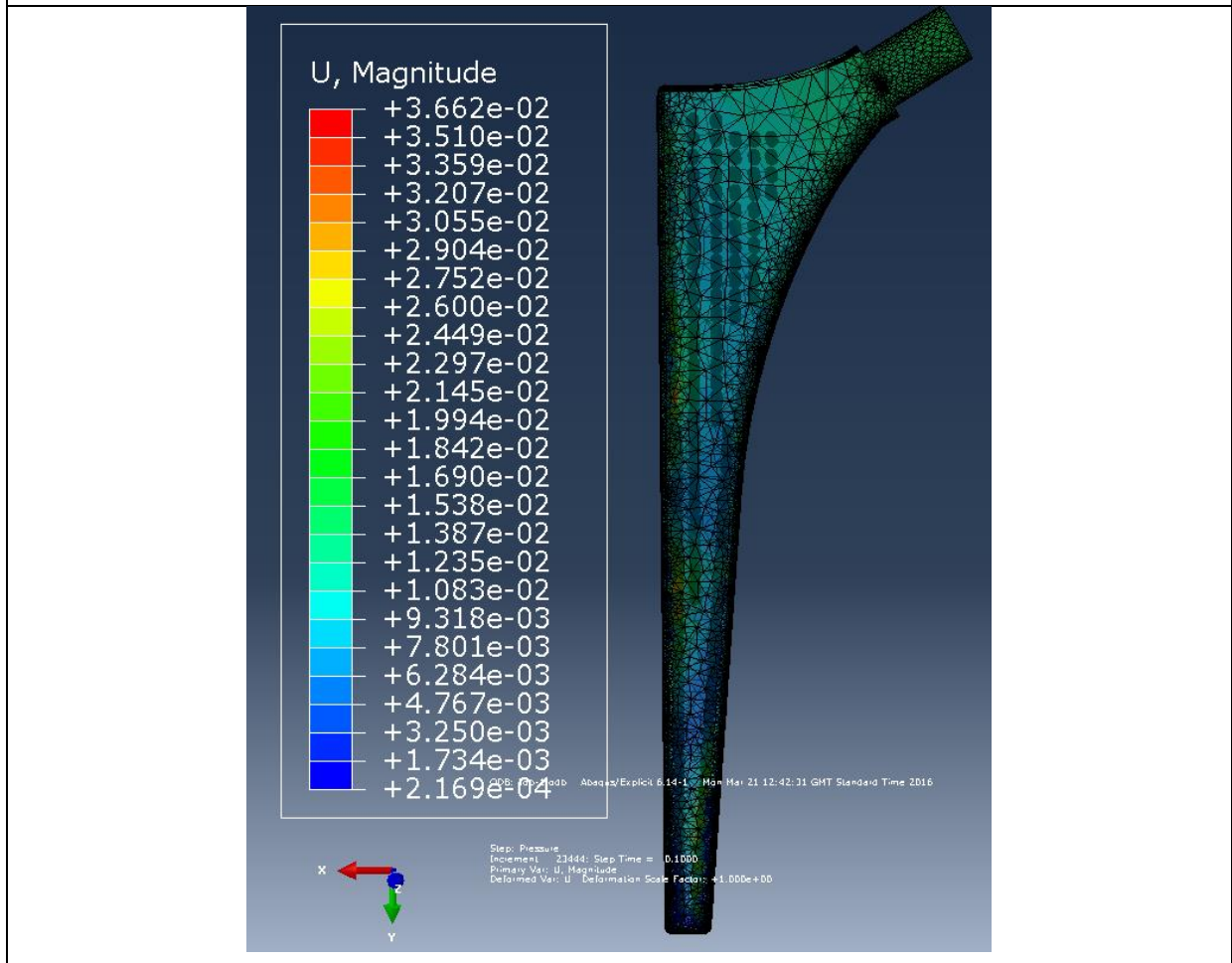


Figure C1: Displacement results in FEA for different implants

C.2 Mathcad rules of mixture relationship for chapter 6

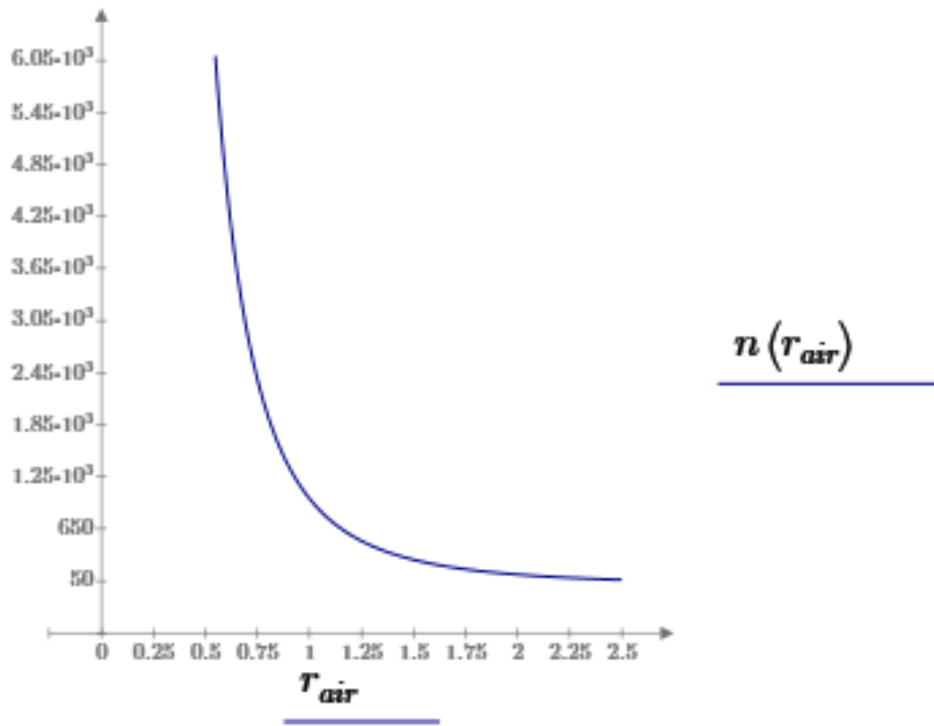


Figure C2: Relationship between radius of spheres (mm) and number of spheres for $f=0.2$

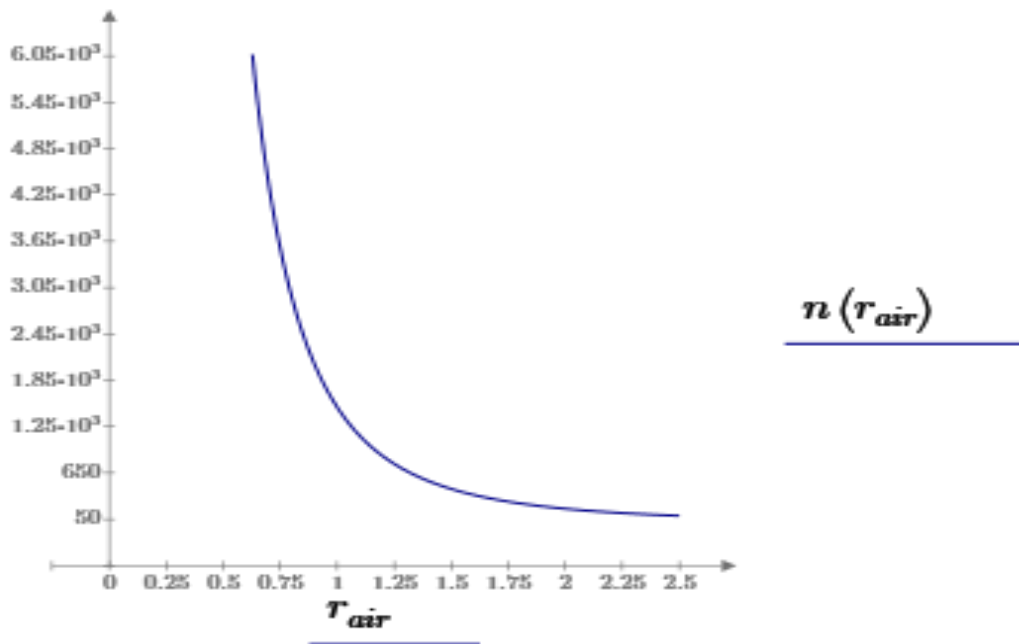


Figure C2: Relationship between radius of spheres (mm) and number of spheres for $f=0.3$

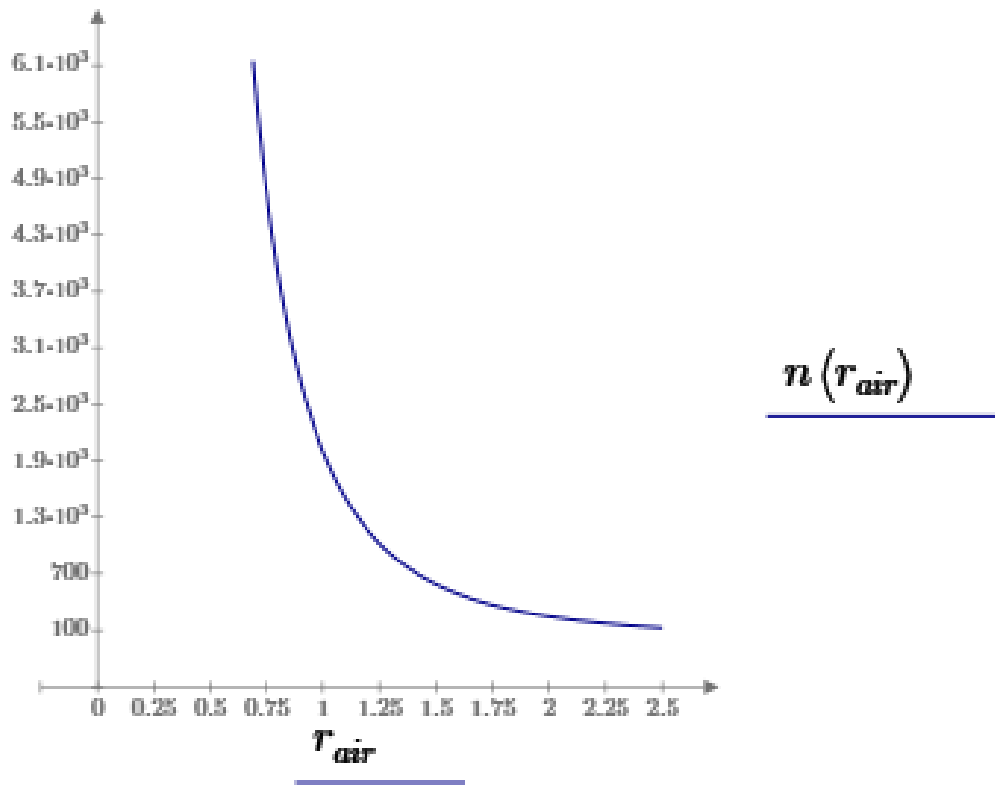


Figure C2: Relationship between radius of spheres (mm) and number of spheres for $f=0.4$